

The Physics of Ultracold Sr₂ Molecules: Optical Production and Precision Measurement

Christopher Butler Osborn

Submitted in partial fulfillment of the
requirements for the degree
of Doctor of Philosophy
in the Graduate School of Arts and Sciences

COLUMBIA UNIVERSITY

2013

©2013

Christopher Butler Osborn

All Rights Reserved

ABSTRACT

The Physics of Ultracold Sr₂ Molecules: Optical Production and Precision Measurement

Christopher Butler Osborn

Ultracold molecules provide an exciting testing ground for studies of fundamental interactions, new states of matter, and metrology. Diatomic molecules based on two-electron atoms are especially suitable for precise tests of interatomic interactions, molecular quantum electrodynamics, electron-proton mass ratio variations, and other measurements in molecular and fundamental physics. This thesis describes the construction of a new strontium apparatus, from initial vacuum system setup through characterization of ultracold atom samples, followed by a new method of efficient, all-optical production of ultracold ⁸⁸Sr₂ molecules in an optical lattice, with detection via optical fragmentation. High- Q spectra of the weakly bound molecules in magnetic fields are studied, yielding precise binding energies, anomalously large molecular g factors resulting from large nonadiabatic effects, and strongly enhanced magnetic susceptibility. The thesis then concludes with an outlook on future experiments in our lab, including studies of forbidden molecular transitions, and longer term studies of fundamental physics from deeply bound Sr₂.

Table of Contents

1	Introduction	1
1.1	Laser cooling and atomic physics	1
1.2	Cold molecules	4
1.3	Thesis overview	6
2	Apparatus	9
2.1	Atom oven and vacuum system	10
2.1.1	Oven heating	10
2.1.2	Atom beam	12
2.1.3	Multispecies oven for future work	16
2.1.4	Vacuum system	18
2.2	461 nm light source	19
2.2.1	Extended cavity diode laser	20
2.2.2	Tapered amplifier	25
2.2.3	Nonlinear crystal and second harmonic generation	26
2.2.4	Locking system	28
2.2.5	Power distribution, frequency offsets	29
2.3	Zeeman slower	32
2.3.1	Design considerations	32
2.3.2	Computer control of the field profile	33
2.3.3	Real-time optimization of atom slowing	35
2.4	The 1S_0 - 1P_1 MOT	40

2.4.1	Principle of a magneto-optical trap	41
2.4.2	Quadrupole coils and compensation coils	42
2.4.3	Repumper lasers	43
2.4.4	Imaging	43
2.4.5	Characteristics of the millikelvin MOT	46
2.5	689 nm light source	50
2.5.1	High-finesse cavity	50
2.5.2	Setup, locking electronics, frequency offset and control	52
2.5.3	Pound-Drever-Hall lock	53
2.6	The 1S_0 - 3P_1 MOT	55
2.6.1	MOT transfer	55
2.6.2	Absorption imaging and the Navitar objective	57
2.6.3	The MOT setup and initial alignment	58
2.6.4	Daily maintenance	58
2.6.5	Characteristics of the microkelvin MOT	59
2.7	The optical lattice trap	61
2.7.1	Magic wavelength	63
2.7.2	Setup	64
2.7.3	Trap parameters	68
2.7.4	3D lattice	70
2.8	The spectroscopy apparatus	71
2.9	The lab control software	72
3	Production of ultracold $^{88}\text{Sr}_2$ molecules	78
3.1	Sr_2 molecular notation	78
3.1.1	The Born-Oppenheimer picture and Hund's case (a)	79
3.1.2	Empirical spectroscopist's notation	80
3.1.3	Relativistic picture and Hund's case (c)	81
3.1.4	Rovibrational indices	82
3.1.5	Selection rules	82
3.2	Photoassociation	83

3.3	Two-color photoassociation	86
3.4	Franck-Condon factors	91
3.4.1	Fitting function	93
3.4.2	Systematic shifts	100
3.5	Molecule production and detection	104
4	Binding energies and QED	110
4.1	Binding energies and systematic effects	116
4.1.1	0_u^+ ($v' = -1, J' = 1$) binding energy	117
4.1.2	0_u^+ ($v' = -2, J' = 1$) binding energy	120
4.1.3	0_u^+ ($v' = -2, J' = 3$) binding energy	127
4.2	Summary and prospects for QED effects in Sr_2	132
5	Linear and quadratic Zeeman shifts in Sr_2	134
5.1	The 0_u^+ and 1_u states are mixed	134
5.2	Linear shifts, g factor measurement	138
5.3	Quadratic and higher order shifts, magnetic susceptibility	141
6	Outlook	145
	Bibliography	147

List of Figures

2.1	Relevant electronic transitions for cooling and trapping ^{88}Sr . The transition wavelengths and decay rates are labeled.	10
2.2	A schematic view of the physical apparatus, for the purpose of understanding the general relationships between the core components. Some detail is left out - e.g. schematics for the laser systems and their locking schemes can be found later in the chapter - and objects are not to scale with one another. The side view is also for general understanding, and has been simplified further from the overhead view.	11
2.3	Log plot of Sr vapor pressure.	12
2.4	Eutectic diagram for Sr and Ni. Source: [Nash, 1990]	13
2.5	Rendering of the oven design, assembled with the fitted microtube holder.	14
2.6	Schematic showing the various apertures reducing the atomic beam divergence and transfer.	15
2.7	Microtube holder, before assembly (left). Cross-sectional photograph of the assembled microtubes in the holder (right).	15
2.8	View of the microtubes inside the nozzle, installed in the oven vacuum component just after installation with accumulated condensation (right), and view on-axis confirming the line-of-sight, illuminated with a flashlight (left).	16
2.9	Schematic of the second generation oven. The nozzles separating the Sr and Yb chambers allow for equal vapor pressures of both species in the central mixing chamber.	17
2.10	Diagram of the differential pumping scheme (two pumps).	19

2.11	Pictures of the atomic beam shutter, before installation into the system. The positive and negative leads to the shutter are designed to be compatible with high vacuum environments.	20
2.12	Schematic of the ECDL feedback principle. The first order off of the diffraction grating is fed back into the diode, causing stimulated emission. The wavelength of the feedback light is determined by the angle of the feedback mirror. The zeroth order is the output from the ECDL.	21
2.13	Blueprint of the current ECDL baseplate design (left). SolidWorks rendering of an older baseplate design, with representative mirror, diffraction grating and diode housing (right).	22
2.14	Schematic of the ECDL feedback principle. The first order off of the diffraction grating is fed back into the diode, causing stimulated emission. The wavelength of the feedback light is determined by the angle of the feedback mirror. The zeroth order is the output from the ECDL.	23
2.15	Booster circuit for the T1 temperature stage.	24
2.16	SolidWorks rendering (left), in which the TA is depicted in green, and picture (right) of the tapered amplifier setup.	26
2.17	Diagram of the bowtie cavity. T is the input transmission coefficient for infrared light, and R is the focusing radius of the curved mirrors.	27
2.18	Blueprint of the ideal bowtie cavity dimensions (breadboard holes are spaced by 1 inch). The initial alignment was achieved by printing this at physical scale, cutting holes for the mirror mounts, and taping to the breadboard. After the alignment was achieved, the blueprint was removed from the breadboard.	28
2.19	Schematic of the 461 nm laser system, with detail given to the electronic feedback for the frequency-doubling cavity, as well as for the saturated-absorption locking feedback system.	30

2.20	Scope traces for the frequency-doubling cavity (left), and the vapor cell atom lock (right). For the doubling cavity, the upper channel trace monitors the error signal, and the lower trace monitors the actual blue power output from the cavity. Note that the full error signal of the vapor cell lock is often not within the mode hop-free scanning range of the diode.	31
2.21	Picture of the ZS installed on the experiment, lid off (left). SolidWorks rendering of the motor attachments to the magnets (right).	33
2.22	(a) Test case in which the field value was halved at all points along the ZS path. (b) Test case in which the field profile was compressed over half the original length. Switching in both cases is achieved in < 0.5 s.	34
2.23	Plot of the best loading rates achieved by various optimization algorithms. The colored lines are several loading rates achieved by the genetic algorithm, and the gray lines are those achieved by the local algorithm.	36
2.24	The field profiles produced by the local algorithm (dark gray) and the genetic (red).	36
2.25	A model of the velocity profile of atoms in the field profiles produced by (a) the original design, (b) the local solution, and (c) the genetic solution. . . .	38
2.26	Picture of the vacuum chamber with a typical mK blue MOT present. . . .	40
2.27	Diagram of the mechanism of a magneto-optical trap. The quadrupole magnetic field profile grows linearly outward from the trap center, as evidenced here by the slope of the $m = \pm 1$ magnetic sublevels of the 1P_1 state. Photons of the MOT laser, at frequency ω_L , are only on-resonance when the Zeeman shift and the Doppler shift match the detuning of the incoming laser beam. Circularly-polarized light ensures that photons will only be absorbed by the beam whose momentum absorption kick restores atoms toward the trap center.	41
2.28	One of the two quadrupole coils, before installation on the system (left). The joining between the hollow, enamel-coated quadrupole coils and the feed from the water cooling system (right).	43

2.29	Plot of the MOT coils field profile along the atom beam axis. The field crossing point marks the trap center, with a field gradient of 25 G/cm for 25 A of current.	44
2.30	Pictures of the compensation coils surrounding the vacuum chamber, where the coils have been traced with dashed white lines. At left, a picture of the large x and y axis compensation coils. These require ~ 75 turns to achieve the 3 G design setpoint. At right, a picture of the vertical z axis coils, mounted closer to the chamber, and therefore requiring only ~ 25 turns to achieve the design setpoint (the opposing pair is out of view). Notice that for the vertical set, there are square as well as circular coils. The circular coils were added recently in order to perform measurements at much higher, ~ 40 G field strengths. These were not used in any of the measurements for this thesis.	45
2.31	Inverting summing amplifier used for feedback on the vertical compensation coils, for steadying the position of the red MOT. The circuit sums the current from the compensation coils driver with the small correction that comes from the MEDA Gaussmeter.	46
2.32	Diagram of the optical repumper scheme (left), as well as a schematic of the apparatus (right). We employ a software feedback system: two channels from our wavemeter monitor the repumpers lasers, and the output controls the PZT controller voltages on the ECDL feedback mirrors. The sensitivity of the wavemeter is sufficient for repumper locking to ~ 1 MHz.	47
2.33	An illustration of the 3-step absorption imaging process. The third image is used to subtract out imperfections in the camera, the second for imperfections in the imaging beam, and the first for the actual picture of the atoms, generated by their shadow.	48
2.34	The absorption imaging sequence.	49
2.35	Schematic of the 689A laser and locking electronics.	51
2.36	Solidworks rendering of The high-finesse ULE cavity.	52

2.37	Error signal from the PDH cavity (left). Spectrum analyzer monitor of the laser lock (right).	54
2.38	The red MOT broadband (left) and final, single-frequency (right) spectra as monitored on the spectrum analyzer. See Fig. 2.39 for details on the transfer sequence.	55
2.39	The MOT transfer sequence voltages applied to control the red trapping beams. We found that a small overshoot on the center frequency detuning to 7.5 V, and then back to 7 V (40 MHz), maximized the transferred atom number. Also note that the signal to the AOM that controls the MOT beam powers is ramped down slightly, to reduce saturation and minimize the final trap temperature.	56
2.40	Calibration of the Navitar objective using the free-fall of the atom sample. .	57
2.41	Magneto-optical trapping force along the vertical axis (left). The offset is due to gravity. The MOT potential energy, where the incline is due to gravity (right). Atoms at μK temperatures pool at the lower edge of the well, creating the bowl shape found in Fig. 2.42.	59
2.42	Super-imposed images of the red MOT for various detunings $\Delta = 2\pi\delta$. For larger detunings, the cold atoms sag to the bottom of the potential well. . .	60
2.43	TOF imaging of the red MOT. Retrieving the expansion of the Gaussian waist of the cloud at several points gives a result for the expansion rate, and therefore the temperature, according to Eq. 2.21. Typical temperatures are $1 - 2 \mu\text{K}$	61
2.44	Diagram of the optical lattice trap. The trap depth and frequency are labeled, as are the red and blue sidebands.	61
2.45	Trapping geometries for the (a) 1D lattice (pancakes), (b) 2D lattice (cigars), and (c) 3D lattice (spheres).	63
2.46	State polarizabilities and magic wavelength crossing point, where m denotes the magnetic sublevel, and p the light polarization relative to the applied magnetic field.	64

2.47	The combined geometry of the 3D lattice (left), broken down into component beams. Black arrows represent pointing vector orientations, and blue arrows represent polarization vectors. Circles represent vector orientations perpendicular to the page.	65
2.48	Schematic for 914 nm lattice laser setup.	66
2.49	Photoassociation losses in 1D and 3D trapping regions. Note that the initial atom number is higher in the 3D region due to greater trap depths from the sum of the substituent beam depths. Our measurements were inconclusive on whether or not there is a distinct, 3D core in which photoassociation is suppressed.	71
2.50	Schematic of the spectroscopy apparatus. Lasers 689B and C are phase-locked to 689A, while 689D is phase-locked to 689C. Each spectroscopy laser is shuttered using a double-pass AOM at a total frequency shift of 420 MHz; together with the 80 MHz shift of the 689A laser, this means that the spectroscopy lasers B and C can probe the $^1S_0 - ^3P_1$ line if they are offset locked to a total of 500 MHz from 689A. For 689D, the setpoint depends on C. . .	74
2.51	Spectrum analyzer traces of the lasers (a) 689A, (b) 689B, (c) 689C, and (d) the beat of 689B with C. Note that in (a) through (c) the span of the trace is 10 MHz to show the servo sidebumps, whereas in (d) the span of the trace is 10 kHz, focused on the central lock feature. The observed width of the central lock peaks are limited by the resolution of the spectrum analyzer. . .	75
2.52	The full experimental sequence schematic.	76
2.53	Screen capture of the sequencer software.	76
2.54	Screen capture of the lab control software.	77
3.1	Angular momentum breakdown for Hund's case (a) (left), and for Hund's case (c) (right). Source: [Atkins and Friedman, 2010].	79
3.2	Hund's case (a) potentials (left), and Hund's case (c) potentials (right). Notice the state-swapping at avoided crossover points in (c) compared with (a). Source: [Skomorowski <i>et al.</i> , 2012b].	80

3.3	One-photon photoassociation from the free atom ground state (dashed line) to, e.g. the $0_u^+(v' = -4, J' = 1)$ excited molecular state.	83
3.4	1PA on the $0_u^+(v' = -5, J' = 1)$ line. A relatively small free bound laser (L_{FB}) power of $80 \mu\text{W}$ was employed to show minimal 1PA linewidths of ~ 200 kHz. For higher powers, depletion can reach as much as 80 to 100%, with linewidths up to 1 MHz. In either case, the thermal tail on the left-hand side is evident.	84
3.5	1PA loss curve on the $(v' = -5, J' = 1)$ line (left). Loss rate vs. L_{FB} intensity (right).	85
3.6	A typical 1PA sequence.	85
3.7	Two-photon photoassociation from the free-atom ground state (dashed line) to, e.g. the $(v = -2, J = 0)$ state in the molecular ground state manifold.	87
3.8	A typical 2PA sequence.	87
3.9	(a) Diagram of a three-state lambda system. The laser represented by the right-hand arrow (in our case, the free-bound, or FB) couples the initial state to the intermediate, and the left-hand arrow (bound-bound, or BB) couples the intermediate to the final state. (b) A schematic plot of trap atom number vs. FB laser frequency, for a fixed BB laser frequency. There are two loss peaks, one at the one-photon frequency, and one at the two-photon frequency, where the FB laser detuning matches that of the BB laser. At small BB detunings, the two peaks become a coherent mixture of the two cases, as in a dressed-state system, and never cross.	89
3.10	(a) Two representative 2PA traces, black for a coupling laser detuning of 0 MHz, and gray for 1 MHz. (b) Aggregate trace of 2PA peak positions for various coupling laser detunings, with vertical lines to mark the example traces from (a).	90
3.11	Two-color loss plot for the $(-6', -3)$ transition (left), and two-color loss rates vs. free-bound PA laser power (right).	91

3.12	Wave functions for the $v = -2$ (solid) and $v' = -5$ (dashed) vibrational levels. The large overlap near the classical turning point leads to the large FCF. Source: [Reinaudi <i>et al.</i> , 2012b].	92
3.13	Plot of Ω_2 (left) and $\delta_1 - \delta_0$ (right) values extrapolated from 2PA fits for various single traces.	96
3.14	Discrete-sum thermal 2PA fit example from one of the traces resulting in an anomalously small Ω_2 value (red), and the smoother, but less accurate, nonthermal two-Lorentzian fit function (blue). For the discrete sum, the same non-smooth artifact of the thermal convolution is present in all of the traces with anomalously low Ω_2 values, and therefore is assumed to be the culprit. The Ω_2 values from these traces have been omitted from the analysis.	97
3.15	Comparison of the 2PA fit function with (red) and without (pink) the additional scaling factor A . All other parameters, such as the optical length l , and the exposure time t , are equal.	98
3.16	Plot of the peak separations of the 2PA fit peaks (black), and the double Lorentzian peaks (red) (left). Difference of the point sets (right). Notice the crossing point at ~ -250 kHz.	99
3.17	(a) A representative 2PA trace for a fixed L_{BB} detuning of 0 MHz. (b) Autler-Townes avoided crossing aggregate of 2PA traces, with dots marking the peak pair positions. (c) Hyperbola of peak position differences, with a fit to extract Ω_2 (Eq. 3.9). (d) Plot of Ω_2 for a pair of high and low L_{FB} intensities, and a resulting linear fit to extrapolate the final shift and uncertainty.	101
3.18	(a) A representative 2PA trace for a fixed L_{BB} detuning of 0 MHz. (b) Autler-Townes avoided crossing aggregate of 2PA traces, with dots marking the two peak positions. (c) Hyperbola of peak positions differences, with fit to extract Ω_2 (Eq. 3.9). (d) Plot of Ω_2 for two high and low BB laser intensities, and resulting linear fit to extrapolate the final shift and uncertainty.	102

3.19	(a) A representative 2PA trace for a fixed L_{BB} detuning of 0 MHz. (b) Autler-Townes avoided crossing aggregate of 2PA traces, with dots marking the two peak positions. (c) Hyperbola of peak positions differences, with fit to extract Ω_2 (Eq. 3.9). (d) Plot of Ω_2 for two high and low lattice laser intensities, and resulting linear fit to extrapolate the final shift and uncertainty.	103
3.20	(a) A representative 2PA trace for a fixed L_{BB} detuning of 0 MHz. (b) Autler-Townes avoided crossing aggregate of 2PA traces, with dots marking the two peak positions. (c) Hyperbola of peak positions differences, with fit to extract Ω_2 (Eq. 3.9). (d) Plot of Ω_2 for two high and low magnetic field biases, and resulting linear fit to extrapolate the final shift and uncertainty.	104
3.21	(a) A representative 2PA trace for a fixed L_{BB} detuning of 0 MHz. (b) Autler-Townes avoided crossing aggregate of 2PA traces, with dots marking the two peak positions. (c) Hyperbola of peak positions differences, with fit to extract Ω_2 (Eq. 3.9). (d) Plot of Ω_2 for two high and low trap densities, achieved by the presence and absence of repumper lasers, which results in a density difference factor of two. The resulting linear fit is used to extrapolate the final shift and uncertainty.	105
3.22	Molecule formation vs. PA time. The optimal PA time is ~ 1 ms, beyond which the molecule loss rate exceeds the formation rate.	106
3.23	Diagram of the molecule creation and atom recovery sequence.	107
3.24	Typical atom recovery sequence.	108
3.25	Images of the lattice-trapped atoms at various stages in the recovery sequence. The wipe pulse serves to remove all un-photoassociated atoms. Imaging at this time will show nothing, because the molecules present are insensitive to the 461 nm imaging beam. The camera sensitivity has been adjusted to show the dim recovery signal.	108
4.1	Representative trace of the least-bound excited state, at ~ -450 kHz binding energy.	111
4.2	Representative trace of the second bound state, at ~ 24 MHz.	112

4.3	Representative trace of the atomic recovery shelf. The fit function can give a frequency uncertainty ~ 3 kHz, which is small enough that this shelf can thus be used as an anchor for measuring absolute binding energies.	113
4.4	Image of an ejected ring of atoms around the central lattice trap. (The cylindrical symmetry has not been confirmed with a separate viewing angle, but the ejection velocity matches the excess photon energy, and there is no reason to believe there is cylindrical anisotropy.)	114
4.5	Successive images of the ejection ring for increasing post-PA delay time. Note that the PA time is fixed in each of these panels. A similar effect could be achieved if both the PA and delay time are fixed, but the laser frequency increased, increasing the excess energy delivered.	114
4.6	Ring separation as a function of recovery laser detuning. The square root dependence is evidence that this is indeed an effect of the excess photon energy.	115
4.7	Trace of the overlapping $(v', J') = (-1, 1)$ and $(-2, 3)$ states. Selection rules and the multiplicity of the ground and excited states dictate the number of peaks observed.	116
4.8	Selection rules and the multiplicity of the ground and excited states dictate the number of peaks observed. For π transitions (black), the number of peaks is determined by the minimum multiplicity of the ground and excited states. For σ transitions (dashed gray), the number of peaks observed is given by the minimum multiplicity plus two, or the maximum multiplicity, whichever is smaller. On occasion we found weak σ transitions leaking through due to imperfect probe laser polarization.	117
4.9	Broad spectrum of all of the observed recovery peaks and shelves. The space between the $J = 2$ and $J = 0$ sets has been omitted, and the frequency zero-point is arbitrary. The three sets of arrows summarize the binding energy measurements that are the results of this chapter.	118

4.10	Plot of ($v' = -1, J' = 1$) peak positions for various magnetic fields (left). On the right is the same data, but lotted versus time, with black lines connecting successive data points, taken to check for any experimental drift dependence. There appears to be negligible drift.	119
4.11	On the left, a plot of the $J' = 1$ shelf position for varying magnetic field. The dip at 0 G is explained by the breakdown of the recovery lineshape when there is no magnetically-defined quantum axis. As expected there does not appear to be strong dependence, and so on the right, the background laser frequency drift in time is observable.	119
4.12	Recovery ($v' = -1, J' = 1$) peak position vs. (a) recovery laser frequency and (b) vs. the time when data was taken. (c) This linear drift was removed, and the final shift dependence was determined from the corrected fit.	121
4.13	Recovery $J' = 1$ shelf position vs. (a) recovery laser frequency, and (b) vs. the time when data was taken. (c) This linear drift was removed, and the final shift dependence was determined from the corrected fit.	122
4.14	Lattice shifts of the (a) $(-1, 1)$ peak and (b) $J' = 1$ dissociation shelf, where the laser frequency drift has been treated as negligible.	123
4.15	(a) The shift in the $J' = 1$ atomic shelf is more suggestive of laser frequency drift than of magnetic field dependence. We do not expect there to be any linear or quadratic dependence of this shelf on the magnetic field, and because the drift is negligible compared to the shifts of the $v' = -2$ state of this section, it is not corrected out of this trace. (b) Plot of ($v' = -2, J' = 1$) peak position for various magnetic fields. Any laser frequency drift is negligible compared to this shift.	124
4.16	(a) Plot of ($v' = -2, J' = 1$) peak position vs. recovery laser power, after correcting for the laser frequency drift as in Sec. 4.1.1. (b) Plot of ($v' = -2, J' = 1$) peak position vs. lattice laser power. The lines connect points that were taken successively; the near-overlap of these lines indicates that there is little frequency drift relative to the lattice laser shift.	125

4.17	Plot of ($v' = -2, J' = 1$) peak position vs. successive repumpers on/off measurement pairs.	126
4.18	(a) The various sublevels of the ($v' = -2, J' = 3$) recovery peak, as well as the obscured ($v' = -1, J' = 1$) peak, plotted vs. applied magnetic field. (b) The ($v' = -2, J' = 1$) vs. applied magnetic field. (c) Their difference, which is used to extrapolate the absolute binding energy of the $J' = 3$ state. Laser frequency drift was deemed negligible for this data set.	129
4.19	(a) The ($v' = -2, J' = 3$) peak vs. recovery laser power, (b) the ($v' = -2, J' = 1$) peak vs. recovery laser power, and (c) their difference, where laser frequency drift was deemed negligible.	130
4.20	(a) The ($v' = -2, J' = 1$) peak vs. lattice laser power, (b) the ($v' = -2, J' = 3$) peak vs. lattice laser power, and (c) their difference, where laser frequency drift was deemed negligible.	131
5.1	The long-range potentials for $^{88}\text{Sr}_2$ for (a) the excited state that dissociates to the $^1\text{S}_0 + ^3\text{P}_1$ asymptote (as shown with the horizontal dashed line) and (b) the ground state that dissociates to $^1\text{S}_0 + ^1\text{S}_0$. Drawn as solid lines in the excited state are the two bound states $v' = -1, -2$, both with angular momentum $J' = 1$. Drawn in the inset is the additional $ v', J'\rangle = -2, 3\rangle$ that is nearly degenerate with $ -1, 1\rangle$. As described in Ch. 4, our ground state molecules occupy the rotational levels $J = 0, 2$ of the $v = -2$ vibrational level. The bound-bound transitions are marked by the solid lines $p_1 - p_5$, and the bound-free transition, are marked by the dashed lines s_1, s_2 . (c) The spectroscopic trace across all five peaks and two continuum shelves, fitted with the appropriate lineshapes as described in the Ch. 4.	137
5.2	The spectroscopy sequence for the measurement. The dashed lines indicate the optional anti-recovery sequence, in which lasers 689B and 689D drive a two-color transfer away from the bound molecular state from which 689C recovers, resulting in a loss from the recovery signal.	138

- 5.3 Sample spectra of (a) p_5 and (b) p_4 from Fig. 5.1, for small magnetic field B values, and showing π -transition peaks. The p_4 trace includes a shifted sublevel of the nearly-degenerate p_3 . (c,d) These peak positions as plotted for varying field amplitudes, and fitted to parabolic equations with the required symmetry constraints. In (d), the outermost $|m'| = 3$ are measured with a rotated polarization to allow for σ -transitions. In (c), the three curves do not cross at the same point, likely due to optical lattice tensor light shifts. The inset in (c) shows the $g(\theta)$ curve from Eq. 5.6, in which is marked the Coriolis mixing angle $\theta = 6.1^\circ$, as measured for $|v', J'\rangle = |-2, 1\rangle$ 139
- 5.4 Sample Zeeman shift measurements of the deeper excited states. The measurement was achieved by Sr_2 production in the ground state -2 in the usual way, but then transferred via a third spectroscopy laser to the deeper excited state before recovery from the ground state is performed. By fixing the recovery spectroscopy laser on transition, and sweeping this third laser, the peaks are marked by "anti-recovery" dips in the otherwise non-zero atom signal. (a) Representative loss peaks to the $v' = -3$ state; (b) Zeeman shifts of the $v' = -3$ peaks, (c) of the $v' = -5$ peaks, and (d) of the $v' = -6$ peaks. . . . 140
- 5.5 The relevant magnetic properties that are strongly sensitive to the nonadiabatic effects in the weakest-bound levels of $^{88}\text{Sr}_2$ near the $^1\text{S}_0 + ^3\text{P}_1$ asymptote. Equations 5.3 and 5.4 define the experimental and theoretical quadratic shift coefficients q (G^{-1}). An asterisk denotes cases that include strong fourth-order contributions (q_4 in Eq. 5.3). Experimental and theoretical g factors are given, as are the Coriolis mixing angles θ . Due to the limitations of the model, for the two deepest states a unique angle cannot be determined from the two provided by the measurements. 143

5.6	<p>Measured \bar{q} versus the binding energy, normalized to the analogous atomic coefficient q_a. The results show a $10^6\times$ enhancement in the weakest-bound region relevant to Fig. 5.3. The various markers are defined in the legend, and the solid gray line represents the magnetic susceptibility model of Eq. 5.7 for the $J' = 1, m' = 0$ levels of the 0_u^+ manifold. Note that this is relevant only for the black squares with $J' = 1$, and is in excellent agreement with the data.</p>	144
6.1	<p>A map of the transition dipole moments between the vibrational states of the excited 0_u^+ and the ground X manifold (for $J' = 1$ and $J = 0$, respectively), with false color to represent the log of the dipole moment. The excited states of 0_u^+ are plotted along the horizontal axis, and the ground states of X on the vertical axis. The contour lines connect levels that can be coupled by the same laser wavelength, where the lines, from left to right, span across wavelengths from ~ 830 to 650nm.</p>	148
6.2	<p>Representative traces for Raman spectroscopy between states $v = -2$ and $v = -1$. (a) Losses from $v = -2$ overlaid with gains to $v = -1$, (b) losses from $v = -2$ at a narrower, 120 Hz linewidth corresponding to a 20 ms coherence time, (c) Rabi flopping between the two states, and (d) a plot of the line frequency vs. lattice laser power. It is suspected that the inhomogeneity of the lattice laser intensity, at a slightly non-magic wavelength, is the cause of the 600 Hz linewidth limit.</p>	149

List of Tables

3.1	Calculated optical lengths	86
3.2	Franck-Condon factors: measured	93
3.3	Franck-Condon factors: calculated	93
4.1	Binding energies (MHz)	132

Acknowledgments

I remember the first time I heard the principle of Doppler cooling explained, as an anecdote in a class at the University of Rochester, where I studied as an undergraduate. I was struck by the clever elegance of the technique, and was amazed that laser light could be used to cool atoms down to the coldest temperatures in the known universe. Before the semester was out, I had secured a spot to work in the atomic physics lab of Professor Nick Bigelow. Working together with his graduate students Kevin Wright and Amy Wakim solidified my interest in the field, and set the stage for my graduate research.

I was introduced to my advisor Tanya Zelevinsky in her first year of appointment as a Professor at Columbia University. I applied to Columbia with the intention of joining her new lab, as I knew that the opportunity to be the first graduate student would come with the rare chance to help build a lab from scratch. I joined her group in June of 2008 as a summer assistant, before official enrollment in the fall. At the time we worked in borrowed space in the applied physics building; the lab space appointed to Tanya's group was still under construction on the sixth floor of the physics building, Pupin Hall, and would not be ready until late in the fall.

Klejda Bega joined the group as a postdoc around the time I did, and by September we were joined by a second postdoc, Gael Reinaudi. While I was completing my master's courses, I accompanied Klejda and Gael part-time in the construction of the oven and vacuum systems, as well as some of the first laser systems. I am indebted to both of them for their excellence not only as scientists, but also as mentors, practicing a hands-off approach to teaching, with assistance provided as needed.

After completing my coursework, I joined Gael in the full-time effort to finish constructing the vacuum system and lasers necessary for producing our first magneto-optical trap (MOT), achieved in September of 2010. At the time we were waiting on an order for broad-

band quarter-wave plates, an essential component to the MOT. Gael had the idea that we could use discarded 3D movie glasses, which to our delight served their purpose very well. This kind of unconventional problem solving is essential when building a new lab. I am thankful that I was able to work so closely with Gael for over four years.

Mickey McDonald joined our lab as its second graduate student in the summer of 2011. During that summer we also hosted a French master's student, Camille Frapoli, who built an improved frequency-doubling cavity for the 461 nm blue light generation. We benefit daily from this cavity's higher output power and improved stability.

Our first major result, the production and detection of ultracold $^{88}\text{Sr}_2$ molecules, was an effort made with Gael and Mickey in the months leading up to the summer of 2012. This event marked an important milestone in the lab: successfully detecting these molecules signaled a shift from the previous three years of building, and toward a wealth of exciting measurements. That July, we took on another postdoc, Bart McGuyer. I spent the next year, into the summer of 2013, working together with Bart and Mickey exploring some of these measurements. I have enjoyed learning from Bart's excellence as a scientific thinker, and from his inexhaustible capacity for careful measurement. Our group has benefitted tremendously from his participation.

As I transitioned into full-time thesis writing, Geoff Iwata joined our lab as its third graduate student, and Mickey took the reigns as the senior graduate student. Thanks to Mickey's enthusiasm and expertise with the numerous spectroscopy lasers, Bart has been able to dedicate time to collaborate with the theorists Robert Moszynski and Wojciech Skomorowski toward improving their Sr_2 binding energies model. Atomic physics benefits from close collaboration between experiment and theory, and such participation is a hallmark of a mature research group. I am also thankful to Svetlana Kotochigova for her ongoing collaboration with our group as we explored the rich structure of Sr_2 .

Looking back on my time at Columbia, I remember one day in particular. Graduate students in physics are required to take qualifying exams in the winter after their first semester. In late January, just before the spring semester, we were invited individually into the office of Professor Bill Zajc, the Department Chair, to be told whether or not we had passed (I did, thankfully!). He asked me how my work with Tanya was going, and then

added, “Have you made it clear to her yet that you want to join her group?” I said I hadn’t, but that I thought it was understood.

“If I were you, I’d make that as clear as possible. Tanya’s going to be a superstar.”

Most of all, I am thankful to Tanya for her excellent mentorship, and for the opportunity to do my graduate work with her. Under her direction, the future of the lab looks bright.

To my parents, who taught me the meaning of fidelity.

The fact is the sweetest dream that labor knows.

- Robert Frost

Chapter 1

Introduction

1.1 Laser cooling and atomic physics

Laser cooling and trapping of atoms has inspired many new fields of physics [Phillips, 1998], including studies of degenerate quantum gases [Cornell and Wieman, 2002], quantum simulation and information [Garcia-Ripoll *et al.*, 2005], precision measurements [Peters *et al.*, 1999], optical time and frequency standards [Diddams *et al.*, 2004], and ultracold collisions. The success of the field hinges on the use of lasers to control atoms, and to cool them to unprecedented temperatures. Trapping was achieved earlier than cooling - trapping via the optical dipole force was first proposed by [Letokhov, 1968]. Indeed, laser light that is red-detuned from an optical transition within an atom will induce an attractive force, and blue-detuned will induce a repulsive one. Early experiments in optical dipole trapping had limited success due to the large laser powers and small trapping volumes required to produce sufficiently deep traps for atoms at room temperature.

Laser cooling of atoms was achieved when it was understood that the momentum transfer of photon absorption could be used in conjunction with the Doppler shift. The momentum kick of a photon absorbed by an atom is

$$\Delta p = \hbar k, \tag{1.1}$$

where $h = 2\pi\hbar$ is the Planck constant and $\lambda = 2\pi/k$ is the wavelength of light. Because optical atomic transitions have finite linewidths, one can red-detune a laser from the atomic

line center and still drive the excitation, assuming the laser linewidth does not exceed the transition linewidth. The result is that photons reemitted during spontaneous decay are on average higher in energy than those absorbed during excitation, resulting in a net energy loss from the system, and therefore cooling. Since the reemission process is spatially isotropic, the momentum kick to the atoms during reemission can be thought of as a random walk in momentum space with a distribution determined by the linewidth of the transition. This linewidth therefore determines the minimum temperature achievable for the given transition [Metcalf and van der Straten, 2002], called the Doppler limit:

$$k_B T_D = \frac{\hbar\Gamma}{2}, \quad (1.2)$$

where k_B is the Boltzmann constant. The Doppler limit is achieved for frequency detuning equal to half the linewidth, $\Gamma/2$.

Many of the commonly studied atom species are solids at room temperature and must be heated in an oven to create a diffuse vapor, which is then collimated into an atomic beam (passively via narrow apertures, or actively via laser pumping). Laser deceleration is then used to slow the atoms, and various techniques have been developed to keep the continuously-Doppler shifting laser light on resonance with the atoms as they are slowed. Such techniques include using broadband light, laser frequency sweeping (also called chirping), as well as Stark shifting or Zeeman shifting the atomic line [Metcalf and van der Straten, 2002]. The slowed atomic beam is then fed into a vacuum chamber in which the atoms will be trapped by additional laser beams. If one uses red-detuned, counter-propagating laser beams along all three axes in space, then the Doppler effect due to an atom's velocity v will shift into resonance the beam whose orientation opposes the atom's movement, thus causing slowing. The laser cooling method described so far however does not provide long-term trapping. Atoms that have been slowed in such a manner experience a strongly viscous frictional force within the beam region which can give holding times on the order of 100ms. Hence the effect was termed an optical molasses, first achieved with Na atoms [Chu *et al.*, 1985; Lett *et al.*, 1989; Ungar *et al.*, 1989].

Optical forces alone cannot provide true atom trapping and cooling at the same time. As a result, the technique of incorporating magnetic fields in conjunction with the light fields produced what is called the magneto-optical trap (MOT), first demonstrated by S. Chu, C.

Cohen-Tannoudji, and W. Phillips [Chu, 1998; Phillips, 1998; Cohen-Tannoudji, 1998]. The final temperature of the atoms in the MOT is given by the Doppler cooling temperature T_D defined above. Various methods exist for reaching sub-Doppler limit temperatures [Metcalf and van der Straten, 2002; Dalibard and Cohen-Tannoudji, 1989], but for atoms with sufficiently narrow transitions, on the order of a kilohertz, microkelvin temperatures can be reached.

How cold is cold enough? The creation of novel states of matter, such as Bose-Einstein condensates (BECs) [Cornell and Wieman, 2002] and degenerate Fermi gases, is motivation in its own right, and a wealth of interesting physics can be learned from studying such systems [Simon *et al.*, 2011; Derevianko and Katori, 2011]. The onset of BEC formation occurs at temperatures as low as nanookelvin, requiring relatively long preparation time due to evaporative cooling. If instead the primary motivation for cooling is to improve measurement precision by suppressing the Doppler broadening of the atom sample, then one can estimate the Doppler broadened linewidth from the temperature by calculating the shift due to the root-mean-square velocity $v_{\text{rms}} = \sqrt{3k_B T/m}$. If the Doppler shift is given by $f(v) = (1 + v/c)f_0$, then

$$\Delta f \sim \frac{2v_{\text{rms}}}{c} f_0 = \frac{2}{c} \sqrt{\frac{3k_B T}{m_{\text{Sr}}}} f_0 \sim 50 \text{kHz} \quad (1.3)$$

for temperature $T = 1 \mu\text{K}$, laser frequency $f_0 = c/\lambda$, and $\lambda \sim 650 \text{ nm}$ for a typical optical wavelength. The quality factor for such a line is

$$Q = f_0/\Delta f \sim 10^{10}. \quad (1.4)$$

There exist methods for further spectroscopic improvement, particularly the use of optical lattice traps (cite). Lattice traps work in the same manner as optical dipole traps: a far off-resonant laser beam focused to a tight waist can induce a light shift in the electronic levels of the atom. With the proper frequency detuning this shift can be negative, creating a trapping region in space. An optical lattice trap is created from a dipole trap by retroreflecting the beam, which creates a standing wave along the axis of beam propagation. Atoms in such a trap are motionally quantized along the standing-wave axis, and therefore have suppressed first-order Doppler shifts. As long as one performs spectroscopy along this axis of tight confinement, photon recoil shifts can also be suppressed. One may add tight confinement

in two or three dimensions by using additional lattice beams. Neutral atom optical clocks in such lattices have been used to achieve new limits in atomic clock precision, at the 10^{-17} level for 10^3 seconds [Bloom *et al.*,], and a wealth of interesting physics can be studied in such motionally quantized systems.

The first neutral atom cooling and trapping experiments were performed using alkali metals, most commonly Na, Cs, K, and Rb, which possess a strong cooling transition on the order of 10 MHz wide. The earliest such work produced atom sample temperatures below 1 mK. More recently, experiments have been performed also using the two-electron species such as Mg, Ca and Sr from the alkaline earth metal group, as well as the isoelectronic species Hg and Yb. These species can offer a set of advantages over the alkali metals. They have zero hyperfine structure in the ground state, allowing for simpler studies of cold atom collisions. Additionally, these two-electron species have both spin singlet and triplet energy level manifolds. Since the ground state 1S_0 is a singlet, the spin-forbidden transitions to the triplet manifold are weakly allowed only by spin-orbit coupling, and as a result have extremely narrow linewidths [Yasuda and Katori, 2004]. The Q factors for such transitions are as high as 10^{18} , offering exciting spectroscopic and precision measurement opportunities. The ~ 1 mHz $^1S_0 - ^3P_0$ transition in ^{87}Sr is setting the standard for a new generation of precision clocks [Nicholson *et al.*, 2012]. For all isotopes, the 7.5 kHz $^1S_0 - ^3P_1$ intercombination line transition serves as an excellent cooling transition to μK temperatures without requiring sub-Doppler cooling methods (the strong, ~ 30 MHz $^1S_0 - ^1P_1$ line serves as an initial cooling and trapping transition). Additionally, the kilohertz resolution of this line allows for high-precision studies of cold atom collisions via photoassociation into long-range molecules. In this work we bridge the gap between atoms and weakly bound molecules in optical lattices.

1.2 Cold molecules

Cold molecules provide rich opportunities for precision measurements and studies of fundamental physics beyond that which is possible with cold atoms [Doyle *et al.*, 2004; Dulieu and Gabbanini, 2009; Carr *et al.*, 2009]. Such experiments include measurement of the proton-

to-electron mass ratio and its possible time variation [Zelevinsky *et al.*, 2008; Kotochigova, 2008; Koelemeij *et al.*, 2007; Shelkownikov *et al.*, 2008], the electron's electric dipole moment [Hudson *et al.*, 2011; Baron *et al.*, a], and bound-system quantum electrodynamics (QED) [Dickenson *et al.*, 2013]. However because of their complex rovibrational structure, production of cold molecules poses a much greater technological challenge than production of cold atoms.

There are four feasible routes to trapped neutral molecules: sympathetic cooling of magnetic species via buffer gases, manipulation of polar molecules via electric fields, direct laser cooling, or using magnetic or optical fields to form molecules out of ultracold trapped atoms. Additionally, recent progress has been made in evaporative cooling.

Buffer gas cooling [Krems *et al.*, 2009; Patterson *et al.*, 2009] utilizes a cryogenic gas source, typically He or Ne, to sympathetically cool the target species, which may be laser-ablated from a solid sample. This target species is then collimated and fed toward the experiment by a process called hydrodynamic entrainment [Maxwell *et al.*, 2005; Patterson and Doyle, 2007]. Recent work on buffer gas-cooled ThO molecules has produced an order-of-magnitude improvement in the search for an electron electric dipole moment [Baron *et al.*, b].

Stark deceleration uses varying electric fields in a technique analogous to that of linear accelerators for charged particles. In this case the sample consists of polar molecules. The first such experiment [Bethlem *et al.*, 1999] was performed on a neutral metastable sample of CO molecules, slowed from an initial thermal velocity to the effective temperature of 15 K.

Because of the high rate of inelastic collisions in molecules as compared with atoms, evaporative cooling of molecules has remained elusive regardless of the method of preparation. Recently, however, evaporative cooling was achieved with a Stark-decelerated source of magnetically-trapped neutral OH radicals, with elastic collisions enhanced by microwaves, decreasing the temperature by an order of magnitude, and increasing the phase-space density by a factor of three [Stuhl *et al.*, 2012].

The last category of cold molecule experiments uses samples of already-cold atoms as the molecule constituents. Although these techniques restrict the variety of molecular species,

the benefit is low temperatures that exceed the current capabilities of direct molecule cooling. At such cold temperatures, the collision mechanisms are greatly simplified, and very high spectral resolution can be attained. These techniques initially create what can be called *physicist's molecules*: weakly-bound, long-range molecules whose electronic structure can be approximated by the structure of its substituent atoms.

Magnetic Feshbach resonance [Chin *et al.*, 2010; Kohler *et al.*, 2006] is used to associate magnetic species with hyperfine structure in the ground state. This has been achieved for many of the alkali metal atoms, such as K, Rb, Na, Cs, and Li. The model owes its name to Herman Feshbach [Feshbach, 1958], and the earliest such observation was for a BEC of Na [Inouye *et al.*, 1998]. Recent work with molecules using the Feshbach association technique have experimentally realized elementary quantum systems, such as a long-range dipolar spin-exchange between polar $^{40}\text{K}^{87}\text{Rb}$ molecules [Yan *et al.*, 2013].

For the bosonic isotopes of the alkaline earth metals that have no hyperfine structure in the ground state this method is not available. Instead, the technique of photoassociation (PA), or optical Feshbach resonance, is employed [Jones *et al.*, 2006]. In this case, the molecular and atomic scattering states are coupled by resonant photons. In this work, PA is achieved via the narrow intercombination transition, as explained in detail in Chapter 3.

1.3 Thesis overview

My doctoral work is focused on production and control of the ultracold molecular species $^{88}\text{Sr}_2$, and on initial precision measurements with implications for quantum chemistry, and molecular and fundamental physics. Producing a stable sample of such molecules is a nontrivial task, and represents one of the major steps of my doctoral work. After the creation of this new class of cold molecules, my colleagues and I have been able to study many unique aspects of ultracold physics and chemistry, including the precise determination of the binding energy of several weakly-bound states that are relevant for molecular QED, as well as their anomalously large magnetic g -factors and magnetic susceptibility. The next major objectives are studies of forbidden molecular transitions, and optical transfer to the absolute rovibrational ground state, from which many of the long-term fundamental physics

measurements will be carried out. These experiments are briefly described in Ch. 6. This document, which is the aggregate of my doctoral work, is structured as follows.

Chapter 2 describes the experimental apparatus. Being the first graduate student in the lab, a postdoctoral researcher and I built the majority of the experiment in its current form. Considerable detail is dedicated to the multistage process of design, construction and testing. Tips and tricks are given as necessary. For optical systems, the technique for the initial alignment of the system often differs from that for daily alignment, and each is accorded its own description. This chronicles the setup of the lab itself, starting with the oven and the collimated atom beam, the vacuum chamber and vacuum technology, the 922 nm cooling and trapping light source and frequency doubling cavity, the permanent-magnet Zeeman atom slower, quadrupole and compensation magnetic fields, repumper lasers, and finally the mK MOT. The transfer of this MOT to the second-stage μK MOT is then detailed, by describing first the 689 nm light source and its stabilization scheme, and then the electronic and optical setup, including the optimal transfer sequence. The optical lattice setup is also described, including methods for alignment and atom transfer from the μK MOT. The lattice trap is then characterized, with details on the trap depth, trap frequency, as well as atom number, density and temperature. The chapter concludes with a description of the spectroscopy lasers, all at 689 nm and phase-locked to the μK cooling and trapping laser.

Chapter 3 picks up where Ch. 2 ends: having produced a stable sample of lattice-trapped ultracold atoms, the process of photoassociating (PA) these atoms into Sr_2 molecules is described. The chapter starts with confirmation of the previous one-color PA results, and continues with new two-color PA results. Most of the chapter is dedicated to the method for molecule production into the electronic ground state, and high-resolution detection. Two-color PA spectroscopy is used to measure coupling strengths between excited- and ground-state vibrational level pairs, in an attempt to identify the excited levels that spontaneously decay predominantly to a single ground state. The molecule creation process that is used is described next, followed by the discussion of the recovery of the atoms via ultracold molecule fragmentation, and imaging of the resulting atoms. The success of this method, which was the topic of [Reinaudi *et al.*, 2012b], concludes the chapter, with an additional

discussion on the likely factors that contribute to the observed lifetime of these molecules.

Chapter 4 extends the recovery method from Ch. 3: fragmentation can be performed using more than just the shallowest vibrational bound state, and moreover, other bound states can be probed indirectly by adding an additional laser beam. Using photo-dissociation as an anchor for zero binding energy, the binding energies of several of several weakly-bound states are measured. These binding energies are tested against systematic experimental shifts, allowing us to quote the final results with uncertainties in the range of only a few kilohertz. Chapter 4 concludes with a brief discussion of the ab initio Sr_2 molecular model built by our collaborators [Skomorowski *et al.*, 2012b], whose degrees of freedom have been constrained by earlier work [Stein *et al.*, 2011], and are currently being fit in the long-range regime to the results of this chapter. This constitutes one of the most precise tests of modern quantum chemistry. Additionally, the binding energies are sensitive to the retardation effect, and can be used for QED tests in this heavy molecule. This is a work in progress.

Chapter 5 discusses surprising results pointing to an anomalously large Zeeman effect in weakly bound molecules [McGuyer *et al.*, 2013]. The linear shifts, or g factor measurements, yield the Coriolis mixing angle of the molecular wave functions. Thus, the g factors provide a highly sensitive probe of nonadiabatic molecular physics that couples the electronic and nuclear (rovibrational) degrees of freedom. The quadratic Zeeman shifts exceed those in free atoms by up to $10^6\times$, indicating an exceptionally large magnetic susceptibility. Besides showing a good agreement with the ab initio model, we demonstrate a simple model that shows how the susceptibility increases cubically with the size of the molecule.

Chapter 6 concludes my Ph.D. work, and gives an outlook on the direction of future research.

Chapter 2

Apparatus

Figure 2.1 shows the electronic transitions in ^{88}Sr that are relevant to our work, with their corresponding wavelengths and decay rates. Briefly described, our objective is as follows: slow a hot, gaseous beam of Sr and then trap the atoms using the strong $^1\text{S}_0 - ^1\text{P}_1$ transition. The final temperature of this magneto-optical trap (MOT) is in the mK regime, from which we will then transfer to a colder, μK MOT using the weak $^1\text{S}_0 - ^3\text{P}_1$ intercombination line at 689 nm. From here the atoms will be loaded into an optical lattice trap, and spectroscopy and molecule formation will be performed using lasers that are phase locked to the master 689 nm laser. Figure 2.2 is a schematic of the vacuum chamber apparatus and surrounding systems. While it does not give detail for all of the experiment's components, it offers a broad reference for the physical system immediately serving the vacuum chamber, and will be referred to throughout this chapter. Some of the earliest work on systems similar to ours was done by [Katori *et al.*, 1999; Ido and Katori, 2003; Loftus *et al.*, 2004a; Loftus *et al.*, 2004b; Boyd, 2007; Ludlow, 2008; Vogel *et al.*, 1999; Xu *et al.*, 2003], which were used while constructing our setup as references. Let's begin with the oven source.

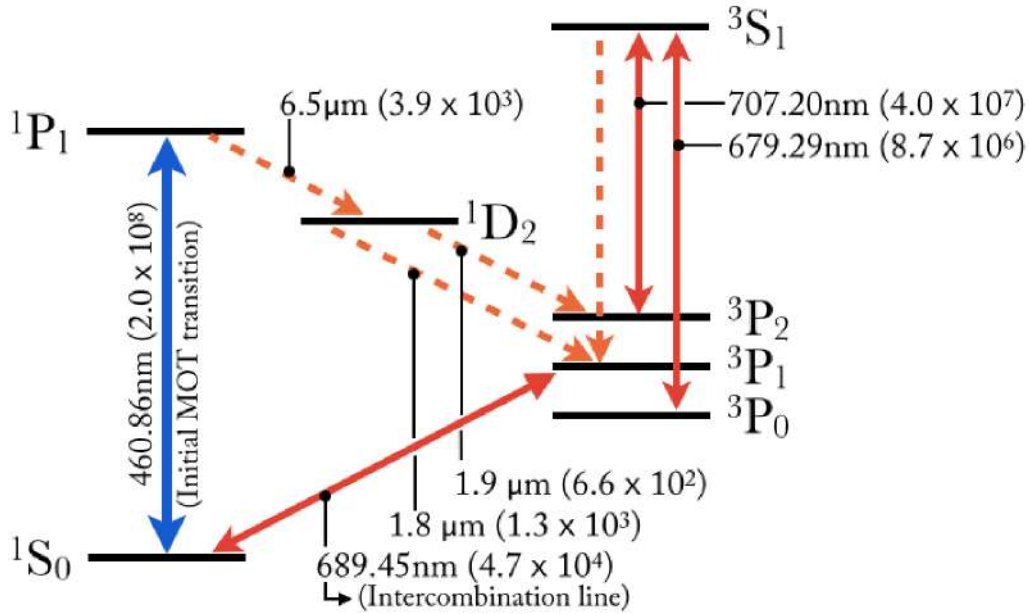


Figure 2.1: Relevant electronic transitions for cooling and trapping ^{88}Sr . The transition wavelengths and decay rates are labeled.

2.1 Atom oven and vacuum system

2.1.1 Oven heating

Strontium is a solid at standard temperature and pressure. Cold atom experiments rely on trapping from the gas phase. To achieve this, solid strontium is heated in an oven to produce a sufficient vapor pressure, which by diffusion and collimation is then directed as an atomic beam into a trapping chamber.

The original oven design was planned for use with strontium and ytterbium. However, strontium requires comparatively high temperatures to reach a desired vapor pressure, as seen in Fig. 2.3, and so early heating tests resulted in melted copper and silver gaskets, due to unanticipated eutectic mixing. To simplify troubleshooting, and in light of our initial interest in single-species Sr experiments, Yb was left out of the first oven. We were therefore able to rely on a simpler, single-species design.

The eutectic diagram for nickel and strontium in Fig. 2.4 suggests that our desired 600°C setpoint is safely within the gas phase for any admixture of the two elements. As a result

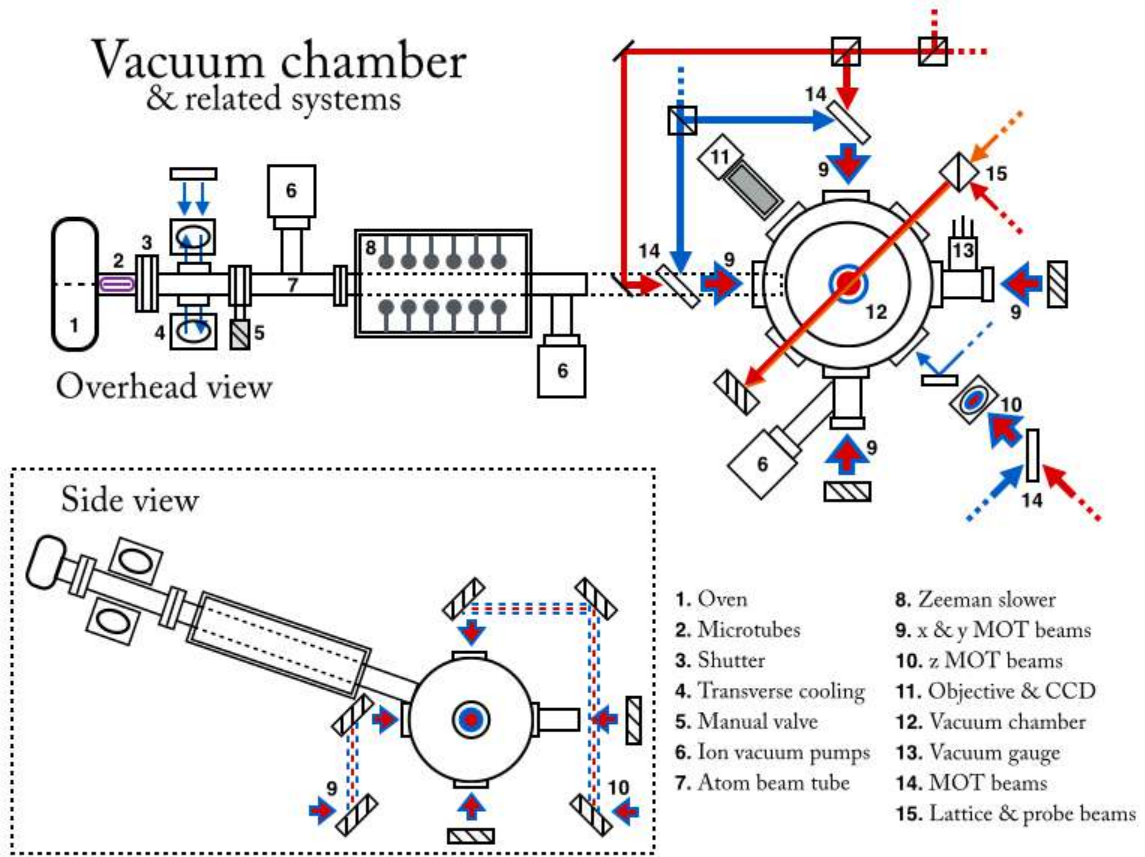


Figure 2.2: A schematic view of the physical apparatus, for the purpose of understanding the general relationships between the core components. Some detail is left out - e.g. schematics for the laser systems and their locking schemes can be found later in the chapter - and objects are not to scale with one another. The side view is also for general understanding, and has been simplified further from the overhead view.

nickel gaskets were used for the final single-species oven design.

Figure 2.5 shows the oven's design where both chambers are directly connected, reflecting its single-species use. The chambers are heated to 575°C , the back wall in the center to 600°C , and the nozzle region, highlighted pink, to 600°C to avoid buildup or clogging. Heating feedback control is achieved using the heating elements (McMaster-Carr parts 3594K112 and 3594K491 for the oven, and 3594K261 for the nozzle region of the pipe), detection thermocouples (McMaster-Carr parts 39095K54), and control device (EX-TECH(R) Process PID Controller 48VFL). Reaching setpoint from room temperature can

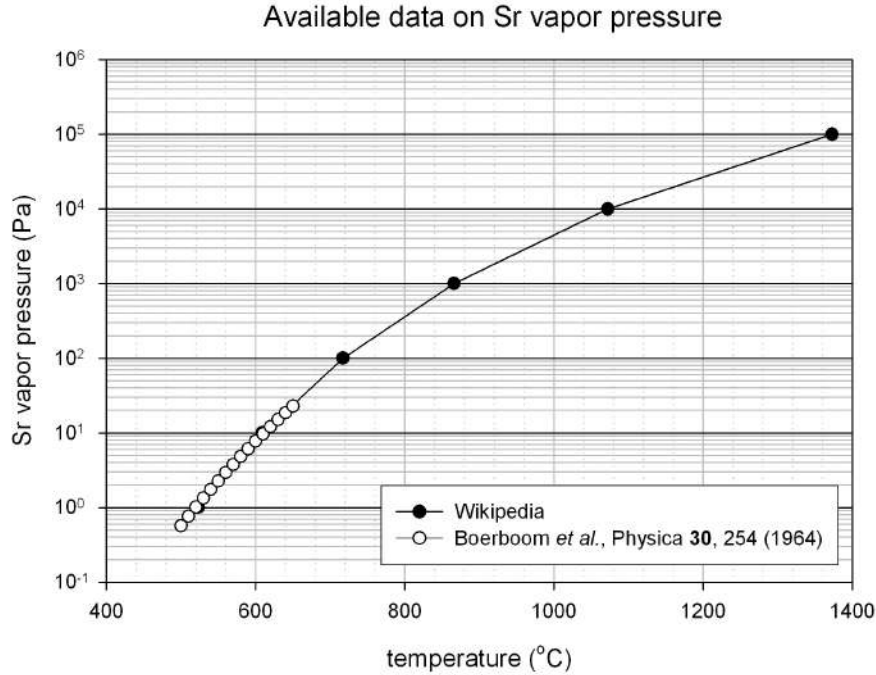


Figure 2.3: Log plot of Sr vapor pressure.

take 1 to 2 hours, so a switch scheduler was installed to conserve our Sr source; the oven turns on at 7 a.m. and shuts off at 7 p.m. The nozzle heater is left on at all times.

2.1.2 Atom beam

The oven is fitted to a long, ~ 1 m pipeline leading to the trapping vacuum chamber. To control the flow and collimation of the beam source, a beam shutter and array of microtubes are installed along the path. The purpose of the shutter is to control the source for timed loading, but its 6 mm inner diameter (ID) also serves as a collimation point. The nozzle highlighted pink in Fig. 2.5 has been fitted with an array of microtubes. This array serves to reduce the solid angle of collision-free trajectories out of the oven toward the vacuum chamber, providing atomic beam collimation. Together with the other elements along the atomic beam pipeline, we can estimate a total fraction of the thermally diffuse oven source atoms that will reach the chamber, and the resulting beam divergence. From this, together with the beam slowing and maximum capture velocities discussed in the next sections, we can estimate a final loading rate of cold atomic Sr into the first stage MOT.

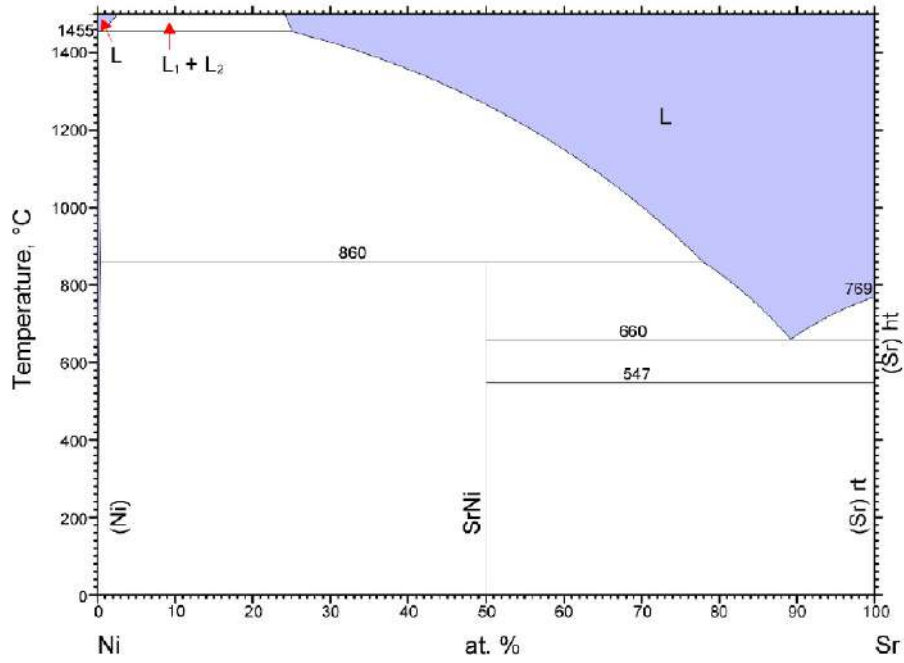


Figure 2.4: Eutectic diagram for Sr and Ni. Source: [Nash, 1990]

Figure 2.6 shows a rough schematic of the sections of the atomic beam pipe leading from the oven to the trapping chamber, with their corresponding lengths and inner diameters.

We first estimate the atom flux rate Q from the oven nozzle. Each microtube is 3.6 cm long and has a 0.36 mm ID and 0.48 mm OD. The flux rate through an individual microtube can be estimated in the following way. The atom density in the oven is given by the vapor pressure and temperature,

$$n = \frac{P}{k_B T}. \quad (2.1)$$

The root mean square (rms) velocity of the atom gas in the oven is given by $v_{\text{rms}} = \sqrt{k_B T / m}$, where m is the atomic mass. Out of the total density n , we consider a subset of the sample within the solid angle $d\Omega$ and within the velocity range dv ,

$$f_{d\Omega, dv} = \frac{\sqrt{2/\pi}}{v_{\text{rms}}^3} e^{-v^2/2v_{\text{rms}}^2} dv \frac{d\Omega}{4\pi}, \quad (2.2)$$

where $d\Omega = d\theta_v d\phi_v$ can be written as a constant fraction because of an isotropic velocity distribution within the oven. The fraction of these atoms that will pass through the microtube aperture area A within the time interval dt is proportional to the volume of a cylinder



Figure 2.5: Rendering of the oven design, assembled with the fitted microtube holder.

of base area A and height vdt ,

$$N_{A,dt,d\Omega,dv} = n \cdot f_{d\Omega,dv} \cdot \cos\theta A v dt = n \cdot \frac{A}{\sqrt{8\pi}} \frac{v^3}{v_{\text{rms}}^3} e^{-v^2/2v_{\text{rms}}^2} dv (d\phi/2\pi) \sin 2\theta d\theta dt, \quad (2.3)$$

where a trig identity has been utilized. By cylindrical symmetry the integration over ϕ is trivial. Integrating over v , we get the total atom flux through one microtube, Q_0 ,

$$Q_0 = \frac{1}{4} n v_{\text{avg}} A \int_0^\infty \sin 2\theta d\theta = \frac{1}{4} n v_{\text{avg}} A I_\theta \quad (2.4)$$

for $I_\theta = 2.5 \cdot 10^{-5}$.

We can estimate the divergence of the atomic beam after the microtube array by

$$\theta_{1/2} = \tan^{-1} \frac{D_{\text{tube}}}{L} = 5 \text{ mrad}. \quad (2.5)$$

What fraction of these atoms make it through the beam shutter? At a distance 19 cm downstream from the microtube array, with zero length and an ID of 6 mm, we estimate a fraction f_1 of transmitted atoms

$$f_1 \approx \frac{D_{\text{shutter}}^2/2}{(D_{\text{nozzle}}/2 + L \cdot \tan\theta_{1/2})^2} = 0.45, \quad (2.6)$$

and through the differential pumping tubes,

$$f_2 \approx \frac{D_{\text{pump}}^2/2}{(D_{\text{shutter}}/2 + L \cdot \tan\theta_{1/2})^2} = 0.71. \quad (2.7)$$

Hence the combined fraction post-microtubes to post-differential pumping tubes is $f = f_1 f_2 = 0.32$. From Fig. 2.7 it is estimated that there are 180 microtubes and 50 comparably large intertube spacings, resulting in ~ 230 total channels in the nozzle through which atoms may pass by the geometry constructed above. Therefore the total atom flux through this portion of the apparatus, after the two differential pumping tubes, is

$$Q = \frac{1}{4} n v_{\text{avg}} A I_0 \cdot f N_T = \frac{1}{\sqrt{2\pi}} \frac{P}{m k_B T} A I_0 f N_T, \quad (2.8)$$

for total number of microtubes N_T . At an estimated vapor pressure 10^1 Pa, $Q \approx 1.6 \cdot 10^{13}$ /s.

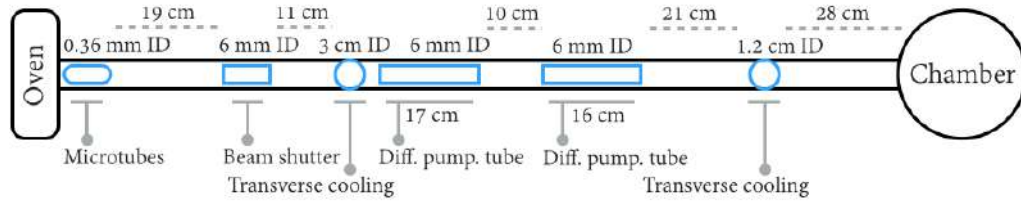


Figure 2.6: Schematic showing the various apertures reducing the atomic beam divergence and transfer.



Figure 2.7: Microtube holder, before assembly (left). Cross-sectional photograph of the assembled microtubes in the holder (right).

Figure 2.7 shows the open holder design, and the final microtube fitting before installation into the oven. The microtubes were purchased from Microgroup. Each is made from

304 stainless steel with dimensions 35.5 mm long by 0.34 mm minimum (0.38 mm maximum) ID, and 0.48mm minimum (0.50mm maximum) OD. Approximately 180 microtubes were required to fill the holder.

In order to secure the microtubes holder into the oven nozzle using vacuum-safe parts, the holder was designed with a slightly larger OD than the nozzle's ID. The holder was then cooled using liquid nitrogen, installed into the oven nozzle and then allowed to expand into place during warming back to room temperature. Figure 2.8 details this installation.

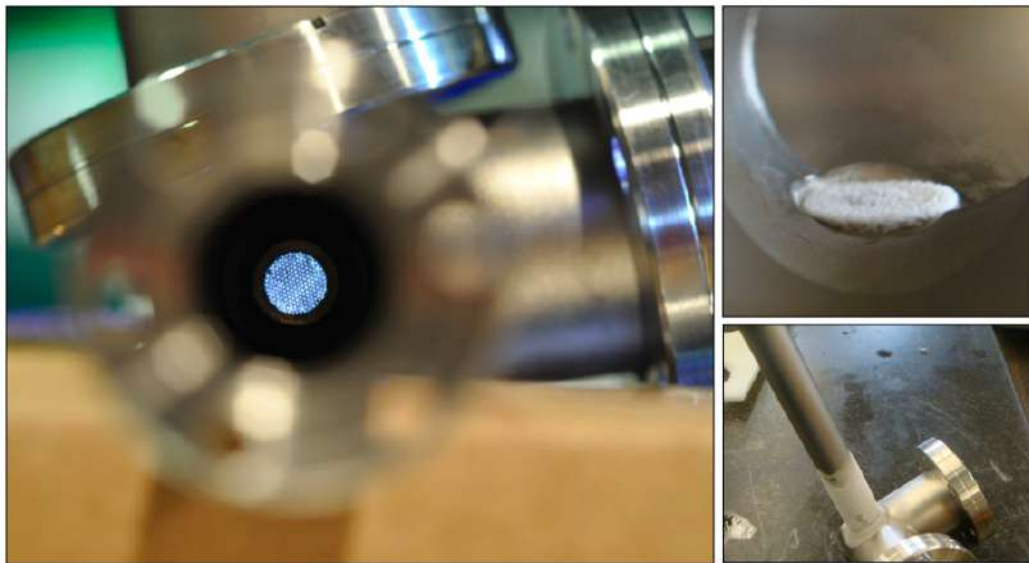


Figure 2.8: View of the microtubes inside the nozzle, installed in the oven vacuum component just after installation with accumulated condensation (right), and view on-axis confirming the line-of-sight, illuminated with a flashlight (left).

2.1.3 Multispecies oven for future work

In the future, we may use multiple atom species in the oven. To overcome the problems encountered with the dual mixture of Sr and Yb cited above, a second-generation oven was designed as shown in Fig. 2.9, although it has not yet been installed. It was designed with inner nozzles separating different chambers within the oven [Stan and Ketterle, 2005] to accommodate the different temperatures required to achieve comparable vapor pressures with different atom species.

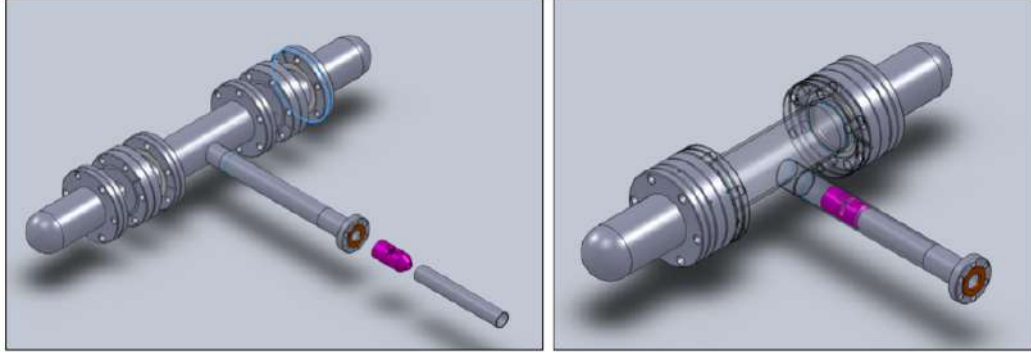


Figure 2.9: Schematic of the second generation oven. The nozzles separating the Sr and Yb chambers allow for equal vapor pressures of both species in the central mixing chamber.

The temperature difference between Sr and Yb at equal vapor pressures is roughly 80°C . It is possible that if both species' ovens and the mixing chamber are not separated by nozzles, Sr from the higher temperature region might condense and coat the Yb sample on the other side of the oven since it is roughly 80°C lower in temperature. Hence any future, two-species oven should include one narrow nozzle between the Yb oven and the rest of the system, similar to the Ketterle design. The purpose of this nozzle is to ensure that Sr doesn't coat the Yb, but also that the Yb and Sr are in the mixing chamber at comparable pressures. To choose the proper design for the nozzle separation, we first calculate the pressure differences for Yb in the oven and in the mixing chamber due to the conductances of the Yb oven nozzle, called C_{Yb} , and the microtubes leaving the oven, called C_{mix} . Assuming that the backflow from atoms that have completely traversed the microtubes is negligible, we may approximate the pressure beyond the tubes to be zero. Under this assumption we determine the relationship between the Yb pressures in the oven and in the mixing chamber, P_{Yb} and P_{mix} respectively, as

$$\frac{P_{\text{Yb}}}{P_{\text{mix}}} = \frac{1}{1 + C_{\text{mix}}/C_{\text{Yb}}}.$$

Therefore if we want n orders of magnitude difference in the conductance of the microtubes and the Yb nozzle (to ensure a low Sr presence in the Yb oven), then we can expect basically n orders of magnitude in the pressure difference between Yb in the oven and Yb in the mixing chamber. Hence adding any nozzle at all between the Yb oven and the mixing

chamber means that if we wish to maintain the same Yb pressure in the mixing chamber, we have to raise the Yb oven temperature.

The volumetric discharge of the microtubes was calculated to be $8.2 \cdot 10^{-8} \text{ m}^2 \cdot v(T)$, the sum of roughly 250 microtubes. The discharge of a 1 mm diameter and 3 cm long nozzle between the Yb oven and the mixing chamber would be $8.3 \cdot 10^{-9} \text{ m}^2 \cdot v(T)$, roughly an order of magnitude lower than the microtubes, since $v(T) \propto T^{1/2}$ (by standard kinetics) suppresses the effects on the discharge due to temperature differences.

Suppose then that we set the Yb oven at 580 °C. This corresponds to an in-oven vapor pressure of $10^{1.4} \text{ Pa} = 25 \text{ Pa}$, which gives a mixing chamber partial pressure for Yb equal to

$$25 \text{ Pa} / (1 + 10) = 2.3 \text{ Pa},$$

similar to the Sr oven partial pressure calculated as a design goal for our current oven.

The components necessary for this oven were designed and then manufactured by Nor-Cal, but are currently set aside until such time that two-species physics is part of the lab agenda.

2.1.4 Vacuum system

We employ a differential pumping scheme [Chambers, 1998] between the oven source and the vacuum chamber, as shown in Fig. 2.10. The scheme represents two-stage differential pumping. The pumps are modeled by a perfect vacuum ($P = 0$), connected to the system through a conductance S . By conservation of the flow of particles in the central section and in the chamber, we may write

$$(P_o - P_d)C_1 = P_d S_1 + (P_d - P_c)C_2, \quad (2.9)$$

$$(P_d - P_c)C_2 = P_c S_2. \quad (2.10)$$

In this ideal model we assume there are no leaks and no out-gasing. One can then express the ratio

$$\frac{P_c}{P_o} = \frac{C_2 C_1}{(C_1 + S_1 + S_2) C_2 + S_2 (C_1 + S_1)}. \quad (2.11)$$

Assuming that $C_1, C_2 \ll S_1, S_2$, one can approximate

$$\frac{P_c}{P_o} = \frac{C_2 C_1}{S_2 S_1}. \quad (2.12)$$

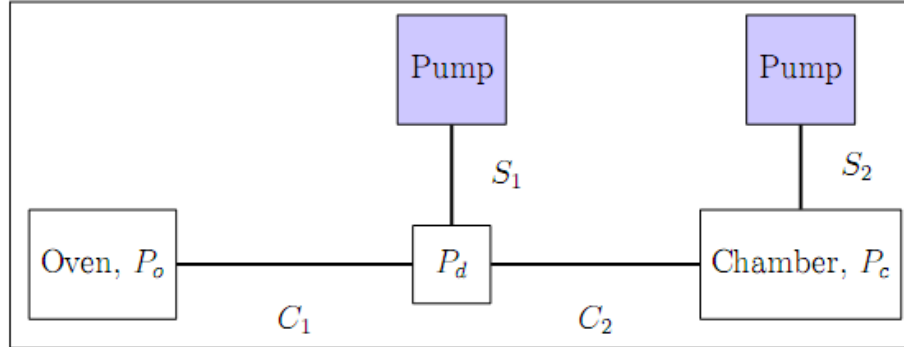


Figure 2.10: Diagram of the differential pumping scheme (two pumps).

As shown in Fig. 2.2, we have three ion pumps installed on the system (Varian Star-Cell ion pumps), monitored by Varian Mini Vac controllers. The currently stable vacuum chamber is at a pressure of $\sim 10^{-10}$ to 10^{-11} mBar ($1 \text{ mBar} = 0.75 \text{ torr} \approx 10^{-3} \text{ atm}$). The controllers give the current draw from the pumps, and have monitors indicating whether high vacuum (H.V.) is on.

Finally, we shutter the atomic beam using the high vacuum shutter shown in Fig. 2.11, and use the manual valve shown in Fig. 2.2 to close off the oven source from the rest of the system while the experiment is not in use.

2.2 461 nm light source

The previous section describes the Sr oven which was calculated to provide a collimated atomic beam of Sr of $1.6 \cdot 10^{13}$ atoms/s with a mean thermal velocity of ~ 450 m/s. This beam must now be slowed and trapped. To achieve this, as well as the eventual atom trapping within the vacuum chamber, a stable source of 461 nm light at sufficient intensity is required.

Diode lasers have become a reliable resource for low-cost light generation [Hollberg and Wieman, 1991; Fox *et al.*, 2003]. However wavelengths in the blue portion of the visible spectrum have been difficult to achieve. One technique for generating light in the blue spectrum is to frequency double infrared light via second harmonic generation (SHG) in a

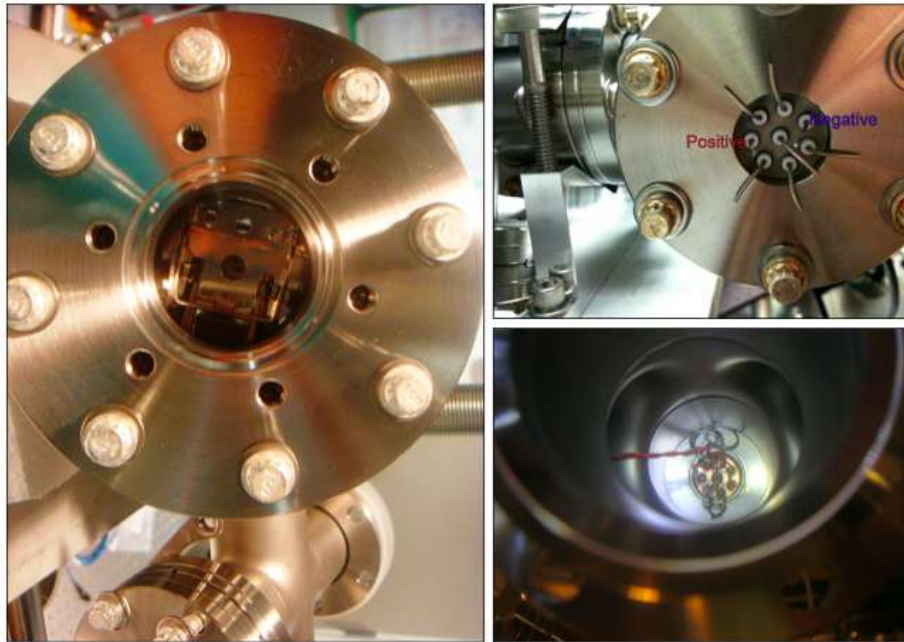


Figure 2.11: Pictures of the atomic beam shutter, before installation into the system. The positive and negative leads to the shutter are designed to be compatible with high vacuum environments.

nonlinear crystal. Infrared light at 922 nm is fed into a highly reflective cavity containing the doubling crystal, in which blue light is generated. The experiment components for these three steps - light generation, light amplification, and frequency doubling - are the topics of the next three sections.

2.2.1 Extended cavity diode laser

Our extended cavity diode laser systems are built in-house. The schematic for ECDL feedback is illustrated in Fig. 2.12. All of our diodes are purchased from Sacher Lasertechnik, with the protective cover removed due to anti-reflection (AR) coating by the company. These diodes are wired to Vescent laser controllers (D2-105) and installed into a custom-designed ECDL housing. Figure 2.13 is a rendering of the ECDL baseplate we designed.

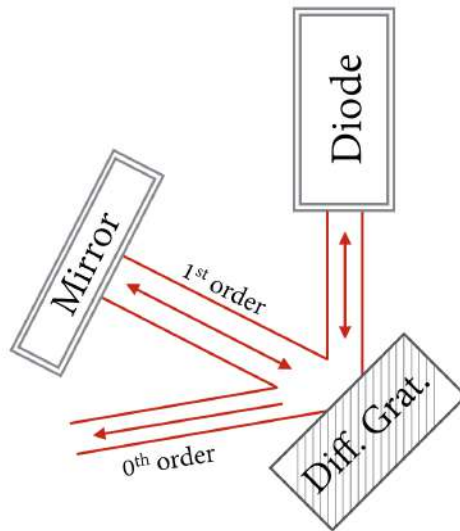


Figure 2.12: Schematic of the ECDL feedback principle. The first order off of the diffraction grating is fed back into the diode, causing stimulated emission. The wavelength of the feedback light is determined by the angle of the feedback mirror. The zeroth order is the output from the ECDL.

2.2.1.1 Temperature control

As shown in Fig. 2.14, the diode and collimating lens holder are installed in the cylindrical hole which is mounted above and thermally isolated from the rest of the baseplate body by a thermo-electric couple (TEC). The TEC is ~ 1 mm thicker than the mount space for it. The resulting small gap between the small upper level for the diode, and the rest of the baseplate, provides thermal isolation. Thermally insulating nylon screws hold the parts together, ensuring that the TEC directs all heat flow across the gap. A thermistor is installed in a small hole drilled on the back face of the mount, ~ 2 mm from the diode holder, and provides temperature feedback for the stabilization scheme.

The Vescent laser controllers provide two-stage temperature locking. The TEC described above constitutes the first stage, fast locking because the diode and holder above it have a relatively small thermal mass. Setpoint is usually somewhere between 19 and 24°C, is achieved in < 30 s and is stable to 10 mK.

The second stage of temperature control is a slow buffer stage responsible for the entire

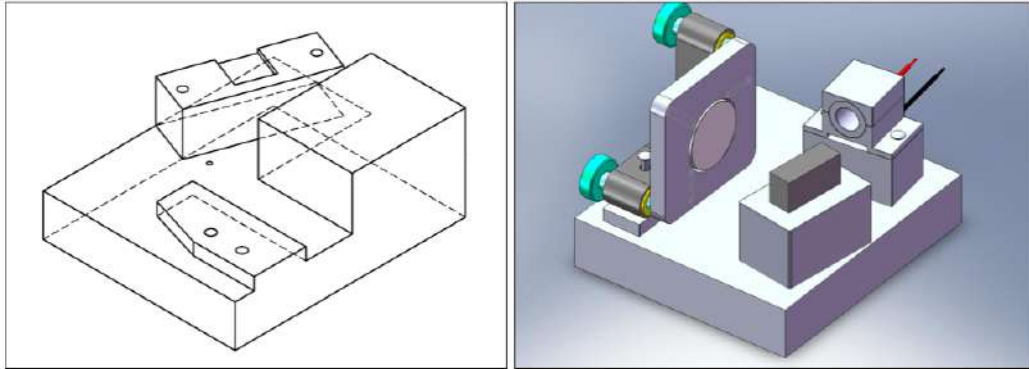


Figure 2.13: Blueprint of the current ECDL baseplate design (left). SolidWorks rendering of an older baseplate design, with representative mirror, diffraction grating and diode housing (right).

baseplate. Because of the large surface area and large thermal mass of the baseplate, the second stage provides heating with a resistive Kapton heating pad rather than a TEC. The heating pad cannot control the direction of heat flow, so this stage’s temperature setpoint is set just above room temperature, and a one-way diode is installed in the heating pad circuit so that “cooling” is achieved by passive heat loss to the environment. This stage is usually set somewhere between 27 and 31°C, but achieving initial lock can sometimes take > 10 minutes. Once achieved however, the temperature is usually stable to within ~ 50 mK unless perturbed by an external shock. We found that the power output from the Vescent controller was often insufficient for stabilizing this setpoint, so we installed the current amplification circuit shown in Fig. 2.15.

2.2.1.2 Electronic feedback

The diffraction grating and optical feedback mirror are installed as shown in Fig. 2.13, the spacing between them varying based on the wavelength of the diode, and usually between 8 and 13 cm. A small recess is drilled into the horizontal knob of the mirror mount face into which a piezo-electric transducer (PZT) is installed - once installed, the knob ball should press against the PZT. Adjusting the mirror mount knob or the embedded PZT changes the wavelength of the laser light that is sent back to the diode, and changes the laser wavelength by stimulated emission. Hence, PZT control is usually used as an auxiliary “slow” feedback

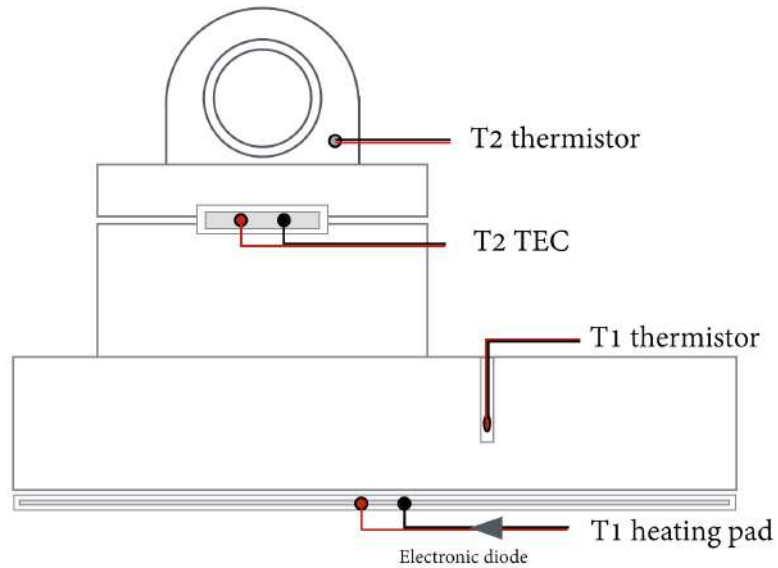


Figure 2.14: Schematic of the ECDL feedback principle. The first order off of the diffraction grating is fed back into the diode, causing stimulated emission. The wavelength of the feedback light is determined by the angle of the feedback mirror. The zeroth order is the output from the ECDL.

stage, while adjusting laser current, which adjusts the wavelength too, is used for primary feedback.

2.2.1.3 Littman configuration, two-stage PZT

One can increase the mode-hop-free tuning range of a diode laser by modifying the feedback mirror geometry. Littman and Liu [Liu and Littman, 1981] introduced a novel geometry that accounts for the fact that adjusting the mirror angle also adjusts the cavity length, both of which compete in defining the optimal cavity wavelength. By defining the mirror pivot point at the intersection point of the planes of the mirror face and the diffraction grating face, this conflict is alleviated. In this geometry, the changing feedback angle and the cavity length cause equal changes in θ , and continuous scanning can be achieved over much larger ranges.

Instead of building a cavity with such a pivot arm, we implemented a “first order”

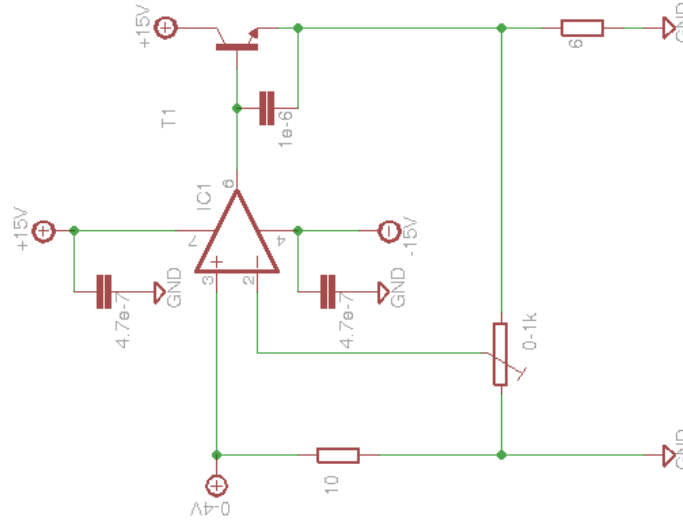


Figure 2.15: Booster circuit for the T1 temperature stage.

Littman configuration. We installed a second PZT between the mirror and the mount face. Applying a voltage to this mirror that is some constant fraction of that applied to the PZT installed at the mirror knob point, we can simulate mirror rotation about a desired point. The larger the fractional voltage, the farther away the pivot point.

This two-stage PZT setup is used in several of our ECDL systems and results in significant increase in continuous scanning range, or a typical improvement from ~ 2 GHz to $\sim 10 - 20$ GHz, or even larger.

2.2.1.4 “Lens tweaking”

Diode laser output is typically collimated using a small aspheric lens with threaded mounting to adjust its distance from the diode (e.g. Thorlabs part no. LT110P-B). Collimation of the laser beam is often achieved by adjusting the lens position while observing the beam spot at several meters. Our group has found that there is a better way to set the beam focus, and that with better alignment the laser ECDL feedback mode is cleaner with larger continuous-mode sweeping ranges. The protocol for “lens tweaking” is as follows:

1. Roughly collimate the beam as described above, install the diode in the ECDL, and find visible feedback by retroreflecting the mirror’s beam back onto the diffraction

grating. This is often easiest to see by adjusting the mirror's vertical knob.

2. Install a laser power meter just outside the ECDL and plot this power on a scope with slow (~ 1 s) time constant
3. Using a very small flat-head screwdriver, or hex key, adjust the lens position by pressing lightly on the notches in the lens face (typically adjusted using a spanner wrench).
4. Constantly adjust the mirror's vertical knob to get real-time feedback on the ECDL's optimal output power.

The feedback power as observed on the scope should change significantly for very small, nearly imperceptible changes in the notch positions, requiring mirror realignment, and should be dependent on the beam focus as determined by the notch position.

We have found that every diode behaves differently, and that some diodes are more responsive than others to improvement from this alignment technique. In any case, we find gains both in the total output power (e.g. > 30 mW where previously we had only ~ 25 mW), as well as in the continuous scanning range, both by PZT as well as by laser current adjustment.

2.2.2 Tapered amplifier

Our diode lasers typically provide no more than 30 to 50 mW of power. For experiments that require higher powers, a tapered amplifier (TA) is a common solution [Walpole, 1996]. After purchase of the TA diode, we assembled the mounting base plate and temperature control ourselves, as seen in Fig. 2.16. There are two focusing optics, one to mode-match the input beam to the TA mode, and the second to shape the output TA beam mode.

Alignment is achieved by carefully mode-matching the input beam to the output mode of the TA, which is set by two lenses on translation stages. The spontaneous emission output power of the TA is ~ 100 mW, and when alignment is achieved, the output jumps in several stages to powers as high as ~ 1.1 W. For power near 1 W, the TA power supply is set to an output current of just under the 3 A safety limit. The quality of the output, and

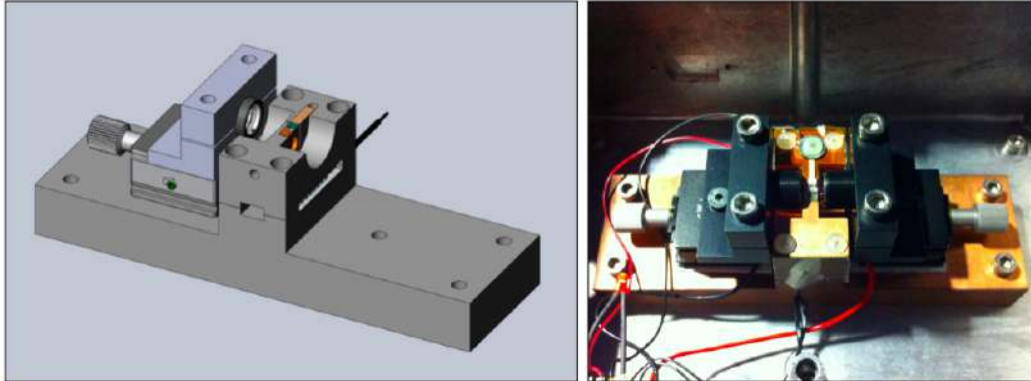


Figure 2.16: SolidWorks rendering (left), in which the TA is depicted in green, and picture (right) of the tapered amplifier setup.

its stability, depends sensitively on the TA temperature setpoint, where the desired setpoint is found iteratively as the system stabilizes.

After a desirable setpoint has been found, the temperature should only rarely need to be adjusted. The primary culprit for low output power is the alignment of the input beam, which should be checked weekly, and sometimes daily.

We use a TA to amplify our 922 nm diode laser, and running the controller (Thorlabs LDC 240 C) at 2.95 A we generate the ~ 1 W of power necessary for generating a sufficient amount of blue light for our cooling and trapping purposes. Section 2.2.3 describes our methods for blue light generation.

2.2.3 Nonlinear crystal and second harmonic generation

The majority of the 1 W output of the 922 nm TA is then sent to the frequency-doubling cavity. After a first-generation cavity using the design from [Klappauf *et al.*, 2004], a second model was designed using the more effective bow-tie cavity described in [Targat *et al.*, 2005; Hemmerich *et al.*, 1990], out of which as much as ~ 600 mW of 461 nm output light can be produced; 400 mW is a more realistic daily amount. Figure 2.17 shows the cavity schematic.

The output power depends very sensitively on the temperature setpoint of the nonlinear crystal. This temperature should be incorporated into the iterative alignment process, since it appears that the optimal temperature setpoint is dependent on the beam input position

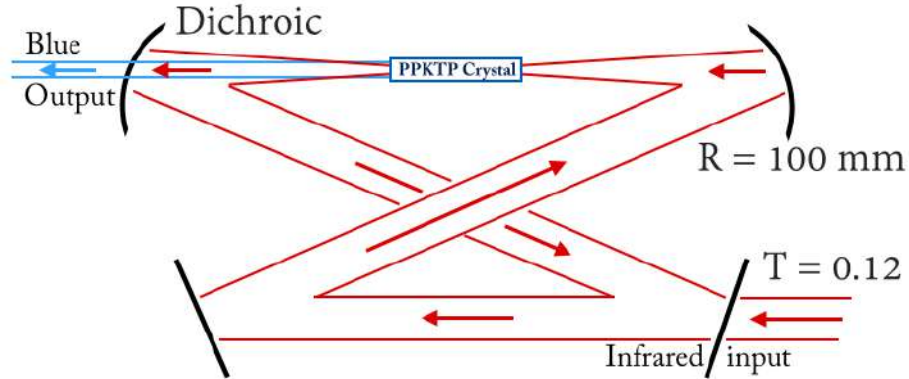


Figure 2.17: Diagram of the bowtie cavity. T is the input transmission coefficient for infrared light, and R is the focusing radius of the curved mirrors.

and alignment to the crystal.

2.2.3.1 Initial alignment

As described in [Targat *et al.*, 2005], there is an optimal focusing parameter for the input infrared beam, which determines the length of the cavity. Using this value, our cavity was drawn using SolidWorks (Fig. 2.18), and then printed to actual scale and taped to the breadboard on which the cavity was being built. The mirrors were then placed over the drawing as a first approximation of the cavity. From there, the first goal was to achieve infrared cavity resonance without the nonlinear crystal. This was observed with an infrared camera, and is achieved by starting with alignment of the input beam and iteratively centering the beam on each cavity mirror. When alignment is close, adjustment of any cavity mirror knob will result in a cavity-resonance flickering of the beam spot as observed by the infrared camera.

Installing the periodically-poled potassium titanyl phosphate (PPKTP) crystal does change the effective cavity length and therefore the beam alignment to the cavity, but one should still be able to detect some output blue light. From this point the cavity must be adjusted incrementally, by tuning the crystal position setpoint temperature, until a higher output power is achieved. It can help to expand the blue output beam spot onto an index card and look at the output TM_{xy} mode. The highest powers are achieved for the desired

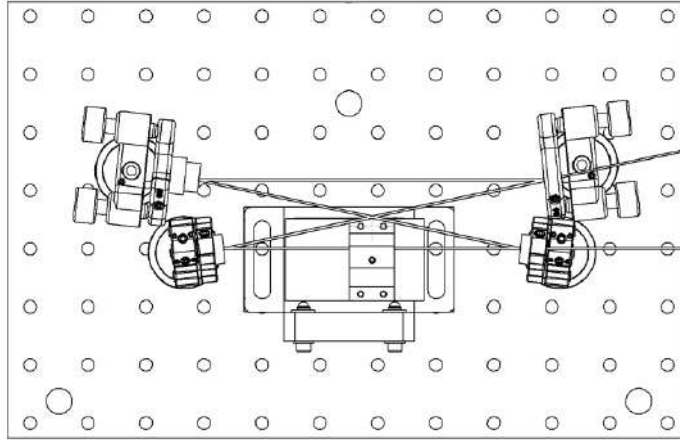


Figure 2.18: Blueprint of the ideal bowtie cavity dimensions (breadboard holes are spaced by 1 inch). The initial alignment was achieved by printing this at physical scale, cutting holes for the mirror mounts, and taping to the breadboard. After the alignment was achieved, the blueprint was removed from the breadboard.

TM₀₀ Gaussian mode.

The blue light system requires daily maintenance. It is important to always start by checking that the 922 nm diode laser mode, and the output power from the TA are satisfactory before adjusting the doubling cavity.

2.2.4 Locking system

The output from the doubling cavity is then sent to the experiment using a high-power fiberoptic cable, whose output is typically between 250 and 300 mW. Approximately 10 mW of this light is directed toward a galvatron vapor cell (Hamamatsu L2783 galvatron series) for saturated absorption locking to the 1S_0 - 1P_1 line in Sr [Preston, 1996; MacAdam *et al.*, 1992; Wieman and Hansch, 1976].

Figure 2.19 also gives a rough schematic of the feedback electronics. The requirements are two-fold: firstly, feedback on the bowtie cavity, via a PZT mounted to one of the cavity mirrors, to provide stable blue light frequency-doubled from the input infrared, and secondly, feedback on the laser current and ECDL PZT to stabilize the laser frequency to the Sr vapor source. A typical error signal for frequency doubling, and saturated absorption

locking are given in Fig. 2.20. These two purposes are divided roughly between the upper and lower parts of Fig. 2.19. As shown, a beam sampler directs part of the output blue light just after the doubling cavity to a photodetector for feedback and monitoring.

2.2.5 Power distribution, frequency offsets

The power of our blue light system is divided between several important tasks, each of which is set via acousto-optic modulators (AOMs) to a specific frequency offset from the atomic transition: saturated absorption feedback locking (4 mW, -67.3 MHz), Zeeman slowing (65 mW, -502.5 MHz), MOT beams (~ 15 mW for horizontal axes, ~ 25 mW for vertical axis, -27.3 MHz), and imaging (~ 5 mW, 0 MHz). The emphasis of the schematic in Fig. 2.19 is on the electronic feedback system. Geometries for the MOT beams can be found in Fig. 2.2. Section 2.3 describes how we achieve atom slowing with the stable blue light source.

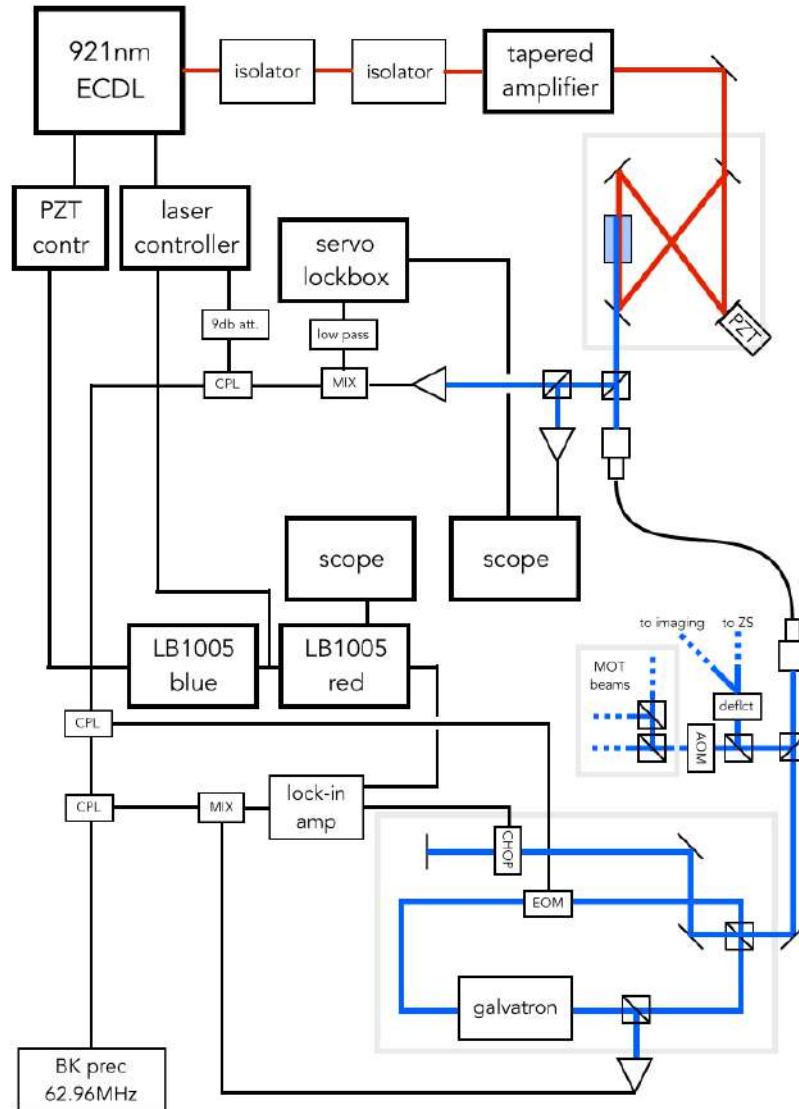


Figure 2.19: Schematic of the 461 nm laser system, with detail given to the electronic feedback for the frequency-doubling cavity, as well as for the saturated-absorption locking feedback system.

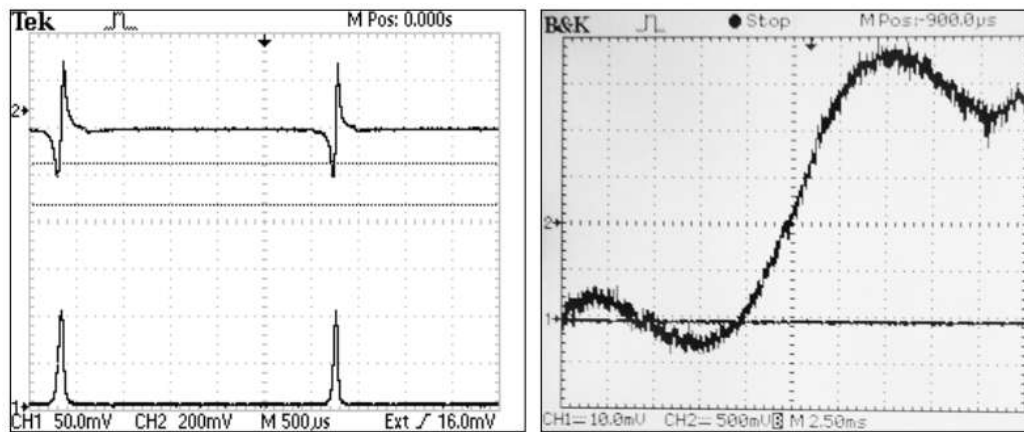


Figure 2.20: Scope traces for the frequency-doubling cavity (left), and the vapor cell atom lock (right). For the doubling cavity, the upper channel trace monitors the error signal, and the lower trace monitors the actual blue power output from the cavity. Note that the full error signal of the vapor cell lock is often not within the mode hop-free scanning range of the diode.

2.3 Zeeman slower

Atom beam slowing is achieved using a Zeeman slower and 461 nm light [Phillips and Metcalf, 1982] to create an electro-magnet with the desired field profile. Radiation pressure from laser light resonant on the strong $^1S_0 - ^1P_1$ transition at 461nm, provides the slowing mechanism, and to account for the changing Doppler shift of the continually decelerating beam, the Zeeman slower provides the magnetic field. A common method for slowing neutral atom beams, Zeeman slowers provide a static but spatially varying field that assumes a particular deceleration profile along the beam axis, providing at each point along the path a magnetic field-induced Zeeman shift to cancel the corresponding Doppler shift.

Zeeman slowers are traditionally constructed by winding carefully designed layers of wire around the atomic beam vacuum tube and running a current through the wire ([Phillips and Metcalf, 1982; Bagnato *et al.*, 1989]). Recently, designs based on permanent magnets have been suggested and implemented [Ovchinnikov, 2008]. There are multiple benefits to using a permanent magnet ZS. These benefits span adaptability, robustness, ease of maintenance, zero power consumption, and low cost; the current-sourcing power supply as well as water cooling are not necessary. As detailed in this work [Reinaudi *et al.*, 2012a], we implemented a dynamically controlled, optimizable permanent magnet Zeeman slower for our experiment.

We designed a permanent magnet Zeeman slower (ZS) based on the model in [Ovchinnikov, 2008]. Described here is the process of modeling the slower for our specific design field, as well as the construction and finally the tuning of the slower. This section follows the work of our recent paper [Reinaudi *et al.*, 2012a].

2.3.1 Design considerations

The magnetic field profile for efficient atom slowing is set by placing an array of permanent magnets at variable distances from the atomic beam. The magnets are neodymium disks of 0.5" diameter, 1/16 to 1/4" thickness, and 0.25 to 0.95 J/T magnetic moment. The entire assembly is enclosed in a μ -metal magnetic shield, as pictured in Fig 2.21. We performed nonlinear optimization simulations to determine the predicted positions and lateral spacing of the magnets, as an advance proof of our intended design.

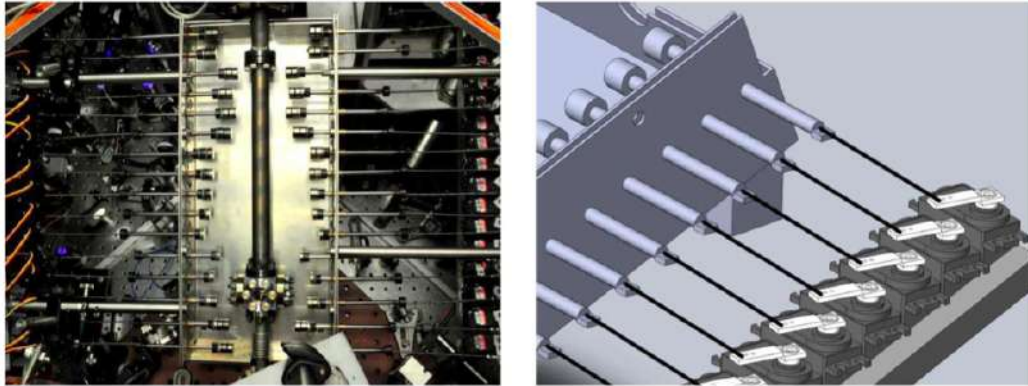


Figure 2.21: Picture of the ZS installed on the experiment, lid off (left). SolidWorks rendering of the motor attachments to the magnets (right).

Design constraints include the finite strength and size of the magnets and the spatial constraints of the vacuum system. Achieving a smooth field profile as well as a high field strength along the atomic beam path is a balancing act since the closer a magnet is to the beam axis, the sharper its local effect on the magnetic field and hence the closer neighboring magnets have to be placed for a smoothing effect. We found that performing the computer simulation is important for determining the right spacing between neighboring magnets and less important for determining magnet distance from the beam axis, since the latter is adjustable, while the former is a fixed feature of the construction.

The resulting magnetic field is transverse to the atomic beam. As atoms travel through the field region, they are decelerated by counterpropagating light that is linearly polarized in the direction normal to the field and is gently focused to match the slight divergence of the 6 mm wide atomic beam.

2.3.2 Computer control of the field profile

In order to allow real-time computer control of the magnetic field profile, the magnets were mounted to stainless steel rods that freely slide in bronze sleeve bearings placed through the walls of the μ -metal case, as can be seen in Fig. 2.21. The actuation of the magnet positions relies on low-cost servomotors that are typically used in model airplanes and cars. Such servomotors provide a rotation range of 90° and a velocity of $\sim 60^\circ/\text{s}$. The model

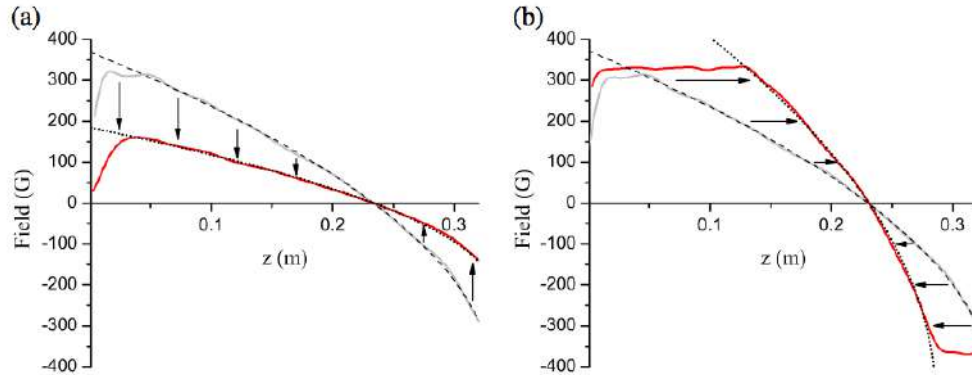


Figure 2.22: (a) Test case in which the field value was halved at all points along the ZS path. (b) Test case in which the field profile was compressed over half the original length. Switching in both cases is achieved in < 0.5 s.

we used is HS-422 by Hitec, but there is a large variety of options available depending on different requirements, such as torque, speed, and size.

In order to transform the rotary motion of the servomotors into linear motion, each sliding rod is linked to the horn of a servomotor through a clevis and a threaded rod (Fig. 2.21(b)). Sixteen servomotors are placed on each side of the ZS. For ease of assembly, the servomotors are glued to each other (with appropriate spacers) and to an aluminum bracket attached to the case of the ZS.

The servomotors are controlled by electronic modules manufactured by Phidgets. While other options are available, these modules were chosen for their cost effectiveness and ease of use since they interface with a computer USB port and provide a straightforward application programming interface (API) for most common programming languages. Four modules are needed to control the 32 servomotors. During the operation of the motors, care must be taken about the range that each of them should be allowed to explore. We limit the movement of the servomotors using the computer program that controls them.

Many modern experiments involve trapping several atomic species. In those cases, the ZS is typically designed for the one that requires a longer slowing region, thus not achieving the maximum efficiency for the other species at this slower length. However, in experiments that routinely change the trapped species, it would be useful to switch rapidly

between magnetic field profiles in a reproducible way so that each species is optimally slowed. The computer-controlled setup described here makes this process straightforward since any number of magnet configurations are saved in the software and can be retrieved when needed. Additionally, for experiments that use two species simultaneously, one can sequentially load each species using its optimal profile, since the switching between field profiles is consistently < 0.5 s.

In general, designing the ZS magnetic field depends on many practical factors such as the available space and laser power, the initial thermal velocity of the atoms, and the presence of transverse cooling of the atomic beam [Dedman *et al.*, 2004]. Our setup allows for tuning the magnetic field profile for an optimal loading given these specific experimental constraints.

As a proof of principle, we demonstrate the accuracy and flexibility of the servomotor control by switching the magnetic field between initial configuration A and configuration B giving the same profile but twice weaker at any point of the ZS (Fig. 2.22(a)). We also demonstrate switching from field configuration A to configuration C, which corresponds to the same field profile but twice compressed along the propagation axis (Fig. 2.22(b)). Note that the number of magnets on three pairs of rods was changed between Figs. 2.22(a) and (b).

The repeatability of our servo-controlled ZS was tested by measuring the field profile after switching from different servo configurations to configuration A. The field profile can be consistently reproduced within an accuracy of 1%, reaching the 1 G resolution limit of our gaussmeter at all points in the ZS. Note that, to achieve this accuracy, the backlash (mechanical hysteresis) of the servomotor assembly has to be accounted for. This is easily accomplished by systematically instructing the computer to move all the servomotors to the outermost position before adopting the desired configuration.

2.3.3 Real-time optimization of atom slowing

One of the advantages of a motorized ZS is that it can be easily controlled by a computer program. This lends itself well to performing complex optimization algorithms that seek out solutions at a pace unmatched by manual tuning. In the scheme presented here, we

feedback on a live measurement of the number of trapped atoms in the MOT.

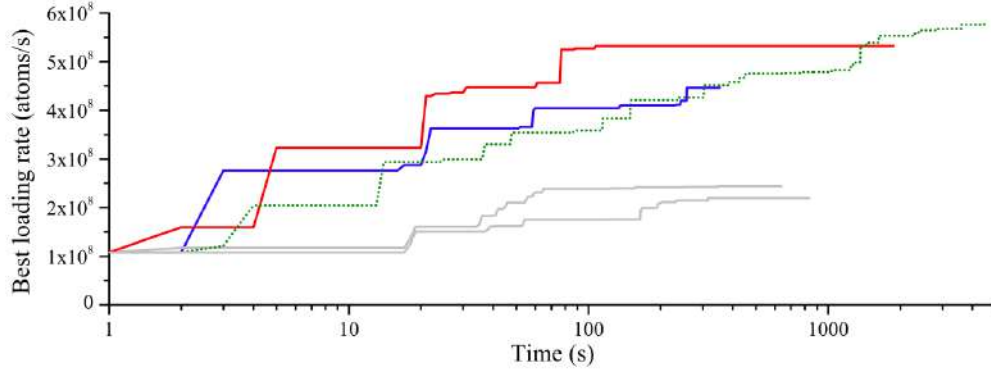


Figure 2.23: Plot of the best loading rates achieved by various optimization algorithms. The colored lines are several loading rates achieved by the genetic algorithm, and the gray lines are those achieved by the local algorithm.

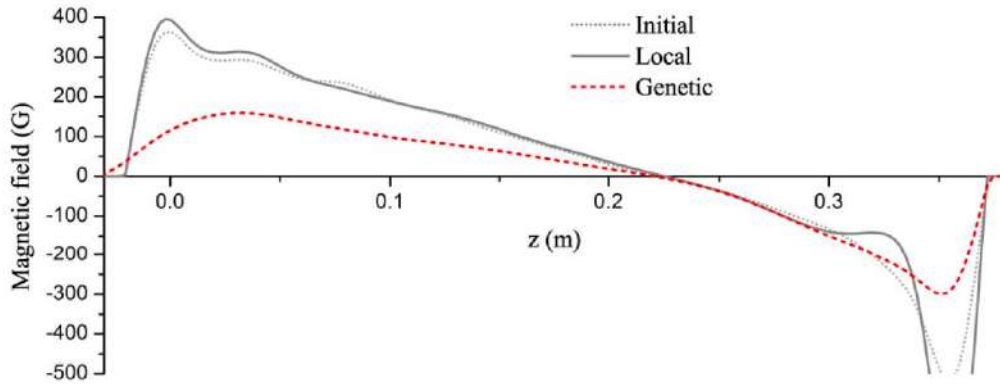


Figure 2.24: The field profiles produced by the local algorithm (dark gray) and the genetic (red).

A CMOS camera connected via USB to the computer provides a live view of the MOT fluorescence light. The experiment control program gives us the ability to actuate the servomotors, to process images from the camera, and to use a versatile optimizing toolkit. During an optimization run, the trapping laser beams and the magnetic field of the MOT are turned on continuously, but the repumper lasers are kept off at all times for the following reasons: (i) the smaller MOT makes the procedure less sensitive to typical instabilities

associated with large atom numbers; (ii) the lifetime of the MOT is short under these conditions, and as a result, switching to a new servomotor configuration leads to a stable fluorescence signal on time scales < 1 s; and (iii) due to the artificially large loss rate, we can assume that the loading rate is well represented by the atom number and thus by the fluorescence signal.

Images are gathered from the camera at a rate of ~ 10 /s. The capture rate of the MOT is inferred by summing the pixel values on the appropriate area of each image and is then fed into the optimizer, which in turn controls the servomotor positions. The detuning of the slowing laser is not a factor in the optimization since the field profile can be shaped with greater freedom than in traditional slowers, achieving a variety of slopes and maximum field values (Fig. 2.22). Typically, the optimizer sets a new configuration every second, allowing the servos to fully reach their designated positions and avoiding any transitory effects in the loading or decay of the MOT.

For the study of the automated optimization, we consider the field configuration A from Section 2.3.2. This field closely matches the theoretical profile for Sr in the 32 cm designated slowing region (assuming 65% of maximum deceleration) and overshoots in the region immediately following. Such overshooting is undesirable in an actual slower since it can cause overslowing, preventing atoms from reaching the trapping region. However, it is illuminating to start the optimization from this field since it will be shown that our optimization algorithms generate different and equally interesting solutions to this initial condition.

We have tested several algorithms for the optimization of the MOT capture rate. Since there is no expression for the derivative of the capture rate as a function of the servomotor positions, only black-box optimization algorithms can be used. The results given by two algorithms will be presented here. These two methods are a local search using the Nelder Mead simplex algorithm and a global search using a genetic algorithm, taken from the NLOpt non-linear optimization package (<http://abinitio.mit.edu/nlopt>), and the Evolving Objects package (<http://eodev.sourceforge.net>). Genetic algorithms mimic the process of natural evolution by using the concepts of inheritance, mutation, and fitness. They perform particularly well on black-box problems with many interdependent variables. The param-

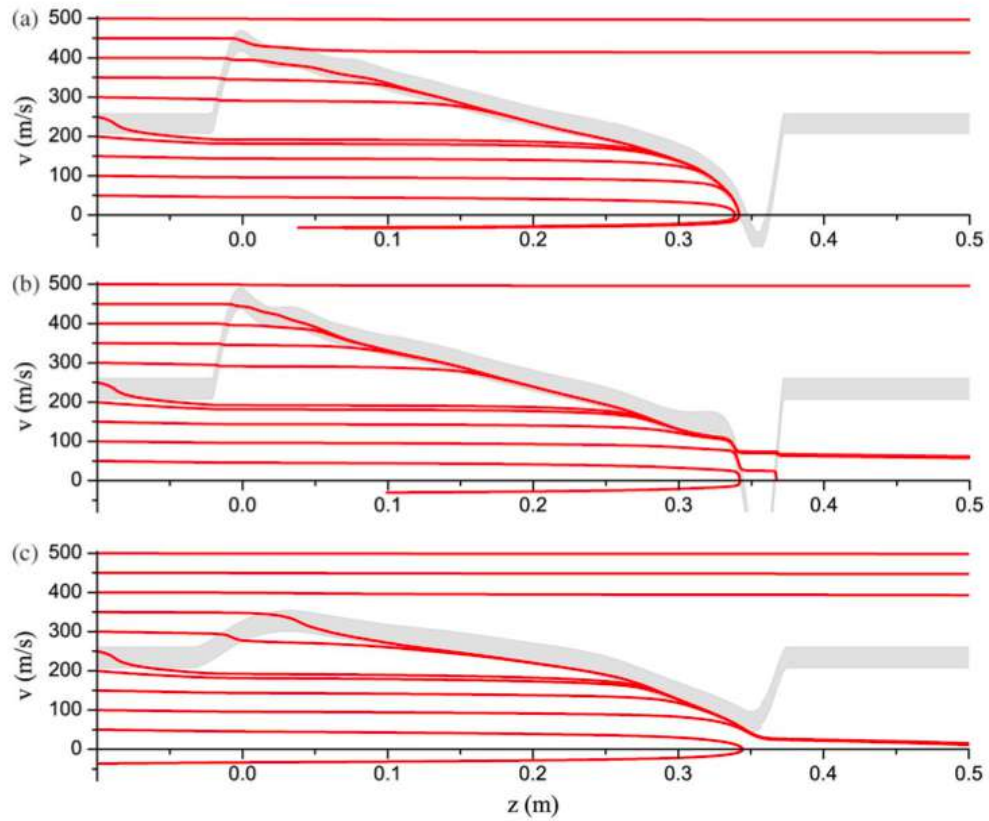


Figure 2.25: A model of the velocity profile of atoms in the field profiles produced by (a) the original design, (b) the local solution, and (c) the genetic solution.

ters used for the genetic algorithm runs were typically as follows: population size of 20 to 40, mutation rate of 40%, crossover rate of 30%, and total number of generations of 100 to 200.

Figure 2.23 depicts typical runs of the optimizer. On these plots, the starting point corresponds to the initial configuration A and is used to normalize the atom capture rate for each run, preventing long-term atom number fluctuations from introducing a bias to our comparative analysis. The vertical axis scale is given by the extrapolated capture rate in the presence of repumpers since this is a more conventional quality measure.

For the local optimization, it takes ~ 100 servomotor configurations to converge to a magnetic profile that yields an actual loading rate of $\sim 2 \cdot 10^8$ atoms/s (as measured with repumpers). The local optimization has to be restarted typically 5 to 10 times before reaching

a steady value. This occurs because it optimizes by probing local configurations that result in small capture rate changes and hence is sensitive to experimental noise. Alternatively, the genetic algorithm delivers a loading rate $\sim 6 \cdot 10^8$ atoms/s in ~ 1000 servomotor configurations. Genetic algorithms are insensitive to noise because they use stochastic operators for selecting the best configurations. Consecutive runs of the genetic algorithm starting from varying initial conditions produce similar field profiles. If the 32 servomotors are allowed to move independently without maintaining strict symmetry about the ZS axis, better results can be achieved through compensating any stray fields or imperfections in magnet alignment (Fig. 2.23), although with a slower initial improvement due to the increased complexity.

Here we present simulations that give an interpretation of the gains achieved in the two final fields resulting from optimizations starting from the initial field. Figure 2.24 shows the initial field and the two final fields as computationally inferred from the magnet positions. There are noticeable differences between these three fields: the locally optimized field exhibits an unexpected plateau followed by a steeper overshoot and the genetically optimized field is shallower overall.

These differences can be explained by using a phase portrait, which depicts the deceleration dynamics in the one-dimensional phase space (z, v) according to the radiation pressure force

$$F(v, z) = -\frac{\hbar k \Gamma}{2} \frac{s_0(z)}{1 + s_0(z) + 4(\delta_0 + kv(z) - \mu B(z)/\hbar)^2/\Gamma^2} \quad (2.13)$$

where B_z is the ZS magnetic field, the average saturation parameter for the cycling transition is chosen to be $s_0(z) = 1.5$, and the detuning of the slowing light is $\delta_0 = 2\pi \cdot 505$ MHz in this case. For Sr, the atomic spontaneous decay rate is $\Gamma = 2\pi \cdot 32$ MHz, and the optical wavenumber is $k = 2\pi/(461 \text{ nm})$.

Figure 2.25(a) shows that the initial profile is overslowing many of the atoms and reversing their velocities. Figure 2.25(b) explains the slowing dynamics of the locally optimized field. The presence of the plateau in the magnetic profile causes the atoms to be slowed less efficiently over the 5 cm region just before the field overshoot. These atoms are then moving fast enough to pass through the region where they were previously stopped, since the interaction time is too short to exert a full stopping force. They do undergo a sudden

slowing kick that brings them within the capture range of the MOT.

The genetic algorithm solution depicted in Fig. 2.25(c) smoothly reduces the maximum field at the end of the slower ($z \simeq 0.3$ m), leading to a velocity distribution that is adequately within the capture range of the MOT, without overslowing. Note that the convergence to a lower field magnitude near the entrance of the slower, and thus to a weaker deceleration in the first part of the slower, led us to suspect that the typical velocity of the atomic beam is below the 510 m/s design speed. The velocity distribution was subsequently measured, and it was confirmed that the most probable velocity of the Sr beam is only 420 m/s.

2.4 The 1S_0 - 1P_1 MOT

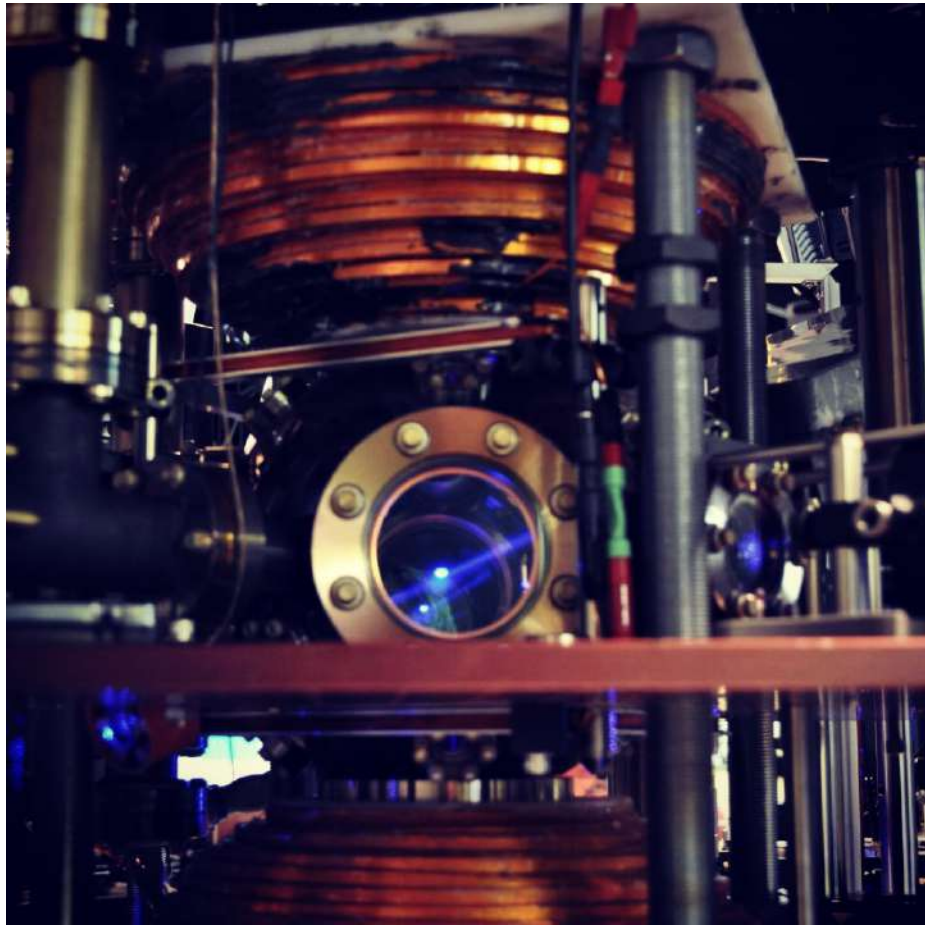


Figure 2.26: Picture of the vacuum chamber with a typical mK blue MOT present.

2.4.1 Principle of a magneto-optical trap

The cooling mechanism described in Ch. 1, where emitted photons are statistically higher in energy than absorbed photons, does not automatically lead to trapping. Without trapping, the cooled atoms form what is called an optical molasses ([Metcalf and van der Straten, 2002]). There are several kinds of traps for neutral molecules; in our experiment we employ a magneto-optical trap (MOT), as seen in Fig. 2.26.

The trapping mechanism of a MOT combines several features to create a region in space. As atoms enter this boundary region, they experience a position-dependent restoring force toward the trap center. This is best described using the 1D illustration of Fig. 2.27.

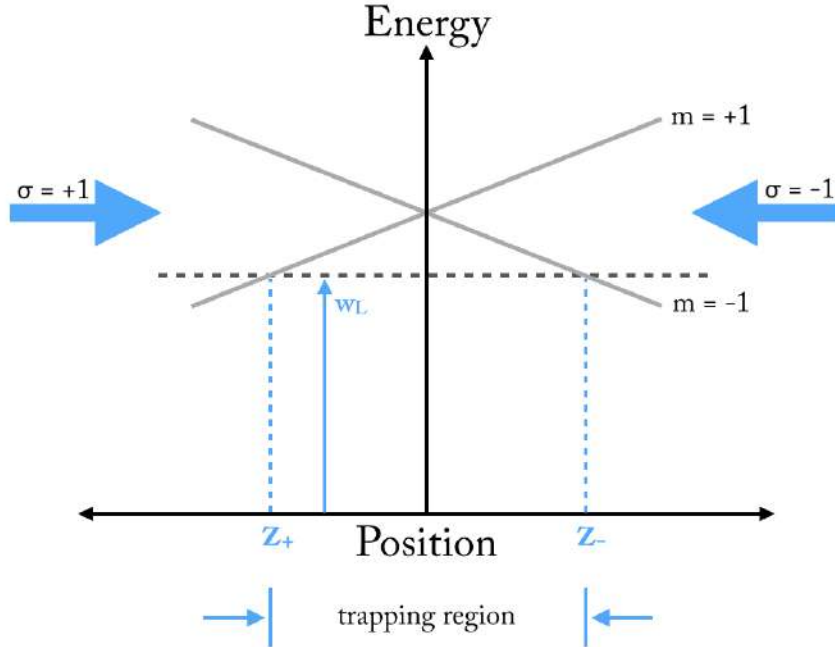


Figure 2.27: Diagram of the mechanism of a magneto-optical trap. The quadrupole magnetic field profile grows linearly outward from the trap center, as evidenced here by the slope of the $m = \pm 1$ magnetic sublevels of the 1P_1 state. Photons of the MOT laser, at frequency ω_L , are only on-resonance when the Zeeman shift and the Doppler shift match the detuning of the incoming laser beam. Circularly-polarized light ensures that photons will only be absorbed by the beam whose momentum absorption kick restores atoms toward the trap center.

Quarter-wave plates before and after the trapping region ensure that the incoming and returning laser beams are both circularly polarized, but with opposite circularity in the lab frame, σ_+ and σ_- . The laser is red-detuned from the transition by an amount $\delta = \omega_L - \omega_0$, where ω_L is defined in the figure. The quadrupole field profile, described in more detail in Sec. 2.4.2, ensures that the field strength is zero at the trap center, and scales linearly outward. As an atom moves into the boundary region, it is Zeeman-shifted into resonance with the laser beam whose orientation will ensure an absorption momentum kick back toward the trap center, ensuring trapping. The Doppler effect enhances absorption from the laser beams whose momentum kicks counteract the atom velocity, leading to cooling.

2.4.2 Quadrupole coils and compensation coils

The MOT coils necessary for producing the field gradient described in Fig. 2.27 were constructed out of enamel-coated, hollow square copper wire with a 1 cm diameter, as shown in Fig. 2.28. A current of 25 A at 30 V is sent through these coils, producing the field profile shown in Fig. 2.29. Because the high current can cause heating, chilled water is fed through the hollow coil center to maintain a low operating temperature. The chilled water is supplied by a closed-system Haskris water chiller with temperature setpoint 65 °F.

Ambient magnetic fields in the lab are on the order of ~ 1 G; to ensure that there is zero field at the trap center, we installed compensation coils for all three axes, as shown in Fig. 2.30. Spatial limitations around the vacuum chamber prevented us from installing true Helmholtz coils - circularly-wound, with coil radius R matching the separation between the opposing pairs - a design that maximizes field uniformity between the coils. These coils do not require cooling, as < 5 A provides suitable magnetic field values for our purposes. Early diagnostics on the $^1S_0 - ^3P_1$ MOT showed that the trap's vertical position was drifting in correlation with changes in the vertical component of the lab's ambient magnetic fields (the source of which, and why it is mostly vertical, was not determined). As a result, we installed an inverting summing amplifier circuit to add a small feedback correction current to the base current supplied to the vertical compensation coils. An illustration of the inverting summing amplifier can be found in Fig. 2.31.

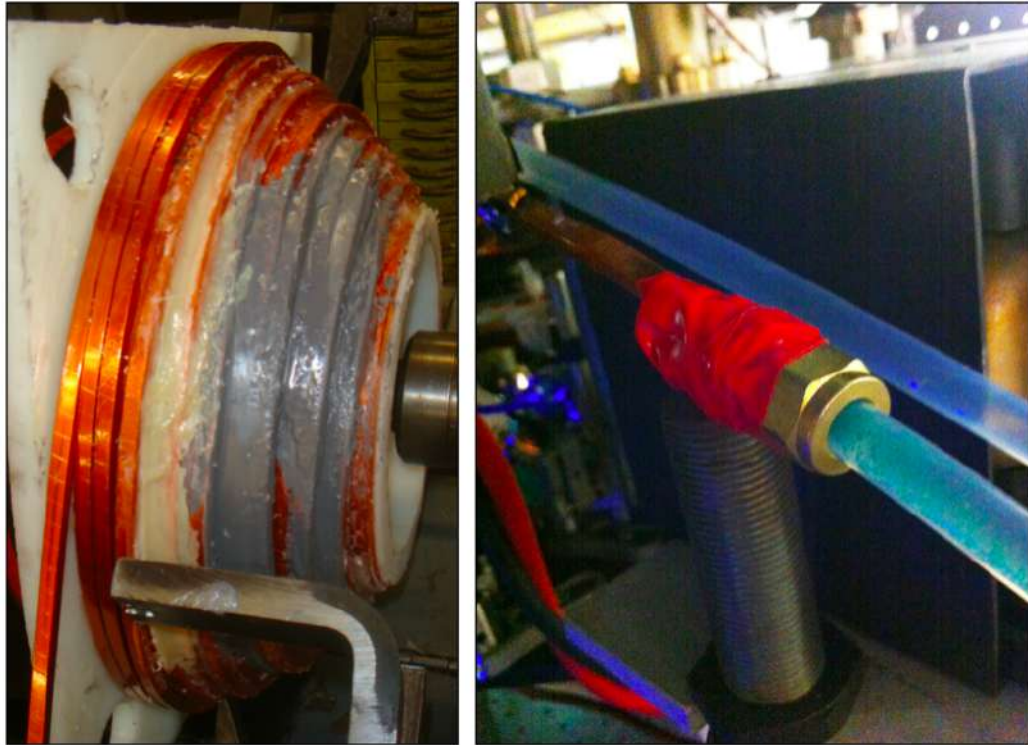


Figure 2.28: One of the two quadrupole coils, before installation on the system (left). The joining between the hollow, enamel-coated quadrupole coils and the feed from the water cooling system (right).

2.4.3 Repumper lasers

We employ a repumping scheme as described in Fig. 2.32. We use a software locking technique: the wavelength as measured by the wavemeter is used as digital feedback on the diode PZT. The wavemeter has MHz to 10s of MHz resolution, which is sufficient for our purposes.

The MOT atom number with repumpers is an order of magnitude larger than without repumpers, but the density increases by only roughly a factor of two.

2.4.4 Imaging

We perform all of our atom imaging using light tuned to the $^1S_0 - ^1P_1$ transition in Sr. We use absorption imaging, and before successfully implementing our lattice trap, imaging was

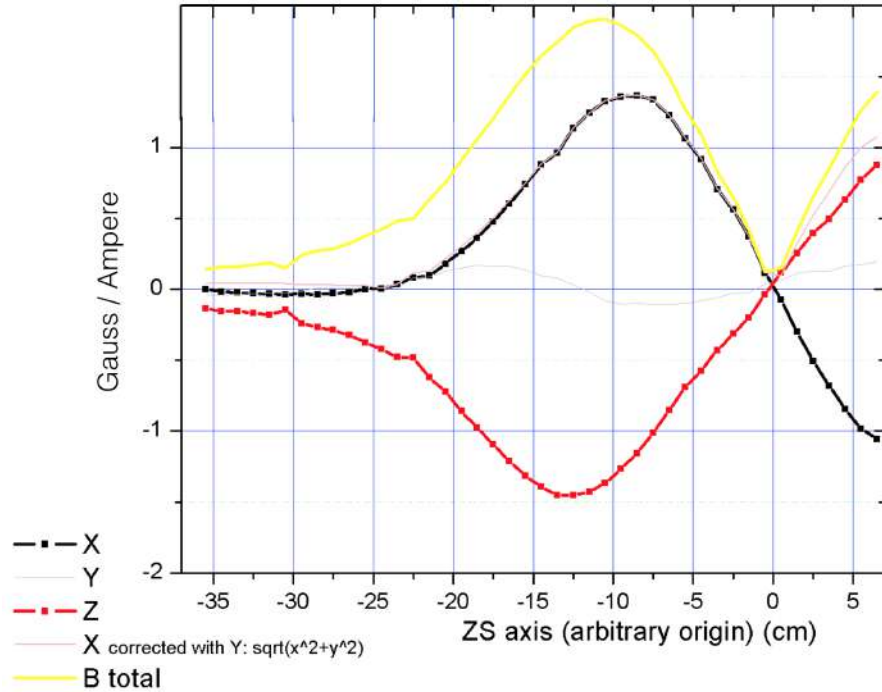


Figure 2.29: Plot of the MOT coils field profile along the atom beam axis. The field crossing point marks the trap center, with a field gradient of 25 G/cm for 25 A of current.

performed using the Thorlabs DCC1240M camera and Thorlabs MVL25 25mm objective. Absorption imaging is described in [Reinaudi *et al.*, 2007]; the three-image technique is illustrated in Fig. 2.33. As shown in Fig. 2.19, 5 mW of blue light is siphoned off from the MOT beams for imaging purposes, and is coupled to a translation stage fiber. The output fiber is located on the vacuum chamber breadboard, followed by optics for alignment and focusing. The beam is expanded via telescope to ~ 1 cm waist. The three steps of absorption imaging are as follows:

1. Image the atom sample; a sufficiently long exposure ensures that the atom sample is thoroughly wiped.
2. Image an empty trap, with the imaging beam still on.
3. Take a dark image with no light pulse.

Once the objective's magnification has been determined (see Sec. 2.6 on the 689 nm MOT for details) and one has a value for the spatial extent per pixel (camera-dependent), imaging

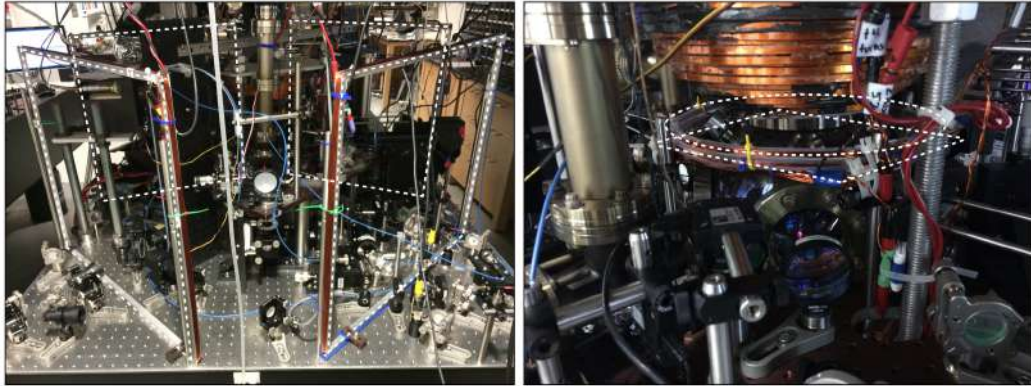


Figure 2.30: Pictures of the compensation coils surrounding the vacuum chamber, where the coils have been traced with dashed white lines. At left, a picture of the large x and y axis compensation coils. These require ~ 75 turns to achieve the 3 G design setpoint. At right, a picture of the vertical z axis coils, mounted closer to the chamber, and therefore requiring only ~ 25 turns to achieve the design setpoint (the opposing pair is out of view). Notice that for the vertical set, there are square as well as circular coils. The circular coils were added recently in order to perform measurements at much higher, ~ 40 G field strengths. These were not used in any of the measurements for this thesis.

can be used to determine several important characteristics of the atom trap.

After a loading sequence as described above, the imaging beam is pulsed for $40 \mu\text{s}$ (gated by the imaging shutter whose minimum shutter time is ~ 4 ms). The image is then fed to the lab computer, and properties of the trap, such as atom number or temperature, determined as described in the next sections. Figure 2.34 shows the approximate time scale for the imaging sequence. The imaging beam is collimated with a diameter comparable to the lens aperture of the objective, ~ 1 cm, and is oriented as shown in Fig. 2.2 (perpendicular to the lattice and probe beams, 45° from the MOT beams). The beam frequency is on resonance with the electronic transition.

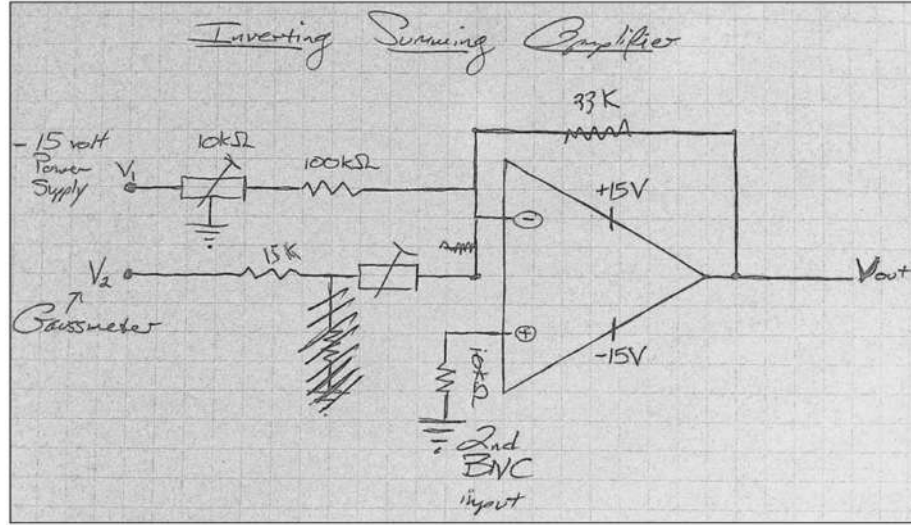


Figure 2.31: Inverting summing amplifier used for feedback on the vertical compensation coils, for steadying the position of the red MOT. The circuit sums the current from the compensation coils driver with the small correction that comes from the MEDA Gaussmeter.

2.4.5 Characteristics of the millikelvin MOT

2.4.5.1 Atom number

The absorption of light by the atom cloud follows the Beer-Lambert law. The absorption images give the computed optical density:

$$\text{OD} \equiv \sigma_0 \rho_c, \quad (2.14)$$

where σ_0 is the cross section of the transition at resonance and ρ_c is the column density, i.e. the density of the cloud integrated along the path of the imaging beam. Recall that $\sigma_0 = 1 \cdot 10^{-13} \text{ m}^2$ for the blue transition at resonance. The fitting function used below is of the form $A \cdot \exp\left(-\frac{x^2}{2\Delta_x^2} - \frac{y^2}{2\Delta_y^2}\right) + B$, for some constant offset B .

The output from our camera are digital units that range from 0 to 255 for the amplitude of the brightness. This value must then be converted into optical density by multiplying by $5.0/255$ (where 5.0 represents entirely opaque). The camera's spatial unit is in pixels, and it is converted to length using the relationship $2.75 \cdot 10^{-6} \text{ m/pixel}$ (this value is for the Navitar objective, and was determined by a free-fall calibration to g , the acceleration due to gravity; see Sec. 2.6.5 for details). Using those units for A , Δ_x , Δ_y the integral of the

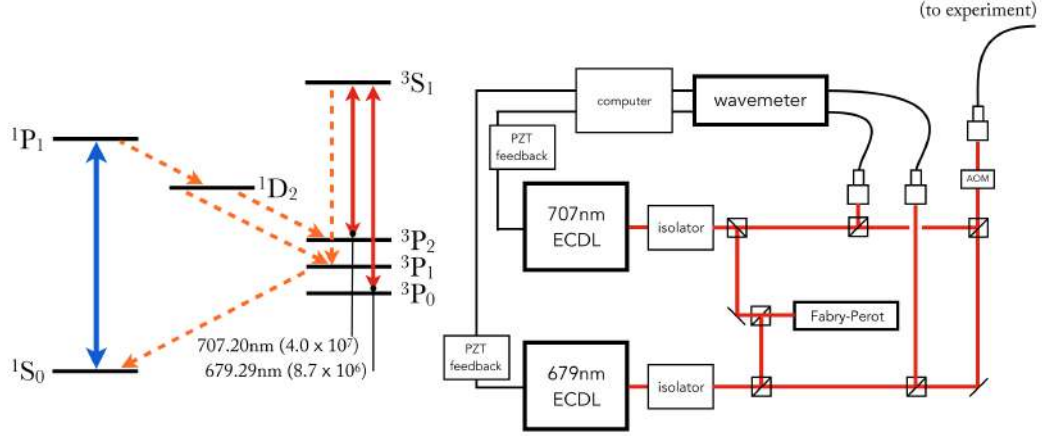


Figure 2.32: Diagram of the optical repumper scheme (left), as well as a schematic of the apparatus (right). We employ a software feedback system: two channels from our wavemeter monitor the repumpers lasers, and the output controls the PZT controller voltages on the ECDL feedback mirrors. The sensitivity of the wavemeter is sufficient for repumper locking to ~ 1 MHz.

Gaussian fit in terms of optical density is given by:

$$\sigma_0 \iint \rho_c dx dy = 2 \pi A \Delta_x \Delta_y \times 1.48 \cdot 10^{-13} \text{ m}^2, \quad (2.15)$$

where $\iint \rho_c dx dy$ is the atom number N_{at} .

The atomic density n can be evaluated by considering the equation

$$N_{\text{at}} = \iiint n dx dy dz = \iint \rho_c dx dy, \quad (2.16)$$

which is also equal to $(2\pi)^{\frac{3}{2}} n_0 \Delta_x \Delta_y \Delta_z$, where n_0 is the density at the center.

One has to estimate the size Δ_z of the atom cloud along the depth axis (the axis along which the imaging beam integrates the column density). In the following we will consider that $\Delta_z \equiv \Delta_y$ since the cloud is elongated horizontally due to our configuration; it has no reason to be more deep than high. We state this assumption explicitly with the following notation:

$$\Delta_{zy} \equiv \Delta_z = \Delta_y \quad (2.17)$$

Using the same units from the fitting function, we can calculate the density n_0 at the

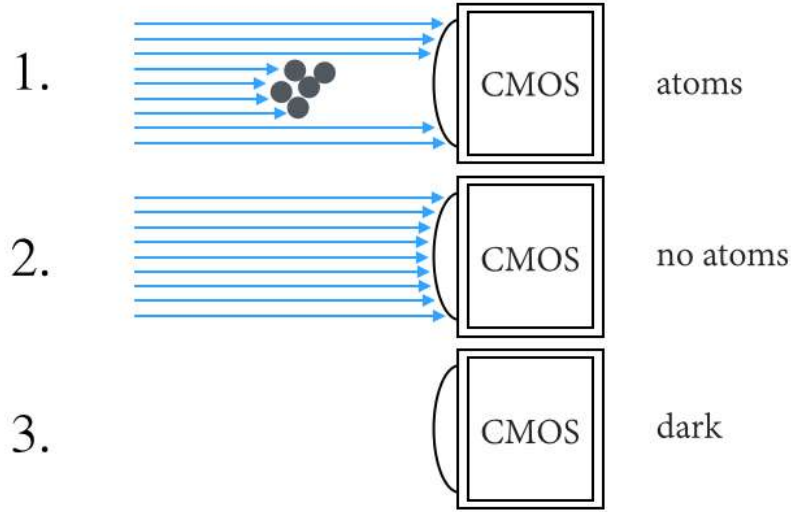


Figure 2.33: An illustration of the 3-step absorption imaging process. The third image is used to subtract out imperfections in the camera, the second for imperfections in the imaging beam, and the first for the actual picture of the atoms, generated by their shadow.

center of the cloud:

$$n_0 = \frac{A}{\sqrt{2\pi}\sigma_0\Delta_{zy}} \times 7.13 \cdot 10^3 \text{ m}^{-3} \quad (2.18)$$

For the loading sequence described above, we capture $\sim 1.5 \cdot 10^7$ atoms in ~ 200 ms, with a peak atom density of $\sim 2 \cdot 10^9 \text{ cm}^{-3}$.

2.4.5.2 Temperature

One standard way to measure the trap temperature is to measure the rate of expansion of the atom cloud during free-fall. Assuming a point-like initial condition ($\Delta_{xi} \ll \Delta_{xf}$), we can make a direct comparison between Δ_{xf} and the mean thermal velocity of the cloud, v_{rms} (if Δ_{xi} is too large, a convolution would be required to relate them).

This relation is given by a velocity parametrization of the spatial distribution. Given a Gaussian distribution after some time t_{TOF} , then the spatial distribution, measured by intensity in a camera picture (normalized here to 1), can be related to the thermal velocity distribution by

$$e\left(-\frac{x^2}{2\Delta_x^2}\right) = e\left(-\frac{(vt_{\text{TOF}})^2}{2\sigma_x^2}\right) = e\left(-\frac{mv^2/2}{k_B T}\right). \quad (2.19)$$

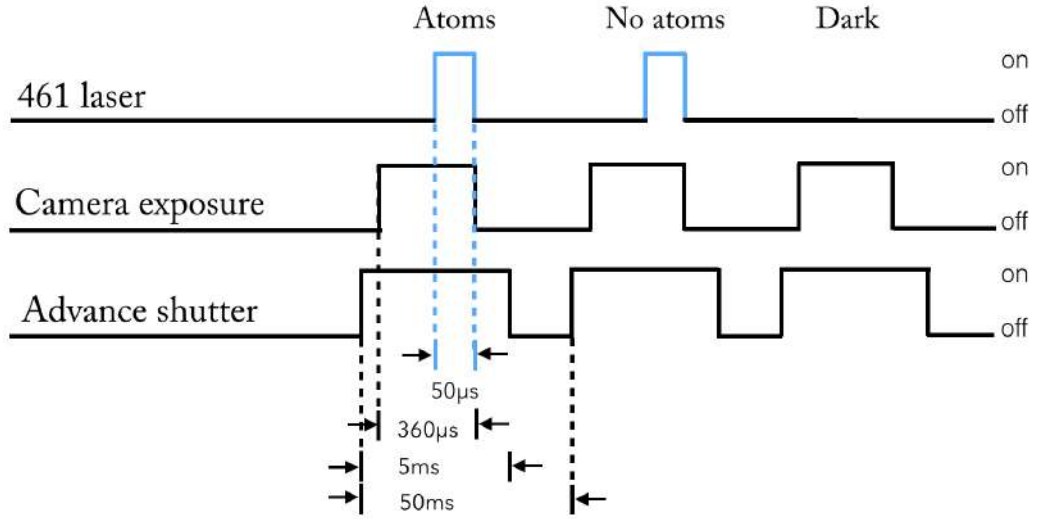


Figure 2.34: The absorption imaging sequence.

Starting with a point source allows us to directly map the position distribution to a velocity distribution by the linear relation. Matching exponentials, then, we get

$$\frac{(v t_{\text{TOF}})^2}{\sigma_x^2} = \frac{m v^2}{k_B T} \quad (2.20)$$

and hence

$$T = \frac{m}{k_B} \left(\frac{\sigma_x}{t_{\text{TOF}}} \right)^2. \quad (2.21)$$

This concludes our description of the 461 nm MOT. Our next objective to describe the light source used for our colder, second-stage MOT, at 689nm.

2.5 689 nm light source

The mK temperatures achieved in the previous section with the $^1S_0 - ^1P_1$ are not sufficient for our spectroscopic purposes, and so the atom sample must be transferred to a second trap using a different Sr transition. Recall that the Doppler temperature T_D scales with the linewidth of the transition,

$$T_D = \frac{\hbar\gamma}{2k_B}. \quad (2.22)$$

Spin-orbit coupling makes the forbidden $^1S_0 - ^3P_1$ weakly allowed, resulting in a 7.5kHz intercombination line, and a Doppler cooling limit $T_D = 480$ nK. This sub- μ K temperature is sufficiently low for the final-stage lattice trap, however a laser whose linewidth is comparable or narrower than this transition's linewidth must first be built. The $^1S_0 - ^3P_1$ intercombination line is accessed with 689 nm light, which is available using standard diode technology. A sufficiently narrow laser linewidth is achieved using Pound-Drever-Hall laser stabilization to a high finesse cavity [Drever *et al.*, 1983; Black, 2001]. Figure 2.35 explains this schematic in detail.

2.5.1 High-finesse cavity

The cavity, shown in Fig. 2.36 consists of an ultralow expansion silica (ULE) glass spacer with optically contacted end mirrors. ULE glass from Corning and Zerodur (low-expansion glass ceramic) both can have very low coefficients of thermal expansion (CTEs), < 10 ppb/K. However, Zerodur is known to experience delayed elasticity (attributed to its alkali oxide content), which can lead to mechanical creep that persists decades after the piece is machined. For a new piece of Zerodur, this creep can exceed any thermal drift by an order of magnitude.

A simple cylindrical configuration used by many time-and-frequency standards groups is made by Advanced Thin Films (ATF) (Fig. 2.36). It is 10 cm long with a 5 cm outer diameter. Its edges are made of one flat mirror and one 50 cm cc/pl mirror. This choice of mirrors leads to a very stable cavity that is quite easy to align, especially for a modest finesse. If thermal effects in the mirror coatings are an issue, then a 1 m mirror can be chosen instead of 50 cm, effectively increasing the beam spot on the mirror and thus decreasing

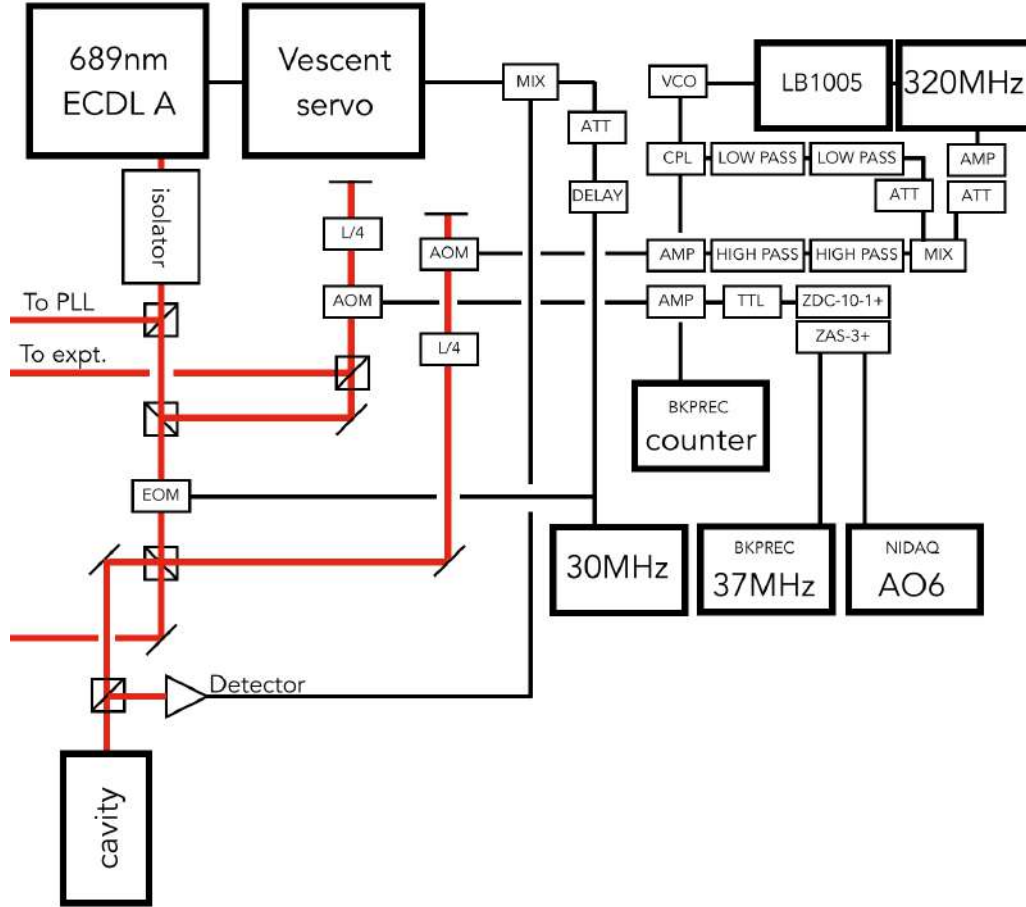


Figure 2.35: Schematic of the 689A laser and locking electronics.

the heating. Both mirrors are coated identically (AR on the outer side, the desired R on the inner side). The flat mirror is slightly simpler to use as the input coupler, since in this case the beam waist falls on the flat mirror surface. For a line width of ~ 100 kHz and $\text{FSR} = 1.5$ GHz, the finesse is $F \approx 15,000$, corresponding to the reflectivity $R \approx 0.9998$. ATF can achieve any desired finesse 10^3 to 3×10^5 ; if the highest finesse is not needed, a more modest finesse simplifies the coupling into the cavity.

What finesse is necessary for our purposes? For example, to stabilize the 689 nm laser to much less than the linewidth of the $^1S_0 - ^3P_1$ intercombination transition (7.5 kHz), then a desirable laser linewidth could be, e.g. ~ 100 Hz. Splitting the cavity linewidth by $\sim 10^3$ with PDH locking is common, and so this justifies the ~ 100 kHz cavity linewidth.

With careful temperature stabilization of the cavity, thermal drifts of ~ 1 Hz/s are typi-

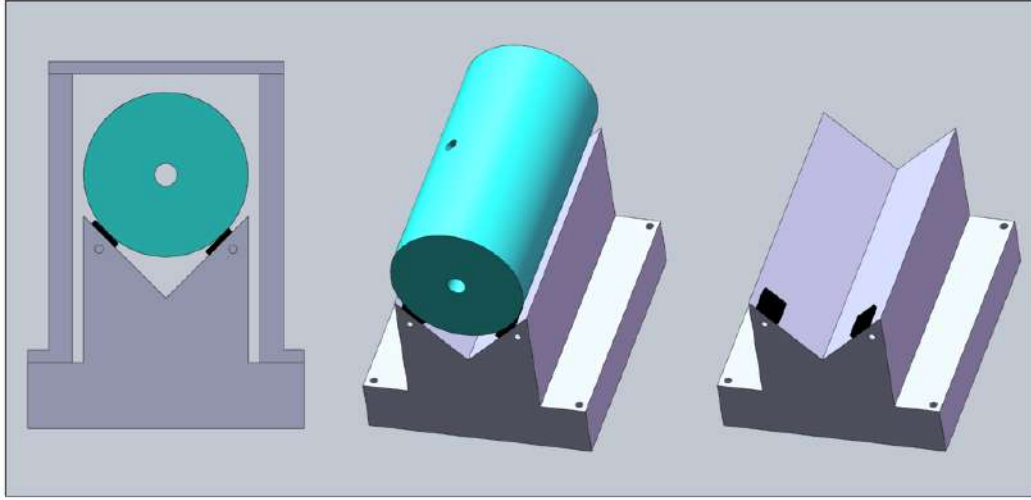


Figure 2.36: Solidworks rendering of The high-finesse ULE cavity.

cally achieved. Conservatively assuming constant linear drift, this gives a typical frequency change of > 30 MHz/year. Therefore the setup would contain an AOM (double-passed to keep the beam path constant) with a bandwidth of at least ~ 100 MHz, to keep up with the drifting cavity over time.

Mounting high-finesse Fabry-Perot cavities can be challenging. A cylindrical 10 cm cavity can be hung, supported ~ 1 cm from each end. For the medium-high finesse of the 689 nm cavity, holding it in a 90° V-groove should be sufficient. Additionally, 4 elastomer pads (e.g. Viton) are inserted to have the cavity contact the V-groove in only 4 places. The pads can be attached to the V-groove with a dot of adhesive such as epoxy. They should be placed such that the reaction force on the cavity cylinder is normal to its tangent.

2.5.2 Setup, locking electronics, frequency offset and control

Figure 2.35 is a schematic of the setup for the 689 nm master laser. After the ECDL and isolator there is ~ 25 mW of usable power. The laser beam is then distributed into four essential parts, which will be explained in the following parts: PDH cavity locking, 30 to $100\mu\text{W}$ (frequency-offset to -420 MHz), ~ 5 mW for Sr heat pipe locking (0 MHz frequency offset, but currently not in use), ~ 5 mW for phase locking slave lasers (-420 MHz), and the rest (up to $\sim 20\text{mW}$) sent to the experiment (-36 to -40 MHz including the broadband

phase), however this is usually about 3 to 4mW out of the fiber on the chamber table.

It is clear that while the ULE cavity described in the section above provides frequency stabilization, it does not carry any information about the desired transition-dependent frequency setpoint. Where the cavity provides precision, a saturated absorption locked (SAL) Sr heat pipe traditionally provides accuracy [Wieman and Hansch, 1976; MacAdam *et al.*, 1992; Preston, 1996]. Such a heat pipe and locking system was built by our group, but it was determined that the optimal lock parameters still resulted in added noise compared to a system that is simply locked to the PDH cavity alone. This added noise is attributed to the poor quality of the error signal. The likely culprit is that the heat pipe is too short, limiting the beam absorption path in the Sr vapor.

One can see in the schematic the electronics for a two stage locking system for the 689 master laser: the PDH cavity feeds back on the laser current (and auxiliary PZT controller), while the SAL system feeds back on the voltage-controlled oscillator (VCO) that determines the AOM frequency, the output of which goes to the MOT beam. The PDH cavity affects the laser frequency upstream of the SAL system, coupling the feedback of the two systems.

In the absence of a SAL system, this means that there is a frequency degree of freedom in the electronics scheme. The output from the New Focus lockbox is therefore adjustable, and must be set by hand when the MOT is first set up. This is described in Sec. 2.6.

2.5.3 Pound-Drever-Hall lock

We use the standard locking technique as described in [Drever *et al.*, 1983; Black, 2001]. First alignment of the beam is achieved by using a surplus of a few mW of laser power, and once optimized, usually no more than a few tens of μW of power incident on the cavity is necessary.

First alignment can be difficult to achieve. The best way to align from scratch is to ensure that the retroreflection of the beam off of the cavity face is always aligned with the incoming beam, as observed on the mirror faces leading to the cavity. When the beam is nearly aligned, its initial coupling to the cavity causes flickering in the retroreflected intensity. Near this alignment, one should be able to find the PDH error signal on a scope set up from the electronics leading from the photodetector.

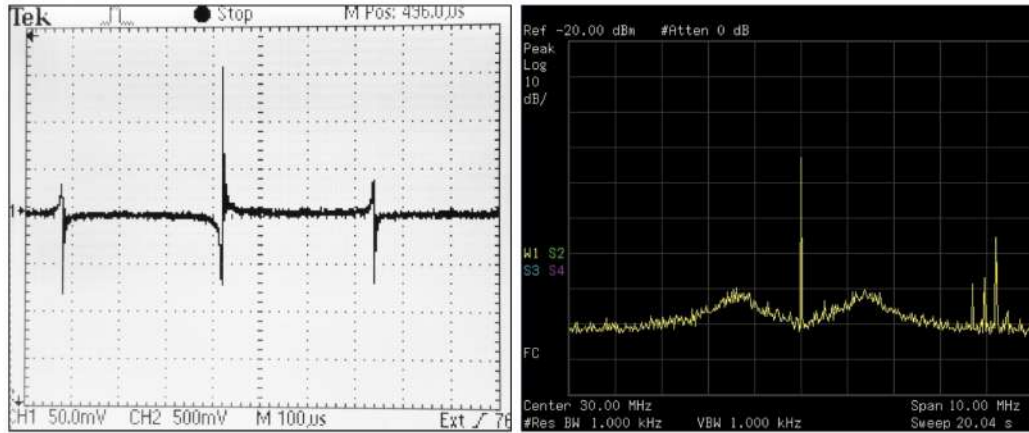


Figure 2.37: Error signal from the PDH cavity (left). Spectrum analyzer monitor of the laser lock (right).

One should be mindful of the FSR of the cavity. It is important to be sure that once an error signal is found on the scope, it corresponds not only to the correct laser wavelength (nearest to the transition), but also to the proper transverse beam mode. Figure 2.37 shows a representative error signal output, as well as a spectrum analyzer monitor of the laser spectrum once a lock has been achieved.

2.5.3.1 Inferring the laser linewidth

We do not have a direct method for measuring the laser linewidth in our lab, as such a measurement is usually performed by beating two independent, similarly narrow line lasers against each other and measuring the bandwidth of the noise. This measurement can be performed with just a single laser: assuming laser noise is uncorrelated in time, splitting the light into two beams and passing one through a long delay fiber before rejoining them, allows one to look at the noise spread of a laser against itself. Such a measurement, known as self-heterodyne linewidth determination, was assigned as an undergraduate project, but our available delay fiber, at 10 km, was deemed insufficient for our laser.

We can set upper limits on the linewidth of the laser through use on known physical systems. Using the spectroscopy lasers phase locked to this master laser, we have been able to measure the intercombination transition near its natural linewidth of 7.5 kHz. Furthermore,

we have performed bound-bound Raman transfer between molecular vibrational levels, with linewidths as small as 200 Hz, as discussed in the last chapter of this thesis. Hence we believe that we can set a conservative upper limit on the linewidth of our PDH-locked laser at a value well within the current needs of our experiment.

2.6 The 1S_0 - 3P_1 MOT

2.6.1 MOT transfer

The ideal spatial extent of a MOT is dependent on its temperature, and therefore on the linewidth of the trapping transition. The 3P_1 MOT therefore should be considerably smaller in size than the 1P_1 MOT. The goal then is to transfer between the two MOTs while losing as few atoms as possible. One method for achieving this is to mode-match the blue and red MOTs by ramping the quadrupole field gradient while simultaneously applying a tapering RF function to the red 689 nm MOT trapping laser. This broadband trapping laser frequency is shown in Fig. 2.38 [Katori *et al.*, 1999].

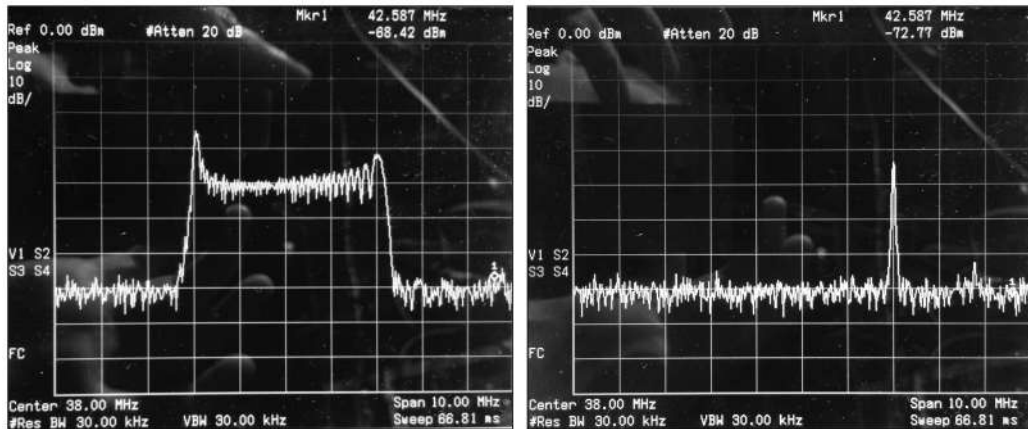


Figure 2.38: The red MOT broadband (left) and final, single-frequency (right) spectra as monitored on the spectrum analyzer. See Fig. 2.39 for details on the transfer sequence.

The field switching between the high blue MOT field gradient and the lower red-MOT gradient was performed by an insulated gate bipolar transistor (IGBT), executing the shut-off in 10 ms. However, during the switch (just before the blue MOT beams are shut off), we observed that the blue MOT atoms were being ejected upward from the trap. We

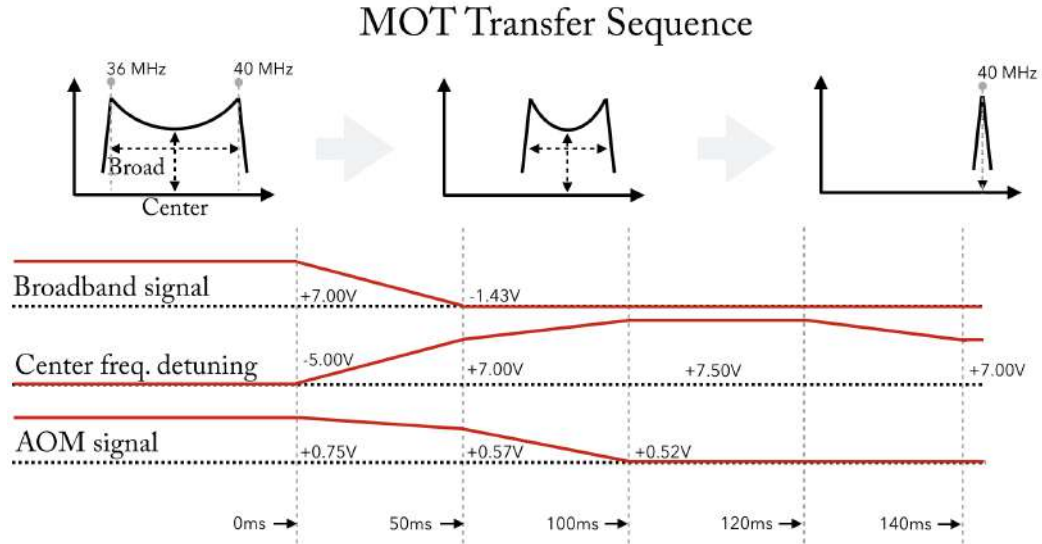


Figure 2.39: The MOT transfer sequence voltages applied to control the red trapping beams. We found that a small overshoot on the center frequency detuning to 7.5 V, and then back to 7 V (40 MHz), maximized the transferred atom number. Also note that the signal to the AOM that controls the MOT beam powers is ramped down slightly, to reduce saturation and minimize the final trap temperature.

determined that this was caused by eddy currents in the apparatus surrounding the vacuum chamber and quadrupole coils. One culprit was the breadboard supporting the vacuum chamber, which is circularly continuous with a central hole cut out in which the chamber resides. To mitigate this effect, we sawed through one side of the breadboard, effectively cutting the circle into a U shape. Unfortunately this modification had little or no effect on the atom ejection.

In the end, the solution to this problem was to no longer ramp the quadrupole coils field gradient. We found that at the final, low 25 A current setpoint for the coils power supply (corresponding to 25 G/cm), we are still able to produce a sufficiently large blue MOT whose transfer efficiency to the red MOT is roughly 10%. Figure 2.39 details the sequence breakdown for the broadband signal to the 40 MHz, center frequency detuning, and AOM signal power used for the MOT transfer.

2.6.2 Absorption imaging and the Navitar objective

As described in the $^1\text{P}_1$ MOT section, a Thorlabs DC1240M CMOS camera is used for imaging, however to resolve on a smaller scale appropriate for the smaller MOT, a different objective is used. We installed a Navitar objective, and performed the final focus on our atom sample only after we had produced a lattice trap; now this method is used for imaging at all stages including and after the red MOT.

The objective was initially focused onto the atom trap by using a real-time Gaussian fit to the trap image. When the Gaussian waist is minimized the trap is in focus. Note that this is better to do with a smaller trap, so it should be repeated after the cigar-shaped lattice trap is found.

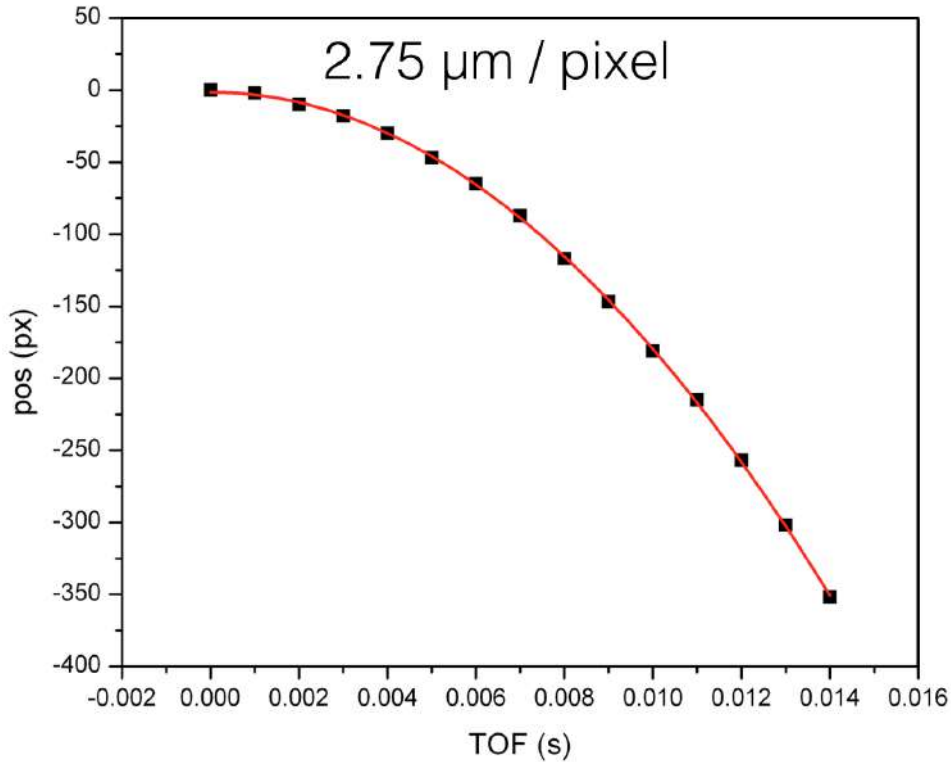


Figure 2.40: Calibration of the Navitar objective using the free-fall of the atom sample.

The magnification of the Navitar objective was determined by using the MOT's free-fall in vacuum and setting this to the value for the acceleration due to gravity, g . Figure 2.40 shows this fit, and the extrapolated value for the space per pixel, $2.75 \mu\text{m}/\text{pixel}$. This should

be remeasured after any time that the focus of the objective is changed.

2.6.3 The MOT setup and initial alignment

The 689 nm MOT beams are coaligned with the 461 nm beams using a dichroic mirror (blue reflection, red transmission). As with the 461 nm, the 689 nm beams are telescopically expanded, but only to roughly 0.5 inch diameter because the red MOT will be considerably smaller in size than the blue MOT. The red beam spot is made just large enough to cover the blue MOT size.

Alignment to the blue MOT is first achieved by eye, and optimized once an atom signal in the red MOT is found. As mentioned in Sec. 2.5, without the vapor cell atom lock, there is a degree of freedom in the frequency control that must be set by hand. Once the MOT beams have been aligned as well as possible by eye, we create a stable and visible blue MOT and adjust the New Focus LB1005 frequency-offset knob that controls this frequency degree of freedom. Careful observation of the blue MOT reveals that, at the right red MOT frequency, a small shell of darkness in the blue MOT appears; the 689 nm laser interaction with the blue MOT atoms eject them from the shell that is on-resonance with the $^1S_0 - ^3P_1$ transition. This dark shell can be difficult to see, but has proven to be the most reliable first step in finding the desirable red MOT 689 nm laser frequency from scratch.

Next, we run the red MOT sequence and look with the Navitar camera objective for any sign of atoms in the red MOT, using the BK Precision function generator in series with the adjustable knob to more finely control the red MOT laser beam frequency. Less than ± 200 kHz adjustment should be sufficient.

Once a signal is found, the MOT laser beams should be tuned until a maximum number of atoms in the trap is reached. When this optimum is reached, we install irises on all three axes centered on each red MOT beam and its retroreflection. This helps considerably if any significant, future alignment is necessary.

2.6.4 Daily maintenance

Daily maintenance of the red MOT is necessary but relatively uninvolved. Because there is no atom lock, the BK Precision function generator that controls the frequency degree of

freedom must usually be adjusted by as much as 100 kHz. This is often all that is necessary for daily adjustment, however the MOT beam alignment should be routinely checked as well.

2.6.5 Characteristics of the microkelvin MOT

Following the characterizations from the work in [Loftus *et al.*, 2004a; Loftus *et al.*, 2004b], we modeled the trap dynamics by considering the trapping force in 1D, given by

$$F(v, x) = \frac{\hbar k \Gamma}{2} \left(\frac{s}{1 + s + 4(\Delta - k \cdot v - \mu d_x B \cdot x)^2 / \Gamma^2} - \frac{s}{1 + s + 4(\Delta + k \cdot v + \mu d_x B \cdot x)^2 / \Gamma^2} \right) - mg, \quad (2.23)$$

where Γ is the natural linewidth, and Δ is the laser frequency detuning (both in rad/s), $s = I/I_s$ is the saturation parameter for the laser intensity ($I_s \approx 3\mu\text{W}/\text{cm}^2$ for the $^1\text{S}_0 - ^3\text{P}_1$), $d_x B = dB/dx$ is shorthand for the magnetic field gradient from the quadrupole coils, v is the atom velocity, and x is the atom position. The gravitational term indicates we have chosen the vertical axis. There is a symmetric relationship between v and x , which means that this restoring force works on both momentum and position (resulting cooling and trapping), as shown in Fig. 2.41. The separation between the lines is set by Δ , and the width by s .

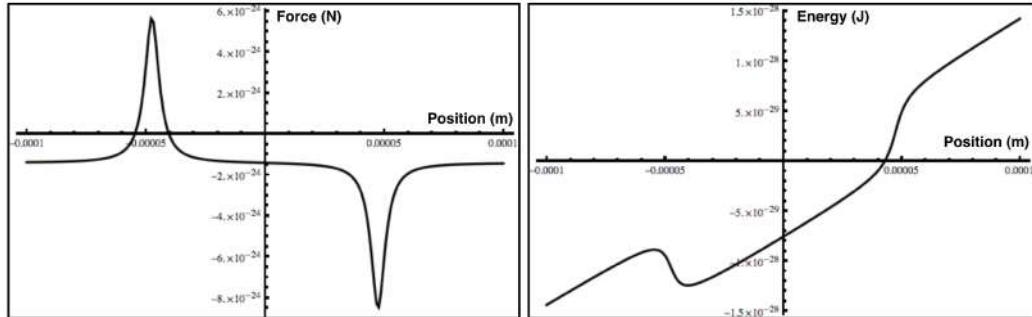


Figure 2.41: Magneto-optical trapping force along the vertical axis (left). The offset is due to gravity. The MOT potential energy, where the incline is due to gravity (right). Atoms at μK temperatures pool at the lower edge of the well, creating the bowl shape found in Fig. 2.42.

Figure 2.41(b) shows the potential energy of the trap, which gives more insight into the

trap shape. The overall slant of the well is the gravitational contribution, and the recession cut in at the center is the space created by the MOT. The width of this recession is set by the detuning Δ , and the depth by the beam intensity I . Assuming the depth is greater than the atom thermal energy, we expect atoms to pool at the bottom of this well. This is indeed what we find: Fig. 2.42 shows that for larger detunings, the atoms occupy the bowl-shaped bottom of the well, and that we can adjust the shape using Δ . Figure 2.42 shows images of the MOT for various detunings Δ .

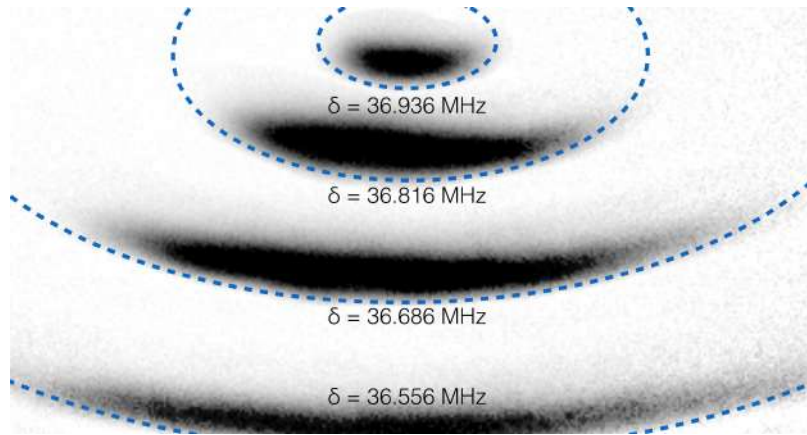


Figure 2.42: Super-imposed images of the red MOT for various detunings $\Delta = 2\pi\delta$. For larger detunings, the cold atoms sag to the bottom of the potential well.

2.6.5.1 Atom number

Using the atom counting technique described in Sec. 2.5, we measure the number of atoms in the MOT to be $N_{\text{atom}} \simeq 2 \cdot 10^6$, and a corresponding density $n_{\text{atom}} \simeq 5 \cdot 10^{11} \text{ cm}^{-3}$.

2.6.5.2 Temperature

Using the time-of-flight technique described in the previous section, we measured the temperature of the atoms in the MOT to be $T_{\text{atom}} \simeq 2 \mu\text{K}$. Figure 2.43 shows the atom cloud in free fall for times (a) 0 ms, (b) 3 ms, (c) 5 ms and (d) 8 ms. For lower laser powers, we can achieve colder temperatures down to $\sim 0.9 \mu\text{K}$, but at the cost of fewer trapped atoms.

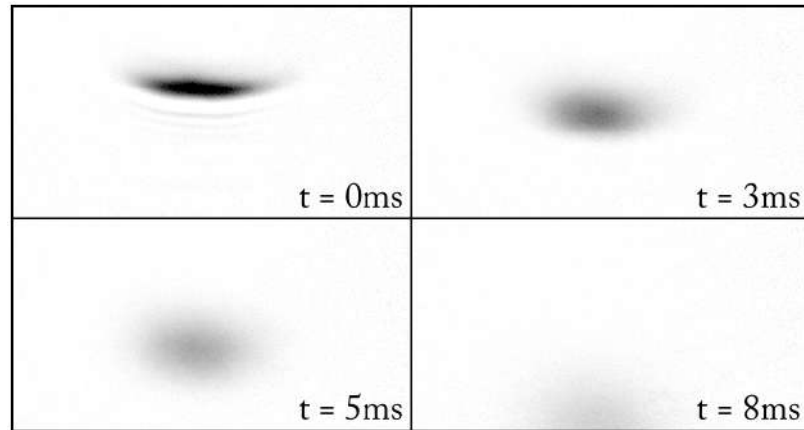


Figure 2.43: TOF imaging of the red MOT. Retrieving the expansion of the Gaussian waist of the cloud at several points gives a result for the expansion rate, and therefore the temperature, according to Eq. 2.21. Typical temperatures are $1 - 2 \mu\text{K}$.

2.7 The optical lattice trap

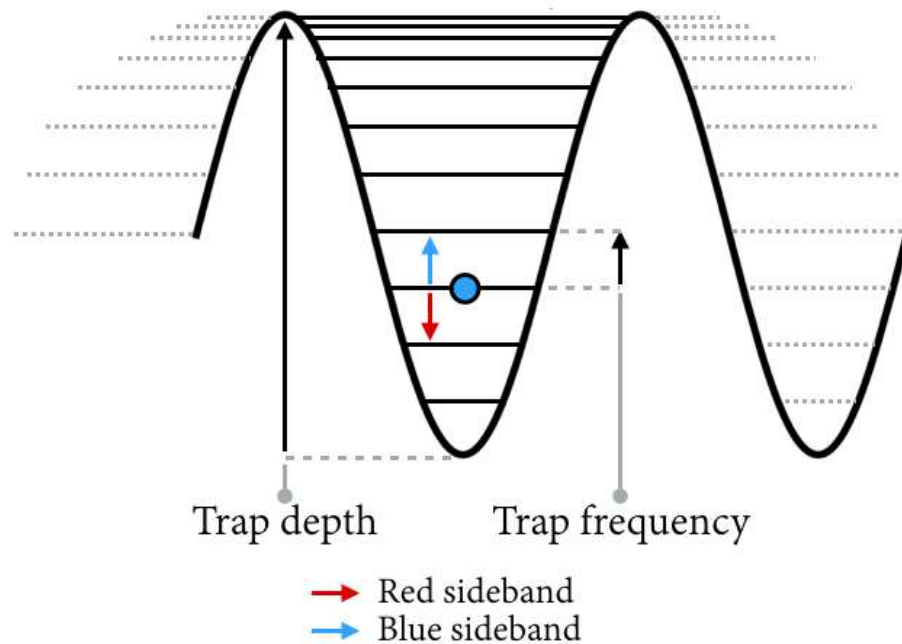


Figure 2.44: Diagram of the optical lattice trap. The trap depth and frequency are labeled, as are the red and blue sidebands.

The Doppler shift for Sr atoms at $1\ \mu\text{K}$ is still substantial compared to the 7 kHz intercombination linewidth [Foot, 2005]:

$$f_{\text{FWHM}} = f_0 \sqrt{\frac{8k_B T \ln 2}{mc^2}} \approx 30\ \text{kHz}. \quad (2.24)$$

However the kinetic energy associated with this temperature is small enough to make optical dipole trapping feasible. In fact, retroreflecting a far off-resonant dipole trap (FORT), known as an optical lattice trap because of its standing-wave nature, is a standard technique for further suppressing unwanted spectroscopic broadening at μK temperatures. Retro-reflection of a single FORT beam provides tight confinement along the axis of beam propagation, suppressing the recoil shift and the first-order Doppler shift by quantizing the motion of the trapped atoms. Figure 2.44 shows a diagram of the trap. For sufficiently deep traps, the sinusoidal potential can be approximated as quadratic, and the quantized states can be treated as those of a simple harmonic oscillator.

If the trap frequency is greater than the recoil frequency of an absorbed photon,

$$\omega_{\text{trap}} > \omega_R = \frac{\hbar k^2}{2m}, \quad (2.25)$$

then the energy associated with the momentum kick of a photon cannot be imparted to the motionally quantized atom, and is instead absorbed by the lattice system. Additionally, if the trap frequency exceeds the natural linewidth of the atomic line under study, $\omega_{\text{trap}} > \Gamma$, then the probe laser can be blue- and red-detuned to select excitation to blue and red sidebands of the lattice trap, allowing the experimenter to control the motional state of the lattice trap. These two regimes are referred to as the Lamb-Dicke ([Leibfried *et al.*, 2003]) and resolved-sideband regimes, respectively, and are crucial requirements for performing the desired spectroscopy in ultracold optical lattice experiments.

Complete motional confinement in 3D is achieved by overlapping mutually orthogonal lattice trap beams. In this section we describe the physical requirements and technical implementation of our 1D lattice trap, with an option for and preliminary measurements with 2D and 3D setups. For a 1D lattice beam, the trapping regions are pancake-shaped cross-sections of the beam; by extension, two lattice beams create cigar-shaped tubes, and three lattice beams create spherical trapping regions. These three geometries are illustrated in Fig. 2.45.

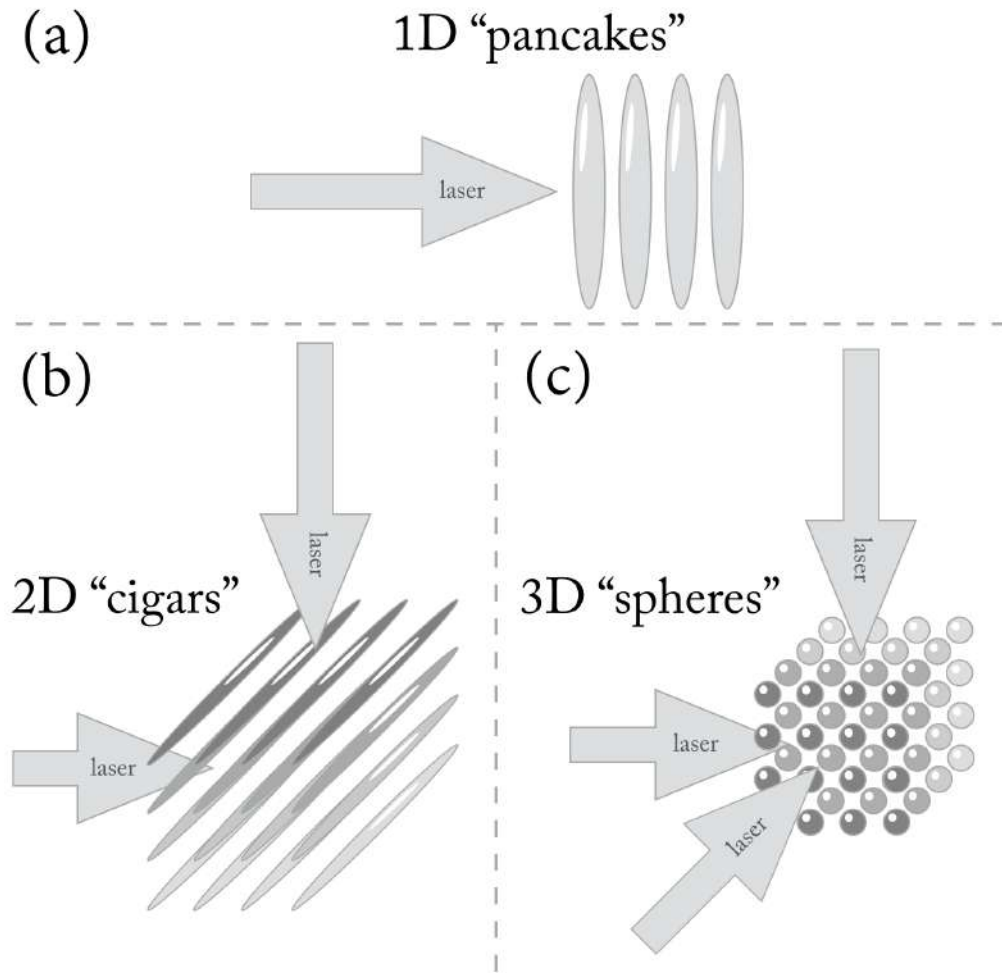


Figure 2.45: Trapping geometries for the (a) 1D lattice (pancakes), (b) 2D lattice (cigars), and (c) 3D lattice (spheres).

2.7.1 Magic wavelength

The potential well of the optical trap is caused by an ac stark shift of the atom energy levels. This results in a shift of the absolute line position given by the differential Stark shift of the ground and excited states, and if the atoms sample various laser intensities within the Gaussian trap profile, it can result in inhomogenous line broadening as well. The shift of an atomic state depends on that state's polarizability α_a . Plotting α_a for the 1S_0 ground state and the various 3P_1 state sublevels, as seen in Fig. 2.46, one can see that the differential shift of the ground state and the $m = 0$ sublevel of the excited state is zero at a specific

wavelength, indicated by the crossing point (solid black and dashed green lines). At this wavelength, measured by [Ido and Katori, 2003] to be 914 ± 1 nm, the zero differential shift means that there should be no observed shift or broadening of the line for σ -polarization of the trapping light. Note that the calculation of Fig. 2.46 predicts 872 nm, off by $\sim 5\%$ from the observed value.

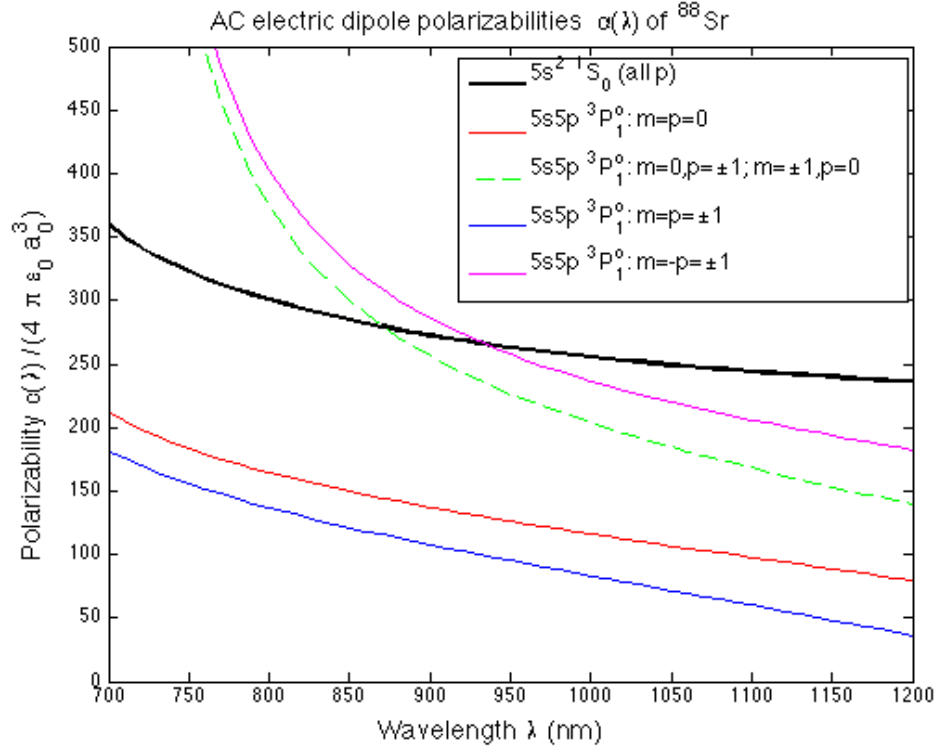


Figure 2.46: State polarizabilities and magic wavelength crossing point, where m denotes the magnetic sublevel, and p the light polarization relative to the applied magnetic field.

We therefore chose a Sacher Lasertechnik diode at 940 nm with a wavelength range allowing for tuning to 914 nm.

2.7.2 Setup

The lattice laser was constructed in an analogous manner to the 922 nm seed for the blue light setup (Sec. 2.2): a home-built ECDL with two-stage temperature control outputs ~ 35 mW, which is then amplified to ~ 1 W using a home-built tapered amplifier from

the same designs as for the blue light setup (see Fig. 2.16). The beam is then split into three parts for creating a 3D lattice. As described in [Greiner, 2003], it is important that the standing waves of the three mutually orthogonal lattice beams not interfere, as this can create unwanted superlattice waves by which atoms could be channeled out of the trap. The polarization geometry for such a trap is shown in Fig. 2.47. In principle choosing orthogonal beam polarizations should prohibit this, but experimentally any small imperfection in orthogonality will result in interferences. Hence it is common practice to offset the frequencies of the three axes using AOMs by 10s of MHz.

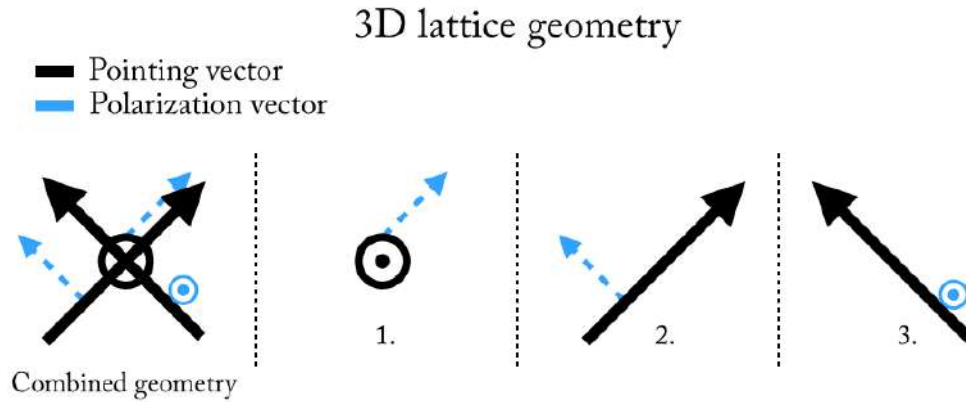


Figure 2.47: The combined geometry of the 3D lattice (left), broken down into component beams. Black arrows represent pointing vector orientations, and blue arrows represent polarization vectors. Circles represent vector orientations perpendicular to the page.

The primary axis lattice beam is picked off before the AOM, while the second- and third- axis beams are separated using the double-pass technique: the zeroth and first orders of the retroreflection of the first order of the first pass.

Each of these axes is fed into a three-stage fiber coupler and sent via polarization-maintaining patchcord to the chamber. The primary axis, which is used for all 1D measurements, is directed into the chamber along the horizontal axis, through one of the two large window pairs, as seen in Fig. 2.48. The other two are directed through the small window ports at 45 degrees from the horizontal. On all three axes, 120 – 150 mm focusing lenses are installed just outside the port windows to provide beam focusing at the trap center. The trap depth and frequency of the lattice trap are determined by the focusing waists of the

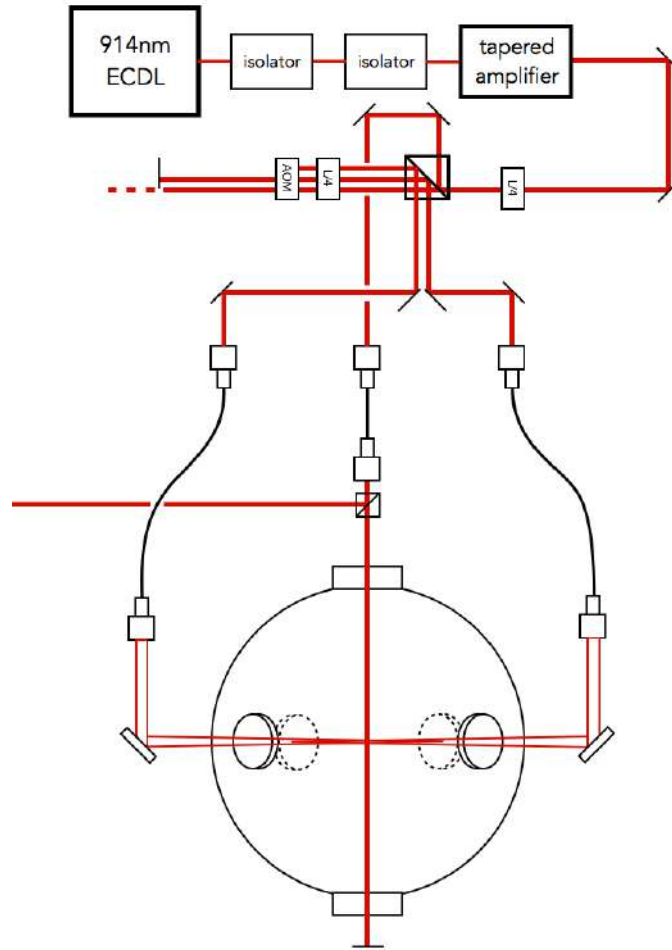


Figure 2.48: Schematic for 914 nm lattice laser setup.

lattice beams, and are the topic of Sec. 2.7.3.

2.7.2.1 Beam alignment - initial detection

Aligning the three lattice beams with the red MOT can be difficult without assistance from another laser. This is especially the case for the two diagonal axes whose port windows are smaller and whose focusing lenses are harder to position. The key is to employ an assisting laser whose effect on the atoms is easier to detect. We use the resonant 461 nm light from the imaging beam, and temporarily replace the fiber of whichever lattice axis we are aligning with the imaging fiber. After maximizing the power output from the fiber,

alignment is achieved by iterating over the following two steps:

1. Adjusting beam alignment and focus into the chamber by using the fiber translation axis and mirror knobs, until maximum atom depletion is achieved.
2. Dialing down the imaging beam power until the atom number is nearly recovered back to full.

Repeating these two steps eventually leads to imaging beam powers small enough that the shape of the beam can be seen cutting through the red MOT atom sample, indicating that the optics are sufficiently aligned. Although geometries for focusing optics are color-dependent, we have found that aligning with the 461 nm seed is sufficient, and after reinstalling the 914 nm lattice beam, minimal adjustment is required to find the lattice trap.

Horizontal alignment of the 1D lattice is achieved in two ways. The retroreflection mirror is first installed with a non-adjustable Thorlabs LMR mount, ensuring that when its back reflection is overlapped with the incoming beam, both are normal to this vertically-mounted reflecting mirror. Alternatively, one may use the atom diffusion from the one-way dipole (not lattice) trap. When the beam is perfectly horizontal, as the atoms diffuse they also undergo a “sloshing” effect as the beam focusing induces a weak restoring gradient. If the beam is not exactly level, this sloshing is lopsided and atom diffusion does not occur symmetrically from the trap center. Once the beam is horizontal, this is also a reliable technique for finding the true beam waist.

2.7.2.2 Beam alignment - daily maintenance

While not always necessary, it is important to make sure that the lattice trap is sufficiently aligned on a daily basis. If any of the axes has been completely misaligned and cannot be found, then refer to Sec. 2.7.2.1 for aligning the lattice trap from scratch. The description here is for daily maintenance to maximize overlap of the three axes, and for aligning the retroreflection beams. The key is to maximize atom confinement by overlapping one-way dipole traps from orthogonal axes.

1. Align the retroreflection of the 1D axis by allowing for a long (~ 100 ms) hold time in the lattice as set in the software sequencer (Sec. 2.9), and adjust the knob on the retroreflecting mirror until the horizontal diffusion of the atoms is minimized.
2. Blocking the retroreflection of the 1D beam, align the one-way beam of another axis until the crossed-dipole trap size is maximized.
3. Horizontally misalign the retroreflection of this second beam by a small amount, and maximize its crossed-dipole trap signal with the horizontal beam as well, so that there are now 2 crossed-dipole traps.
4. Horizontally realign the retroreflection of this axis until the return beam crossed-dipole trap is overlapped with the incoming one.
5. Blocking the retroreflection of the second beam again, align the incoming third beam with the horizontal axis, and then with the incoming beam of the second axis, until the trap signal is maximized.
6. Perform the same retroreflection alignment technique for the third axis as was performed for the second: horizontally misalign from the incoming beam, and maximize the crossed-dipole signal with the horizontal axis. Then horizontally align back onto the incoming beam until the overlap is maximized.
7. Unblock all retroreflections.

For aligning the retroreflection of any given axis, one can monitor the coupling of the retroreflection back into that axis' fiber by installing a polarizing beam splitter and photodetector pre-fiber, monitoring the small polarization leak. Return powers of 10% are easily expected.

2.7.3 Trap parameters

The vacuum chamber size prohibits use of lenses with focal lengths less than 120 mm. For the horizontal 1D lattice, a large 2" diameter 150 mm lens is mounted to the breadboard supporting the chamber. The original collimated lattice beam diameter was measured to be

$w = 1.6$ mm. By standard Gaussian optics [Kogelnik and Li, 1966], the calculated focused waist w_0 is then

$$w(z) = w_0 \sqrt{1 + \left(\frac{z}{z_R}\right)^2} \quad (2.26)$$

for Rayleigh length $z_R = \pi w_0^2/\lambda$ and laser wavelength λ . The Rayleigh length is the distance from the waist to where the beam radius is larger by $w(z_R) = \sqrt{2}w_0$. Of interest to us is the full length of this trap range, called the confocal parameter $b = 2z_R$. At large distances from the waist the beam diverges linearly, and the waist is related to this divergence θ by

$$w_0 \approx \frac{\lambda}{\pi\theta}. \quad (2.27)$$

Our geometry predicts a $27 \mu\text{m}$ waist, and in fact our first direct measurements of the waist were $27 \mu\text{m}$. However after the focusing lens is secured in place, the easiest way to adjust the focal point for maximal alignment with the red MOT atoms is to adjust the focus of the beam's output fiber stage. We have since found that the optimal alignment gives a $23 \mu\text{m}$ waist.

The trap depth for an optical lattice with one-way power P is given by [Ludlow, 2008]

$$\langle |U_a| \rangle = \alpha_a \frac{4P}{\epsilon_0 c \pi w_0^2}, \quad (2.28)$$

where ϵ_0 is the permittivity of free space, c is the speed of light, and α_a is the state-specific polarizability introduced earlier.

For a quantum harmonic oscillator, $H = T + U = p^2/2m + (U_{\min} + m\omega_{\text{trap}}^2 x^2/2)$. For our time averaged lattice trap,

$$U = -\langle |U_a| \rangle \cos^2(kx) \approx -\langle |U_a| \rangle (1 - (kx)^2/2)(1 - (kx)^2/2) \approx -\langle |U_a| \rangle (1 - (kx)^2) \quad (2.29)$$

where we have Taylor expanded in (kx) to second order. If we match these two potentials, then $U_{\min} = -\langle |U_a| \rangle$ and we can find the trap frequency ω_{trap} . We obtain

$$\omega_{\text{trap}} = \sqrt{\frac{2\langle |U_a| \rangle k^2}{m}} = \sqrt{\frac{8\pi^2 \langle |U_a| \rangle}{m \lambda^2}}. \quad (2.30)$$

With 60% double-pass AOM efficiency and 70% fiber-coupling efficiency, up to 500 mW of 1D lattice power can be expected, or dividing across all three axes, roughly 175, 100 and 100 mW, respectively. From the expressions above, for the range 100 to 175 mW, this

corresponds to trap depths and frequencies from 23 to 116 μK (0.48 to 2.4 MHz), and 3.5 to 8 μK (70 to 160 kHz), respectively. However, when 1D measurements are being taken, 1D beam powers usually do not exceed 200 mW, corresponding to

$$\langle |U_a| \rangle (P = 175 \text{ mW}) / h = 850 \text{ kHz} = 40 \mu\text{K} \cdot h / k_B, \quad (2.31)$$

$$\omega (P = 175 \text{ mW}) / 2\pi = 100 \text{ kHz} = 4.5 \mu\text{K} \cdot h / k_B. \quad (2.32)$$

These values meet the Lamb-Dicke and resolved-sideband requirements. The Lamb-Dicke parameter η is defined as

$$\eta^2 \equiv \frac{\omega_R}{\omega_{\text{trap}}} \simeq \frac{30 \text{ kHz}}{100 \text{ kHz}} = 0.3, \quad (2.33)$$

where $\omega_R = \hbar k^2 / 2m$ is the recoil frequency. The last important requirement to meet is that the horizontal, 1D beam must be able to hold the atoms against gravitational pull. Linearly estimating the radial trap gradient and comparing it to the force of gravity on a single Sr atom,

$$\Delta U / \Delta x = \langle |U_a| \rangle / 23 \mu\text{m} = 2.4 \cdot 10^{-23} \text{ N} > mg = 1.4 \cdot 10^{-24} \text{ N}, \quad (2.34)$$

we find that the radial trap gradient is greater than the gravitational force by an order of magnitude.

2.7.4 3D lattice

Based on the atom densities from the previous section, we expect ~ 200 atoms/site in a 1D lattice, ~ 10 atoms/site in a 2D lattice, and less than 0.03 atoms/site in a 3D lattice. In a scenario with tight confinement along all three axes, and with significantly less than 1 atom/site in a 3D lattice, photoassociation (Sec. 3.2) should be suppressed. This is not quite what we observe, but our 3D lattice has not been exhaustively tested. What we have observed to date is the possible existence of core of non-photoassociated atoms in the 3D cross-over region above that of the 1D peripheral regions, as plotted in Fig. 2.49.

For some of our tests, the tail for the 3D section does not trail to zero, but rather to some finite value, suggesting a non-photoassociated core of atoms. However, the initial atom number in the 3D region is significantly higher than in the 1D (due to its greater trap depth), which may explain the longer tail and conflate the observed finite asymptote. Not

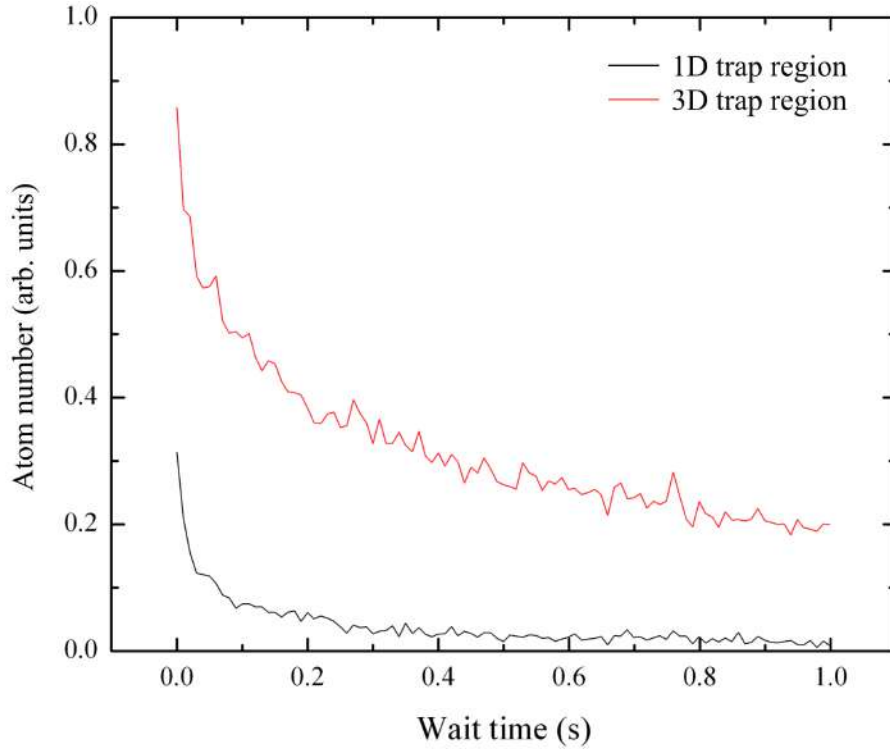


Figure 2.49: Photoassociation losses in 1D and 3D trapping regions. Note that the initial atom number is higher in the 3D region due to greater trap depths from the sum of the substituent beam depths. Our measurements were inconclusive on whether or not there is a distinct, 3D core in which photoassociation is suppressed.

all of our tests confirmed whether there is a non-photoassociated core. The rest of my thesis requires only a 1D lattice, and so further diagnostics of the 3D lattice must be revisited.

2.8 The spectroscopy apparatus

We employ three spectroscopy lasers that are phase-locked to the master 689 nm laser (or “689A”), and are named sequentially as 689B, 689C, and 689D. The locking scheme is described in Fig. 2.50.

Lasers B and C are both phase-locked to A by the same EOT ET-4000 photodetector, while D is locked to C on a second detector of the same make. All three spectroscopy lasers are fed to the experiment via the same single-mode fiber patchcord, and joined via

beamsplitter with the 1D horizontal optical lattice beam (see Fig. 2.48). Because these beams co-propagate with the lattice laser, they are also co-focused. Adjusting the beam waist relative to the lattice is therefore achieved upstream from the joining beamsplitter, usually by adjusting the longitudinal focus of the output fiber translation stage. For many of our measurements the spectroscopy beams shared the same focus as the lattice trap beam, $w_0 = 26 \mu\text{m}$; however for some of the spectroscopy, where very little power is necessary, we expanded the waist to provide a more uniform laser intensity in the region of the trapped lattice atoms, expanding to a waist $w_0 = 38 \mu\text{m}$.

When locked, the error signals for these lasers are similar to the spectrum analyzer traces shown in Fig. 2.51. To check the quality of the phase locks, we looked at the signal of the beat between lasers B and C while both were locked to A. One can see that the central feature linewidth is not larger than several hundred Hz, resolution-limited by the spectrum analyzer.

Our lab sequencing software has been programmed with the capability for the generic sequence shown in Fig. 2.52. This gives us extensive measurement flexibility.

2.9 The lab control software

We use software for control and sequencing that was written in-house, and communicates with our hardware using a National Instruments Data Acquisition (NIDAQ) system. The NIDAQ system has input and output for both digital and analog signals, and has timing precision to $10 \mu\text{s}$. Sequencing is performed by software separate from that which receives images from the camera and processes data; communication between the two is triggered by the NIDAQ signal that controls the camera. Figure 2.53 is a screen capture of the sequencing software. The left-hand panel is used to select portions of the sequence - blue MOT loading, red MOT loading, lattice loading, spectroscopy, and imaging - while the right-hand portion shows the resulting time sequence: columns represent segments of time, and rows represent various digital and analog channels for NIDAQ control of hardware. Figure 2.54 are two screen captures of the imaging, analysis, and data logging software. Images are retrieved from the camera using the Thorlabs UEye software application pro-

gramming interface (API), displayed real-time in the imaging bench as shown (with tiling if the camera AOI is smaller than the bench window) and the output data is logged to text file. The output data is most commonly the atom number (or more directly, just the pixel brightness), and this is measured either using a pixel-summing tool or a Gaussian-fitting tool. One of the primary advantages of our homemade software is that it was written as a core framework with an exposed API for writing plugins. The pixel-summing, Gaussian-fitting, and the text-logging tools were all written as plugins in this way. New plugin tools may be written without any knowledge of how the core framework operates, allowing both experienced as well as inexperienced programmers to expand the capabilities of the software by writing new plugins. And each plugin benefits from the features of the core framework, which include highly modular drag-and-drop functionality and the ability to change output measurements real-time without having to pause the sequencer.

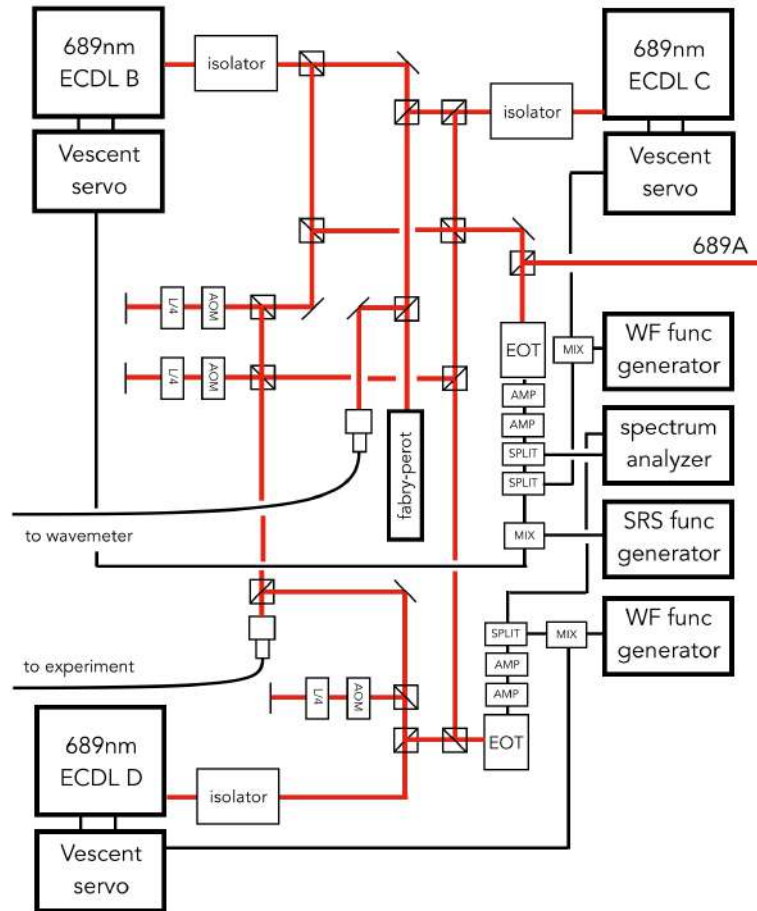


Figure 2.50: Schematic of the spectroscopy apparatus. Lasers 689B and C are phase-locked to 689A, while 689D is phase-locked to 689C. Each spectroscopy laser is shuttered using a double-pass AOM at a total frequency shift of 420 MHz; together with the 80 MHz shift of the 689A laser, this means that the spectroscopy lasers B and C can probe the $^1S_0 - ^3P_1$ line if they are offset locked to a total of 500 MHz from 689A. For 689D, the setpoint depends on C.

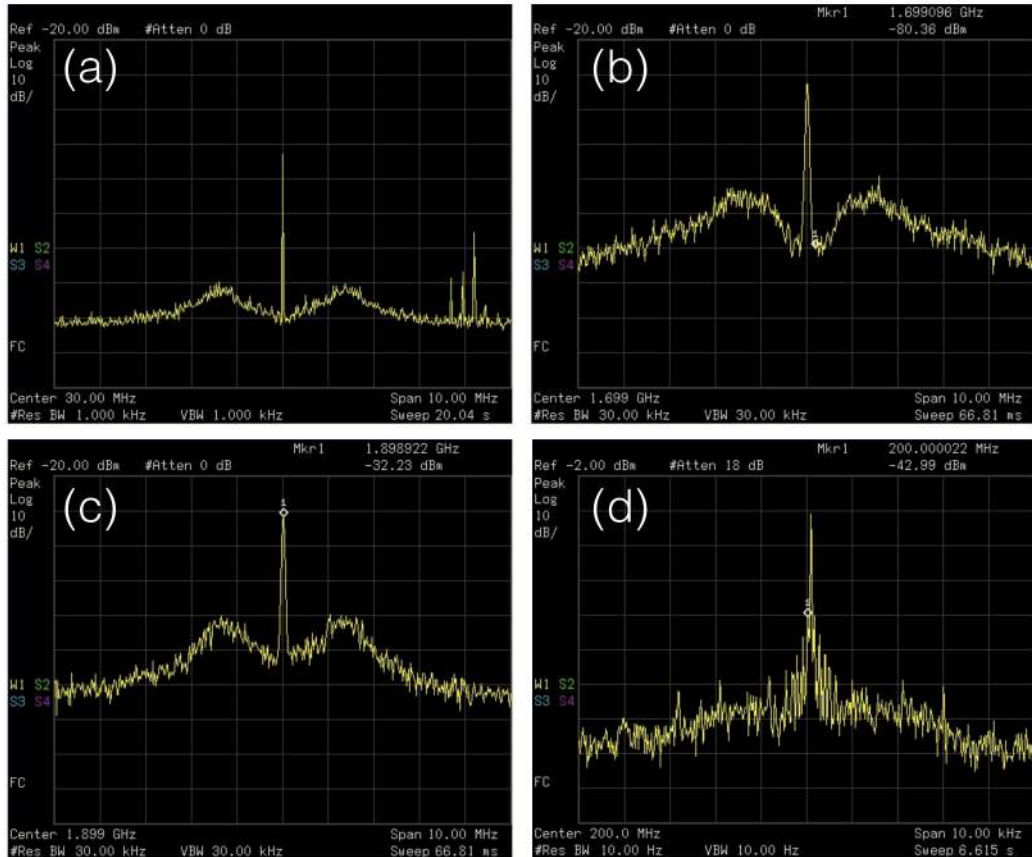


Figure 2.51: Spectrum analyzer traces of the lasers (a) 689A, (b) 689B, (c) 689C, and (d) the beat of 689B with C. Note that in (a) through (c) the span of the trace is 10 MHz to show the servo sidebumps, whereas in (d) the span of the trace is 10 kHz, focused on the central lock feature. The observed width of the central lock peaks are limited by the resolution of the spectrum analyzer.

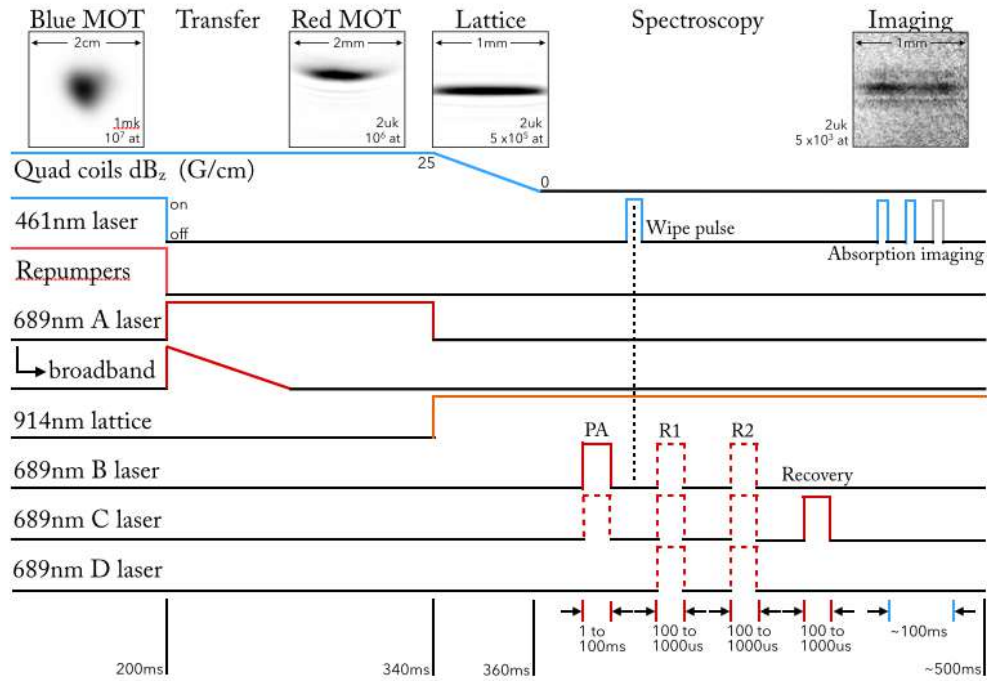


Figure 2.52: The full experimental sequence schematic.

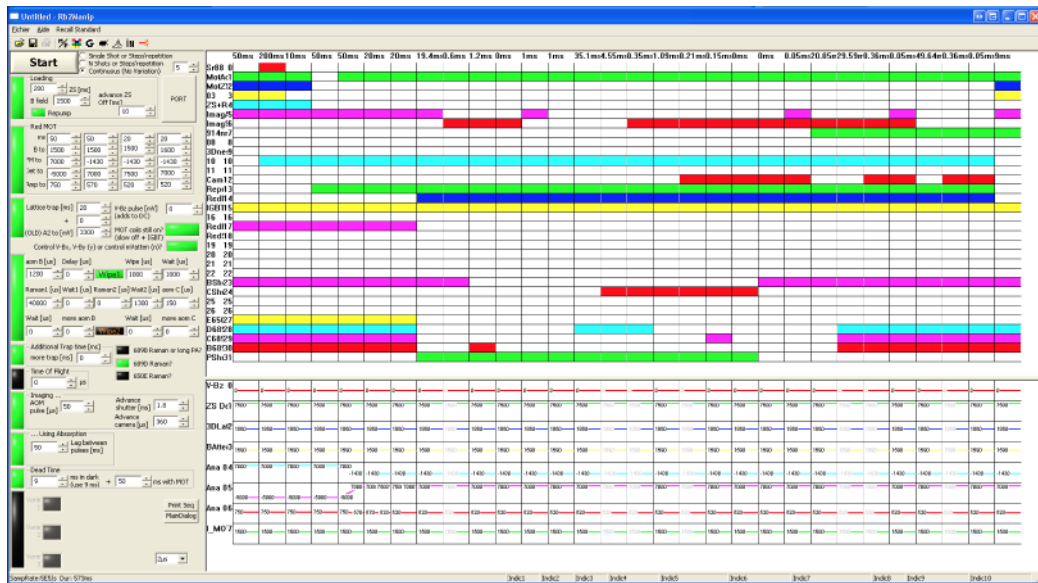


Figure 2.53: Screen capture of the sequencer software.

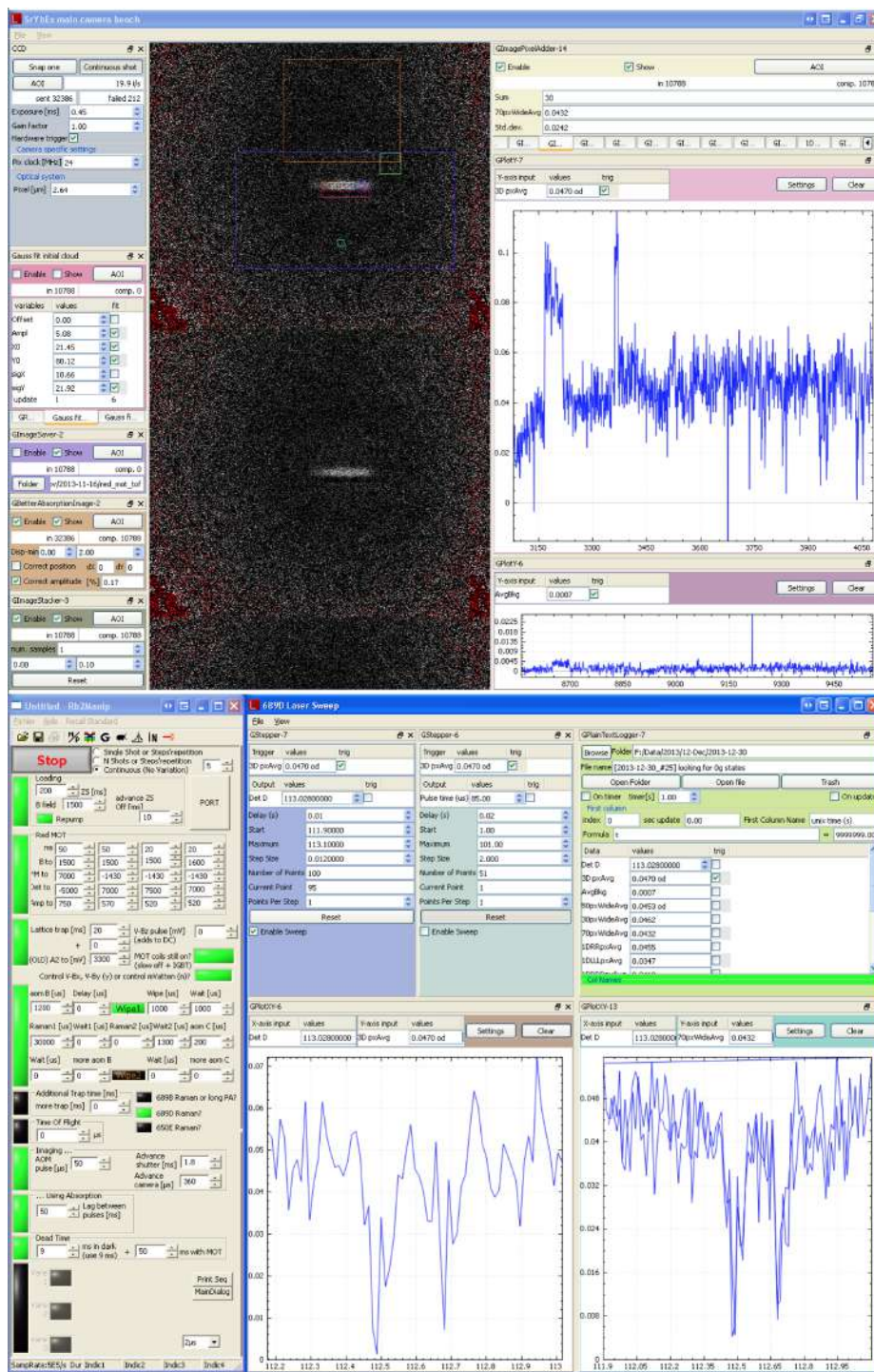


Figure 2.54: Screen capture of the lab control software.

Chapter 3

Production of ultracold $^{88}\text{Sr}_2$ molecules

Because the energy level structure of molecules is significantly more complicated than that of atoms, and few closed optical transitions are available, methods for direct cooling and trapping of molecules have been limited. As a result ultracold molecule production often relies on an already cold sample of constituent atoms [Doyle *et al.*, 2004; Dulieu and Gabbanini, 2009; Carr *et al.*, 2009]. One such method utilizes magnetic fields to tune bound molecular channels to resonance with the incident open channel. These resonances, known as Feshbach resonances, rely on the species having hyperfine magnetic structure in the ground state. For species that do not have this structure, such as in our case with Sr, an analogous optical technique, photoassociation [Jones *et al.*, 2006], is employed.

3.1 Sr_2 molecular notation

In an idealized molecule, electronic, vibrational and rotational degrees of freedom can be separated. Analogous with atomic structure, the electronic state of the molecule is specified by a term symbol. Recall that an atom's term symbol is described by $^{2S+1}L_J$, where S is the spin, L is the orbital angular momentum, and J is the total electronic angular momentum. Molecular term symbols depend on the details of the molecule in question. Any choice in term symbol represents an approximation of the true picture, and for any given picture,

mixing can occur between the various states, complicating the system. It is important to choose the picture that most closely represents the properties of the atom or molecule at hand.

For each electronic state there is an internuclear potential that describes the energy of the system for varying nuclear separation. Figures 3.1 and 3.2 (a) and (b) shows two of the most relevant for our work.

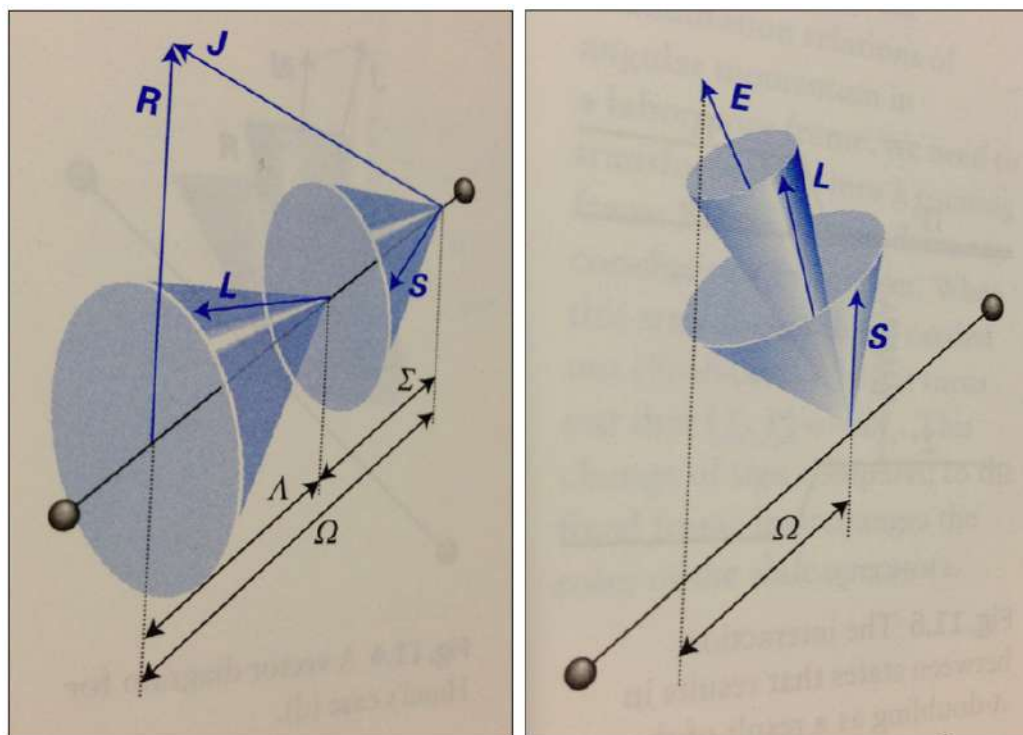


Figure 3.1: Angular momentum breakdown for Hund's case (a) (left), and for Hund's case (c) (right). Source: [Atkins and Friedman, 2010].

3.1.1 The Born-Oppenheimer picture and Hund's case (a)

The most common molecular term symbol models the atomic term symbol closely [Budker *et al.*, 2008],

$$^{2S+1}|\Lambda|_{\Omega, (g/u)}^{\pm}, \quad (3.1)$$

where S is the total electronic spin, Λ is a projection of the total electronic orbital angular momentum L , and Ω is a projection of the total angular momentum J . In this case, Hund's

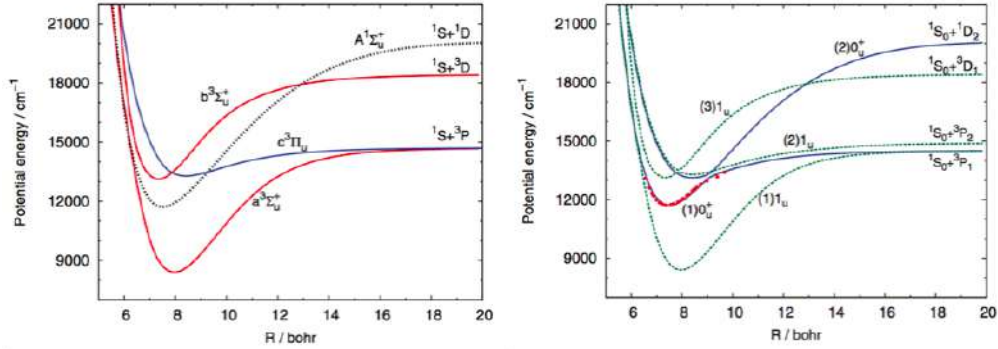


Figure 3.2: Hund's case (a) potentials (left), and Hund's case (c) potentials (right). Notice the state-swapping at avoided crossover points in (c) compared with (a). Source: [Skomorowski *et al.*, 2012b].

case (a), there is strong electrostatic coupling, and very little molecule rotational coupling, explaining its similarity to the atomic symbol.

Because diatomic molecules are symmetric in rotation about the internuclear axis, λ is conserved. Hence the projection onto that axis, Λ , is used as a label. We refer to the absolute value, so $\Lambda = |\lambda| > 0$, and its sign is accounted for as a symmetry. Once again, to distinguish from atomic notation, where $L = 0, 1, 2, 3 \rightarrow S, P, D, F$, values of Λ are tracked using greek symbols, $\Lambda = \Sigma, \Pi, \Delta, \Phi, \dots$. The superscript \pm labels the sign of the angular momentum L projection, and signifies whether or not there is a wave function sign change under reflection across the plane perpendicular to the internuclear axis.

For homonuclear dimers there is one more symmetry: electronic sign change about the molecule center of mass. For even (odd) symmetry, the subscript g (u) is used, following the traditional gerade/ungerade symmetry labeling system.

3.1.2 Empirical spectroscopist's notation

A variant on the Hund's case (a), the empirical spectroscopist's notation adds a letter prefix on each symbol above, X for the ground state, and A, B, C, \dots (a, b, c, \dots) to denote states with the same (different) Ω multiplicity of that of the ground state, ordered by increasing energy [Brown and Carrington, 2003]. In this case,

- $X^1\Sigma_g^+$ corresponds to the $^1S + ^1S$ ground state asymptote,

- $A^1\Sigma_u^+$ and $A^1\Pi_u$ correspond to the $^1D + ^1S$ asymptote,
- $B^1\Sigma_u^+$ and $B^1\Pi_u$ correspond to the $^1P + ^1S$ asymptote, and
- $a^3\Sigma_u^+$ and $c^3\Pi_u$ correspond to the $^3P + ^1S$ asymptote.

3.1.3 Relativistic picture and Hund's case (c)

Heavy dimers with strong spin-orbit coupling are best described using Hund's case (c) notation [Jones *et al.*, 2006; Ciurylo *et al.*, 2004; Ulmanis *et al.*, 2012]. In this approximation, the coupling means that neither Λ nor Σ are well defined, and so the molecular term symbol denotes the combined value Ω :

$$(n)|\Omega|_{(g/u)}^{\pm}. \quad (3.2)$$

The \pm superscript here is different than that for Hund's case (a) coupling, and denotes whether or not there is a sign change of the electronic wave function under reflection along a plane *containing* the internuclear axis. Naturally then, this symmetry only exists for $\Omega = 0$ states.

There is an ambiguity here, since this labeling system doesn't identify the asymptotic atomic states of the substituent atoms. To account for this, the traditional label places a number in parenthesis in front of the term symbol, denoting the ordering of these states for increasing energy at the asymptotic line, as in $(1)0_u$, $(2)0_u$, etc. This is described in Fig. 3.2. In this system the ground state X is unique,

- $X^1\Sigma_g^+$ corresponds to the $^1S + ^1S$ ground state asymptote,
- $(1)0_u^+$ and $(1)1_u$ correspond to the $^3P_1 + ^1S$ asymptote (a shorthand for these lowest two states omits the prefix: 0_u^+ and 1_u), and
- $(2)0_u^+$ corresponds to the $^1D_2 + ^1S$ asymptote,

and so on. This notation, as well as the empirical spectroscopist's, is used extensively in the works [Skomorowski *et al.*, 2012b; Skomorowski *et al.*, 2012a], in which an ab initio model is used to construct the potential energy states of $^{88}\text{Sr}_2$, used for comparison with our results in the coming chapters.

3.1.4 Rovibrational indices

The various notation systems above denote manifolds with a given electronic state, and depending on the system, projections of the total spin, orbital angular momentum, and combined angular momentum of the dimer. For any one of these manifolds, there are then a set of vibrational bound states, denoted v , and so long as the non-projected, total angular momentum J is a good quantum number [Brown and Carrington, 2003], rotational states as well. These are the last two indices to fully define a state, and depending on how deeply bound the state is, two different conventions can be used:

- For weakly-bound states, one can count the vibrational index downward from dissociation: $v' = 0, -1, -2$, etc. denotes the atomic asymptote, the least-bound molecular state, second least-bound, etc.
- For more deeply-bound states, one can count the vibrational index upward from the most deeply-bound state: $v' = 0, 1, 2$, etc. denotes the vibrational ground state, first excited state, second excited state, and so on.

And lastly, quantum numbers permitting, one may assign a total angular momentum value J to a given state. With all of these prescriptions, one has then identified a single quantum state that corresponds to a unique binding energy. The resulting, full molecular prescription (for the first three states for Hund's case (c)) would then be [McGuyer *et al.*, 2013]

- $X^1\Sigma_g^+ (5s^2 + 5s^2) (v = \dots, J = \dots, m = \dots)$
- $(1)0_u^+ (5s^2 + 5s5p) (v = \dots, J = \dots, m = \dots)$
- $(1)1_u (5s^2 + 5s5p) (v = \dots, J = \dots, m = \dots)$.

3.1.5 Selection rules

As will be described in more detail in the next section, one drives atom pairs between these states by one- and two-photon photoassociation (1PA and 2PA). We assume that sufficiently cold atoms interact only by s-wave collisions, so by conservation of momentum, $\Delta J = \pm 1$ for 1PA. For 2PA, we expect $\Delta J = 0, \pm 2$, for electric-dipole transitions.

3.2 Photoassociation

Photoassociation (PA) [Jones *et al.*, 2006; Thorsheim *et al.*, 1987] is a process by which two colliding ground state atoms, and a photon red-detuned from an electronic transition, form a weakly bound molecule. In this weakly bound regime, the molecule can be approximated as its substituents: one atom in the ground state and one in the electronic excited state.



The interaction between such a pair of atoms results in a set of bound rovibrational states. The detuning of the PA photon from the electronic transition must match the binding energy of one of these states for photoassociation to take place, as shown in Fig. 3.3.

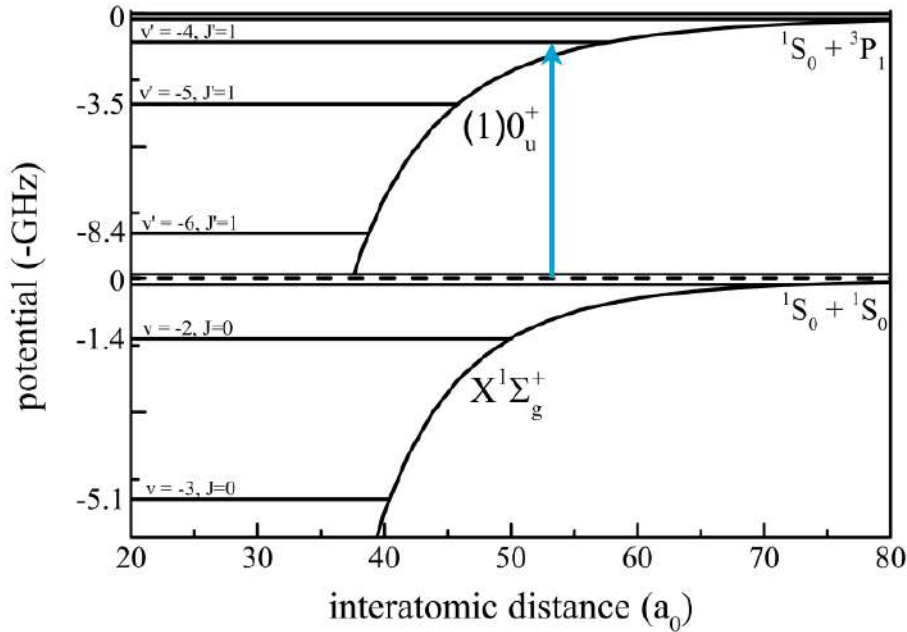


Figure 3.3: One-photon photoassociation from the free atom ground state (dashed line) to, e.g. the $0_u^+(v' = -4, J' = 1)$ excited molecular state.

Previous work has been done on the strong $^1S_0 - ^1P_1$ line [Nagel *et al.*, 2005]. The locations of the nine least-bound states of the $^1S_0 - ^3P_1$ manifold have also been previously

reported [Zelevinsky *et al.*, 2006], and the majority of which have been confirmed again in our work. Figure 3.4 shows a representative example of 1PA losses on the ($v' = -5, J' = 1$) line, at ~ -3.5 GHz binding energy, for minimum PA laser power (for larger PA intensity, the line is deepened and widened); Fig. 3.5 shows the loss rate for this line, as well as the rate vs. PA laser intensity. Also note that the ~ 7 kHz intercombination line allows us to resolve the least-bound state at ~ -450 kHz. Resolving this line relative to the strong atomic line near it is a balancing act for the measurement. For observations of the -450 kHz line in this work, we instead rely on a bound-bound transfer to the state, rather than a free-bound. This is discussed in detail in Ch. 4.

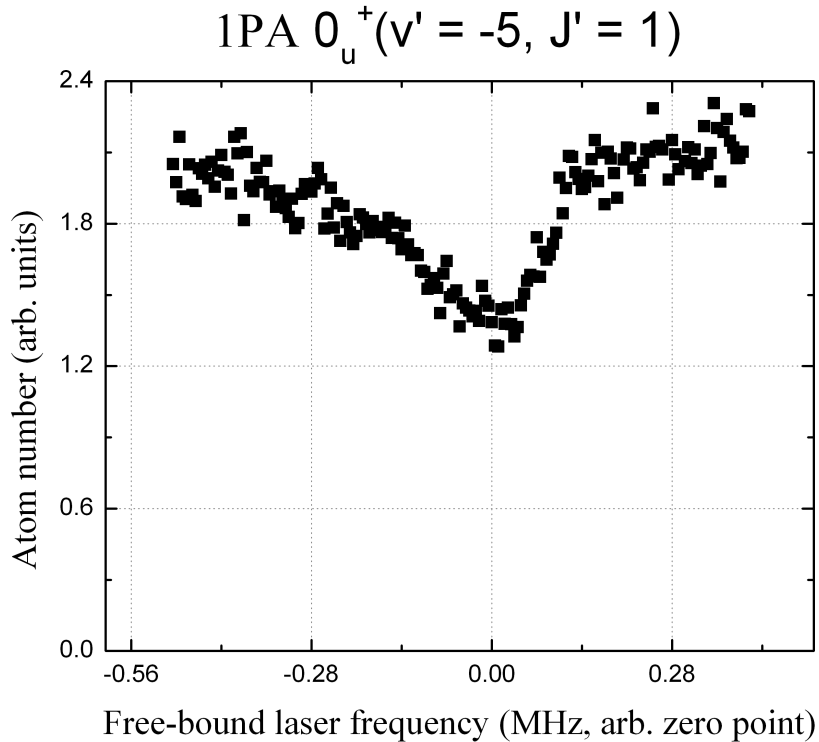


Figure 3.4: 1PA on the $0_u^+(v' = -5, J' = 1)$ line. A relatively small free bound laser (L_{FB}) power of $80 \mu\text{W}$ was employed to show minimal 1PA linewidths of ~ 200 kHz. For higher powers, depletion can reach as much as 80 to 100%, with linewidths up to 1 MHz. In either case, the thermal tail on the left-hand side is evident.

Photoassociation can be modeled by the pseudo-Lorentzian scattering matrix element

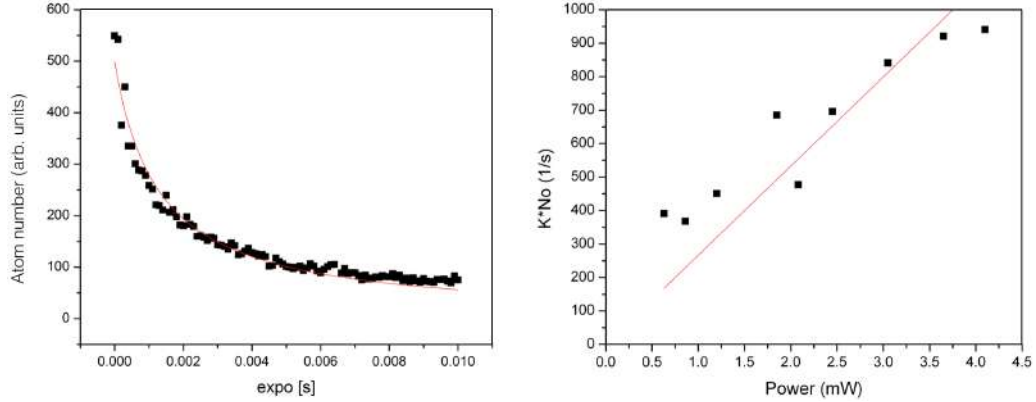


Figure 3.5: 1PA loss curve on the ($v' = -5, J' = 1$) line (left). Loss rate vs. L_{FB} intensity (right).

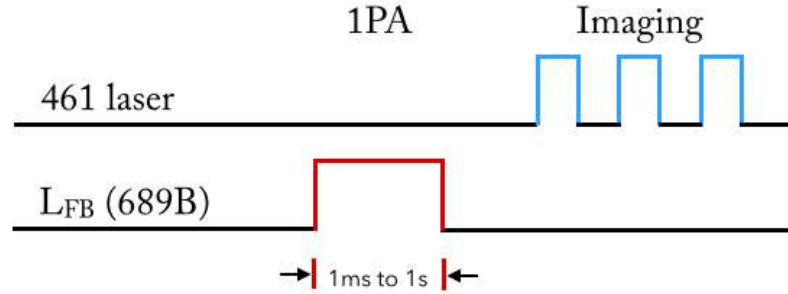


Figure 3.6: A typical 1PA sequence.

[Napolitano *et al.*, 1994; Bohn and Julienne, 1996; Jones *et al.*, 1999]

$$S_{1g}(\epsilon, l, \delta, I_1) = \frac{\gamma_1 \gamma_s(\epsilon, l, I_1)}{(\delta + \epsilon)^2 + (\gamma/2)^2}, \quad (3.4)$$

where δ is the laser detuning from the PA line, $\delta = \delta_L - \delta_1$, ϵ is the collision interaction energy, $\gamma = \gamma_1 + \gamma_s$, where γ_1 is atomic linewidth, and γ_s is the linewidth of the stimulated emission process from the excited state. The linewidth γ_s depends on the laser intensity I_1 , the collision interaction energy ϵ , and the total angular momentum of the atom pair, l , and the resulting bound state b_1 [Ciurylo *et al.*, 2005],

$$\gamma_s = 2\pi \langle b_1 | V_{\text{las}}(I_1) | \epsilon, l \rangle^2. \quad (3.5)$$

Microkelvin trap temperatures guarantee that s -wave collisions dominate, so for our treat-

ment of photoassociation, $l = 0$. From γ_s we can define a scaling parameter that is a useful gauge of the strength of a transition, called the optical length,

$$l_{\text{opt}} = \frac{\gamma_s}{2k_r\gamma_1}. \quad (3.6)$$

Table 3.1 has a list of predicted l_{opt} values, as calculated by our collaborators.

Table 3.1: Calculated optical lengths

v'	E/cm $^{-1}$	l_{opt}
-1	-1.2407E-05	8.06E+05
-2	-7.8541E-04	9.15E+03
-3	-7.4420E-03	6.13E+01
-4	-3.6237E-02	4.70E+01
-5	-1.1422E-01	3.15E+00
-6	-2.6982E-01	3.48E-02
-7	-5.2651E-01	2.22E-01
-8	-8.8540E-01	1.22E-02
-9	-1.3196E+00	7.51E-03

The lifetime of these states is dominated by the short lifetime of the atomic excited state, and so the molecules rapidly deexcite either to molecules in the ground state manifold, or back to free atoms. In general this is an unreliable method for producing a large number of molecules in a single, long-lived rovibrational state.

3.3 Two-color photoassociation

The problem of 1PA deexcitation to many ground states can be side-stepped if instead one uses a pair of lasers to perform a coherent, two-photon transfer directly to the ground state. To ensure that one only drives the coherent process while minimizing scattering off of the one-photon line, both lasers are detuned from the excited state by a common amount, as shown in Fig. 3.7. However this process has its own experimental limitations,

since higher laser power is required to drive the transition for larger common detuning. A typical sequence for 2PA spectroscopy is illustrated in Fig. 3.8.

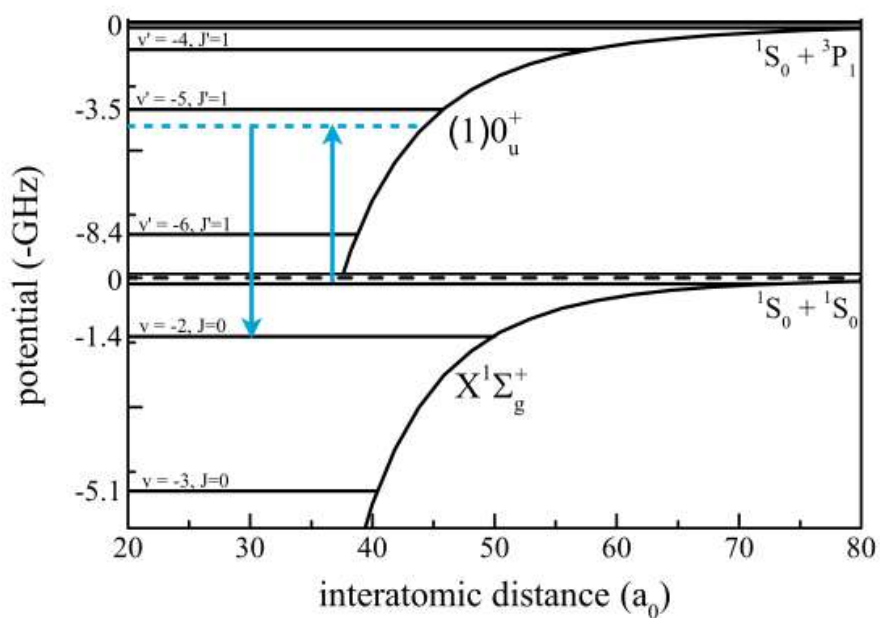


Figure 3.7: Two-photon photoassociation from the free-atom ground state (dashed line) to, e.g. the $(v = -2, J = 0)$ state in the molecular ground state manifold.

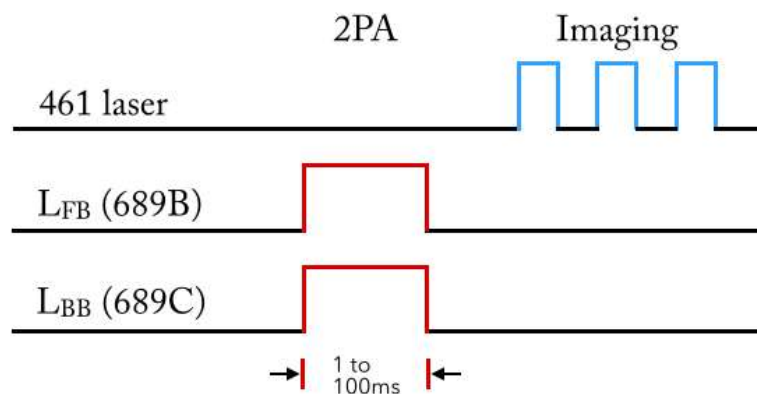


Figure 3.8: A typical 2PA sequence.

Two-photon photoassociation can be modeled by the scattering matrix element [Bohn

and Julienne, 1996; de Escobar *et al.*, 2008],

$$|S|^2 = \frac{((\delta_1 - \delta_0) - \delta_2 + \epsilon)^2 \gamma_1 \gamma_s}{((\delta_1 - \delta_0) - \delta_2/2 + \epsilon)^2 - \frac{1}{4}(\delta_2^2 + \Omega_2^2)^2 + (\gamma/2)^2((\delta_1 - \delta_0) - \delta_2 + \epsilon)^2}, \quad (3.7)$$

where $(\delta_1 - \delta_0)$ is the detuning of the L_{FB} frequency from the free-bound PA line (with δ_0 a free parameter to account for the non-zero location of the 1PA line), δ_2 is the detuning of the bound-bound laser from the bound-bound transition frequency (i.e. independent of the L_{FB} frequency δ_1), Ω_2 is the Rabi frequency of the bound-bound transition, $\gamma_1 = 2\gamma_{\text{atomic}}$ is twice the atomic linewidth, and γ_s is the stimulated emission linewidth. The linewidth γ_s can be expressed as a function of the optical length,

$$\gamma_s = 2k_r \gamma_1 l_{\text{opt}}, \quad (3.8)$$

where the optical length is a measure of the ease with which a FB transition may be excited; it depends linearly on the laser intensity, and in principle should be measurable from this result.

The actual locations of the peaks in this function can be found at the derived frequencies δ_{\pm} given by the expressions

$$\delta_{\pm} = \frac{1}{2}((\delta_1 - \delta_0) + \delta_2) \pm \frac{1}{2}\sqrt{((\delta_1 - \delta_0) - \delta_2)^2 + 4\Omega_2^2}. \quad (3.9)$$

The dynamics of 2-photon photoassociation are similar to those of a 3-state lambda system as seen in Fig. 3.9. If one plots the peak positions for various BB laser detunings, one finds a hyperbolic avoided crossing curve as seen in Fig. 3.10. For large detunings, the dominant central peak can be described as the 1PA line, while the detuned line is the coherent, 2PA transition. At small detunings, the system is described best by the dressed-state model, where each peak is a coherent mixture of both the excited molecular state accessed via 1PA, and the ground molecular state accessed via 2PA. The mixture is determined by the dressed state re-diagonalization:

$$|+\rangle = e^{-i(\Omega' - \delta - \omega_0)t/2} \cdot (\cos\theta|1\rangle + e^{-i\omega t}\sin\theta|2\rangle) \quad (3.10)$$

$$|-\rangle = e^{-i(\Omega' - \delta + \omega_0)t/2} \cdot (-e^{i\omega t}\cos\theta|1\rangle + \sin\theta|2\rangle) \quad (3.11)$$

for $\Omega' = \sqrt{\Omega^2 + \delta^2}$ and for angles

$$\cos 2\theta = \delta/\Omega' \quad (3.12)$$

$$\sin 2\theta = -\Omega/\Omega' \quad (3.13)$$

For larger values of Ω , one must detune farther in order to separate the 1PA and 2PA processes. For fixed exposure time and PA laser intensity, increased detuning reduces the

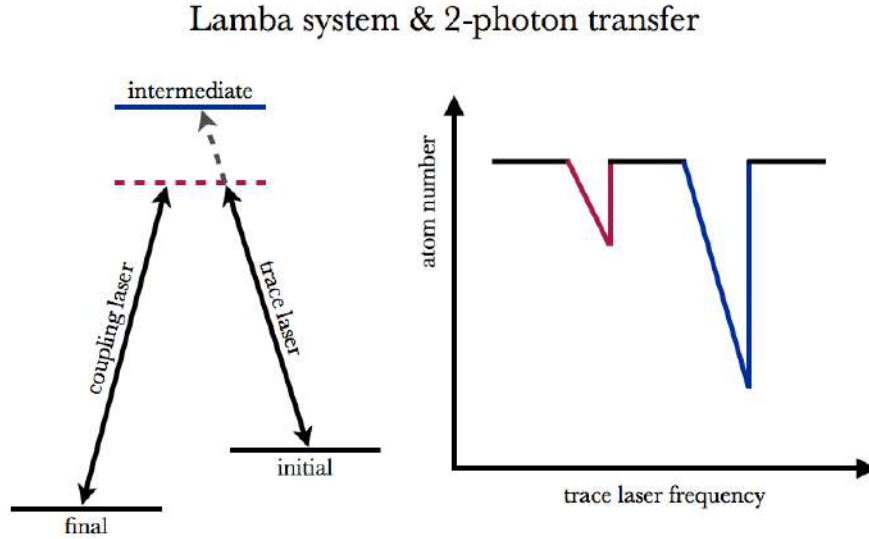


Figure 3.9: (a) Diagram of a three-state lambda system. The laser represented by the right-hand arrow (in our case, the free-bound, or FB) couples the initial state to the intermediate, and the left-hand arrow (bound-bound, or BB) couples the intermediate to the final state. (b) A schematic plot of trap atom number vs. FB laser frequency, for a fixed BB laser frequency. There are two loss peaks, one at the one-photon frequency, and one at the two-photon frequency, where the FB laser detuning matches that of the BB laser. At small BB detunings, the two peaks become a coherent mixture of the two cases, as in a dressed-state system, and never cross.

peak depth of the 2PA line. This is the 2PA tradeoff: purer transfers that decrease the likelihood of scattering off of the excited intermediate state require more laser power to drive.

We can estimate the feasibility of this production method using a simple model: simultaneously setting a detuning-dependent upper limit on the laser intensity in order to keep photon scattering off of the 1PA (or atomic) line to a minimum, while also setting a lower

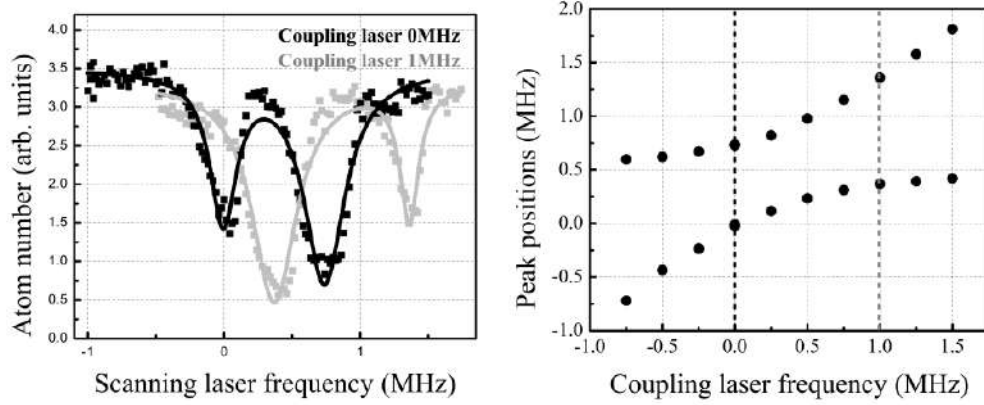


Figure 3.10: (a) Two representative 2PA traces, black for a coupling laser detuning of 0 MHz, and gray for 1 MHz. (b) Aggregate trace of 2PA peak positions for various coupling laser detunings, with vertical lines to mark the example traces from (a).

limit on the molecular formation rate K . Recall from [Foot, 2005] that the spontaneous scattering rate R_s is related to the excited state density matrix element ρ_{ee} by the saturation intensity,

$$R_s = s_0 \rho_{ee} = \frac{s_0 \Gamma / 2}{1 + s_0 + (2\Delta / \Gamma)^2}. \quad (3.14)$$

Our estimate is that the molecular lifetimes will be on the order of $\tau_1 \sim 5 - 10$ ms, and so our formation rate must not exceed this. Using the relation $s_0 = 2\Omega_2^2 / \Gamma^2$ on resonance, and for the bound-bound transition Rabi frequency Ω_2 ,

$$\tau_1 \leq \frac{\Delta^2 4\Gamma}{\Gamma^2 \Omega_2^2}, \quad (3.15)$$

where the 1 in the denominator of the above expression has been removed because we are dealing with an open molecular transition that is not susceptible to the effects of saturation. The 1 in the numerator has been dropped because we expect our detunings to be large (\sim MHz) compared to the transition linewidth (~ 10 kHz).

In addition, the two-photon Rabi frequency Ω_{12} must be much faster than the decoherence time, setting the relation

$$\Omega_{12} = \frac{K\Omega_2}{2\Delta} \geq \frac{\pi}{\tau_2} \quad (3.16)$$

for a conservative estimate of $\tau_2 \sim 1$ ms. The inequality for τ_1 sets the detuning restriction

$$\frac{\Delta}{\Omega_2} \geq \frac{\sqrt{\Gamma\tau_1}}{2} \sim 15, \quad (3.17)$$

while together with the expression for Ω_{12} we set a lower limit on the formation rate K ,

$$K \geq \frac{\Delta}{\Omega_2} \frac{2\pi}{\tau_2} \sim 9 \cdot 10^4/\text{s}. \quad (3.18)$$

However, based on our existing 2PA measurements, such as that shown in Fig. 3.11, we do not achieve sufficiently high rates for K . And this is indeed what we have found; we have had no success explicitly detecting molecule formation with 2PA via several different promising state pairs. We must therefore explore alternative methods for molecule production.

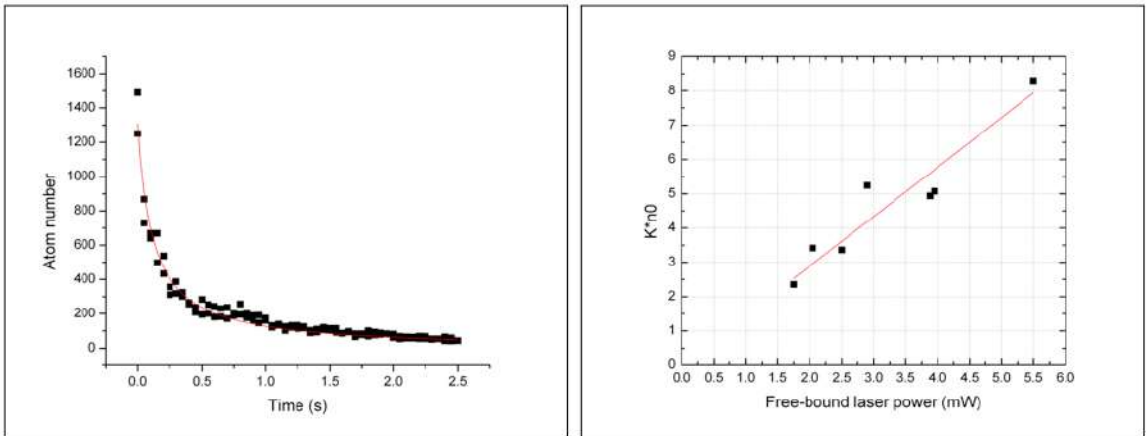


Figure 3.11: Two-color loss plot for the $(-6', -3)$ transition (left), and two-color loss rates vs. free-bound PA laser power (right).

3.4 Franck-Condon factors

We conclude this chapter exploring possible routes toward the production and detection of Sr_2 , the final result published in [Reinaudi *et al.*, 2012b]. This begins with a discussion on Franck-Condon Factors (FCFs), the overlap between wavefunctions in the electronic ground and excited states.

Because of the narrow $^1S_0 - ^3P_1$ intercombination line, the interaction potential for the weakly bound molecular states has a small, attractive C_3 coefficient, and a C_6 coefficient

similar to that of the ground state [Kotochigova, 2008; Skomorowski *et al.*, 2012a; Reinaudi *et al.*, 2012b]. Therefore the wave function of the excited state is very similar to the ground state at the Franck-Condon point, as seen in Fig. 3.12. It is presumable then that some excited rovibrational states have large FCFs with some ground rovibrational state. The

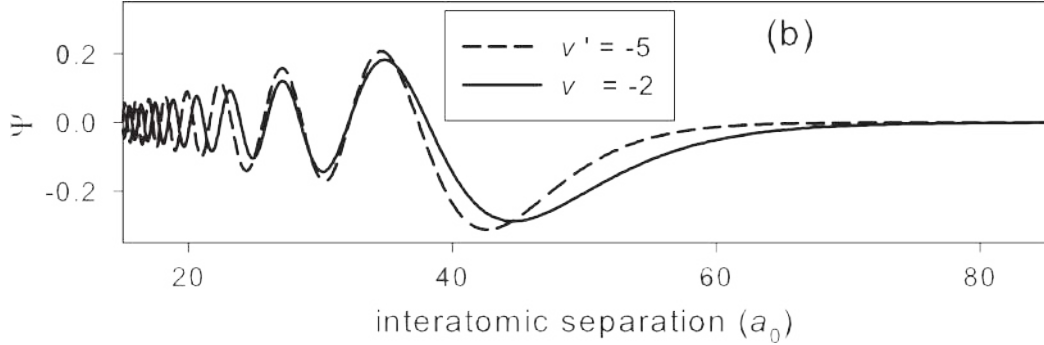


Figure 3.12: Wave functions for the $v = -2$ (solid) and $v' = -5$ (dashed) vibrational levels. The large overlap near the classical turning point leads to the large FCF. Source: [Reinaudi *et al.*, 2012b].

advantage of a large FCF between two states is that spontaneous emission from the upper state will occur predominantly to this single lower state. In such a scheme, 1PA can be used together with this selective spontaneous emission to produce a large sample of molecules in a single rovibrational state of the electronic ground state manifold.

We would therefore like to find as large an FCF as possible to use in our production method. One measures FCFs of pairs of states by measuring the Rabi splitting of the Autler-Townes doublets discussed in Sec. 3.3, by the relationship

$$f_{vv'} = \frac{1}{2\alpha^2} \frac{\Omega_{vv'}^2}{\Omega_a^2}, \quad (3.19)$$

where $\Omega_a = \Gamma_a \sqrt{s/2}$ the Rabi frequency of the atomic line, Γ_a the natural atomic linewidth, s the saturation parameter of the BB laser, and α the line strength between rotational states (1/3 in this case, for $(J = 0, J' = 1)$). Note that here we denote the BB Rabi frequency using the vibrational numbers of the excited and ground states, but in Sec. 3.3 we used the simpler notation Ω_2 , the Rabi frequency of the “second leg” of the 2PA transition.

Table 3.2 is the final result of the work summarized in this section: FCFs for 10 different state pairs, compared to the values calculated by our collaborators [Skomorowski *et al.*,

2012b] (this data was received through private correspondence; it is related to, but not included in, the published work). The final uncertainty was determined after measuring against various systematics: L_{FB} and L_{BB} intensities, lattice laser intensity, magnetic field bias, and atom density. In the interest of time, these systematics were measured on a representative trace, ($v' = -5, v = -1$), and used for all other traces in the manner discussed below.

Table 3.2: Franck-Condon factors: measured

	-1'	-2'	-3'	-4'	-5'	-6'
-1	-	-	0.331(173)	-	0.103(7)	-
-2	-	$4.07(9) \cdot 10^{-4}$	$2.65(23) \cdot 10^{-3}$	0.157(22)	1.018(139)	-
-3	-	-	$5.692(2.525) \cdot 10^{-5}$	$9.951(1.575) \cdot 10^{-4}$	0.0368(227)	1.67(70)

Table 3.3: Franck-Condon factors: calculated

	-1'	-2'	-3'	-4'	-5'	-6'
-1	-	-	0.4849	-	0.02889	-
-2	-	$3.438 \cdot 10^{-4}$	$3.622 \cdot 10^{-3}$	0.1084	0.8067	-
-3	-	-	$1.939 \cdot 10^{-4}$	$8.783 \cdot 10^{-4}$	0.04117	0.8382

3.4.1 Fitting function

In the following discussion a suitable 2PA fitting function is obtained, and then compared to the simpler approach of using a two-peak Lorentzian. It is found that the results are similar enough that it is beneficial to perform the bulk of the analysis using the simpler function, with significant decrease in time spent on the analysis. But first, the better model is constructed.

3.4.1.1 Derivation

Photoassociation, being a two-body interaction, is modeled by density-squared dynamics with a proportional term to account for vacuum lifetime losses. For atom density $n(t)$ the expression is

$$\frac{dn}{dt} = -2Kn^2 - n/\tau, \quad (3.20)$$

for molecule formation rate K and atom trap vacuum lifetime τ . As quoted in Ch. 2, the vacuum lifetime is on the order of ~ 10 s, whereas our photoassociation time scales are ~ 10 ms. It is therefore reasonable to neglect the trap lifetime proportional term, which simplifies the analytic solution. Integrating the density-squared term alone yields the the expression for the atom density,

$$n(t) = \frac{1}{2Kt + 1/n_0} \quad (3.21)$$

for initial atom density n_0 and photoassociation time t . The spectroscopic dependence of this function is built into the molecular formation rate K :

$$K(\epsilon, l, \delta_1, \delta_2, I_1, I_2) = \left\langle \frac{\pi v}{k^2} \sum_{l=0}^{\infty} (2l+1) |S(\epsilon, l, \delta_1, \delta_2, I_1, I_2)|^2 \right\rangle, \quad (3.22)$$

where v is the interaction velocity of the colliding atom pair, $k = \sqrt{2\mu\epsilon}/\hbar$ is the collision wave number, ϵ the collision energy (in frequency units Hz), μ the reduced mass of the atom pair, l is the total angular momentum of the system, and $S(\dots)$ is the 2PA scattering matrix element as defined in the previous section.

The spectroscopic arguments in K and S are the two laser detunings and intensities, respectively, and δ_{\pm} are the dressed state peak locations at a given set of laser detunings. Details on the scheme can be found in [Bohn and Julienne, 1996]. However, note that Bohn's and Julienne's definition of Δ_2 is dependent on Δ_1 , whereas in our case we have defined it as a detuning from resonance with the intermediate and final states. Rather, our δ_1 and δ_2 are defined similarly to those in [de Escobar *et al.*, 2008].

The collision energy term ϵ has been introduced because our atomic ensemble is in a thermal distribution in collision energy ϵ , and therefore our lineshape is the convolution of the expression above with the energy distribution

$$f_{3D}(\epsilon h) = \frac{2}{\sqrt{\pi}} e^{-\epsilon h/k_B T} \frac{\sqrt{\epsilon h}}{(k_B T)^{3/2}}, \quad (3.23)$$

resulting in a final expression for the rate K ,

$$K_{3\text{D}} = \int_{\epsilon} f_{3\text{D}}(\epsilon) K(\epsilon, l = 0, \dots) d\epsilon. \quad (3.24)$$

Because of the Wigner threshold law [Ciurylo *et al.*, 2004], at $T \sim 1, \mu\text{K}$ no higher order angular momentum states can contribute to the collision interaction, and so it is accurate to calculate for strictly s-wave collisions ($l = 0$). Since we are in a 1D lattice our dimensionality is 2D. However at our $\sim 1, \mu\text{K}$ temperatures the thermal tail should contribute relatively little to the overall line shape, and so the calculation was performed using a 3D thermal ensemble.

It is the number of atoms in the lattice trap that we measure, which is converted to an atom density. This function $K_{3\text{D}}$ is then used in the expression for n_{atom} defined at the beginning of this section, and is then fit to the data.

3.4.1.2 Implementation and fitness

Data fitting is performed in Origin, and the thermal convolution above is composed of a 50-term discrete summation. This was found to achieve the desired level of smoothness for the majority of the 2PA peaks, even at large detunings from the 1PA line. The free parameters of the system are $\delta_0, \delta_1, \delta_2, \Omega_2$ (which define δ_{\pm}), n_0, l_{opt} , and a final parameter A which is defined below. However the exact implementation of this set of free variables comes with three qualifications that require explanation.

First, for an avoided crossing set of traces, $\delta_1 - \delta_0$ and Ω_2 should each have only a single value, but each can be extrapolated from just a single constituent trace. The solution then is to set each either as a singly-defined global free parameter across the whole set of traces, or to still leave each as fully free, and look at the spread and error across the set of traces. We opted for the latter solution, and have plotted $\delta_1 - \delta_0$ and Ω_2 across the traces as shown in Fig. 3.13 (a) and (b).

The spread of values for $\delta_1 - \delta_0$ gives a mean and standard deviation of

$$\delta_0 = 739(23) \text{ kHz}, \quad (3.25)$$

which is quite consistent. But for the Ω_2 trace a little more analysis is required. The three low-lying outliers happen to correspond to traces whose fit line was not smooth, as shown

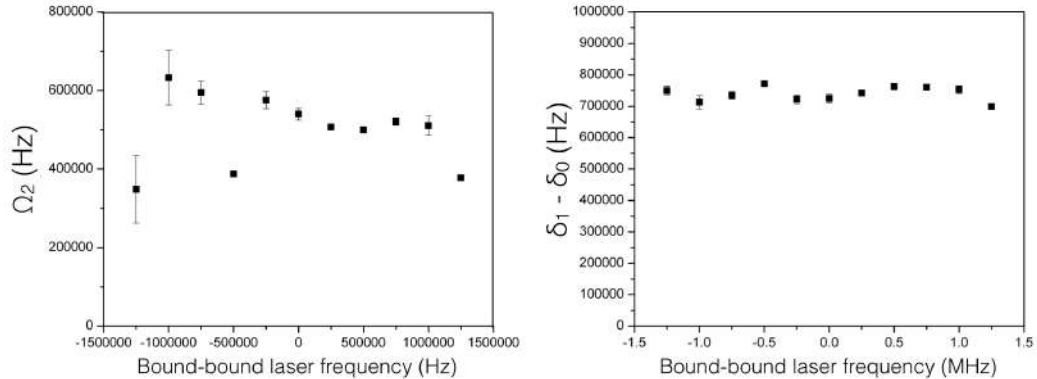


Figure 3.13: Plot of Ω_2 (left) and $\delta_1 - \delta_0$ (right) values extrapolated from 2PA fits for various single traces.

in Fig. 3.14. Ignoring these three, there are still 8 data points, and from their spread we can average the value of Ω_2 to

$$\Omega_2 = 548(48) \text{ kHz.} \quad (3.26)$$

The globally-extrapolated value for Ω_2 , i.e. the value of the minimum spacing between the two peaks as found from the data in Fig. 3.16 below, is $\Omega_2 = 503(18) \text{ kHz}$, which is in agreement with the spread from the trace as quoted above.

The second qualification for the fitting function concerns l_{opt} . Our collaborators predicted values for the optical length per unit of laser intensity. This value can either be fixed, or left as a free parameter to independently check the prediction. Our attempts at independent confirmation found the fit relatively insensitive to l_{opt} , and so we decided to fix them to their predicted values.

The third qualification is regarding the free parameter A . The original model did not include such a term, and the first attempts at fitting produced results similar to the pink trace in Fig. 3.15. This fit implies that, for our exposure times (and for tests at any reasonably larger times), it is not feasible to induce losses as deep as the data shows. This makes intuitive sense, because the photoassociation rate is a density-squared loss process; as PA loss drives the atom density down, it becomes increasingly difficult to further induce PA losses. But there must still be a discrepancy between our measurement and the fit. One possible explanation is that the atom density is different than what we measure with our

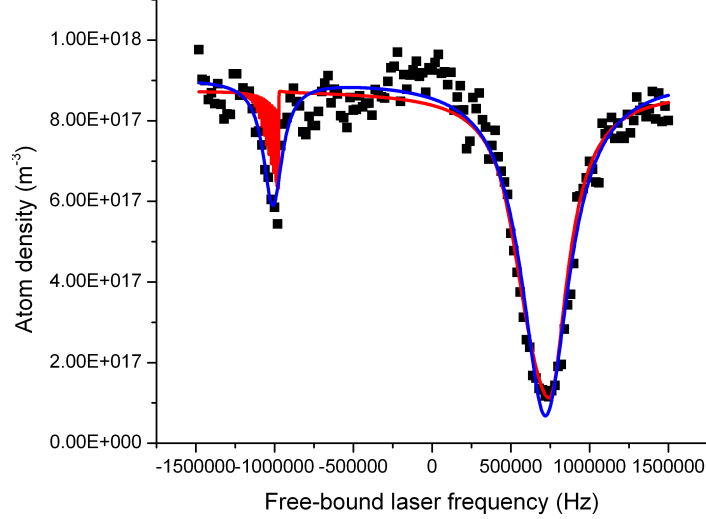


Figure 3.14: Discrete-sum thermal 2PA fit example from one of the traces resulting in an anomalously small Ω_2 value (red), and the smoother, but less accurate, nonthermal two-Lorentzian fit function (blue). For the discrete sum, the same non-smooth artifact of the thermal convolution is present in all of the traces with anomalously low Ω_2 values, and therefore is assumed to be the culprit. The Ω_2 values from these traces have been omitted from the analysis.

camera. If we introduce a scaling factor A on the overall density in Eq. 3.20, it cancels from all terms, except to linear order in the n^2 term:

$$n(t) = \frac{1}{2AKt + 1/n_0}. \quad (3.27)$$

It is clear that fits including the free parameter A match the data significantly better, as shown in Fig. 3.15, with a resulting value $A \sim 5.5$. It only remains to explain why such a density compression factor is necessary. One possible explanation is lattice trap density compression. Our CMOS camera resolution, at $\sim 3 \mu\text{m}$, is significantly larger than the lattice site size scale, $\sim 500 \text{ nm}$, and so the atom density measured from the CMOS underestimates the true, local value experienced by atoms. We can estimate the lattice density compression factor with the following reasoning. The total lattice trap depth for a

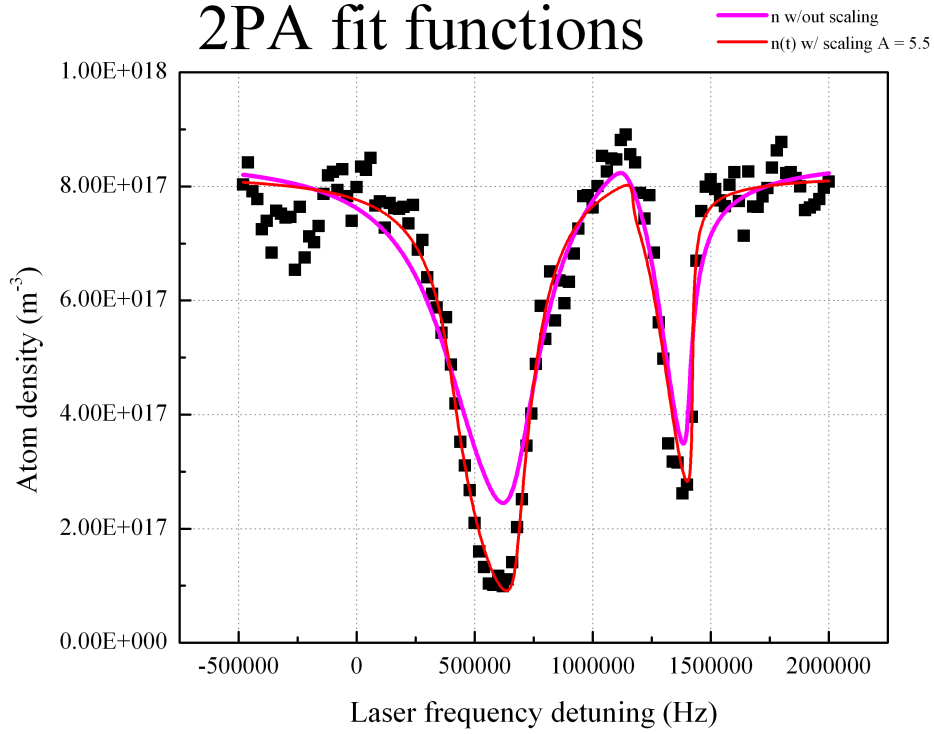


Figure 3.15: Comparison of the 2PA fit function with (red) and without (pink) the additional scaling factor A . All other parameters, such as the optical length l , and the exposure time t , are equal.

one-way laser power $P = 180$ mW and beam waist $w_0 = 25 \mu\text{m}$ is $U/k_B \sim 35 \mu\text{K}$. Our atom sample is typically at a temperature $T < 2 \mu\text{K}$. If the atoms only occupy the spatial extent $2x$ of the well at or below $2 \mu\text{K}$, then for a sinusoidal trap profile, the fractional compression for this ratio is

$$\frac{x}{\lambda/4} = 4 \sin^{-1} \left(\sqrt{2 \mu\text{K}/35 \mu\text{K}} \right) / 2\pi \simeq 0.153 \simeq 1/6.5. \quad (3.28)$$

Because A is introduced such that $n \rightarrow An$, this means that A is the reciprocal of the compression factor above. Hence,

$$A = \left(\frac{\lambda/4}{x} \right) \simeq 6.5, \quad (3.29)$$

which matches the fit result of $A \sim 5.5$ within 20%. We believe this is a credible explanation for why this additional parameter A is necessary for the fit function.

With these qualifications accounted for, the fit function appears sufficient because it accounts for the thermal asymmetry of the peak points and has the PA-suppressing interference point that can be found between the two peaks, a feature clearly evident in the data.

3.4.1.3 Evaluation

We evaluate the fitness of this function, and the two-Lorentzian, by comparing their success on a representative data set, as shown in Fig. 3.16.

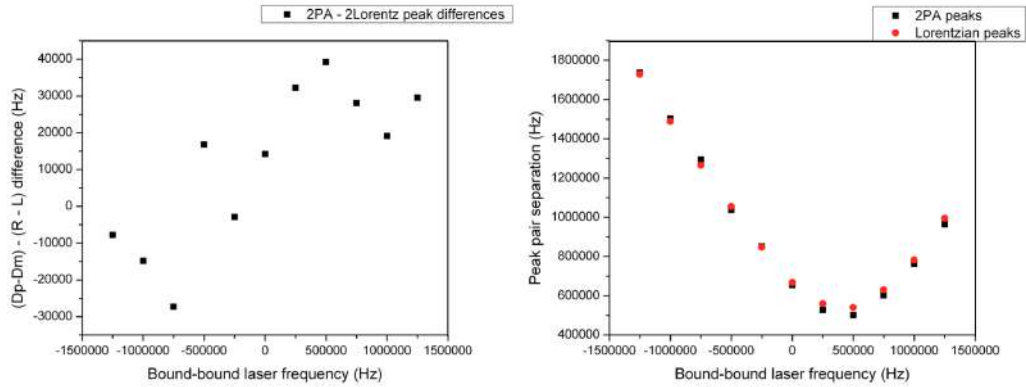


Figure 3.16: Plot of the peak separations of the 2PA fit peaks (black), and the double Lorentzian peaks (red) (left). Difference of the point sets (right). Notice the crossing point at ~ -250 kHz.

It is clear from the data that the interference point of zero PA between the two peaks is real, and that the two-Lorentzian function fails to account for it. But what matters the most is simply that the two-Lorentzian function sufficiently identify the peak positions. By eye we can see that it does not account for thermal tail-induced asymmetry in the peak. However, for calculating FCFs, it is only the peak separations that matter, and because this shift is systematically leftward for both peaks, its effect could very well cancel out. Figure 3.16 is a plot of this measure, $(\delta_+ - \delta_-) - (\delta_R - \delta_L)$, where $\delta_{R/L}$ are the frequencies of the right and left peaks of the two-Lorentzian peaks. The overall spread is within ± 40 kHz, and there appears to be a linear dependence on detuning. This is not surprising; as detuning is increased, the thermal asymmetry is not exhibited equally by the two peaks (the

narrower line is more symmetric), and therefore the imperfection of the Lorentzian fit does not subtract out in the difference. But the difference is approximately zero at zero detuning, where Ω_2 is most sensitively determined. Hence if the two-Lorentzian function is used, it is appropriate to add a pessimistic ± 30 kHz additional uncertainty to the extrapolated value of Ω_2 .

3.4.2 Systematic shifts

The FCF values were measured against five possible sources of systematic shifts:

- L_{FB} intensity
- L_{BB} intensity, although this laser intensity factors directly in to the expression for Ω_2
- Lattice laser intensity
- Magnetic fields
- Atom/molecule density

Because each FCF data point requires a full avoided crossing set of traces, any systematic shift is extrapolated from a repeated binary measurement, four data points in total. There is concern that on the apparatus there is an overall laser frequency drift on the order of ~ 2 kHz/min (possibly from thermal drift of the high-finesse cavity), and since each avoided crossing set takes ~ 40 minutes, both the individual traces as well as the binary sets were taken in an interlaced fashion, to avoid conflating any measurement axis with time. All measurements were made on the representative pair ($v = -1, v' = -5$), and the resulting uncertainties are extrapolated from this pair for all other state pairs.

3.4.2.1 L_{FB} intensity

From the slope in Fig. 3.17 (d) we estimate a possible L_{FB} intensity-induced shift of $20(40)$ kHz/mW L_{FB} .

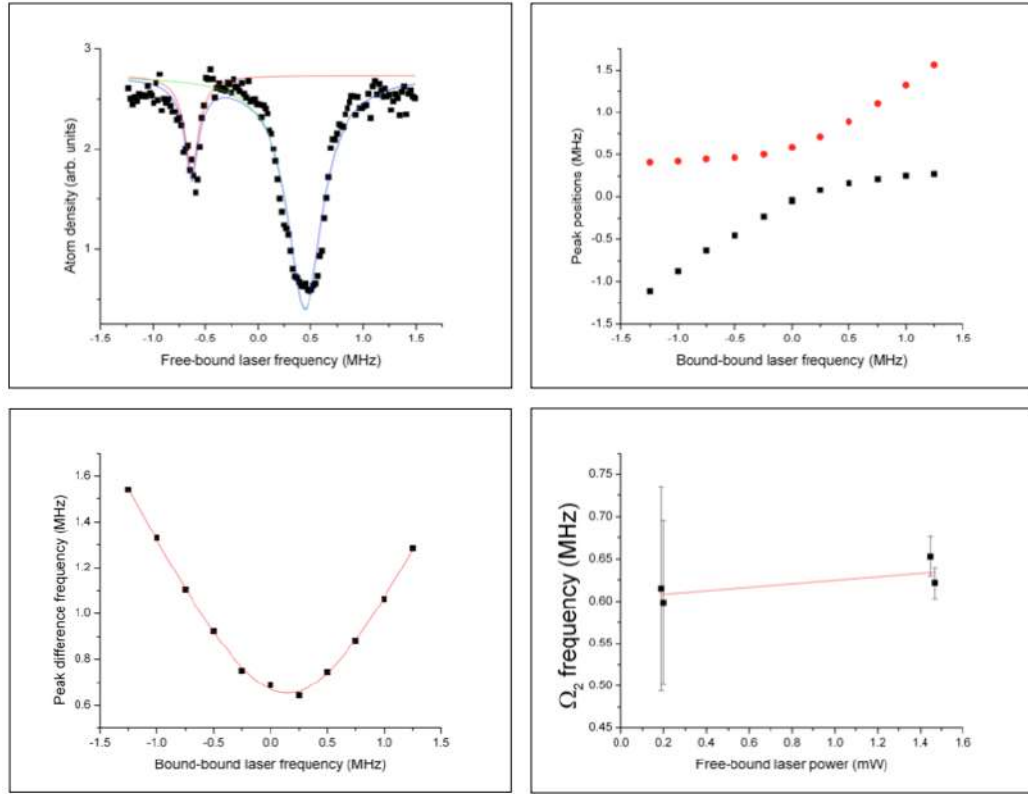


Figure 3.17: (a) A representative 2PA trace for a fixed L_{BB} detuning of 0 MHz. (b) Autler-Townes avoided crossing aggregate of 2PA traces, with dots marking the peak pair positions. (c) Hyperbola of peak position differences, with a fit to extract Ω_2 (Eq. 3.9). (d) Plot of Ω_2 for a pair of high and low L_{FB} intensities, and a resulting linear fit to extrapolate the final shift and uncertainty.

3.4.2.2 L_{BB} intensity

The FCF depends explicitly on the L_{BB} intensity, and so Ω_2 depends on it as more than a systematic shift. Therefore it is implicit in each measurement's uncertainty, and is not treated here.

3.4.2.3 Lattice laser intensity

From the slope in Fig. 3.19 (d) we estimate a possible lattice laser intensity-induced shift of 30(30) kHz/200 mW lattice laser power.

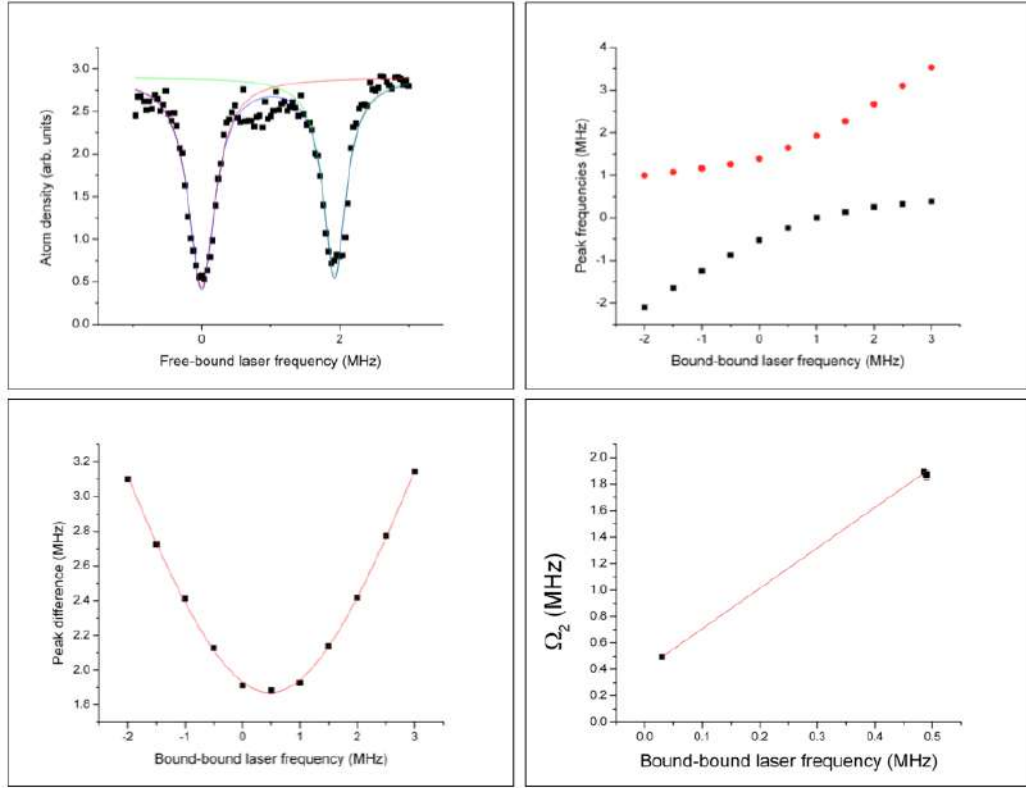


Figure 3.18: (a) A representative 2PA trace for a fixed L_{BB} detuning of 0 MHz. (b) Autler-Townes avoided crossing aggregate of 2PA traces, with dots marking the two peak positions. (c) Hyperbola of peak positions differences, with fit to extract Ω_2 (Eq. 3.9). (d) Plot of Ω_2 for two high and low BB laser intensities, and resulting linear fit to extrapolate the final shift and uncertainty.

3.4.2.4 Magnetic fields

From the slope in Fig. 3.20 (d) we estimate a possible magnetic field-induced shift of $3(2)$ kHz/G vertical magnetic field offset. This is negligible compared to the other sources of uncertainty, and so will be neglected.

3.4.2.5 Atom/molecule density

From the slope in Fig. 3.21 (d) we estimate a possible density-induced shift of $-20(10)$ kHz/ $5 \cdot 10^{-11}$ cm^{-3} atom density.

This concludes our measurement of the systematics, which gives us our error bars on the

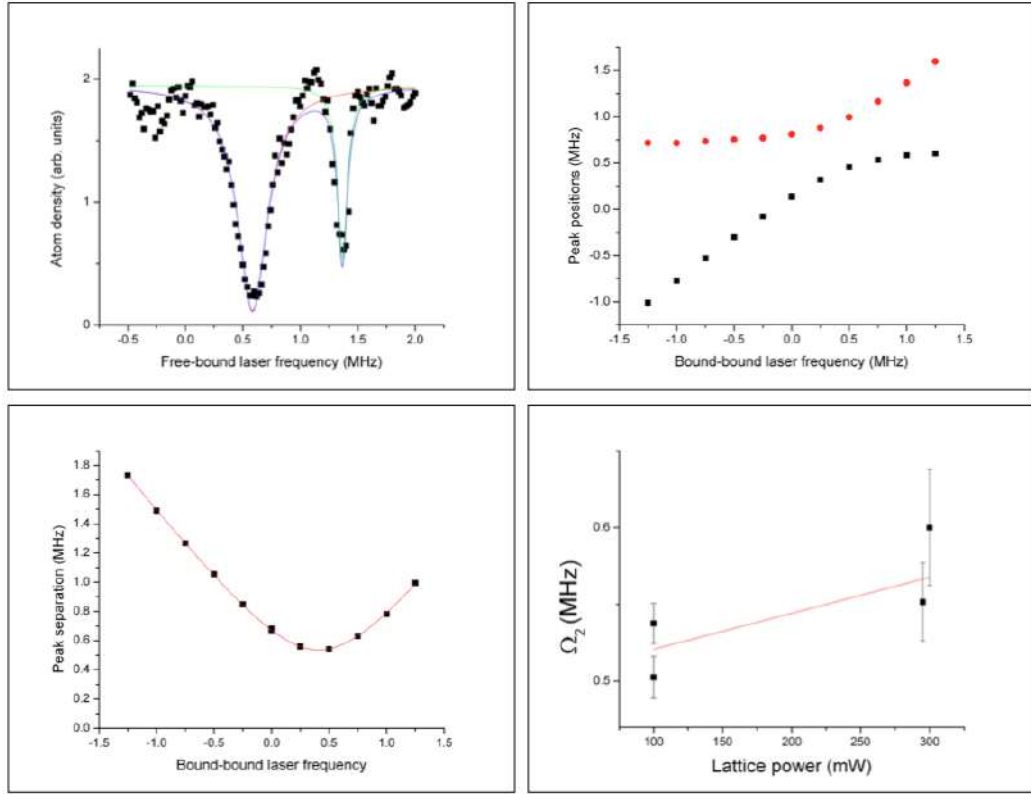


Figure 3.19: (a) A representative 2PA trace for a fixed L_{BB} detuning of 0 MHz. (b) Autler-Townes avoided crossing aggregate of 2PA traces, with dots marking the two peak positions. (c) Hyperbola of peak positions differences, with fit to extract Ω_2 (Eq. 3.9). (d) Plot of Ω_2 for two high and low lattice laser intensities, and resulting linear fit to extrapolate the final shift and uncertainty.

results from Table 3.2 from the previous section. Our goal however was simply to find large FCFs, and it can be seen in the table that two state pairs have near-unity FCFs: $(-2, -5')$ and $(-3, -6')$. Given the limitations of laser power, it is much easier to drive the $(-2, -5')$ pair, and so we opt for this state as a reliable step in the molecule production sequence. The details of production are the topic of the next and final section.

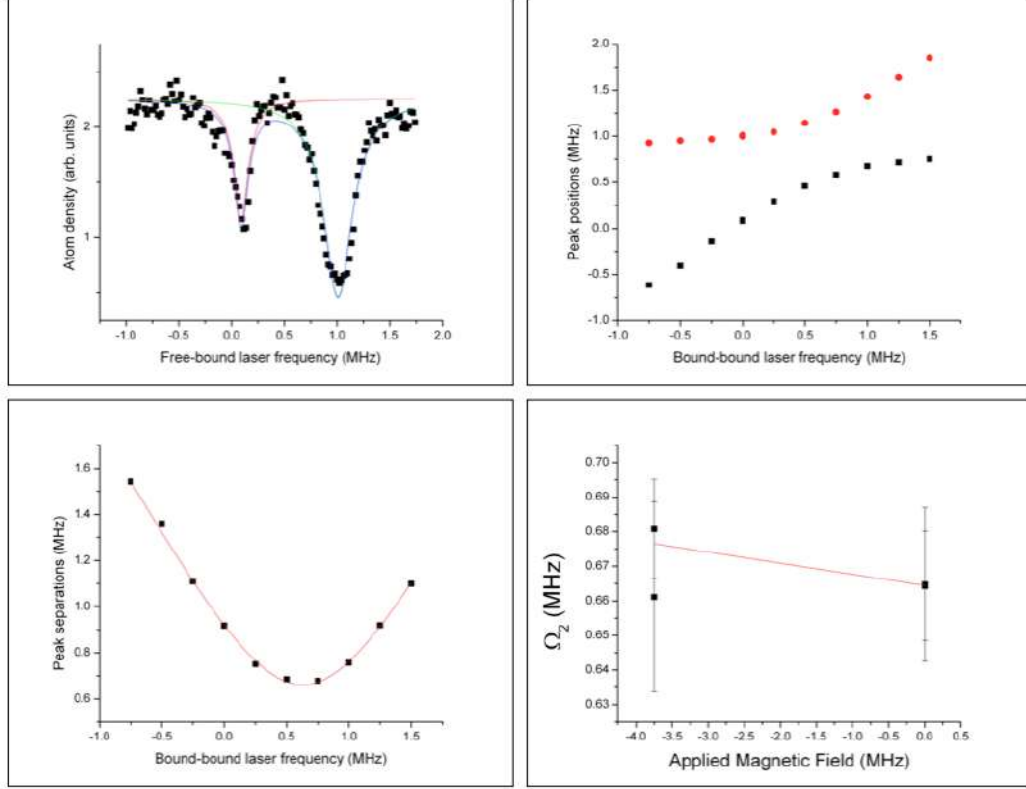


Figure 3.20: (a) A representative 2PA trace for a fixed L_{BB} detuning of 0 MHz. (b) Autler-Townes avoided crossing aggregate of 2PA traces, with dots marking the two peak positions. (c) Hyperbola of peak positions differences, with fit to extract Ω_2 (Eq. 3.9). (d) Plot of Ω_2 for two high and low magnetic field biases, and resulting linear fit to extrapolate the final shift and uncertainty.

3.5 Molecule production and detection

It should be noted that in order to detect a positive signal for molecule formation, our sequence utilizes a final step of molecule fragmentation back to atoms, since we have decided that this process is favorable over the difficult process of direct molecule imaging [Wang *et al.*, 2010], currently developed for polar molecules.

We model the ground state molecule density using an expression similar to that of standard density-squared interaction dynamics,

$$\frac{d}{dt} \frac{n_m}{n_0} = \frac{b}{(1 + at)^2} - c \frac{n_m}{n_0} = bf_a^2 - cf_m \quad (3.30)$$

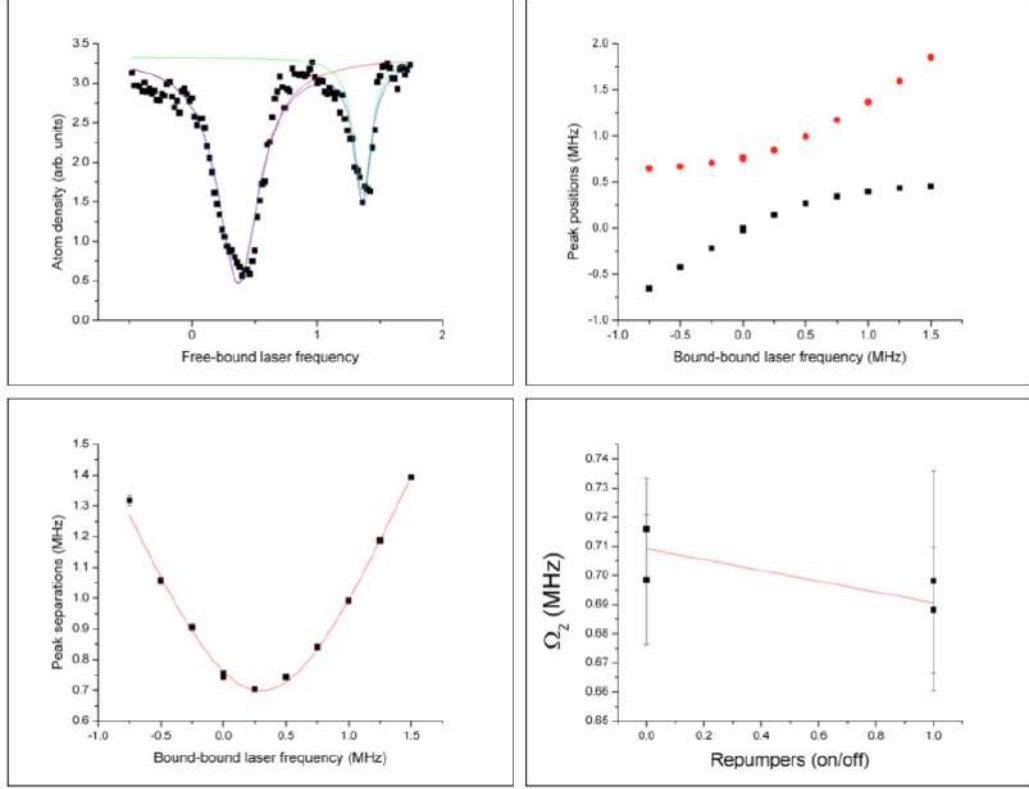


Figure 3.21: (a) A representative 2PA trace for a fixed L_{BB} detuning of 0 MHz. (b) Autler-Townes avoided crossing aggregate of 2PA traces, with dots marking the two peak positions. (c) Hyperbola of peak positions differences, with fit to extract Ω_2 (Eq. 3.9). (d) Plot of Ω_2 for two high and low trap densities, achieved by the presence and absence of repumper lasers, which results in a density difference factor of two. The resulting linear fit is used to extrapolate the final shift and uncertainty.

where n_0 is the initial atom density, $f_a = n/n_0$ and $f_m = n_m/n_0$ are the fractional atom and molecule densities, respectively, and the constants a , b and c are expressions derived from the usual density-squared interaction with a linear loss term. The fractional atom density $n(t)/n_0 = f_a(t) = 1/(1+at)^2$. In this case $a = 2Kn_0$, $b = \alpha f_{vv'}Kn_0$, and c must be experimentally determined using atom-molecule and molecule-molecule collision dynamics. If we assume a relatively small molecule number relative to the atom reservoir in which they are produced, then it is safe to assume atom-molecule collisions dominate. In this case the molecule loss rate can be estimated as $c \simeq 2hn_0R_6/\mu \sim 200/\text{s}$ for trap densities

$n_0 \sim 10^{12}/\text{cm}^3$. This $\sim 5\text{ms}$ lifetime limits the time frame for the photoassociation step, since once PA has been performed for long enough, a resonant $^1S_0 - ^1P_1$ 461 nm blue pulse can be used to clear away the atom source, leaving only whatever molecules have been created. For the $(-2, -5')$ pair, the initial PA rate is $a \sim 1680/\text{s}$ and ground-state molecule production rate is $b \sim 220/\text{s}$.

Plotting this expression in Fig. 3.22, we find an optimal PA time beyond which molecule formation drops and molecule loss begins to dominate the overall signal.

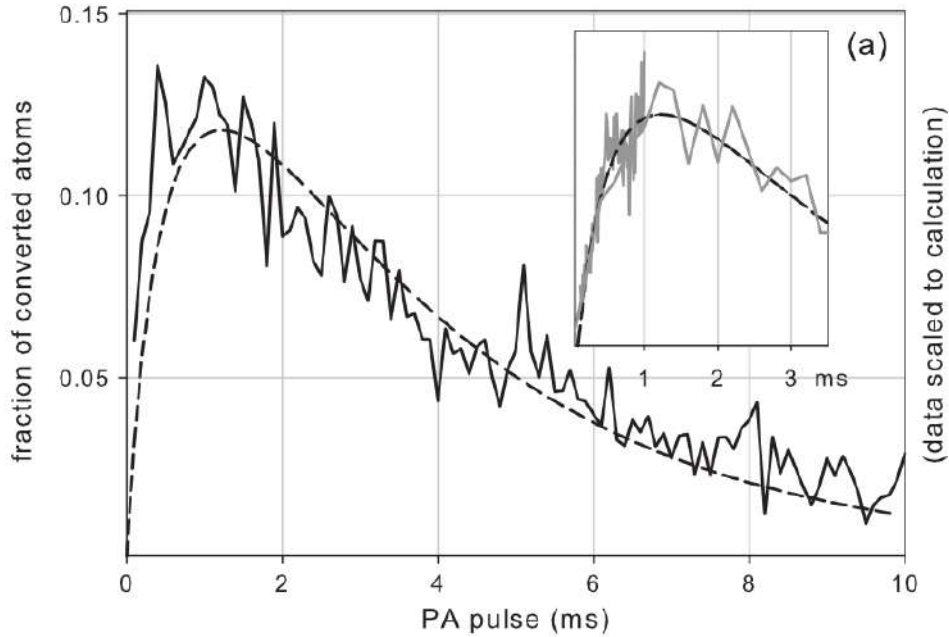


Figure 3.22: Molecule formation vs. PA time. The optimal PA time is ~ 1 ms, beyond which the molecule loss rate exceeds the formation rate.

Atoms can then be recovered by use of another spectroscopy laser tuned from the bound state to a weakly-bound excited state, from which a large portion of the molecules will spontaneously decay to free atoms, which can then be imaged. Figure 3.23 describes this full process, and Fig. 3.24 lays out the sequence timing, with a pictorial analog in Fig. 3.25.

We first presented these results in [Reinaudi *et al.*, 2012b], and at the time we modeled the molecule loss using a simple linear term, but later attributed the short molecule lifetime to atom-molecule collisions, because the molecule density is still too low to account for the

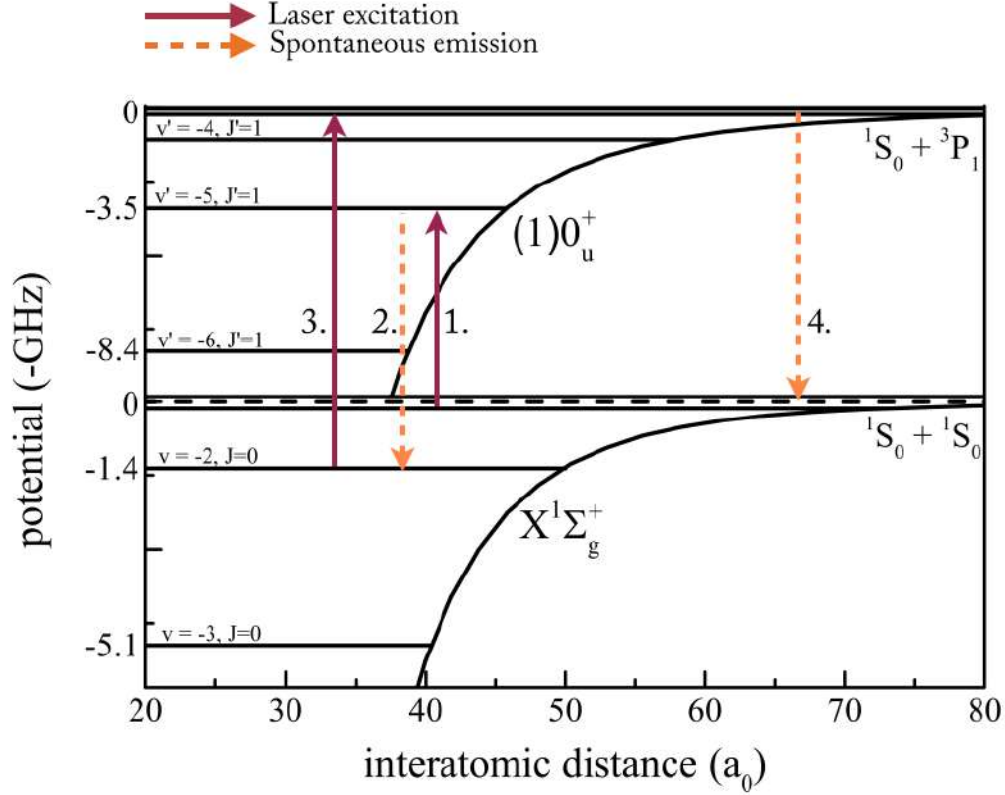


Figure 3.23: Diagram of the molecule creation and atom recovery sequence.

loss rate, and the lifetime appeared to increase significantly after using the resonant blue laser pulse to wipe away the background atom bath. If this is the dominant molecule loss term, then the differential equation should reflect that. Modifying the form of the loss term,

$$\frac{df_m}{dt} = f_a^2 - cf_m f_a, \quad (3.31)$$

but we found that in order to reproduce the result that matched the data, we had to inflate the coefficient by a factor of 5, to $c \approx 1000/\text{s}$.

Another proposed molecule loss mechanism is that the free-bound laser is off-resonantly driving a bound-bound transition, from the final ($v = -2, J = 0$) to some other electronically excited state. Although not intentionally near resonance with any transitions, the intensity I_{FB} is high for bound-bound processes. Therefore we introduced an addi-

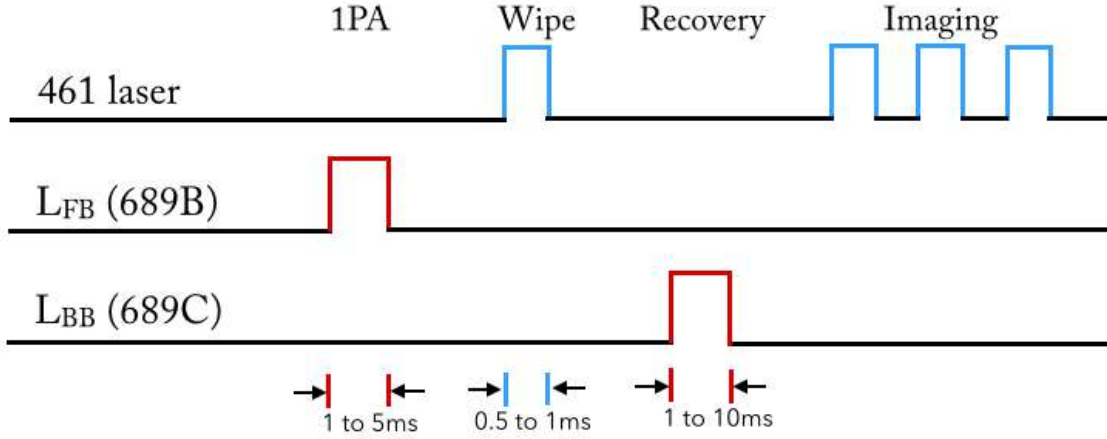


Figure 3.24: Typical atom recovery sequence.

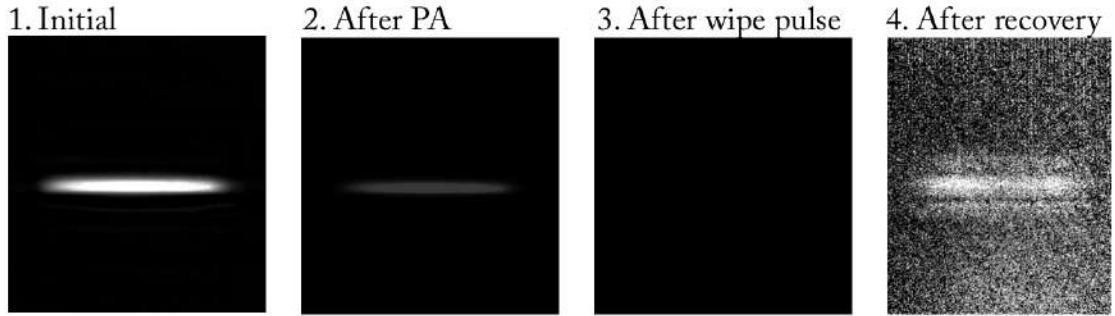


Figure 3.25: Images of the lattice-trapped atoms at various stages in the recovery sequence. The wipe pulse serves to remove all un-photoassociated atoms. Imaging at this time will show nothing, because the molecules present are insensitive to the 461 nm imaging beam. The camera sensitivity has been adjusted to show the dim recovery signal.

tional term to our equation, to account for laser-induced molecule losses, while keeping the $c \simeq 200/\text{s}$ value for the atom-molecule loss rate:

$$\frac{df_m}{dt} = bf_a^2 - cf_a - df_m f_a. \quad (3.32)$$

With both of these terms we are able to model the observed loss curve from above, with the laser-induced loss coefficient d a phenomenologically-chosen parameter. This is no proof of the mechanism, but as will be explained in later chapters, the free-bound laser can indeed

be used together with an additional bound-bound laser to drive coherently between bound states.

Chapter 4

Binding energies and QED

At the end of Ch. 3 we showed a positive detection of molecules formed in the $v = -2$ vibrational state of the ground electronic state. Detection was achieved by atomic fragmentation & recovery by transfer to the weakly bound $v' = -1$ vibrational state of the electronic excited state. This state then largely spontaneously dissociates to free atoms which are then imaged in the usual way. If we perform this recovery process, iteratively sweeping the recovery laser frequency, we find a Lorentzian peak as shown in Fig. 4.1. The next logical question to ask is: can we recover molecules by way of the next-deeper $v' = -2$ excited state?

We do find a recovery peak at an expected detuning of ~ -24 MHz for the $v' = -2$ state, as shown in Fig. 4.2. We also tested recovery off of the atomic dissociation line at 0 kHz. Instead of the usual Lorentzian peak we found that recovery could be performed for large blue detunings beyond the dissociation limit, resulting in a recovery “shelf” as seen in Fig. 4.3, where excess laser energy must be transferred to atom kinetic energy.

This hypothesis is confirmed by the following observation. If a sufficient delay is inserted after the recovery pulse but before imaging, atoms are ejected from the trap as seen in Fig. 4.4. What appears to be two lattice trap-shaped ejections, one below and one above, is actually the projection onto the camera axis of a cylindrically-symmetrical ring-shaped ejection, although this has not been confirmed with a second camera. Fitting the ring distance versus the laser detuning follows a square root velocity dependence expected from such a kinematic process.

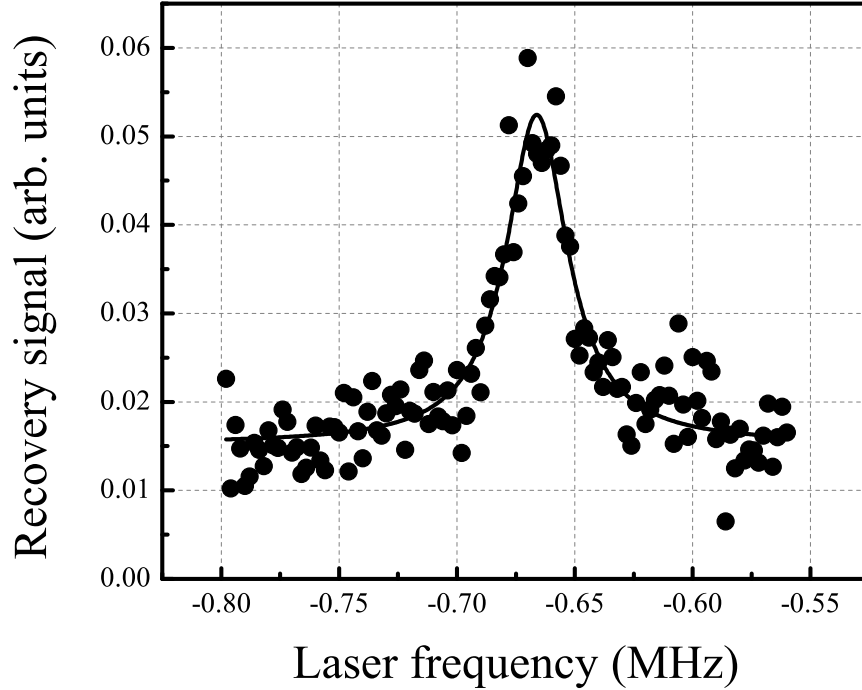


Figure 4.1: Representative trace of the least-bound excited state, at ~ -450 kHz binding energy.

Additionally, for larger laser detunings above the shelf, or for longer wait times, a second ejection ring appears, as shown in Fig. 4.5. This suggests that the first, more energetic ring may actually belong to another dissociation shelf at some farther red-detuning. Using the square root fit of Fig. 4.6, we extrapolate a zero-detuning frequency at ~ 150 MHz below the nearby shelf. This is consistent with the prediction that the ground state $J = 2$ rotational levels are ~ 150 MHz above the $J = 0$ states [private correspondence with S. Kotochigova].

Detuning our recovery laser frequency by ~ 150 MHz we find an analogous dissociation shelf as expected, as well as $v' = -1$ and -2 bound states. These states should only differ by the properties of the ground states $J = 0$ and 2 , but closer inspection of the individual peaks reveals otherwise. Application of a small ~ 1 G magnetic field splits the alleged $v' = -1$ peak into six separate peaks. The explanation for this is that five of these peaks belong to a weakly bound ($v' = -2, J' = 3$), and one to the expected ($v' = -1, J' = 1$) state

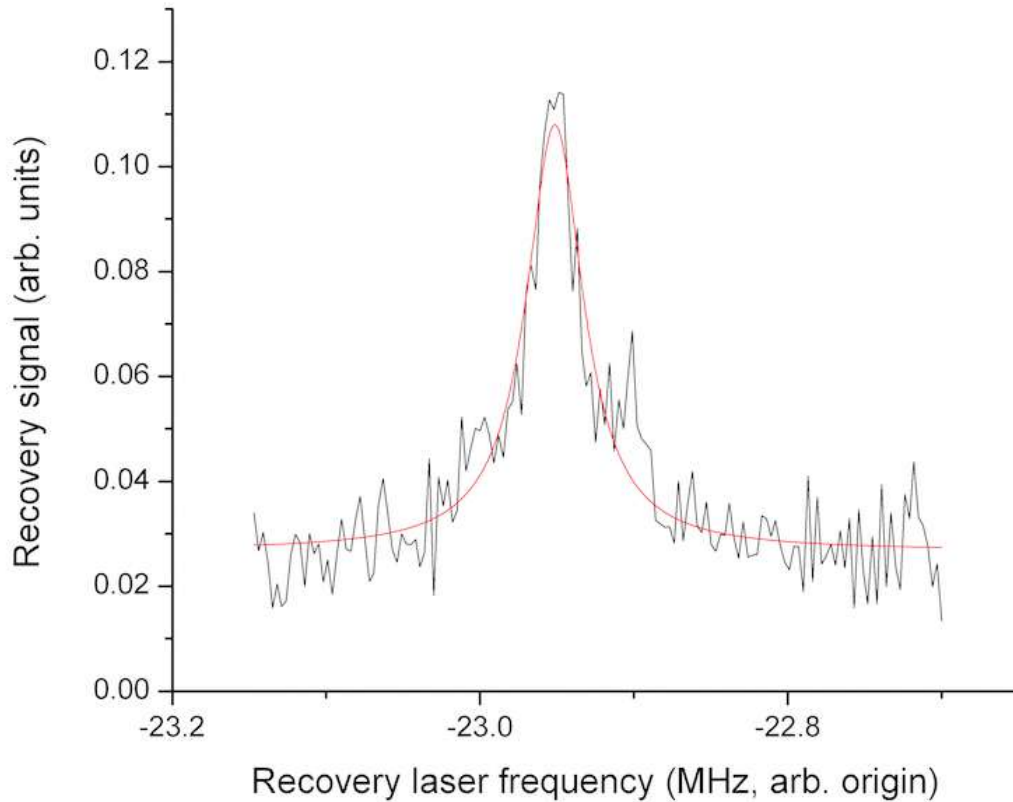


Figure 4.2: Representative trace of the second bound state, at ~ 24 MHz.

(for an explanation of the number of peaks, see Fig. 4.8). The location of this $J' = 3$ state will be discussed at the end of this chapter. It and the other states' magnetic susceptibility are topics of the next chapter, and will not be discussed further here.

Figure 4.9 gives an inventory of the recovery peaks discovered so far. The $v' = -1$ and -2 are fit using a standard Lorentzian, but to fit the dissociation shelf more thought is required.

Atomic fragmentation can be modeled as the reverse process of photoassociation. Whereas in the previous case the underlying Lorentzian lineshape must be convoluted over the initial thermal distribution, in this case the initial state has no Boltzmann distribution, and the convolving integration is over the final thermal state determined by excess thermal energy. Dropping the Boltzmann factor from Eq. 5 in [Zelevinsky *et al.*, 2006] and integrating over

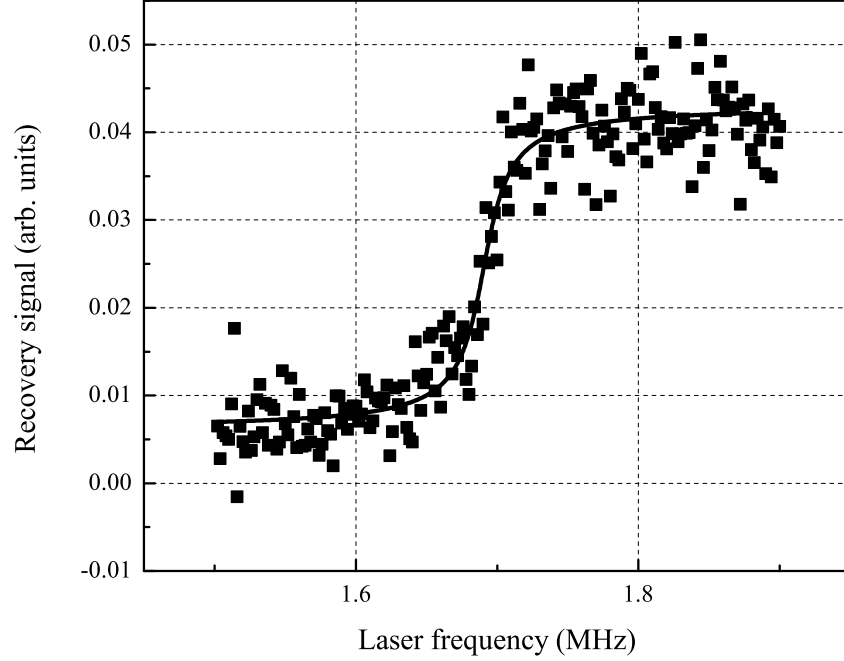


Figure 4.3: Representative trace of the atomic recovery shelf. The fit function can give a frequency uncertainty ~ 3 kHz, which is small enough that this shelf can thus be used as an anchor for measuring absolute binding energies.

positive energy,

$$W(\nu) \propto \int_0^{\infty} L(\nu, \epsilon) d\epsilon \propto \frac{1}{2\epsilon} \arctan(2\delta/\gamma) \quad (4.1)$$

for the Lorentzian

$$L(\nu, \epsilon) \propto \frac{1}{(\nu - \nu_0 - \epsilon/h)^2 + (\gamma/2)^2}, \quad (4.2)$$

and using the standard arctan result of an integral over a Lorentzian. This model is therefore implemented with the fitting function

$$W(\nu, \nu_0, \gamma, A, y_0) = y_0 + A \left(\frac{1}{2} + \frac{1}{\pi} \arctan \left[\frac{2(\nu - \nu_0)}{\gamma} \right] \right) \quad (4.3)$$

with an overall offset y_0 , a frequency offset ν_0 , shelf height A , and shelf steepness parameter γ .

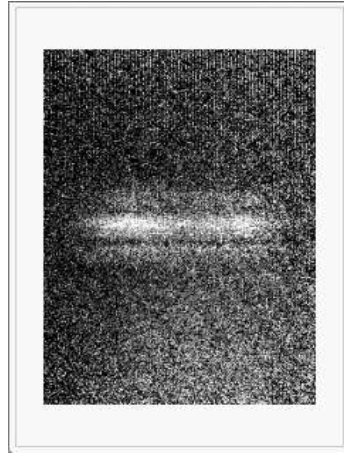


Figure 4.4: Image of an ejected ring of atoms around the central lattice trap. (The cylindrical symmetry has not been confirmed with a separate viewing angle, but the ejection velocity matches the excess photon energy, and there is no reason to believe there is cylindrical anisotropy.)

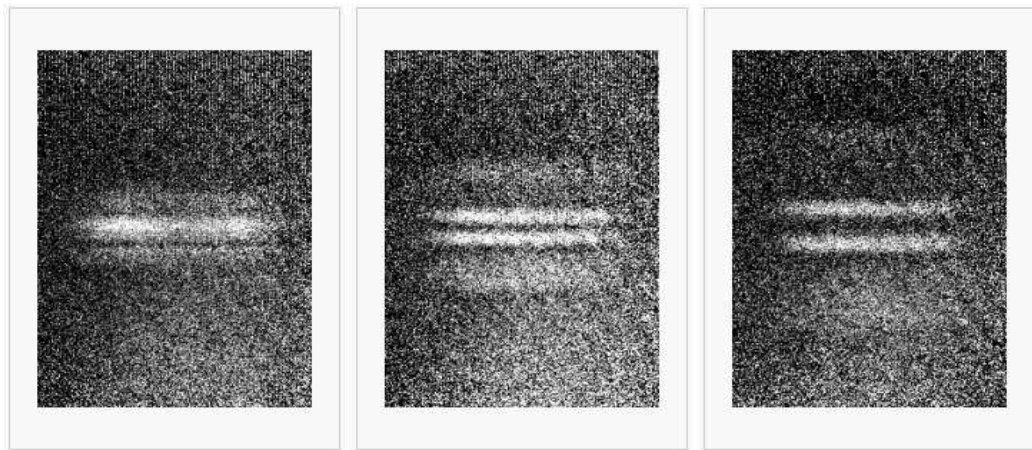


Figure 4.5: Successive images of the ejection ring for increasing post-PA delay time. Note that the PA time is fixed in each of these panels. A similar effect could be achieved if both the PA and delay time are fixed, but the laser frequency increased, increasing the excess energy delivered.

Using the fit function from Eq. 4.3, the dissociation line can be found to within 3 kHz. Naturally one could then use this shelf as an anchor for measuring the absolute binding energies of the other discovered peaks. From the broad spectrum from Fig. 4.9, we have

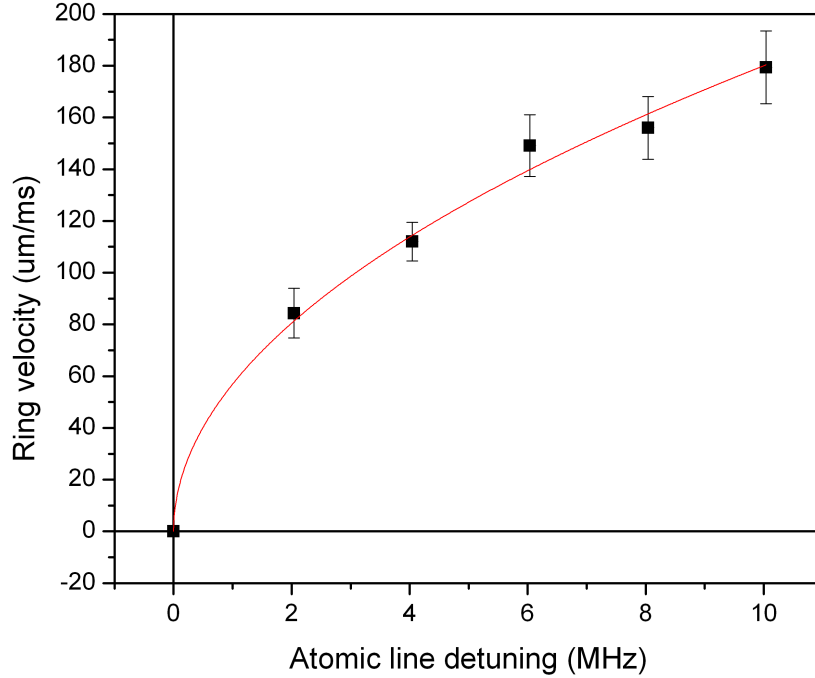


Figure 4.6: Ring separation as a function of recovery laser detuning. The square root dependence is evidence that this is indeed an effect of the excess photon energy.

five different peaks that correspond to three different excited bound states and two different rotational ground states. Of these states we can reliably measure:

- The $v' = -1$ binding energy using peak 1 and shelf 1. In principle peak 3 should give the same result, but it is unusable for this measurement because it is largely obscured by peak 4.
- The $v' = -2$ binding energy using peak 2 and shelf 1, or peak 5 and shelf 2.
- The $(v' = -2, J' = 3)$ binding energy using peak 4 and shelf 1.
- The binding energy difference between the ground states $J = 0$ and $J = 2$ using peaks 2 and 5.

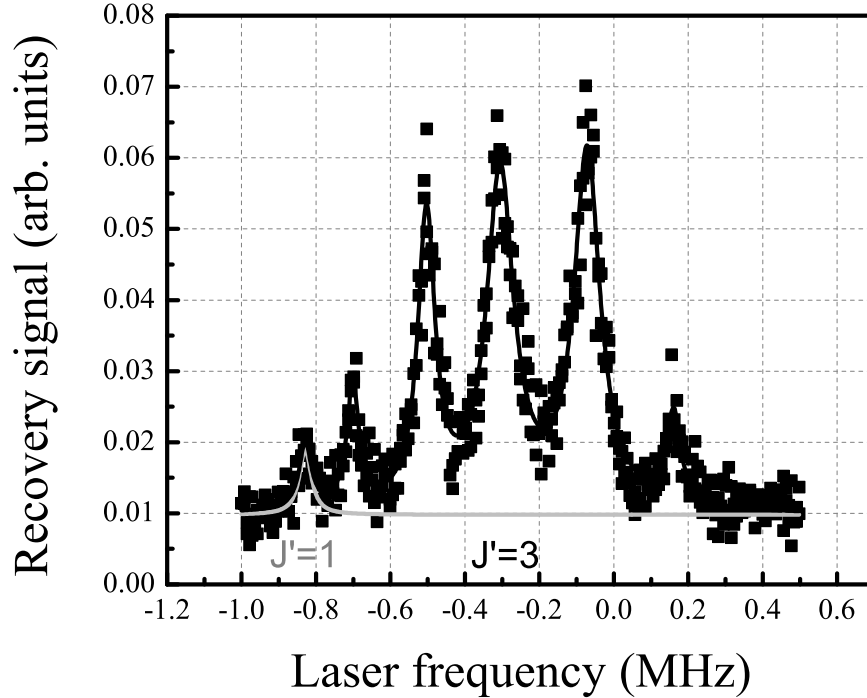


Figure 4.7: Trace of the overlapping $(v', J') = (-1, 1)$ and $(-2, 3)$ states. Selection rules and the multiplicity of the ground and excited states dictate the number of peaks observed.

4.1 Binding energies and systematic effects

As with the 2PA data, the reported values for binding energies are extrapolated from measurements of systematic shifts for a set of four experimental parameters:

1. Recovery laser power
2. Lattice laser power
3. Magnetic shifts
4. Atom/molecule trap density

Systematics were not performed for the free-bound PA laser because it is switched off by the time recovery takes place. We will now discuss the effects of each of these sources of uncertainty on the relevant binding energies, one by one.

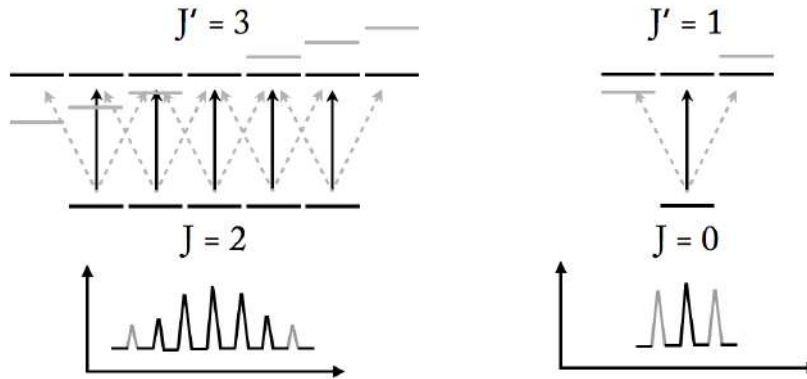


Figure 4.8: Selection rules and the multiplicity of the ground and excited states dictate the number of peaks observed. For π transitions (black), the number of peaks is determined by the minimum multiplicity of the ground and excited states. For σ transitions (dashed gray), the number of peaks observed is given by the minimum multiplicity plus two, or the maximum multiplicity, whichever is smaller. On occasion we found weak σ transitions leaking through due to imperfect probe laser polarization.

4.1.1 0_u^+ ($v' = -1, J' = 1$) binding energy

As mentioned above, we do not have the $J = 2$ ground state available for this measurement because it is obscured by an overlapping ($v' = -2, J' = 3$). Therefore this measurement can be made most directly by measuring the frequency difference between the f'_0 shelf and $v' = -1$ accessed from the $J = 0$ ground state. Additionally, the less direct method of measuring the f'_0 to $v' = -2$ and then to $v' = -1$ can be used. We use the direct method.

Our approach for measurement is to consider the shift and uncertainty contributions for each of the light shifts and the density shift, and then add these to a final value obtained by an extrapolation of the binding energy to zero magnetic field.

4.1.1.1 Magnetic shifts

We determined that the dominant source of uncertainty for the binding energy of this peak is the magnetic field-induced shift. This state's binding energy is inferred from the zero magnetic field value for the central of three peaks. Although this central peak does

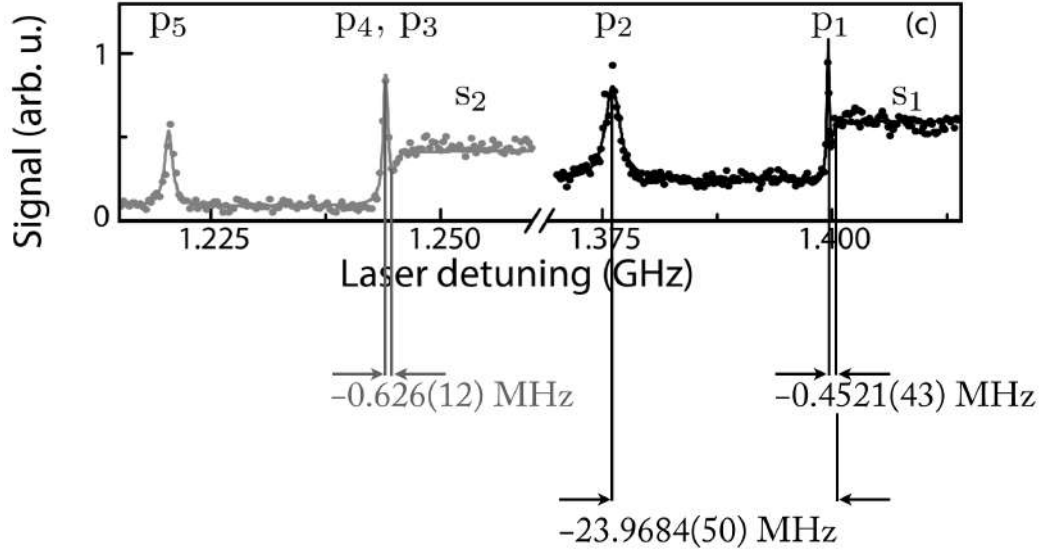


Figure 4.9: Broad spectrum of all of the observed recovery peaks and shelves. The space between the $J = 2$ and $J = 0$ sets has been omitted, and the frequency zero-point is arbitrary. The three sets of arrows summarize the binding energy measurements that are the results of this chapter.

not appear to have linear order Zeeman shifts, it does appear to undergo quadratic and possibly higher-order shifts.

Data was taken for various applied magnetic field values within the range of ± 1 G, and is plotted in Figs. 4.10 and 4.11. The field was applied using a circuit switch on the vertical pair of compensation coils. Therefore the applied field direction is parallel (perpendicular) to the probe (lattice) laser polarization, and therefore only accesses π transitions.

The results of this measurement are plotted in Fig 4.10. For each peak a simple quadratic line fit was used to find the zero point. Extrapolating to this point for the central peak, we get $\Delta = (-0.4452 \pm 0.0030)$ MHz. For this measurement, 165 mW of lattice laser power and $20 \mu\text{W}$ of recovery laser power. Incorporating a 5% uncertainty on these powers, and including the corresponding light shifts from these two lasers as determined in the other sections, the final result for the binding energy of the 0_u^+ ($v' = -1, J' = 1$) state is

$$\Delta_{0_u^+(v'=-1, J'=1)} = -0.4521(43) \text{ MHz.} \quad (4.4)$$

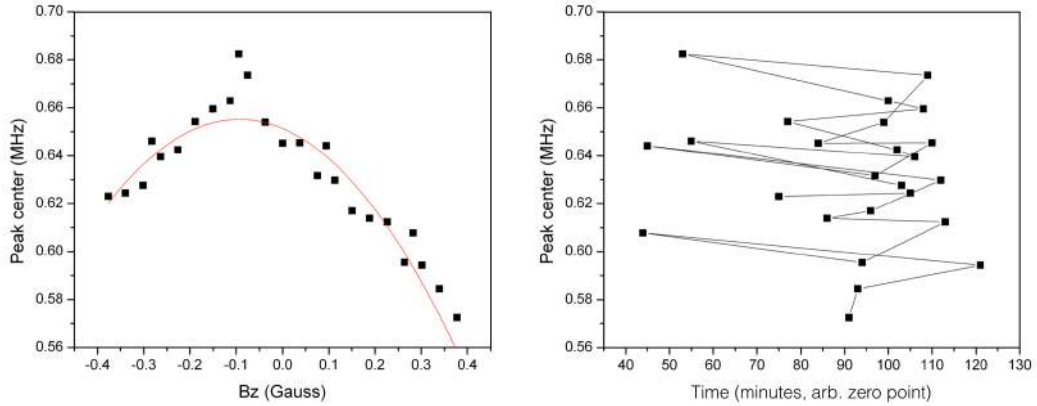


Figure 4.10: Plot of ($v' = -1, J' = 1$) peak positions for various magnetic fields (left). On the right is the same data, but lotted versus time, with black lines connecting successive data points, taken to check for any experimental drift dependence. There appears to be negligible drift.

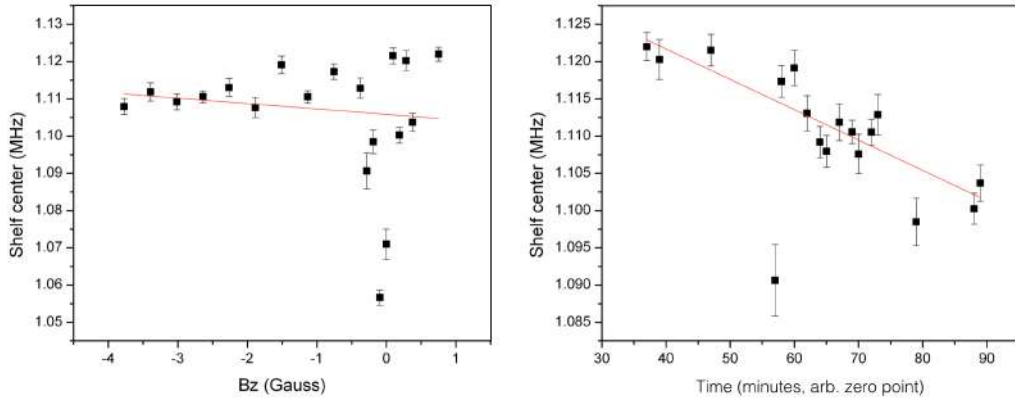


Figure 4.11: On the left, a plot of the $J' = 1$ shelf position for varying magnetic field. The dip at 0 G is explained by the breakdown of the recovery lineshape when there is no magnetically-defined quantum axis. As expected there does not appear to be strong dependence, and so on the right, the background laser frequency drift in time is observable.

4.1.1.2 Recovery laser light shift

The probe laser light shift of this state was difficult to pin down. Two initial attempts resulted in nearly opposite final values. It was determined that whatever shift may exist was being obscured by the experimental laser frequency drift mentioned earlier, which can

be as large as ~ 2 kHz/min and whose sign and value changes often. Therefore the light shift of this state was linearly inferred from a repeated “binary” measurement: one at high probe power, and one at low power, repeated many times.

The raw data, as found in Fig. 4.12 (a), suggests there may be a small shift, but that the spread of measured values at either high or low power dominates the uncertainty. We time-stamped each measurement, and Fig. 4.12 (b) shows a plot versus time instead, where the drift of the laser frequency is clear. This drift was fit to a line whose slope was assumed to represent a constant drift in time that could then be removed from the original data. Figure 4.12 (c) shows the original set with this correction. Our binary measurements force us to assume a linear shift dependence, and fitting to a line we get our final result.

Our result for the recovery laser light shift of the dissociation shelf is (-0.129 ± 0.077) kHz/ μ W, and for the bound state is (-0.061 ± 0.021) kHz/ μ W.

4.1.1.3 Lattice laser light shift

The lattice laser light shift of this state is significantly larger than that of the probe laser shift, making the shift dependence easier to measure against background laser frequency drift. Data was taken for lattice laser power in the range of 100 – 400 mW and is plotted in Fig. 4.14. To account for any possible frequency drift however, the measurements were taken in an interlaced fashion, where the lines between data points portray their chronology. It is immediately apparent that the lattice shift is larger than the background drift.

Our result for the lattice light shift of the dissociation shelf is $(+0.0812 \pm 0.0138)$ kHz/mW, and for the bound state is $(+0.1148 \pm 0.0131)$ kHz/mW.

4.1.1.4 Density shifts

There were no observed density shifts for this state. For a more detailed explanation of our method for measuring possible density shifts, see Sec. 4.1.2.

4.1.2 0_u^+ ($v' = -2, J' = 1$) binding energy

For the 0_u^+ ($v' = -2, J' = 1$) it appears as if both the $J = 0$ and $J = 2$ ground states are available for measurement, however details of the behavior of the dissociation shelf from the

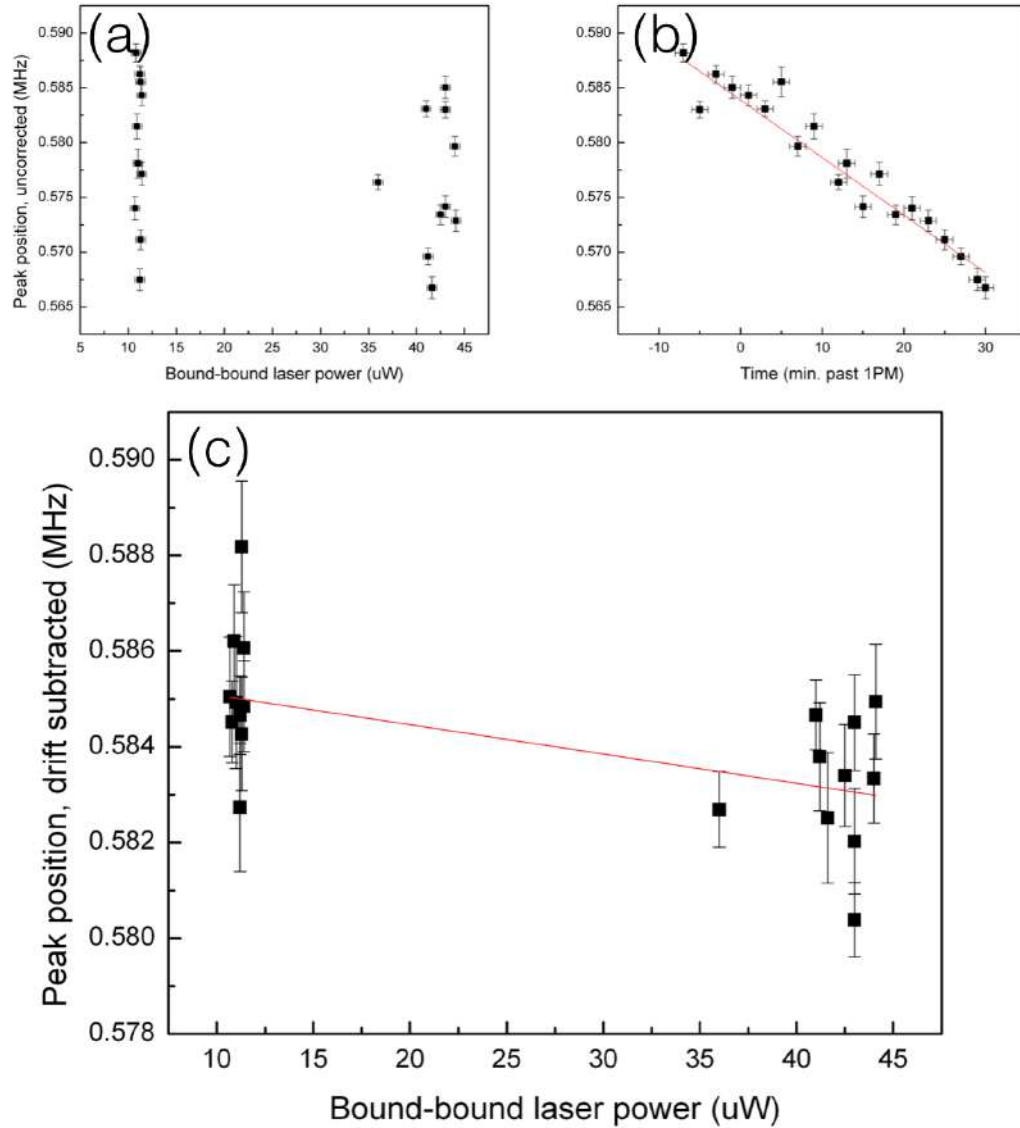


Figure 4.12: Recovery ($v' = -1, J' = 1$) peak position vs. (a) recovery laser frequency and (b) vs. the time when data was taken. (c) This linear drift was removed, and the final shift dependence was determined from the corrected fit.

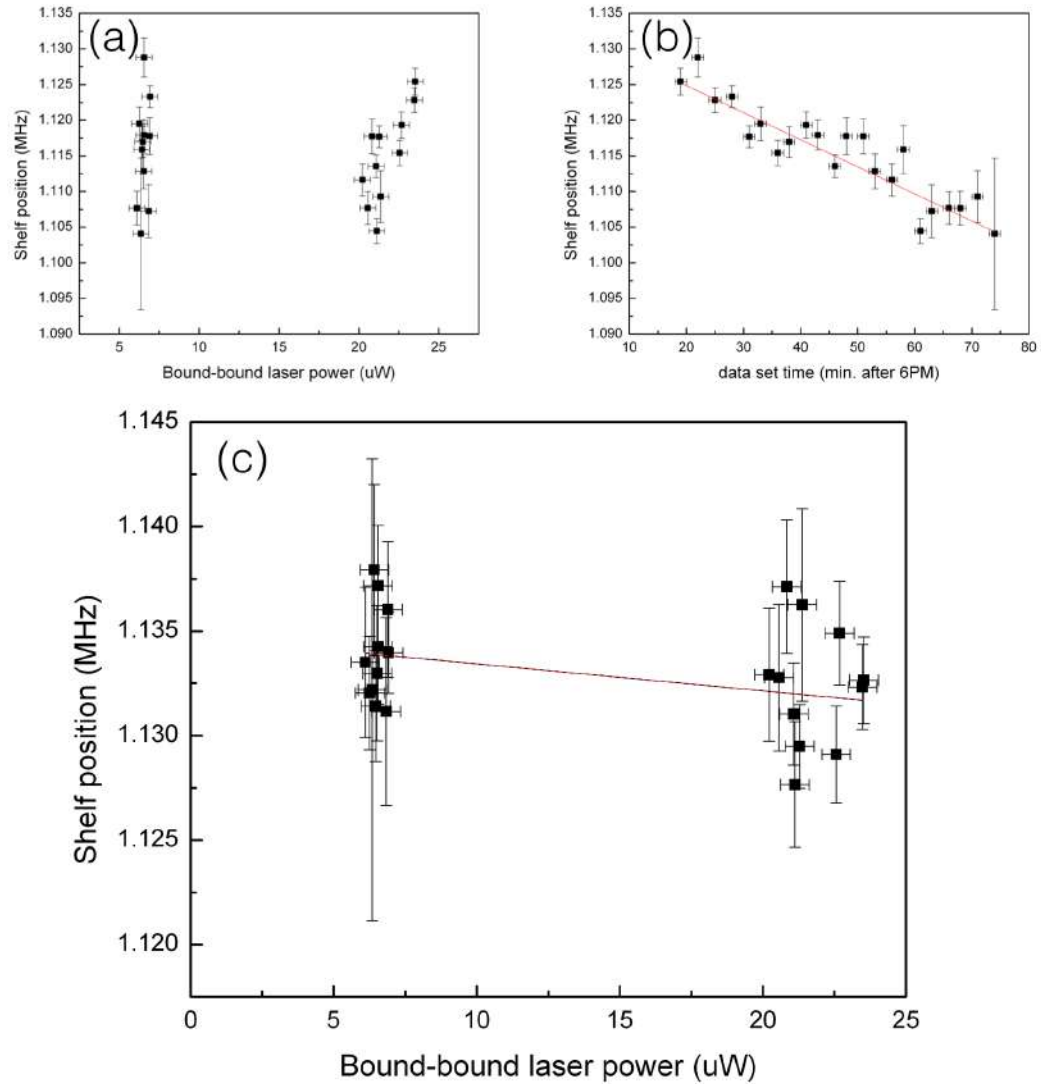


Figure 4.13: Recovery $J' = 1$ shelf position vs. (a) recovery laser frequency, and (b) vs. the time when data was taken. (c) This linear drift was removed, and the final shift dependence was determined from the corrected fit.

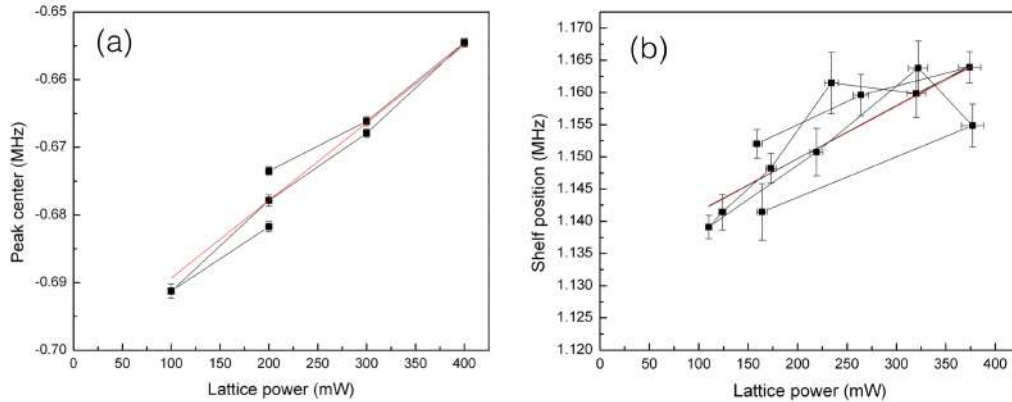


Figure 4.14: Lattice shifts of the (a) $(-1, 1)$ peak and (b) $J' = 1$ dissociation shelf, where the laser frequency drift has been treated as negligible.

$J = 2$ state make the latter unfeasible. More specifically, if our recovery laser is π -polarized, then from Fig. 4.8 we can see that recovery from the $J = 0$ ground state can occur only to the $m' = 0$ sublevel. From the $J = 2$ ground state, however, recovery can occur through all three sublevels $m' = 0, \pm 1$. Because of this, and because of the fact that the dissociation shelf is not a narrow function like a Lorentzian, the $m' = \pm 1$ shelves obscure the zero-point of the $m' = 0$ shelf. Therefore we can only measure this binding energy using the $J = 0$ ground state.

As with the previous state, the magnetic field-induced shifts are the dominant source of uncertainty. We therefore tally the shifts and uncertainties due to the other contributions, and then add these to the final value obtained by an extrapolation of the binding energy to zero magnetic field.

4.1.2.1 Magnetic shifts

This state's binding energy is inferred from the zero magnetic field value for the central of three peaks. Although this central peak does not suffer from linear order Zeeman shifts, it does appear to undergo quadratic and possibly higher-order shifts.

Data was taken for various applied magnetic field values within the range of ± 1 G, and is plotted in Figures 4.15 (a) and (b). The field was applied using a circuit switch on the vertical pair of compensation coils. Therefore the applied field direction is paral-

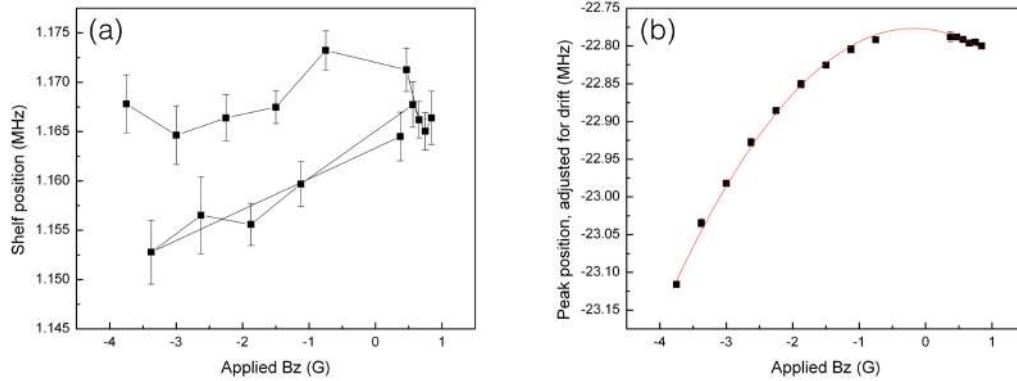


Figure 4.15: (a) The shift in the $J' = 1$ atomic shelf is more suggestive of laser frequency drift than of magnetic field dependence. We do not expect there to be any linear or quadratic dependence of this shelf on the magnetic field, and because the drift is negligible compared to the shifts of the $v' = -2$ state of this section, it is not corrected out of this trace. (b) Plot of $(v' = -2, J' = 1)$ peak position for various magnetic fields. Any laser frequency drift is negligible compared to this shift.

l (perpendicular) to the probe (lattice) laser polarization, and therefore only accesses π transitions.

For each peak a simple quadratic line fit was used to find the zero point. Extrapolating to this point for the central peak, we get $\Delta = (-23.9563 \pm 0.0020)$ MHz. For this measurement, 160 mW of lattice laser power and $6.6 \mu\text{W}$ of recovery laser power. Incorporating a 5% uncertainty on these powers, and including the corresponding light shifts from these two lasers, the final result for the binding energy of the 0_u^+ ($v' = -1, J' = 1$) state is

$$\Delta_{0_u^+ (v'=-2, J'=1)} = -23.9684(50) \text{ MHz}. \quad (4.5)$$

4.1.2.2 Recovery laser light shift

As with the previous state, the probe laser light shift of this state was difficult to pin down. Two initial attempts resulted in nearly opposite final values. It was determined that whatever shift may exist was being obscured by the experimental laser frequency drift mentioned earlier, which can be as large as ~ 2 kHz/min and whose sign and value changes

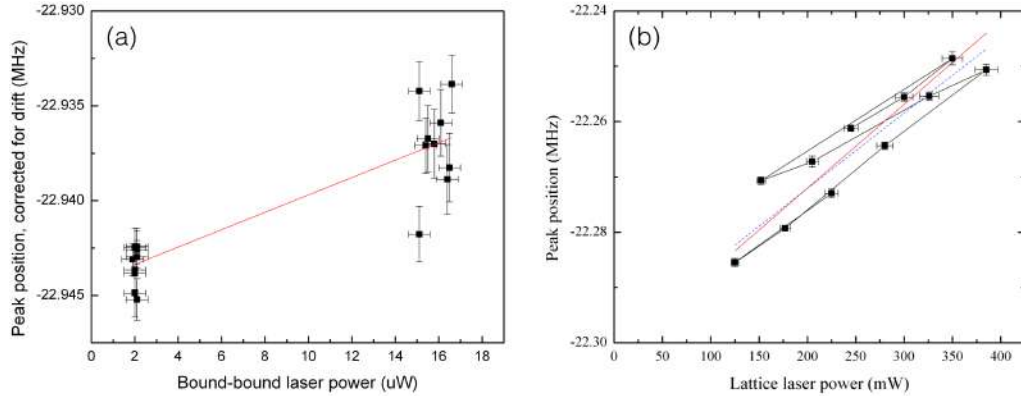


Figure 4.16: (a) Plot of ($v' = -2, J' = 1$) peak position vs. recovery laser power, after correcting for the laser frequency drift as in Sec. 4.1.1. (b) Plot of ($v' = -2, J' = 1$) peak position vs. lattice laser power. The lines connect points that were taken successively; the near-overlap of these lines indicates that there is little frequency drift relative to the lattice laser shift.

often. Therefore the light shift measurement was performed using a repeated “binary” measurement: one at high probe power, and one at low power, repeated many times.

The data showed a measurable shift comparable in magnitude to the background drift. Still, the spread of measured values at either high or low power contributes significantly to the uncertainty. Figure 4.16 (a) shows the data after removing suspected residual cavity drift, performed in the same way as in Sec. 4.1.1. The result for the recovery laser light shift of the dissociation shelf is (-0.129 ± 0.077) kHz/ μ W, and for the bound state is (-0.458 ± 0.059) kHz/ μ W.

4.1.2.3 Lattice laser light shift

Once again, the lattice laser light shift of this state is significantly larger than that of the probe laser shift, making the shift dependence easier to measure against background drift. Data was taken for lattice laser power in the range of 100 – 400 mW and is plotted in Fig. 4.16 (b). As with the previous state, to account for any possible frequency drift, the measurements were taken in an interlaced fashion, where the lines between data points delineate their chronology. It is apparent that the lattice shift is larger than the background

drift. The data set used for the dissociation shelf is the same as was used for the previous peak.

Our result for the lattice light shift of the dissociation shelf is $(+0.0812 \pm 0.0138)$ kHz/mW, and for the bound state is $(+0.1364 \pm 0.0196)$ kHz/mW.

4.1.2.4 Density shifts

There were no observed density-dependent shifts for this transition. We measured the line position with and without repumper lasers, which approximately halves the density, from $\sim 10^{12} \text{ cm}^{-3}$ to $\sim 5 \cdot 10^{11} \text{ cm}^{-3}$. In an attempt to find an observable shift within the system noise, especially the background laser frequency drift, we took successive traces with and without repumpers, as plotted in Fig. 4.17.

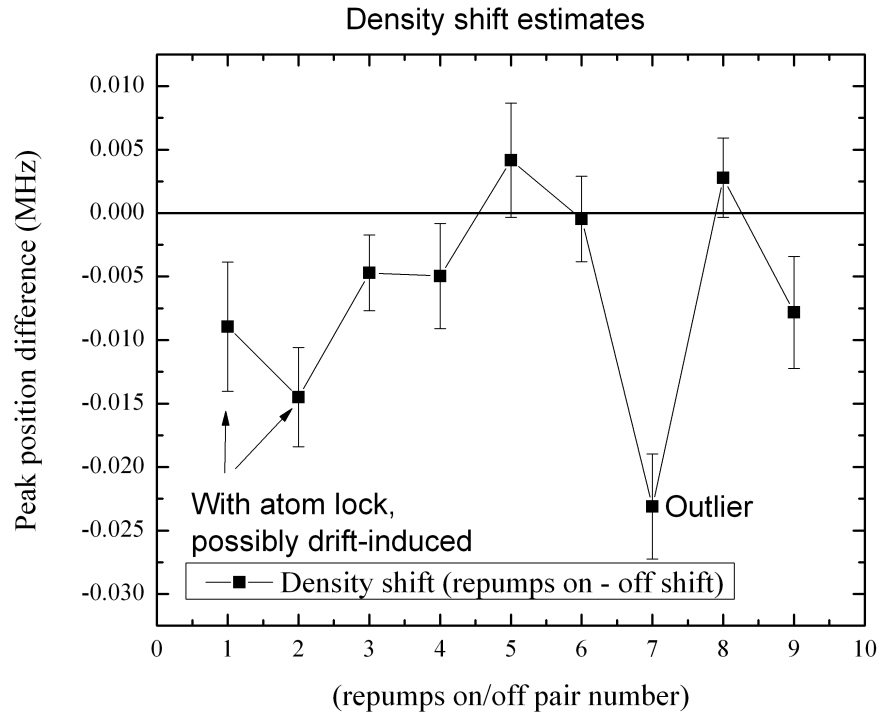


Figure 4.17: Plot of $(v' = -2, J' = 1)$ peak position vs. successive repumpers on/off measurement pairs.

Each data point is a measure of the difference in peak position for repumpers on and

off. The first two data points were taken with the 689 nm atomic heat pipe lock engaged, but this lock has been unreliable, and could have possibly induced oscillations or overall drift. With the exception of the one additional outlier, there is very little evidence for a density-induced shift, We found such absence of dependence for the other measured states, and so as a result we have chosen to neglect density shifts in our calculations of the binding energies.

4.1.3 0_u^+ ($v' = -2, J' = 3$) binding energy

For the 0_u^+ ($v' = -2, J' = 3$) state there are complications in measuring the binding energy from the nearby dissociation shelf. As a result, its binding energy is measured relative to the adjacent 0_u^+ ($v' = -2, J' = 1$), whose binding energy was determined above. In other words, we chain this state's binding energy to the binding energy of another. This results in an a larger overall uncertainty, but still provides the best result available for this state.

Once again we tally the shift and uncertainty contributions for each of the light shifts and the density shift, and then add these to a final value obtained by an extrapolation of the binding energy to zero magnetic field.

4.1.3.1 Magnetic shifts

As with the other states, the dominant source of uncertainty for the binding energy of this state is the magnetic field-induced shift. The binding energy is inferred from the zero magnetic field value for the central of its seven peaks, only five of which are observed due to probe laser polarization. Although this central peak does not suffer from linear order Zeeman shifts, it does appear to undergo quadratic and possibly higher-order shifts.

Data was taken for various applied magnetic field values within the range of ± 1 G, and is plotted in Fig. 4.18. The field was applied using a circuit switch on the vertical pair of compensation coils. Therefore the applied field direction is parallel (perpendicular) to the probe (lattice) laser polarization, and therefore only accesses π transitions.

Extrapolating to zero magnetic field, we get $\Delta = (-23.9563 \pm 0.0020)$ MHz. For this measurement, 160 mW of lattice laser power and $6.6 \mu\text{W}$ of recovery laser power. Incorporating a 5% uncertainty on these powers, and including the corresponding light shifts from

these two lasers, the final result for the binding energy of the 0_u^+ ($v' = -1, J' = 1$) state is

$$\Delta_{0_u^+(v'=-2, J'=3)} = -0.626(12) \text{ MHz.} \quad (4.6)$$

4.1.3.2 Recovery laser light shifts

Unlike the measurements of the previous states, the probe laser light shift of this state was discernible from the background frequency drift in our original measurements. The data was taken over probe laser powers in the range of $10 - 100 \mu\text{W}$ in an interlaced fashion, where the lines connecting the dots delineate the chronology.

This data is plotted in Fig. 4.19, and is strongly linear in laser power, with little apparent drift in time, so no correction was made for drift. The result for the recovery laser light shift of the dissociation shelf is $(-0.129 \pm 0.077) \text{ kHz}/\mu\text{W}$, and for the bound state is $(-0.458 \pm 0.059) \text{ kHz}/\mu\text{W}$.

4.1.3.3 Lattice laser light shifts

Once again, the lattice laser light shift of this state is significantly larger than that of the probe laser shift, making the shift dependence easier to measure against background drift. Data was taken for lattice laser power in the range of $100 - 400 \text{ mW}$, and is plotted in Fig. 4.20. As with the previous state, to account for any possible frequency drift, the measurements were taken in an interlaced fashion, where the lines between data points delineate their chronology. It is apparent that the lattice shift is larger than the background drift. The data set used for the dissociation shelf is the same as was used for the previous peak.

Our result for the lattice light shift of the dissociation shelf is $(+0.0812 \pm 0.0138) \text{ kHz}/\text{mW}$, and for the bound state is $(+0.1148 \pm 0.0131) \text{ kHz}/\text{mW}$.

4.1.3.4 Density shifts

There were no observed density shifts for this state. For a more detailed explanation, see the density shifts portion of Sec. 4.1.2.

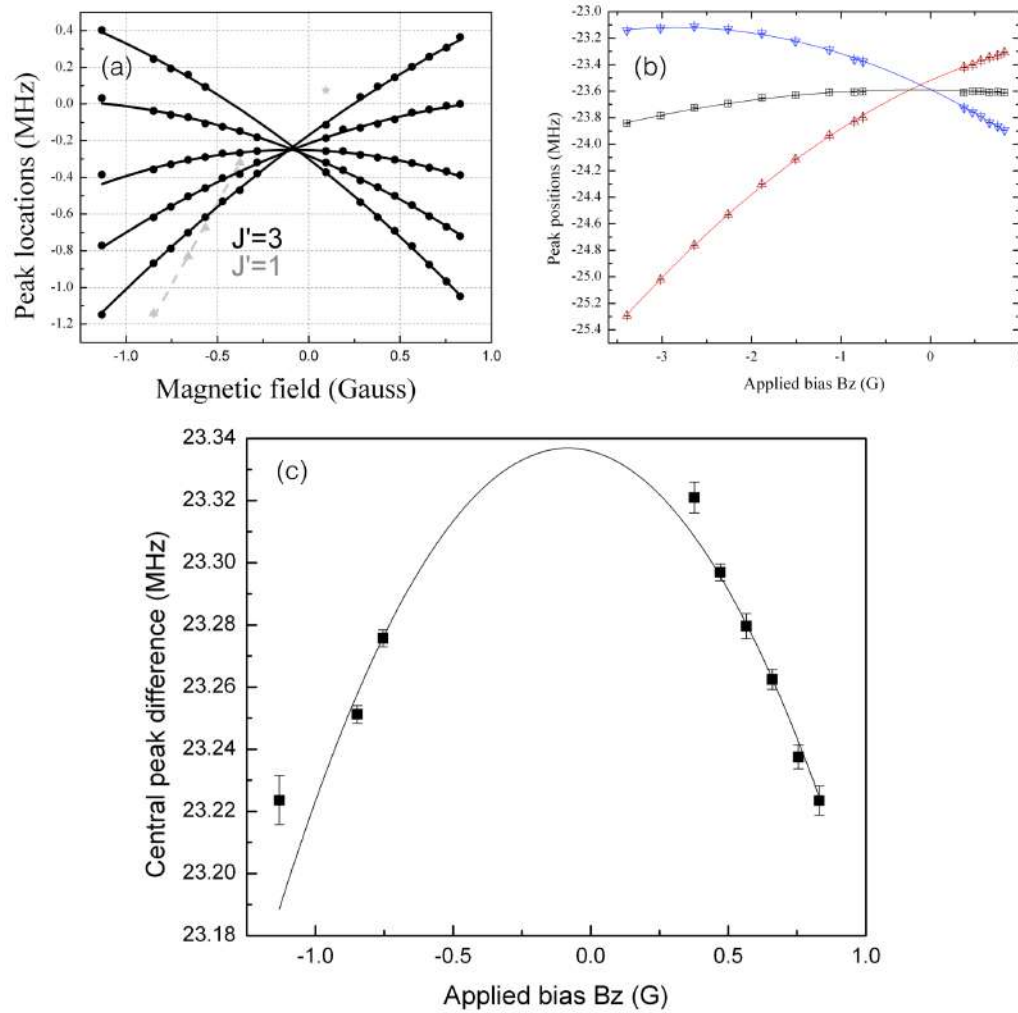


Figure 4.18: (a) The various sublevels of the ($v' = -2, J' = 3$) recovery peak, as well as the obscured ($v' = -1, J' = 1$) peak, plotted vs. applied magnetic field. (b) The ($v' = -2, J' = 1$) vs. applied magnetic field. (c) Their difference, which is used to extrapolate the absolute binding energy of the $J' = 3$ state. Laser frequency drift was deemed negligible for this data set.

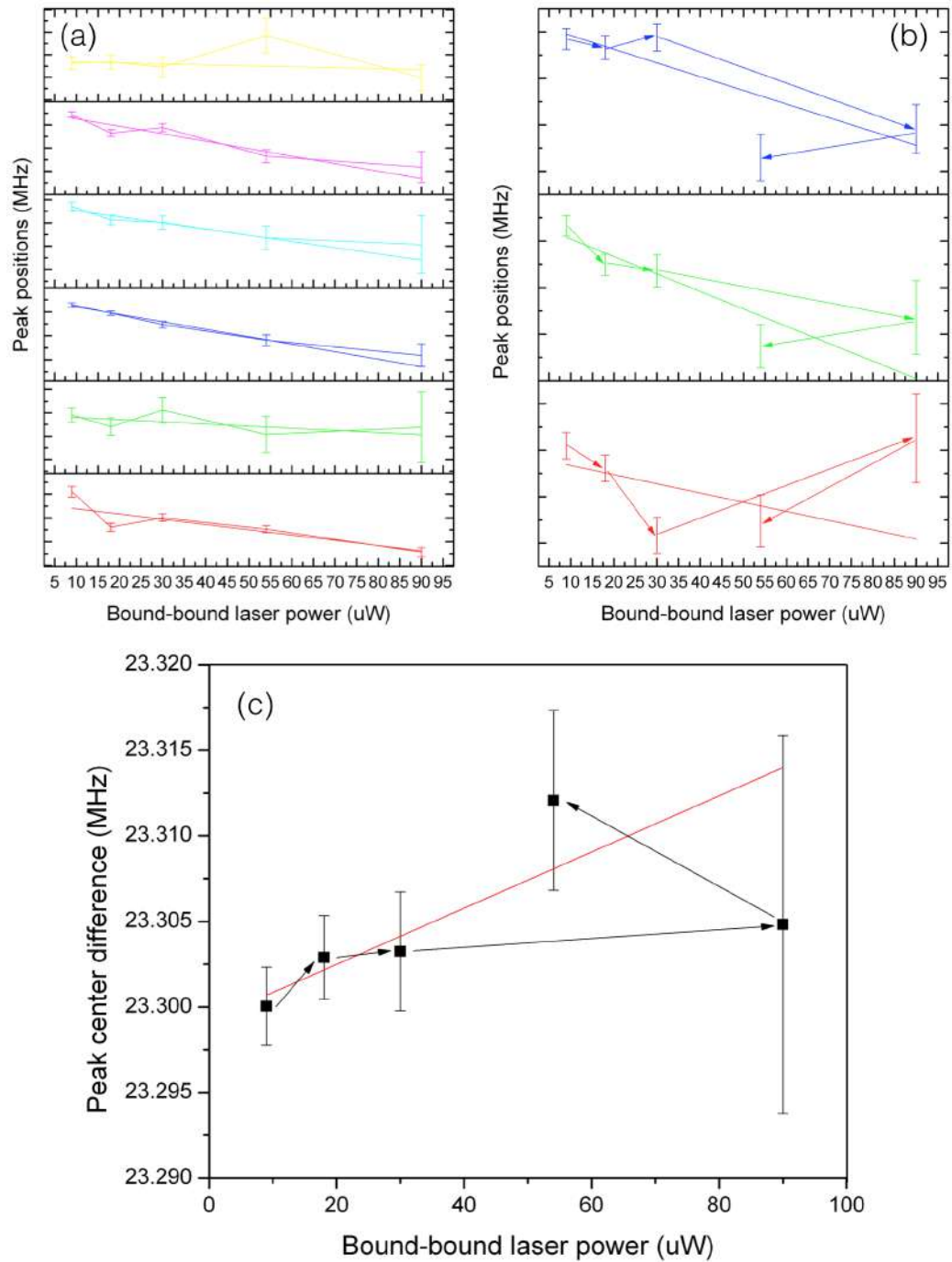


Figure 4.19: (a) The $(v' = -2, J' = 3)$ peak vs. recovery laser power, (b) the $(v' = -2, J' = 1)$ peak vs. recovery laser power, and (c) their difference, where laser frequency drift was deemed negligible.

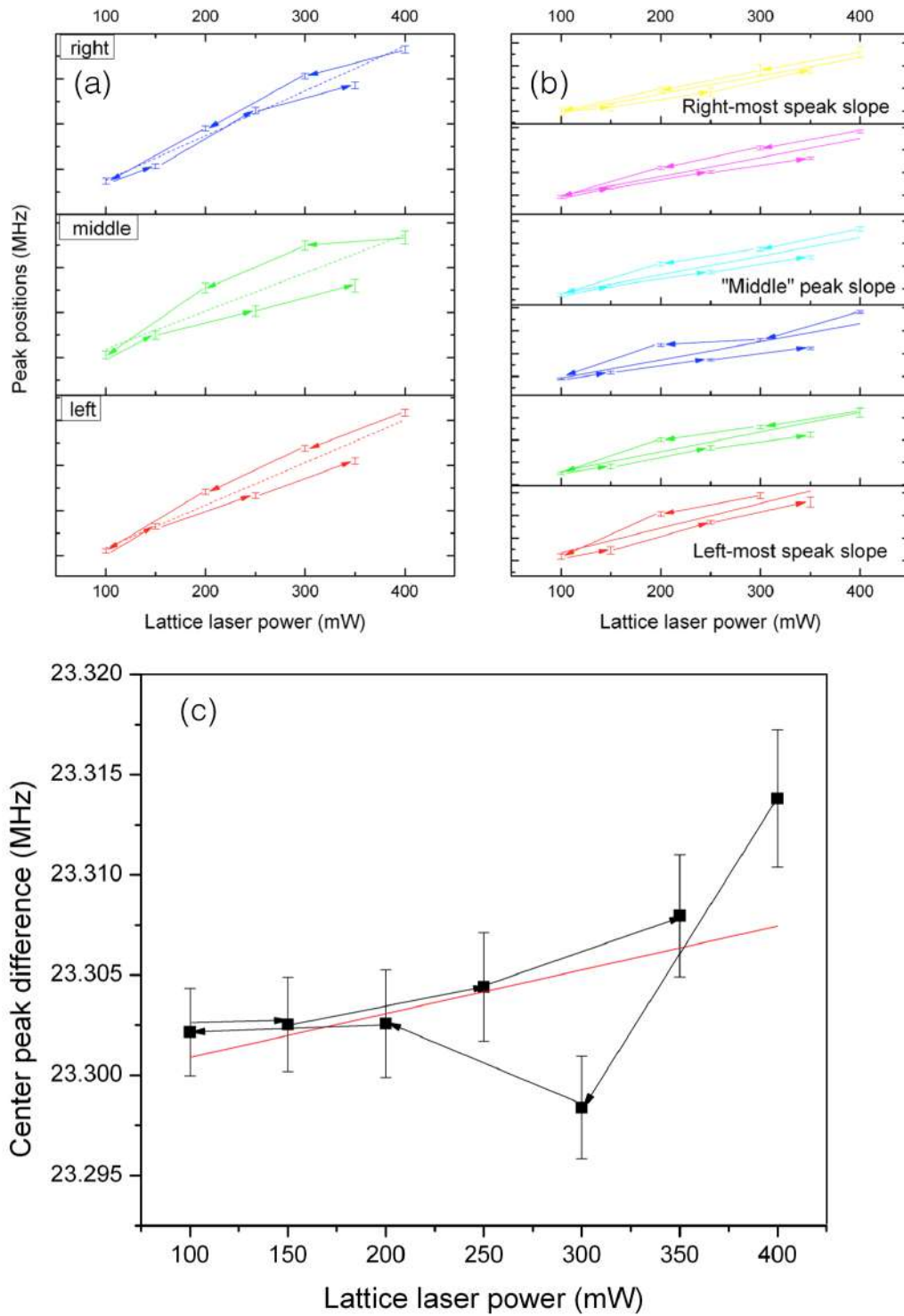


Figure 4.20: (a) The ($v' = -2, J' = 1$) peak vs. lattice laser power, (b) the ($v' = -2, J' = 3$) peak vs. lattice laser power, and (c) their difference, where laser frequency drift was deemed negligible.

4.2 Summary and prospects for QED effects in Sr₂

Table 4.1 summarizes the binding energies whose measurements are the topic of this chapter.

Table 4.1: Binding energies (MHz)

	0_u^+ ($v' = -1, J' = 1$)	0_u^+ ($v' = -2, J' = 1$)	0_u^+ ($v' = -2, J' = 3$)
experiment	-0.4521(43)	-23.9684(50)	-0.626(12)
theory	-0.37195	-23.546	-0.5368

The theoretical predictions are the result of a model for Sr₂ built by our collaborators [Skomorowski *et al.*, 2012a; Skomorowski *et al.*, 2012b]. The model utilizes an ab initio approach constructing the molecular potentials, relying on the fact that, being a heavy dimer, ⁸⁸Sr₂ conforms to Hund's case (c), with strong spin-orbit coupling (see Sec. 3.1). The Hamiltonian for the interaction is then

$$V^{0_u^+} = \begin{pmatrix} V^{c^3\Pi_u}(R) - A(R) & \xi_1(R) & \xi_2(R) \\ \xi_1(R) & V^{A^1\Sigma_u^+}(R) & 0 \\ \xi_2(R) & 0 & V^{B^1\Sigma_u^+}(R) \end{pmatrix}$$

and

$$V^{1_u} = \begin{pmatrix} V^{a^3\Sigma_u^+}(R) & 0 & \varphi_1(R) & \zeta_1(R) \\ 0 & V^{b^3\Sigma_u^+}(R) & \varphi_2(R) & \zeta_2(R) \\ \varphi_1(R) & \varphi_2(R) & V^{c^3\Pi_u}(R) & \varphi_3(R) \\ \zeta_1(R) & \zeta_2(R) & \varphi_3(R) & V^{B^1\Pi_u}(R) \end{pmatrix},$$

with the notation as described in [Skomorowski *et al.*, 2012b]. The goal of the model is to generate values for these various matrix elements, where an analytical expression is used to calculate the value of each matrix element at a given internuclear distance R. The short-range degrees of freedom are fit to the results of [Stein *et al.*, 2011], and the long-range to the results of this chapter and of [Zelevinsky *et al.*, 2006]. Because of the highly nonlinear nature of the model, it has yet to produce results that are within the experimental uncertainty. For more deeply-bound states, the uncertainty on the model is around 1%, which is still considerably worse than the spectroscopic precision of our measurements and those of related experiments.

The sensitivity of the two $^{88}\text{Sr}_2$ most-weakly bound levels to QED retardation effects is unusually high, at $\sim 10\%$ to $\sim 30\%$ [Moszynski, Skomorowski private comm.]. Moreover, the sensitivity to higher-order QED is $\sim 1\%$, well within reach of our experimental precision. Despite extensive tests of QED in atomic systems, few such tests exist for bound molecules [Jones *et al.*, 1996; Salumbides *et al.*, 2011], and none exist for higher-order QED effects.

Chapter 5

Linear and quadratic Zeeman shifts in Sr_2

In this chapter we discuss novel results originally discovered in the process of measuring systematic shifts of the binding energies reported in Ch. 4. We compare these results with the ab initio model from [Skomorowski *et al.*, 2012b]. We found that there exist strong nonadiabatic effects in the most weakly bound levels of $^{88}\text{Sr}_2$. In particular, anomalously large linear and quadratic shifts were observed, and it is understood that due to nonadiabatic Coriolis coupling and the long-range interatomic interactions, the quadratic shifts scale cubically with the molecule size. From the linear shifts we quantify the mixing of the 0_u^+ and 1_u molecular potentials. Additionally, we are able to detect fourth-order contributions in the quadratic term, and test the ab initio model with accuracy not achievable by linear shifts alone.

5.1 The 0_u^+ and 1_u states are mixed

As described in Ch. 3 and Fig. 3.2, the ground state X dissociates to the $^1\text{S}_0 + ^1\text{S}_0$ asymptote, and the Hund's case (c) states, 0_u^+ and 1_u , dissociate to the $^1\text{S}_0 + ^3\text{P}_1$ asymptote with total electronic angular momentum projection onto the nuclear axis $|\Omega'| = 0$ and $|\Omega'| = 1$, respectively. However, near the asymptote, the long-range molecules undergo ($L \cdot J$)-type Coriolis coupling, which strongly mixes these two Hund's case (c) states. Therefore each

observed state is actually a combination of the 0_u^+ and 1_u states with a mixing angle θ ,

$$|v', J'\rangle = \cos\theta|v'(0), J'\rangle + \sin\theta|v'(1), J'\rangle. \quad (5.1)$$

The solid horizontal lines in Fig. 5.1 (a) identifies the two weakly-bound levels $v' = -1, -2$ (both $J' = 1$), while the inset shows the third $|v', J'\rangle = |-2, 3\rangle$ that is nearly degenerate with the $|-1, 1\rangle$ level (in this notation, the vibrational quantum numbers are assigned before the rotational ones). These are the states whose binding energies were measured in the previous chapter. For these various states, recall that selection rules forbid $J' = 0$, and require that J' be odd for 0_u^+ states, and J be even. The vertical lines in Fig. 5.1 (a,b) represent the electric dipole-allowed transitions, which are then spectroscopically plotted in Fig. 5.1 (c). The various peaks are denoted p_1 to p_5 , with the two dissociation shelves marked as s_1 and s_2 for transitions from the $J = 0$ and $J = 2$ ground states, respectively.

To measure the magnetic field dependence of the energy levels, we apply a small field $B \leq 3$ G. This field is produced by the existing compensation Helmholtz coils on the experiment, and defines the quantum axis for the system, pointing vertically along the z -axis in the lab frame. For the majority of our measurements, the spectroscopy probe laser polarization is aligned parallel to this quantum axis, allowing for π transitions. In cases where σ transitions must be observed, the probe laser polarization is rotated by $\sim 45^\circ$ to allow observation of both. We employ the recovery method described in Ch. 4, which gives us a recovery peak signal against a nearly zero background signal. Additionally, we employ a second spectroscopy technique: a third laser is used to drive a bound-bound transition that depletes the $v = -2$ ground state population before it can be recovered. Fixing the recovery laser on a recovery peak or shelf, and sweeping the bound-bound third laser, we get recovery “loss” spectra: dips in the background recovery signal whose amplitude is that of the recovery peak from the previous, simpler method. For all of the following measurements, we confirmed that none of the measured field shifts are due to shifts in the ground state $J = 0$ and $J = 2$ levels, as a comparison between p_2 and p_5 yielded no observable difference. (In principle, only very small ground-state magnetic shifts are expected, due to the rotational factor g_r .)

The general spectroscopy sequence is depicted in Fig. 5.2. The dotted exposure times for lasers 689B and 689D represent the optional anti-recovery sequence, where the expo-

sure drives molecules via two-color transfer away from the bound state from which 689C eventually recovers.

Figures 5.3 (a) and (b) are typical recovery traces from p_5 and p_4 , respectively. The asymmetry in the three subpeaks of p_5 are a result of the strong quadratic shifts resulting from the applied magnetic field (-3.22 G in this case). Figures 5.3 (c) and (d) show the peak positions for p_5 and as plotted for various applied fields B , fitted to parabolic shapes with the required symmetry constraints. Figure 5.4 shows similar data for several more deeply bound states. Strong linear and quadratic shift dependence is apparent (note that the adiabatic picture predicts no such linear dependence for 0_u^+ states). Recent work [Kahmann *et al.*,] on intercombination line photoassociation reported absolute values for linear shifts in Ca atoms. We can model the Zeeman effect for these molecules using the usual Hamiltonian

$$H_z = \mu_B(g_L L + g_s S) \cdot B, \quad (5.2)$$

where L and S are the electronic orbital and spin angular momentum, respectively, and $g_L = 1$, $g_S \approx 2$, and μ_B is the Bohr magneton. The calculated first- and higher-order shifts of the binding energies are then

$$\Delta E_b = g\mu_B m' B + \sum_{n>1} q_n \mu_B B^n \quad (5.3)$$

$$\approx g\mu_B m' B + \bar{q}\mu_B B^2, \quad (5.4)$$

where the effective \bar{q} contains contributions from higher even-order terms. Here, g is defined effectively as

$$g = \langle H_z \rangle / (m' \mu_B B), \quad (5.5)$$

and since it depends on the expectation value $\langle H_z \rangle$, it will therefore depend on θ as well. The value m' is the projection of J' onto the quantum axis defined by B , and note that $q_n = q_n(v', J', m')$ depends on m' , but $g = g(v', J')$ only depends on the magnitude J' . The ab initio theory generates coefficients according to Eq. 5.3, while the experimental data is fit to Eq. 5.4.

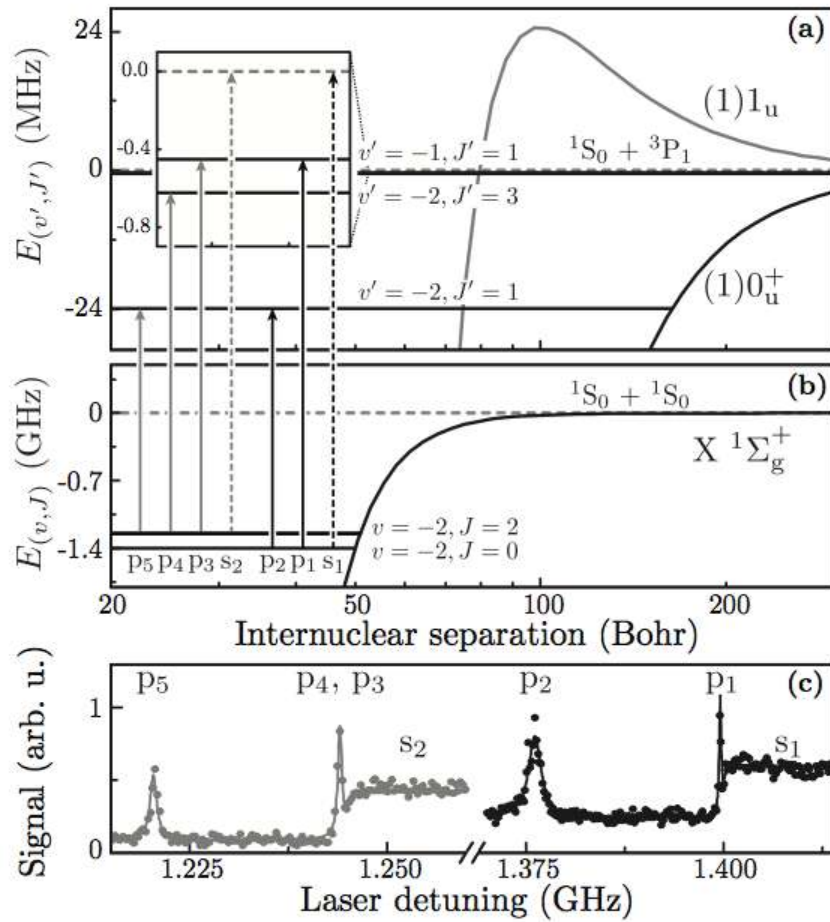


Figure 5.1: The long-range potentials for $^{88}\text{Sr}_2$ for (a) the excited state that dissociates to the $^1S_0 + ^3P_1$ asymptote (as shown with the horizontal dashed line) and (b) the ground state that dissociates to $^1S_0 + ^1S_0$. Drawn as solid lines in the excited state are the two bound states $v' = -1, -2$, both with angular momentum $J' = 1$. Drawn in the inset is the additional $|v', J'\rangle = |-2, 3\rangle$ that is nearly degenerate with $|-1, 1\rangle$. As described in Ch. 4, our ground state molecules occupy the rotational levels $J = 0, 2$ of the $v = -2$ vibrational level. The bound-bound transitions are marked by the solid lines $p_1 - p_5$, and the bound-free transition, are marked by the dashed lines s_1, s_2 . (c) The spectroscopic trace across all five peaks and two continuum shelves, fitted with the appropriate lineshapes as described in the Ch. 4.

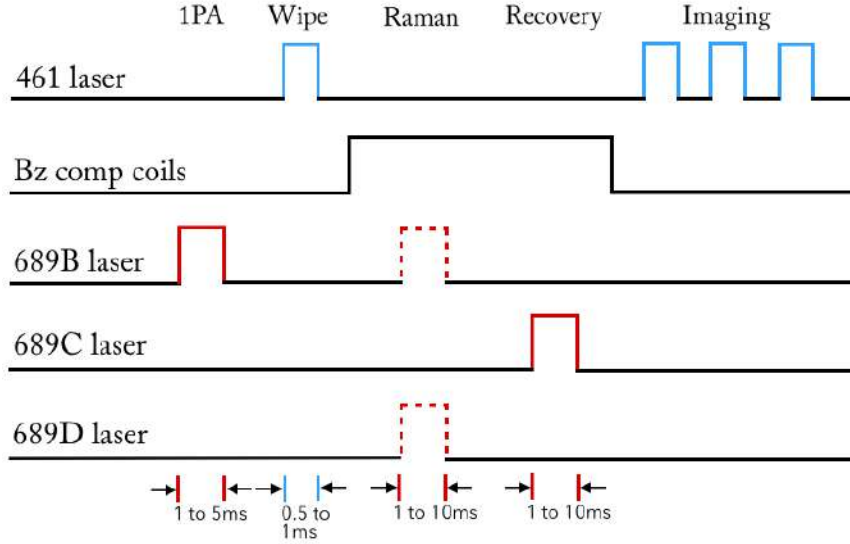


Figure 5.2: The spectroscopy sequence for the measurement. The dashed lines indicate the optional anti-recovery sequence, in which lasers 689B and 689D drive a two-color transfer away from the bound molecular state from which 689C recovers, resulting in a loss from the recovery signal.

5.2 Linear shifts, g factor measurement

From Eq. 5.1 and 5.2 we may write g for the $|v', J'\rangle$ level with its θ dependence.

$$g = g(\theta) = \frac{g_a \sin^2 \theta}{J'(J'+1)} + \frac{g_a \sin 2\theta}{\sqrt{J'(J'+1)}} \langle v'(0) | v'(1) \rangle. \quad (5.6)$$

The atomic $g_a = 1.5$ and the overlap for the vibrational parts of the basis states is $\langle v'(0) | v'(1) \rangle \sim 1$. Theoretical mixing angles θ are calculated from the updated ab initio model of [Skomorowski *et al.*, 2012b] as constrained to the data from [Stein *et al.*, 2011], which predicts most of the measured $J' = 1, 3$ states at the percent-level accuracy. For pure 0_u^+ states there should be no linear Zeeman shift ($\theta = 0^\circ$), and 1_u levels ($\theta = 90^\circ$) have $g = 0.75$ for $J' = 1$. The inset in Fig. 5.3 (c) shows $g(\theta)$ for $J' = 1$ for the assumed vibrational overlap of 1. Because θ varies from 0 to π , it includes both the relative amplitude and phase of the two wavefunction components, and therefore for each measured g -factor there are two solutions for θ . The example given in the inset is for $|v', J'\rangle = |-2, 1\rangle$ and gives $\theta = (6.1^\circ, 103.4^\circ)$, the first of which closely matches the ab initio prediction $\theta = 5.9^\circ$.

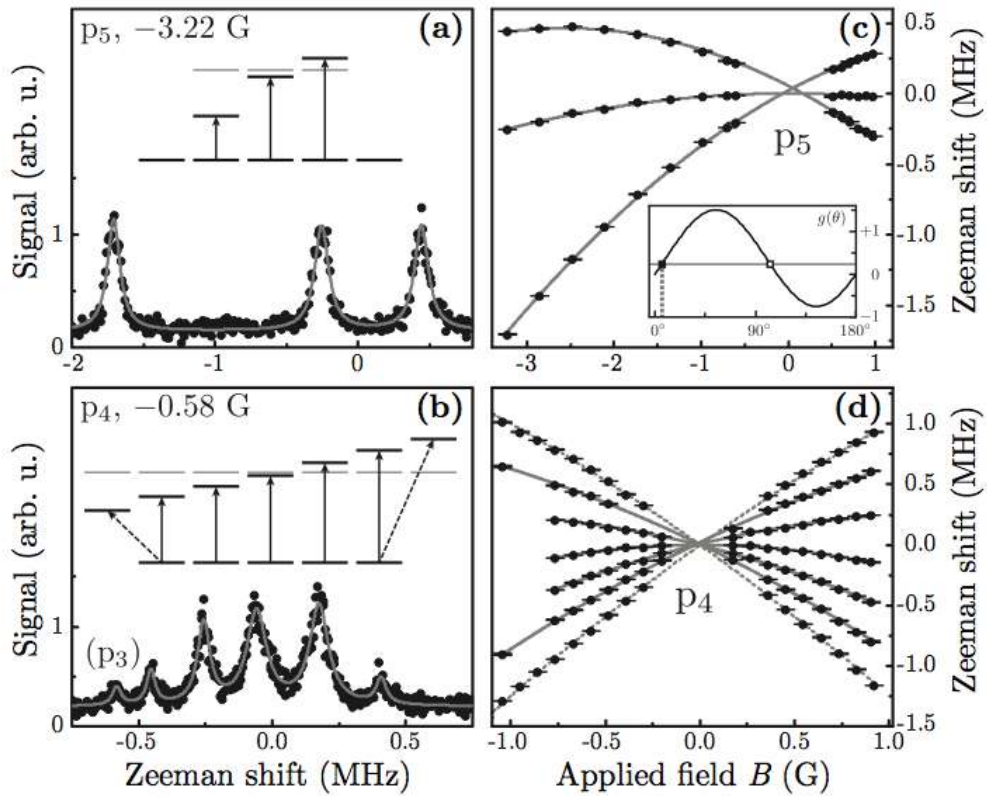


Figure 5.3: Sample spectra of (a) p_5 and (b) p_4 from Fig. 5.1, for small magnetic field B values, and showing π -transition peaks. The p_4 trace includes a shifted sublevel of the nearly-degenerate p_3 . (c,d) These peak positions as plotted for varying field amplitudes, and fitted to parabolic equations with the required symmetry constraints. In (d), the outermost $|m'| = 3$ are measured with a rotated polarization to allow for σ -transitions. In (c), the three curves do not cross at the same point, likely due to optical lattice tensor light shifts. The inset in (c) shows the $g(\theta)$ curve from Eq. 5.6, in which is marked the Coriolis mixing angle $\theta = 6.1^\circ$, as measured for $|v', J'\rangle = |-2, 1\rangle$.

Figure 5.5 gives a list of measured g factors and angles θ . The average agreement between experiment and theory is $\sim 5\%$, if the two most deeply-bound levels are excluded, while the typical experimental uncertainty barely exceeds 1%. As for θ , in the cases where only one value is given, the value predicted from the model closely matched one of the measured values, allowing us to identify the correct value from two possibilities (Eq. 5.6; inset in

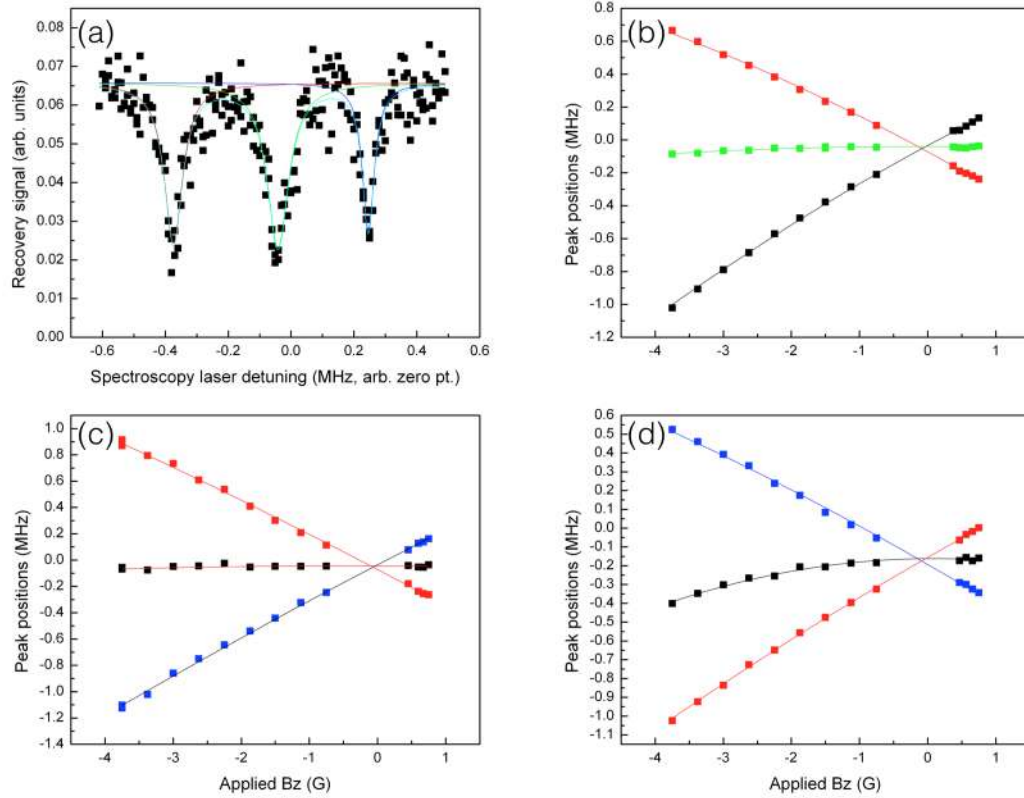


Figure 5.4: Sample Zeeman shift measurements of the deeper excited states. The measurement was achieved by Sr_2 production in the ground state -2 in the usual way, but then transferred via a third spectroscopy laser to the deeper excited state before recovery from the ground state is performed. By fixing the recovery spectroscopy laser on transition, and sweeping this third laser, the peaks are marked by "anti-recovery" dips in the otherwise non-zero atom signal. (a) Representative loss peaks to the $v' = -3$ state; (b) Zeeman shifts of the $v' = -3$ peaks, (c) of the $v' = -5$ peaks, and (d) of the $v' = -6$ peaks.

Fig. 5.3). However in the case of the two deepest levels, the predicted value for θ was not sufficiently close to either of the measured values, hence we've quoted both; these states are strongly mixed due to their similar binding energies.

5.3 Quadratic and higher order shifts, magnetic susceptibility

To calculate the quadratic and higher-order shifts, there are two approaches. First, one may calculate the quadratic shifts from the ab initio model by using second-order perturbation theory, but for higher order terms this becomes difficult. To calculate the second-order perturbative effect, one must sum over contributions from the continuum as well as from bound rovibrational levels. Each of these states belongs to one of two groups. One group contains states with the same $J' = 1$ or 3 that belong to the coupled 0_u^+ or 1_u manifolds. These contribute only for $m' \neq 0$, and the contribution is negative for 0_u^+ and positive for 1_u . The second group contains states with $J' = 2$ or 4 , must have opposite f -parity that belong to the 1_u manifold, and for all these levels the contribution is negative and significant for all m' . The limitation to this approach, as stated above, is that the calculation is only for the second-order quadratic contribution. For small magnetic fields this can be sufficient.

For the four most weakly bound levels, the dominant contribution to the quadratic shift is from the continuum of scattering states above the dissociation limit, while for deeper levels it is from the nearest bound level. Because the correct prediction of the quadratic Zeeman shifts requires precise description of the continuum and bound levels with $\Delta J' = 0, \pm 1$, this second-order measurement provides a substantially more stringent test of the molecular model than do the linear shifts alone.

The second approach does not calculate the higher-order shifts explicitly. Rather, the approach is to incorporate the magnetic field shift directly into the Hamiltonian and calculate the energy levels analytically for each given magnetic field value. One then gets a calculated plot similar to the experimental plot of Fig. 5.3. In this case the higher-order contributions are not known explicitly. Instead, one fits the plotted data to the same parabolic function as was performed on the experimental data, extrapolating the quadratic and higher-order coefficients from the fit. And as with the experimental fit, for small magnetic fields, one may truncate after the quadratic contribution and absorb such smaller, higher-order effects into an effective \bar{q} (Eq. 5.4).

Figure 5.5 gives a list of values for the effective quadratic coefficient calculated by the

second method, \bar{q} , for various bound rovibrational states (and m'), along with our experimentally measured equivalent. The disagreement between theory and experiment on average only slightly exceeds the experimental uncertainty. In the most weakly-bound state, we also find sensitivity to fourth-order shifts, which have been absorbed into the \bar{q} coefficient. The results for \bar{q} are plotted in Fig. 5.6, and normalized to the atomic $q_a = 1.28 \cdot 10^{-7} \text{ G}^{-1}$. The anomalously large quadratic Zeeman shifts grow by several orders of magnitude with decreasing binding energy. A qualitative explanation can be offered by considering the magnetic susceptibility χ , i.e. $\Delta E_b^{(2)} = -\chi B^2/2$. The susceptibility for the 0_u^+ states is then

$$\chi(R) \approx C_{J'}^{m'} \frac{\mu_B^2}{V_1(R) - V_0(R)} \approx C_{J'}^{m'} \frac{\mu_B^2 R^3}{3C_3}, \quad (5.7)$$

for internuclear separation R , $V_{|\Omega'|}$ the potentials from Fig. 5.1 (a), and coefficients $C_{J'}^{m'}$ that result from the transformation of the magnetic susceptibility tensor from the molecule-fixed frame to the space-fixed frame [Brown and Carrington, 2003] (of order unity). This result assumes that near the asymptote, C_3 terms dominate over C_6 in the long-range potentials. The result is an effective paramagnetic component of the susceptibility, while the diamagnetic component is negligible. The line plotted in Fig. 5.6 is χ for the $J' = 0$, $m' = 0$ levels of 0_u^+ , with C_3 quoted from [Zelevinsky *et al.*, 2006] and R set to the classical outer turning point. The χ model is in excellent agreement with the relevant data points (black squares for $J' = 1$). The $V_1(R) - V_0(R)$ in Eq. 5.7 approximates that the dominant contribution is from the continuum, as is true for these weakly-bound states.

To summarize, we have performed precise measurements of the strongly nonadiabatic effects in ultracold molecules via determination of Zeeman shifts of the weakly-bound states. These measurements were compared with ab initio studies that are the work of our collaborators [Skomorowski *et al.*, 2012b]. We found close agreement between theory and measurement for both the linear g factors and 0_u^+ (to within 5%) and for the higher-order shifts, accounted for by the quadratic coefficient \bar{q} (within $\sim 20\%$). The g -factors yield (model-dependent) experimental determinations of the nonadiabatic Coriolis mixing angle, a subtle property of molecule wavefunctions that is otherwise difficult to access.

E_b	J'	g (exp)	g (th)	θ (exp)	$ m' $	$-\bar{q}$ (exp)	$-\bar{q}$ (th)
0.45	1	0.666(14)	0.636	16.5°	0	0.325(34)*	0.266*
					1	0.546(44)*	0.780*
0.63	3	0.270(2)	0.271	18.5°	0	0.130(5)	0.114
					1	0.102(5)	0.113
					2	0.095(6)	0.112
					3	0.090(4)	0.110
24.0	1	0.232(3)	0.222	6.1°	0	0.0181(6)	0.0147
					1	0.0444(13)	0.0388
132	3	0.173(2)	0.160	11.6°	0	0.0041(15)	0.0039
					1	0.0043(5)	0.0042
					2	0.0061(9)	0.0050
					3	0.0060(14)	0.0062
222.2	1	0.161(2)	0.148	4.2°	0	0.0023(6)	0.0022
					1	0.0066(4)	0.0057
353.2	1	0.625(9)	0.610	93.3°	0	0.0126(26)	0.0111
					1	0.0077(10)	0.0065
1084.1	1	0.142(2)	0.128	3.8°	0	0.0019(7)	0.0013
					1	0.0041(3)	0.0031
2683.7	1	0.584(8)	0.571	94.6°	0	0.0080(18)	0.0067
					1	0.0034(11)	0.0031
3463.3	1	0.193(3)	0.174	5.1°	0	0.0016(8)	0.0017
					1	0.0029(5)	0.0028
8200.2	1	-0.149(2)	-0.592	{113.6°, 175.9°}	0	0.0112(12)	0.0076
					1	0.0040(4)	0.0017
8429.7	1	0.931(13)	1.333	{24.6°, 84.9°}	0	0.0008(6)	0.0009
					1	0.0060(13)	0.0047

Figure 5.5: The relevant magnetic properties that are strongly sensitive to the nonadiabatic effects in the weakest-bound levels of $^{88}\text{Sr}_2$ near the $^1\text{S}_0 + ^3\text{P}_1$ asymptote. Equations 5.3 and 5.4 define the experimental and theoretical quadratic shift coefficients q (G^{-1}). An asterisk denotes cases that include strong fourth-order contributions (q_4 in Eq. 5.3). Experimental and theoretical g factors are given, as are the Coriolis mixing angles θ . Due to the limitations of the model, for the two deepest states a unique angle cannot be determined from the two provided by the measurements.

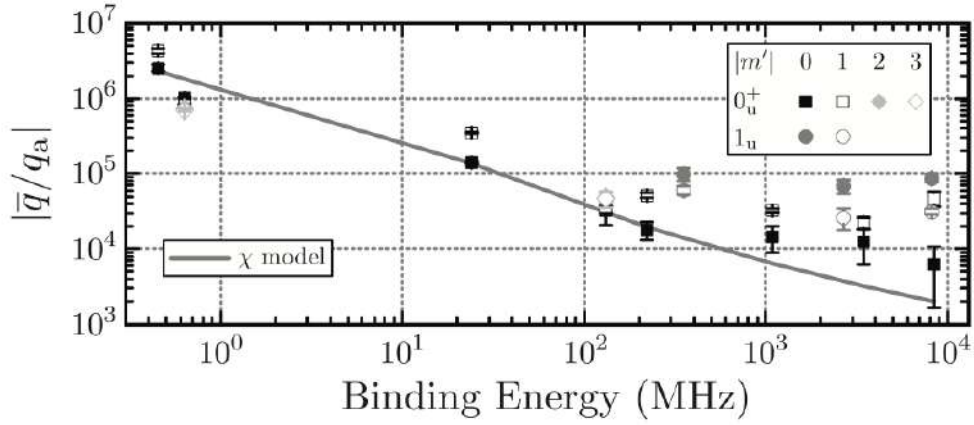


Figure 5.6: Measured \bar{q} versus the binding energy, normalized to the analogous atomic coefficient q_a . The results show a $10^6 \times$ enhancement in the weakest-bound region relevant to Fig. 5.3. The various markers are defined in the legend, and the solid gray line represents the magnetic susceptibility model of Eq. 5.7 for the $J' = 1$, $m' = 0$ levels of the 0_u^+ manifold. Note that this is relevant only for the black squares with $J' = 1$, and is in excellent agreement with the data.

Chapter 6

Outlook

The conclusion of my Ph.D. work marks the end of a chapter in the story of the Zelevinsky lab. My contemporaries and I saw through the construction of the main apparatus - from setup of the initial vacuum chamber through the successful creation of ultracold, μK samples of atomic Sr trapped in an optical lattice [Reinaudi *et al.*, 2012a]. Our first major result was the successful production and detection of photoassociated ultracold $^{88}\text{Sr}_2$ molecules from this cold atom sample [Reinaudi *et al.*, 2012b]. Our all-optical photoassociation technique makes weakly-bound molecules in the shallowest rovibrational states of the electronic ground state. This afforded us the opportunity to measure the binding energies of several of these states to new levels of accuracy. The two weakest-bound of these states are predicted to have as much as 10 – 30% contribution from QED retardation effects, allowing us to use our experiment as a rare test of molecular QED. Additionally, we measured the unusually large magnetic susceptibility of these long-range molecules, detecting a million-fold enhancement of the quadratic Zeeman shifts as compared to those of unbound atoms, and allowing us to compare our results to a state-of-the-art ab initio theoretical model created by our collaborators [Skomorowski *et al.*, 2012b]. Our measurements of the weakly-bound Sr_2 g-factors lead to precise determinations of the nonadiabatic Coriolis mixing angle of the molecular wave functions [McGuyer *et al.*, 2013].

But while the structure of this new class of ultracold molecules is worthy of study in its own right, from the perspective of quantum chemistry and ultracold physics, our long-term interest in the $^{88}\text{Sr}_2$ system is motivated by broader questions in fundamental physics, such

as the creation of a molecular clock. Such a clock could discern subtle ($< 10^{-16}$ /year) variations of the electron-to-proton mass ratio [Zelevinsky *et al.*, 2008], and possibly help constrain mass-dependent Yukawa-type interactions at the nanometer scale [Adelberger *et al.*, 2003].

To accomplish these goals, we require production of Sr_2 in the deeply-bound rovibrational levels of the electronic ground state. Figure 6.1 is a map of the bound states of both the electronic excited and electronic ground state manifolds ($J' = 1$ and $J = 0$, respectively), with the heat map giving the dipole moment of the transition between any two given states. Our current work has been limited to the white rectangle indicated in the upper-right corner, with the absolute ground state indicated by the bottom row. The contour lines span state pairs that can be coupled by light of the same color. To achieve transfer to the ground state, at ~ 30 THz binding energy relative to the continuum, weakly-bound molecules must be coherently transferred by a two-color (Raman) process via frequency comb-locked [Cundiff *et al.*, 2001] lasers.

Our lab has installed a fiber-laser frequency comb (Menlo Systems) at 1550 nm and frequency-doubled to span the visible and near-infrared range. We have added a 650 nm ECDL to be locked to the 689 nm master laser for the purpose of transferring the molecules to these deeper states. To test the principle, we have initially transferred between the weakest-bound states already under study. Figure 6.2 (a) shows the successful transfer from the X ($v = -2, J = 0$) to the ($v = -1, J = 0$) state. The relevant control sequence is as follows: before recovery, an additional spectroscopy laser is used (689D), in conjunction with the 689B laser, to perform a far-detuned two-color transfer. Figure 6.2 (b) shows the same transfer at a smaller, 120 Hz linewidth. With decreasing probe power the linewidth approaches this ~ 100 Hz limit. We believe this limit is dominated by slightly unequal lattice light shifts for the two molecular states, due to the inhomogeneity of the lattice intensity over the extent of the trap. Figure 6.2 (d) shows the empirically-determined differential lattice light shift of ~ 4 Hz/mW, substantiating the ~ 100 Hz residual line broadening. For more deeply bound molecular levels, we will search for a “magic” lattice wavelength and polarization combinations to cancel the differential shifts.

In the meantime, our shorter-term goals include further study of the weakest-bound

levels. Recent work has suggested there may be a rovibrational dependence on the collisional lifetime [Mayle *et al.*, 2013]. Additionally, my colleagues have been probing the gerade 1_g states that are only coupled to the X $^1\Sigma_g$ states via weak magnetic-dipole transitions. It is possible that transfer to the absolute molecular ground state may prove easier from one of these states, and that the magnetic-dipole transitions are strongly enhanced on weakly bound molecules. Another type of forbidden transition currently being explored is electric-dipole, with $\Delta J > 1$. We have been able to enhance its transition strength by $10^5\times$ with modest magnetic fields. The richness of this ultracold molecular system in the high-precision regime is only beginning to be explored.

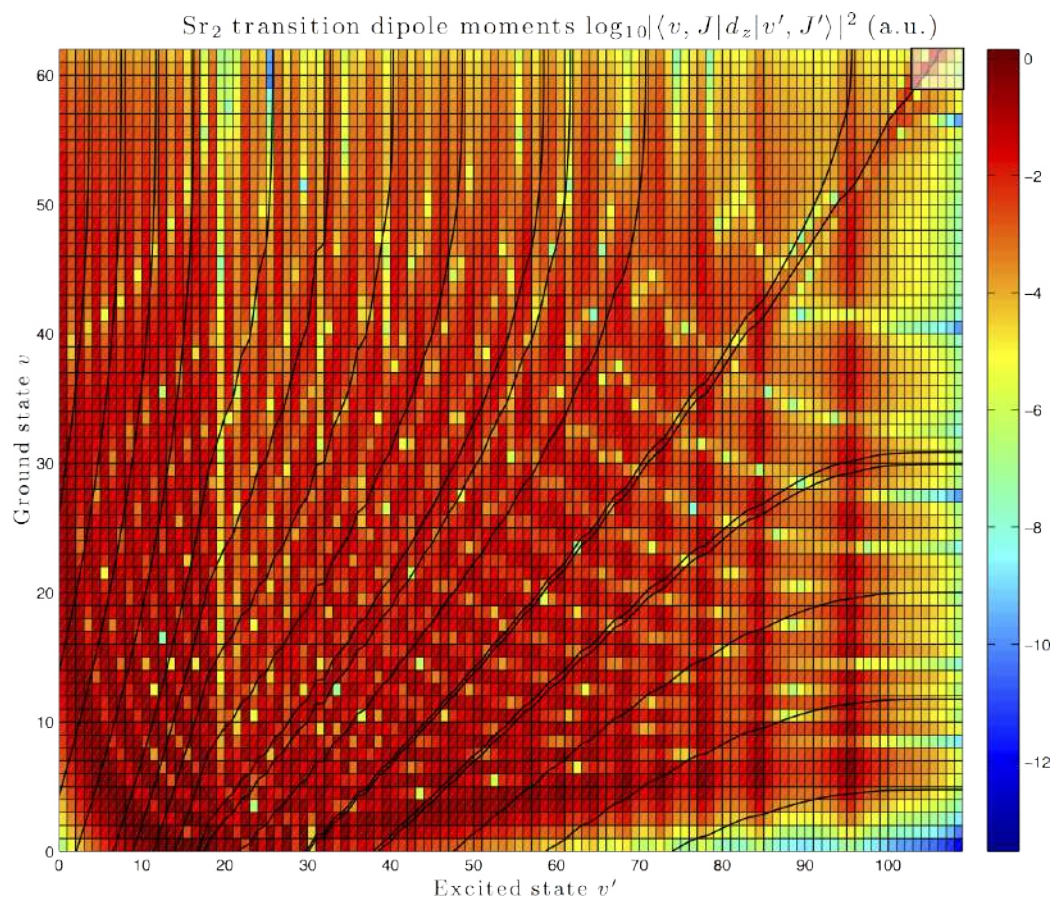


Figure 6.1: A map of the transition dipole moments between the vibrational states of the excited 0_u^+ and the ground X manifold (for $J' = 1$ and $J = 0$, respectively), with false color to represent the log of the dipole moment. The excited states of 0_u^+ are plotted along the horizontal axis, and the ground states of X on the vertical axis. The contour lines connect levels that can be coupled by the same laser wavelength, where the lines, from left to right, span across wavelengths from ~ 830 to 650nm .

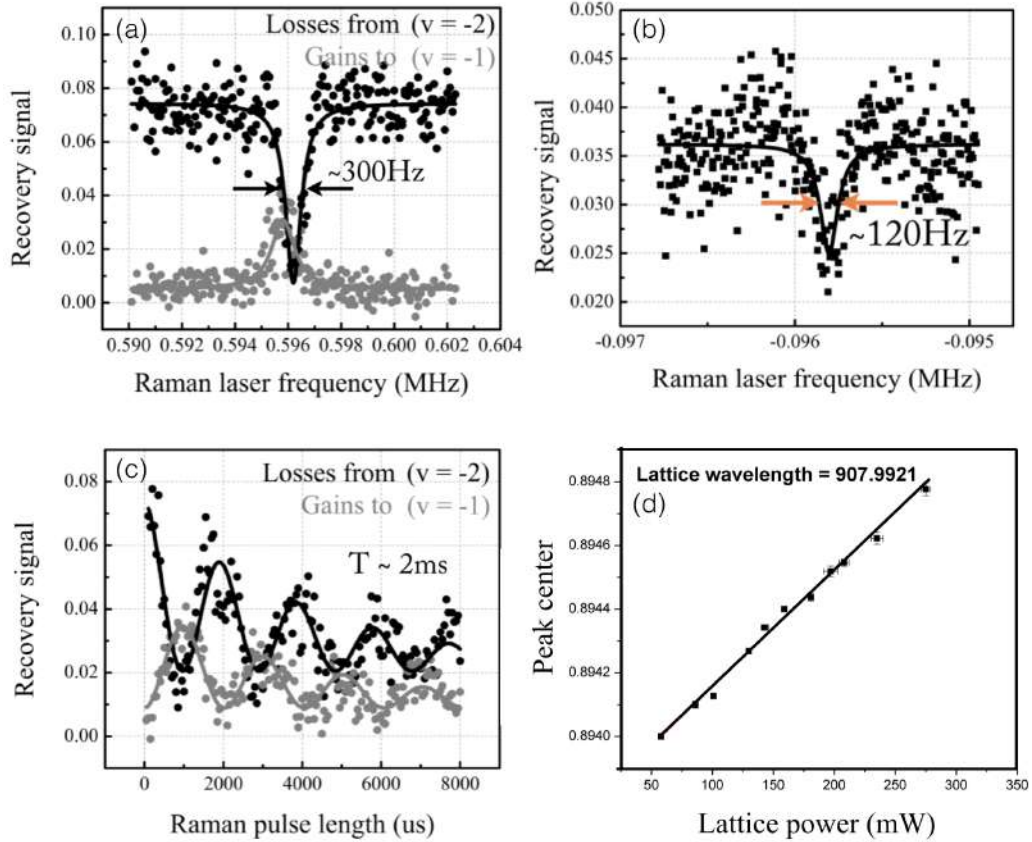


Figure 6.2: Representative traces for Raman spectroscopy between states $v = -2$ and $v = -1$. (a) Losses from $v = -2$ overlaid with gains to $v = -1$, (b) losses from $v = -2$ at a narrower, 120 Hz linewidth corresponding to a 20 ms coherence time, (c) Rabi flopping between the two states, and (d) a plot of the line frequency vs. lattice laser power. It is suspected that the inhomogeneity of the lattice laser intensity, at a slightly non-magic wavelength, is the cause of the 600 Hz linewidth limit.

Bibliography

- [Adelberger *et al.*, 2003] E. G. Adelberger, B. R. Heckel, and A. E. Nelson. Test of the gravitational inverse-square law. *Nuclear and Particle Science*, 53:77–121, December 2003.
- [Atkins and Friedman, 2010] Peter W. Atkins and Ronald W. Friedman. *Molecular Quantum Mechanics*. Oxford University Press, Oxford, UK, 2010.
- [Bagnato *et al.*, 1989] V. S. Bagnato, A. Aspect, and S. C. Zilio. Study of laser deceleration of an atomic beam by monitoring the fluorescence along the deceleration path. *Optics Communications*, 72(1):76–81, July 1989.
- [Baron *et al.*, a] J. Baron, W. C. Campbell, D. DeMille, J. M. Doyle, G. Gabrielse, Y. V. Gurevich, P. W. Hess, N. R. Hutzler, E. Kirilov, I. Kozyryev, B. R. O’Leary, C. D. Panda, M. F. Parsons, E. S. Petrik, B. Spaun, A. C. Vutha, and A. D. West. Order of magnitude smaller limit on the electric dipole moment of the electron.
- [Baron *et al.*, b] J. Baron, W. C. Campbell, D. DeMille, J. M. Doyle, G. Gabrielse, Y. V. Gurevich, P. W. Hess, N. R. Hutzler, E. Kirilov, I. Kozyryev, B. R. O’Leary, C. D. Panda, E. S. Petrik, B. Spaun, A. C. Vutha, and A. D. West. Order of magnitude smaller limit on the electric dipole moment of the electron. Submitted.
- [Bethlem *et al.*, 1999] Henrick L Bethlem, Giel Berden, and Gerard Meijer. Decelerating neutral dipolar molecules. *Physical Review Letters*, 83(8):1558–1561, August 1999.
- [Black, 2001] Eric D. Black. An introduction to Pound-Drever-Hall laser frequency stabilization. *American Journal of Physics*, 69(1):79–87, January 2001.

- [Bloom *et al.*,] B. J. Bloom, T. L. Nicholson, J. R. Williams, S. L. Campbell, M. Bishof, X. Zhang, W. Zhang, S. L. Bromley, and J. Ye. A new generation of atomic clocks; accuracy and stability at the 10^{-18} level.
- [Bohn and Julienne, 1996] John L. Bohn and Paul S. Julienne. Semianalytic treatment of two-color photoassociation spectroscopy and control of cold atoms. *Physical Review A*, 54(6):1–4, December 1996.
- [Boyd, 2007] Martin M. Boyd. *High Precision Spectroscopy of Strontium in an Optical Lattice: Towards a New Standard for Frequency and Time*. PhD thesis, University of Colorado at Boulder, May 2007.
- [Brown and Carrington, 2003] John M. Brown and Alan Carrington. *Rotational Spectroscopy of Diatomic Molecules*. Cambridge University Press, Cambridge, UK, 2003.
- [Budker *et al.*, 2008] Dmitry Budker, Derek F. Kimball, and David P. DeMille. *Atomic Physics: An Exploration through Problems and Solutions*. Oxford University Press, New York, 2008.
- [Carr *et al.*, 2009] Lincoln D. Carr, David DeMille, Roman V. Krems, and Jun Ye. Cold and ultracold molecules: science, technology and applications. *New Journal of Physics*, 11(055049):1–87, May 2009.
- [Chambers, 1998] A. Chambers. *Basic Vacuum Technology*. Taylor & Francis, Abingdon, Oxford, UK, 1998.
- [Chin *et al.*, 2010] Cheng Chin, Rudolf Grimm, Paul S. Julienne, and Eite Tiesinga. Feshbach resonances in ultracold gases. *Reviews of Modern Physics*, 82(2):1225–1286, April 2010.
- [Chu *et al.*, 1985] Steven Chu, L. Hollberg, J. E. Bjorkhold, Alex Cable, and A. Ashkin. Three-dimensional viscous confinement and cooling of atoms by resonance radiation pressure. *Physical Review Letters*, 55(1):48–51, July 1985.
- [Chu, 1998] Steven Chu. The manipulation of neutral particles. *Reviews of Modern Physics*, 70(3):685–706, July 1998.

- [Ciurylo *et al.*, 2004] R. Ciurylo, E. Tiesinga, S. Kotochigova, and P. S. Julienne. Photoassociation spectroscopy of cold alkaline-earth-metal atoms near the intercombination line. *Physical Review A*, 70(062710):1–14, December 2004.
- [Ciurylo *et al.*, 2005] R. Ciurylo, E. Tiesinga, and P. S. Julienne. Optical tuning of the scattering length of cold alkaline-earth-metal atoms. *Physical Review A*, 71(030701):1–4, March 2005.
- [Cohen-Tannoudji, 1998] Claude N. Cohen-Tannoudji. Manipulating atoms with photons. *Reviews of Modern Physics*, 70(3):707–719, July 1998.
- [Cornell and Wieman, 2002] E. A. Cornell and C. E. Wieman. Nobel lecture: Bose-Einstein condensation in a dilute gas, the first 70 years and some recent experiments. *Reviews of Modern Physics*, 74(3):875–893, July 2002.
- [Cundiff *et al.*, 2001] Steven T. Cundiff, Jun Ye, and John L. Hall. Optical frequency synthesis based on mode-locked lasers. *Review of Scientific Instruments*, 72(10):3749–3771, October 2001.
- [Dalibard and Cohen-Tannoudji, 1989] J. Dalibard and C. Cohen-Tannoudji. Laser cooling below the Doppler limit by polarization gradients: simple theoretical models. *The Journal of the Optical Society of America*, 6(11):2023–2045, November 1989.
- [de Escobar *et al.*, 2008] Y. N. Martinez de Escobar, P. G. Mickelson, P. Pellegrini, S. B. Nagel, A. Traverso, M. Yan, R. Cote, and T. C. Killian. Two-photon photoassociative spectroscopy of ultracold ^{88}Sr . *Physical Review A*, 78(062708):1–8, December 2008.
- [Dedman *et al.*, 2004] C. J. Dedman, J. Nes, T. M. Hanna, R. G. Dall, K. G. H. Baldwin, and A. G. Truscott. Optimum design and construction of a Zeeman slower for use with a magneto-optic trap. *Reviews of Scientific Instruments*, 75:5136–5142, 2004.
- [Derevianko and Katori, 2011] Andrei Derevianko and Hidetoshi Katori. Physics of optical lattice clocks. *Reviews of Modern Physics*, 83, April 2011.

- [Dickenson *et al.*, 2013] G. D. Dickenson, M. L. Niu, E. J. Salumbides, J. Komasa, K. S. E. Eikema, K. Pachucki, and W. Ubachs. Fundamental vibration of molecular hydrogen. *Physical Review Letters*, 110(193601):1–5, May 2013.
- [Diddams *et al.*, 2004] S. A. Diddams, J. C. Bergquist, S. R. Jefferts, and C. W. Oates. Standards of time and frequency at the outset of the 21st century. *Science*, 306:1318–1324, November 2004.
- [Doyle *et al.*, 2004] J. Doyle, B. Friedrich, R. V. Krems, and F. Masnou-Seeuws. Quo vadis, cold molecules? *The European Physical Journal D*, 31:149–164, 2004.
- [Drever *et al.*, 1983] R. W. P. Drever, J. L. Hall, F. V. Kowalski, J. Hough, G. M. Ford, A. J. Munley, and H. Ward. Laser phase and frequency stabilization using an optical resonator. *Applied Physics B*, 31:97–105, February 1983.
- [Dulieu and Gabbanini, 2009] O. Dulieu and C. Gabbanini. The formation and interactions of cold and ultracold molecules: new challenges for interdisciplinary physics. *Reports on Progress in Physics*, 72(086401):1–35, July 2009.
- [Feshbach, 1958] Herman Feshbach. Unified theory of nuclear reactions. *Annals of Physics*, 5(4):357–390, December 1958.
- [Foot, 2005] C. J. Foot. *Atomic Physics*. Oxford University Press, Oxford, UK, 2005.
- [Fox *et al.*, 2003] Richard W. Fox, Chris W. Oates, and Leo W. Hollberg. Stabilizing diode lasers to high-finesse cavities. *Experimental Methods in the Physical Sciences*, 40:1–46, 2003.
- [Garcia-Ripoll *et al.*, 2005] J. J. Garcia-Ripoll, P. Zoller, and J. I. Cirac. Quantum information processing with cold atoms and trapped ions. *Journal of Physics B*, 38:567–578, April 2005.
- [Greiner, 2003] Markus Greiner. *Ultracold quantum gases in three-dimensional optical lattice potentials*. PhD thesis, Ludwig-Maximilians-Universitat Munchen, January 2003.

- [Hemmerich *et al.*, 1990] A. Hemmerich, D. H. McIntyre, C. Zimmermann, and T. W. Hansch. Second-harmonic generation and optical stabilization of a diode laser in an external ring resonator. *Optics Letters*, 15(7):372–374, April 1990.
- [Hollberg and Wieman, 1991] Leo Hollberg and Carl E. Wieman. Using diode lasers for atomic physics. *Review of Scientific Instruments*, 62(1):1–20, January 1991.
- [Hudson *et al.*, 2011] J. J. Hudson, D. M. Kara, I. J. Smallman, B. E. Sauer, M. R. Tarbutt, and E. A. Hinds. Improved measurement of the shape of the electron. *Nature*, 473:493–496, May 2011.
- [Ido and Katori, 2003] Tetsuya Ido and Hidetoshi Katori. Recoil-free spectroscopy of neutral Sr atoms in the Lamb-Dicke regime. *Physical Review Letters*, 91(5):1–4, August 2003.
- [Inouye *et al.*, 1998] S. Inouye, M. R. Andrews, J. Stenger, H. J. Miesner, D. M. Stamper-Kurn, and W. Ketterle. Observation of Feshbach resonances in a Bose-Einstein condensate. *Nature*, 392:151–154, March 1998.
- [Jones *et al.*, 1996] K. M. Jones, P. S. Julienne, P. D. Lett, W. D. Phillips, E. Tiesinga, and C. J. Williams. Measurement of the atomic Na(3P) lifetime and of retardation in the interaction between two atoms bound in a molecule. *Europhysics Letters*, 35(2):85–90, July 1996.
- [Jones *et al.*, 1999] Kevin M. Jones, Paul D. Lett, Eite Tiesinga, and Paul S. Julienne. Fitting line shapes in photoassociation spectroscopy of ultracold atoms: A useful approximation. *Physical Review A*, 61(012501):1–11, December 1999.
- [Jones *et al.*, 2006] Kevin M. Jones, Eite Tiesinga, Paul D. Lett, and Paul S. Julienne. Ultracold photoassociation spectroscopy: Long-range molecules and atomic scattering. *Reviews of Modern Physics*, 78(2):483–535, April 2006.
- [Kahmann *et al.*,] Max Kahmann, Eberhard Tiemann, Oliver Appel, Uwe Sterr, and Fritz Riehle. High accuracy photoassociation of ^{40}Ca near the $^1\text{S}_0$ - $^3\text{P}_1$ asymptote and its Zeeman effect.

- [Katori *et al.*, 1999] Hidetoshi Katori, Tetsuya Ido, Yoshitomo Isoya, and Makoto Kuwata-Gonokami. Magneto-optical trapping and cooling of strontium atoms down to the photon recoil temperature. *Physical Review Letters*, 82(6):1–4, February 1999.
- [Klappauf *et al.*, 2004] Bruce G. Klappauf, Yannick Bidel, David Wilkowski, Thierry Chaneliere, and Robin Kaiser. Detailed study of an efficient blue laser source by second-harmonic generation in a semimonolithic cavity for the cooling of strontium atoms. *Applied Optics*, 43(2):2510–2527, April 2004.
- [Koelemeij *et al.*, 2007] J. C. J. Koelemeij, B. Roth, A. Wicht, I. Ernsting, and S. Schiller. Vibrational spectroscopy of HD^+ with 2-ppb accuracy. *Physical Review Letters*, 98(173002):1–4, April 2007.
- [Kogelnik and Li, 1966] H. Kogelnik and T. Li. Laser beams and resonators. *Applied Optics*, 5(10):1550–1567, October 1966.
- [Kohler *et al.*, 2006] Thorsten Kohler, Krzysztof Goral, and Paul S. Julienne. Production of cold molecules via magnetically tunable Feshbach resonances. *Reviews of Modern Physics*, 78(4):1311–1361, October 2006.
- [Kotochigova, 2008] Svetlana Kotochigova. Relativistic electronic structure of the Sr_2 molecule. *The Journal of Chemical Physics*, 128(024303):1–5, January 2008.
- [Krems *et al.*, 2009] Roman Krems, Bretislav Friedrich, and William C. Stwalley. *Cold Molecules: Theory, Experiment, Applications*. CRC Press, Boca Raton, Florida, 2009.
- [Leibfried *et al.*, 2003] D. Leibfried, R. Blatt, C. Munroe, and D. Wineland. Quantum dynamics of single trapped ions. *Reviews of Modern Physics*, 75(1):281–324, March 2003.
- [Letokhov, 1968] V. S. Letokhov. Doppler line narrowing in a standing light wave. *Pis'ma Zh. Eksp. Teor. Fiz.*, 7(9):348–351, May 1968.
- [Lett *et al.*, 1989] P. D. Lett, W. D. Phillips, S. L. Rolston, C. E. Tanner, R. N. Watts, and C. I. Westbrook. Optical molasses. *Journal of the Optical Society of America B*, 6(11):2084–2107, November 1989.

- [Liu and Littman, 1981] Karen Liu and Michael G. Littman. Novel geometry for single-mode scanning of tunable lasers. *Optics Letters*, 6(3):117–118, 1981.
- [Loftus *et al.*, 2004a] Thomas H. Loftus, Tetsuya Ido, Martin M. Boyd, Andrew D. Ludlow, and Jun Ye. Narrow line cooling and momentum-space crystals. *Physical Review A*, 70(063413):1–14, December 2004.
- [Loftus *et al.*, 2004b] Thomas H. Loftus, Tetsuya Ido, Andrew D. Ludlow, Martin M. Boyd, and Jun Ye. Narrow line cooling: Finite photon recoil dynamics. *Physical Review Letters*, 93(7):1–4, August 2004.
- [Ludlow, 2008] Andrew D. Ludlow. *The Strontium Optical Lattice Clock: Optical Spectroscopy with Sub-Hertz Accuracy*. PhD thesis, University of Colorado at Boulder, May 2008.
- [MacAdam *et al.*, 1992] K. B. MacAdam, A. Steinbach, and C. Wieman. A narrow-band tunable diode laser system with grating feedback, and a saturated absorption spectrometer for Cs and Rb. *American Journal of Physics*, 60(12):1098–1111, December 1992.
- [Maxwell *et al.*, 2005] S. E. Maxwell, N. Brahms, R. deCarvalho, D. R. Glenn, J. S. Helton, S. V. Nguyen, D. Patterson, J. Petricka, D. DeMille, and J. M. Doyle. High-flux beam source for cold, slow atoms or molecules. *Physical Review Letters*, 95(173201):1–4, October 2005.
- [Mayle *et al.*, 2013] Michael Mayle, Goulven Quemener, Brandon P. Ruzic, and John L. Bohn. Scattering of ultracold molecules in the highly resonant regime. *Physical Review A*, 87(012709):1–8, January 2013.
- [McGuyer *et al.*, 2013] B. H. McGuyer, C. B. Osborn, M. McDonald, G. Reinaudi, W. Skomorowski, R. Moszynski, and T. Zelevinsky. Measurement of nonadiabatic effects in ultracold molecules via anomalous linear and quadratic Zeeman shifts. *Physical Review Letters*, 111(243003):1–5, December 2013.
- [Metcalf and van der Straten, 2002] Harold J. Metcalf and Peter van der Straten. *Laser Cooling and Trapping*. Springer, New York, 2002.

- [Nagel *et al.*, 2005] S. B. Nagel, P. G. Mickelson, A. D. Saenz, Y. N. Martinez, Y. C. Chen, T. C. Killian, P. Pellegrini, and R. Cote. Photoassociative spectroscopy at long range in ultracold strontium. *Physical Review Letters*, 94(083004):1–4, March 2005.
- [Napolitano *et al.*, 1994] Reginaldo Napolitano, John Weiner, Carl J. Williams, and Paul S. Julienne. Line shapes of high resolution photoassociation spectra of optically cooled atoms. *Physical Review Letters*, 73(10):1–4, September 1994.
- [Nash, 1990] P. Nash. *ASM Binary Alloy Phase Diagrams*. ASM International, Materials Park, OH, 1990.
- [Nicholson *et al.*, 2012] T. L. Nicholson, M. J. Martin, J. R. Williams, B. J. Bloom, M. Bishof, M. D. Swallows, S. L. Campbell, and J. Ye. Comparison of two independent Sr optical clocks. *Physical Review Letters*, 109(230801):1–5, December 2012.
- [Ovchinnikov, 2008] Y. B. Ovchinnikov. A permanent Zeeman slower for Sr atomic clock. *The European Physical Journal Special Topics*, 163:95–100, 2008.
- [Patterson and Doyle, 2007] David Patterson and John M. Doyle. Bright, guided molecular beam with hydrodynamic enhancement. *The Journal of Chemical Physics*, 126(154307):1–5, April 2007.
- [Patterson *et al.*, 2009] David Patterson, Julia Rasmussen, and John M. Doyle. Intense atomic and molecular beams via neon buffer-gas cooling. *New Journal of Physics*, 11(055018):1–12, May 2009.
- [Peters *et al.*, 1999] Achim Peters, Keng Yeow Chung, and Steven Chu. Measurement of gravitational acceleration by dropping atoms. *Nature*, 400:849–852, August 1999.
- [Phillips and Metcalf, 1982] William D. Phillips and Harold Metcalf. Laser deceleration of an atomic beam. *Physical Review Letters*, 48(9):596–599, March 1982.
- [Phillips, 1998] William D. Phillips. Laser cooling and trapping of neutral atoms. *Reviews of Modern Physics*, 70(3):721–741, July 1998.
- [Preston, 1996] Daryl W. Preston. Doppler-free saturated absorption: Laser spectroscopy. *American Journal of Physics*, 64(11):1432–1436, November 1996.

- [Reinaudi *et al.*, 2007] G. Reinaudi, T. Lahaye, Z. Wang, and D. Guery-Odelin. Strong saturation absorption imaging of dense clouds of ultracold atoms. *Optics Letters*, 32(21):3143–3145, November 2007.
- [Reinaudi *et al.*, 2012a] G. Reinaudi, C. B. Osborn, K. Bega, and T. Zelevinsky. Dynamically configurable and optimizable Zeeman slower using permanent magnets and servomotors. *Journal of the Optical Society of America B*, 29(4):729–733, April 2012.
- [Reinaudi *et al.*, 2012b] G. Reinaudi, C. B. Osborn, M. McDonald, S. Kotochigova, and T. Zelevinsky. Optical production of stable ultracold $^{88}\text{Sr}_2$ molecules. *Physical Review Letters*, 109(115303):1–5, September 2012.
- [Salumbides *et al.*, 2011] E. J. Salumbides, G. D. Dickenson, T. I Ivanov, and W. Ubachs. QED effects in molecules: Test on rotational quantum states of H_2 . *Physical Review Letters*, 107(043005):1–4, July 2011.
- [Shelkovnikov *et al.*, 2008] A. Shelkovnikov, R. J. Butcher, C. Chardonnet, and A. Amy-Klein. Stability of the proton-to-electron mass ratio. *Physical Review Letters*, 100(150801):1–4, April 2008.
- [Simon *et al.*, 2011] Jonathan Simon, Waseem S. Bakr, Ruichao Ma, M. Eric Tai, Philipp M. Preiss, and Markus Greiner. Quantum simulation of antiferromagnetic spin chains in an optical lattice. *Nature*, 472:307–313, April 2011.
- [Skomorowski *et al.*, 2012a] Wojciech Skomorowski, Robert Moszynski, and Christiane P. Koch. Formation of deeply bound ultracold Sr_2 molecules by photoassociation near the $^1\text{S}+^3\text{P}_1$ intercombination line. *Physical Review A*, 85(043414):1–10, April 2012.
- [Skomorowski *et al.*, 2012b] Wojciech Skomorowski, Filip Pawlowski, Christiane P. Koch, and Robert Moszynski. Rovibrational dynamics of the strontium molecule in the $a^1\Sigma_u^+$, $c^3\Pi_u$, and $a^3\Sigma_u^+$ manifold from state-of-the-art ab initio calculations. *The Journal of Chemical Physics*, 136(194306):1–13, May 2012.
- [Stan and Ketterle, 2005] C. A. Stan and W. Ketterle. Multiple species atom source for laser-cooling experiments. *Review of Scientific Instruments*, 76(063113), 2005.

- [Stein *et al.*, 2011] A. Stein, H. Knockel, and E. Tiemann. The states $1^1\Sigma_u^+$, $1^1\Pi_u$ and $2^1\Sigma_u^+$ of Sr_2 studied by Fourier-transform spectroscopy. *The European Physical Journal D*, 64(2):227–238, October 2011.
- [Stuhl *et al.*, 2012] Benjamin K. Stuhl, Matthew T. Hummon, Mark Yeo, Goulven Quemener, John L. Bohn, and Jun Ye. Evaporative cooling of the dipolar hydroxyl radical. *Nature*, 492:396–400, December 2012.
- [Targat *et al.*, 2005] R. Le Targat, J.-J. Zondy, and P. Lemonde. 75%-efficiency blue generation from an intracavity PPKTP frequency doubler. *Optics Communications*, 247:471–481, November 2005.
- [Thorsheim *et al.*, 1987] H. R. Thorsheim, J. Weiner, and P. S. Julienne. Laser-induced photoassociation of ultracold sodium atoms. *Physical Review Letters*, 58(23):1–4, June 1987.
- [Ulmanis *et al.*, 2012] Juris Ulmanis, Johannes Deiglmayr, Marc Repp, Roland Wester, and Matthias Weidemuller. Ultracold molecules formed by photoassociation: Heteronuclear dimers, inelastic collisions, and interactions with ultrashort laser pulses. *Chemical Reviews*, 112:4890–4927, 2012.
- [Ungar *et al.*, 1989] P. J. Ungar, D. S. Weiss, E. Riis, and Steven Chu. Optical molasses and multilevel atoms: theory. *Journal of the Optical Society of America B*, 6(11):2058–2071, November 1989.
- [Vogel *et al.*, 1999] Kurt R. Vogel, Timothy P. Dinneen, Alan Gallagher, and John L. Hall. Narrow-line doppler cooling of strontium to the recoil limit. *IEEE Transactions on Instrumentation and Measurement*, 48(2):618–621, April 1999.
- [Walpole, 1996] J. N. Walpole. Semiconductor amplifiers and lasers with tapered gain regions. *Optical and Quantum Electronics*, 28:623–645, February 1996.
- [Wang *et al.*, 2010] D. Wang, B. Neyenhuis, M. H. G. de Miranda, K. K. Ni, S. Ospelkaus, D. S. Jin, and J. Ye. Direct absorption imaging of ultracold polar molecules. *Physical Review A*, 81(061404):1–4, June 2010.

- [Wieman and Hansch, 1976] C. Wieman and T. W. Hansch. Doppler-free laser polarization spectroscopy. *Physical Review Letters*, 36(20):1–4, May 1976.
- [Xu *et al.*, 2003] Xinye Xu, Thomas H. Loftus, John L. Hall, Alan Gallagher, and Jun Ye. Cooling and trapping of atomic strontium. *The Journal of the Optical Society of America B*, 20(5):968–976, May 2003.
- [Yan *et al.*, 2013] Bo Yan, Steven A. Moses, Bryce Gadway, Jacob P. Covey, Kaden R. A. Hazzard, Anna Maria Rey, Deborah S. Jin, and Jun Ye. Observation of dipolar spin-exchange interactions with lattice-confined polar molecules. *Nature*, 501:521–525, September 2013.
- [Yasuda and Katori, 2004] Masami Yasuda and Hidetoshi Katori. Lifetime measurement of the 3P_2 metastable state of strontium atoms. *Physical Review Letters*, 92(15):1–4, April 2004.
- [Zelevinsky *et al.*, 2006] T. Zelevinsky, M. M. Boyd, A. D. Ludlow, T. Ido, J. Ye, R. Ciurylo, P. Naidon, and P. S. Julienne. Narrow line photoassociation in an optical lattice. *Physical Review Letters*, 96(203201):1–4, May 2006.
- [Zelevinsky *et al.*, 2008] T. Zelevinsky, S. Kotochigova, and Jun Ye. Precision test of mass-ratio variations in lattice-confined ultracold molecules. *Physical Review Letters*, 100(043201):1–4, February 2008.